MICROWAVE PERFORMANCE AND APPLICATIONS OF ADDITIVE MANUFACTURED COMPONENTS

Richard James Gumbleton
School of Engineering
Cardiff University

A thesis submitted to Cardiff University
for the Degree of Doctor of Philosophy

June 2021

ABSTRACT

Additive manufactured (AM) metals are of increasing interest for their performance in passive microwave applications, however several barriers exist to their large scale uptake. This thesis hopes to help address some of these barriers through the contribution of novel microwave techniques for the characterisation of metal AM parts and reporting of results from supporting experimental studies.

A novel parallel plate resonator fixture is developed for the accurate measurement of the surface resistance of flat metal plates produced by AM. This allows for microwave current flow in two orthogonal directions by simply exciting a different resonant mode. This has significance for the detection of anisotropy in a given plane that might arise through the laser scan path or vertical layer boundaries, for example, and is used here to assess the performance of individual wall surfaces, as they might appear in a manufactured waveguide component.

Experimental studies are performed on the use of AM processes parameters to optimise the manufactured surfaces for low microwave loss, as well as quantifying the effects of several commonly used post-processing treatments. Improving microwave performance of unsupported, downward facing, surfaces is of particular interest and is investigated in this thesis, culminating in a $\sim 40\%$ reduction in surface resistance.

Finally, a focus on practical applications in satellite technology is given through the evaluation of thermal properties of AM parts. A technique is described that uses fractional frequency shifts to evaluate the thermal expansion (CTE) of a cylindrical AM microwave cavity over an extreme temperature range (6–450 K) without the need for strict calibration. To the authors knowledge, this is the first time that CTE has been assessed over such a wide temperature range for AM parts, as is appropriate for space based components, using a passive microwave structure that can be adopted in a satellite communications system.

ACKNOWLEDGEMENTS

The time I have spent at Cardiff University has been enriched by the support and guidance of my supervisory team, *Prof. Adrian Porch* and *Dr. Jonny Lees*. In particular, I would like to express my sincere gratitude and appreciation towards *Prof. Adrian Porch* for his mentorship and friendship, which have been vital in the pursuit of the research contained within this thesis.

I wish to acknowledge the financial and technical support of Renishaw PLC. My thanks go especially to *Dr. Kenneth Nai* for many insightful conversations and technical discussions regarding the additive manufacturing process.

My friends and colleagues at the Centre for High Frequency Engineering have gone a long way to making this work possible. Special thanks goes to *Dr. Sam Hefford, Dr. Mike Barter, Dr. Heungjae Choi, Dr. Jerome Cuenca, Rob Batson* and *Jaafar Harari* who ensured that the office was filled laughter, stimulation and warmth. They will forever have my gratitude. I also wish to extend my thanks to all the staff in the Engineering workshops, *Andrew Rankmore, Denley Slade, David Billings*, to mention a few.

A particular source of inspiration was my friend *Dr. Nyle Parker*, whose infectious enthusiasm kept me moving forward. He is missed greatly.

Finally, I would like to offer my thanks to my amazing family. To my Parents, *Carolyn* and *Mark*, and to my brothers, *Simon* and *Nigel*, for their unwavering support and belief in me. To my wife, *Beth*, to whom I am eternally grateful for her encouragement, love and patience. And to my son, *Ellis*, for the overwhelming joy he has brought to my life.

PUBLICATIONS

Published (Peer-reviewed)

International Journal Papers

R. Gumbleton, J. A. Cuenca, G. M. Klemencic, N, Jones and A. Porch, 'Evaluating the Coefficient of Thermal Expansion of Additive Manufactured AlSi10Mg using Microwave Techniques', *Additive Manufacturing*, vol. 30, Art no. 100841, 2019. *DOI: 10.1016/j.addma.2019.100841.*

R. Gumbleton, J. A. Cuenca, S. Hefford, K. Nai and A. Porch, 'Measurement Technique for Microwave Surface Resistance of Additive Manufactured Metals', *IEEE Transactions on Microwave Theory and Techniques,* vol. 69, no. 1, pp. 189-197, 2021. *DOI: 10.1109/tmtt.2020.3035082.*

R. Gumbleton, R. Batson, K. Nai and A. Porch, 'Effect of Build Orientation and Laser Power on Microwave Loss in Metal Additive Manufactured Components', *IEEE Access,* vol. 9, pp. 44514-44520, 2021. *DOI: 10.1109/ACCESS.2021.3067306.*

S. Hefford, N. Clark, R. Gumbleton and A. Porch, 'Lift-Off Dielectric Resonator for the Microwave Surface Resistance Measurement of Metal Plates', *IEEE Transactions on Instrumentation and Measurement,* vol. 70, Art no. 8002208, 2021. *DOI: 10.1109/TIM.2020.3040834.*

Conference Proceedings

R. Gumbleton, K. Nai, S. Hefford and A. Porch, 'Effects of Post Processing Techniques on the Microwave Performance of Additively Manufactured Samples', in *Proceedings of 13th European Conference on Antennas and Propagation (EuCAP)*, 2019, Krakow. *INSPEC Accession number: 18775805.*

N. Parker, J. A. Cuenca, R. Gumbleton, A. Dimitriou, G. Ormondroyd and D. Slocombe, 'Broadband Dielectric Measurement & Simulation of E-field Curing Systems', in *Proceedings of Timber 2018,* pp. 89-98, 2018, London.

Submitted (Under peer-review)

R. Batson, R. Gumbleton, S. Hefford, K. Nai and A. Porch, 'Microwave Surface Resistance of As-grown and Post-processed Additive Manufactured Metal Parts', *Ampere Conference 2021*, -Under Review.

ABBREVIATIONS

AC	Alternating Current
ALM	Additive Layer Manufacture
AM	Additive Manufacturing
CNC	Computer Numeric Control
CTE	Coefficient of Thermal Expansion
DC	Direct Current
DR	Dielectric Resonator
EM	Electromagnetic
LED	Laser Energy Density
LODR	‘Lift off’ Dielectric Resonator
OMT	Ortho Mode Transducer
PBF	Powder Bed Fusion
PPR	Parallel Plate Resonator
Q Factor	Quality Factor
RMS	Root-Mean-Squared
TE	Transverse Electric
TEM	Transverse Electromagnetic
TM	Transverse Magnetic
VNA	Vector Network Analyser

TABLE OF CONTENTS

CHAPTER 1

INTRODUCTION

1.1 Introduction and Motivation

Additive manufacturing (AM) is described as the 'process of joining materials to make objects from 3D model data, usually layer upon layer' [1]. The first introductions into AM technologies appear in the 1980s as a method for prototyping new designs. In recent years, with improvements in geometrical accuracy and material properties, there has been significant interest in the transition of AM from a rapid prototyping tool to an industrial production method [2, 3].

Several recent reports have highlighted the potential of AM technology growth within the global manufacturing sector, with estimations that AM products and services worldwide were worth $\sim$ \$6bn in 2017 and continually growing [4]. This sum however represents only 0.05% of the global manufacturing market, a share which is expected to grow rapidly. In the UK, AM has been identified as a 'priority technology' to develop as a national competency [5], where areas of existing expertise, such as healthcare, motor sports and aerospace have already been active in the use of AM technology, albeit currently on a relatively small scale [6]. Some business case drivers for industrial uptake include: reduction in part and tooling costs, reduction of waste material through powder recycling and exploiting benefits from redistributed manufacturing [7]. Furthermore, with continued technological developments and enhancements in green electricity production, AM may be able to offer improved environmental impact when compared to conventional manufacturing [8].

Manufacturing systems for metal powder bed fusion (PBF), one form of AM, such as the Renishaw AM250 and RenAM500, are capable of producing near full density parts [9] with the benefits of significant weight reduction [10] and increased geometric design freedom [11] compared with subtractive manufacturing methods. From an engineering point of view, the use of under-utilised technologies such as PBF depends on a comprehensive understanding of how the final product will perform in a given environment. Mechanical properties of PBF parts such as hardness [12, 13, 14], tensile strength [15, 16, 17] and ductility [18, 19, 20], to name a few, are well represented in academic literature. For aerospace applications the knowledge of such properties, along with the promised weight reduction that AM offers is highly desirable, with AM having been identified as an enabling technology for next-generation microwave / communications devices [21]. However, AM adoption for aerospace applications is still in its relative infancy [22] due to the limited knowledge available on the material electrical properties. The relatively poor surface finish of AM parts, suggesting poor microwave performance, perhaps leads to an assumption that the surfaces will require heavy post-processing and may be an inhibiting factor in uptake.

The main theme of this thesis is to investigate the application of PBF processes to the production of passive microwave devices, as applicable for aerospace applications, through the evaluation of material electrical and thermal properties. A variety of metal powders are available for PBF, including titanium, steel, nickel and cobalt alloys. However, due to its higher electrical conductivity, that is demanded by passive microwave devices, an aluminium alloy (AlSi10Mg) is used throughout this thesis.

1.2 Research Goals

The research goals outlined here have been developed in partnership with the commercial / industrial sponsor, Renishaw plc. To thoroughly understand and test the microwave surface resistance of PBF parts a compact, accurate and easy to use test fixture is to be developed. Any three-dimensional structure, such as a microwave waveguide section, will contain surfaces of various orientations, therefore the test fixture should be capable of testing each surface individually. Complementary to the test fixture, a simulated waveguide model is to be developed where individual surface properties can be combined into a three-dimensional component. Microwave performance of PBF parts with and without undergoing post processing treatments will be investigated and thermal expansion will be measured over typical space environment thermal cycling ranges.

1.3 Thesis Summary and Original Contributions

Having established the motivation and objectives for the body of work, this thesis can be broken down into four primary areas of research;

1. Development of microwave cavity resonator fixtures to aid in the measurement of surface resistance.
2. Effects of process parameters on the microwave performance of PBF surfaces.
3. Effect of post-processing methods on the microwave performance of PBF surfaces.
4. Thermal characterisation of AlSi10Mg for space applications.

Each research area will be covered in detail in their own chapter; a summary of which is included below.

Chapter 2: Literature Review and Background

This chapter covers an introduction to the powder bed fusion process (including common terminology used throughout this thesis) as well as a review of previously published works on PBF state of the art, material properties and industrial uptake. A summary of additive manufacturing of passive microwave components is also included. An overview of microwave measurement theory and techniques already existing in literature is provided and common post processing methods are also described.

Chapter 3: Microwave Measurement of Surface resistance

In this chapter two measurement techniques are presented for the evaluation of microwave surface resistance. Firstly an established 'lift off' dielectric resonator (LODR) technique developed over the course of previous projects and utilised in some measurements within this thesis. Secondly a novel parallel plate resonator technique designed specifically for use with PBF material samples.

An overview of the LODR fixture is given, including a description of the unique calibration technique where the z position of the dielectric puck is varied; with the resulting quality factor (Q) measurements fitted to a characteristic equation. The curve fitting process allows for extraction of dielectric loss ($\tan\delta$) and surface resistance without the need for additional test fixtures. Simulation, calibration and initial measurement results are presented, along with descriptions of the geometrical factor and dielectric filling factor calculations.

The main section of this chapter is used to provide detailed development and design information regarding a novel microwave cavity resonator for PBF sample measurements. The cavity is based on a parallel plate geometry and operates at 5.3 and 6.4 GHz by exciting two orthogonal resonant mode; each mode inducing a one directional surface current in the sample-under-test, with 90^o rotation between modes. The orthogonality of the resonant modes and induced currents allows for direct compression between the surface resistance seen by currents flowing in x and y directions; assessing isotropy without the need for removal and re-fixing the sample. A combination of an a-Priori calibration step, detailed finite element model simulations and careful geometry design leads to a measurement technique with very low error. Design equations, simulations and initial measurement results are presented for several design iterations.

Original Contributions arising from Chapter 3

- A novel microwave cavity resonator for measuring surface resistance in flat PBF samples.

These original contributions have resulted in the publication of a peer-reviewed journal article [23].

Chapter 4: Effect of PBF Process Parameters on Surface Resistance

Here an investigation is undertaken into the influence of various process parameters on measured surface resistance. Firstly the effect of build orientation is considered through the measurement of samples manufactured in horizontal, vertical and 45^o (relative to the build plate) build orientations. Secondly, a variety of process laser powers are applied to specific parameter sets to consider the effect of laser energy density on surface resistance. The chapter is concluded by investigating the influences of the laser scan path through the creation of directional roughness profiles in theoretical best and worse case scenarios relating to microwave current flow. Supporting simulations of the microwave loss relationship to surface roughness are also presented.

Original Contributions arising from Chapter 4

- Major variations in microwave surface resistance are described between various build orientations.
- A correlation is established between an increase in down skin laser power and a reduction is surface resistance of downward facing surfaces.
- x-y plane surface resistance is found to be isotropic for AlSi10Mg samples produced in a horizontal orientation.

These original contributions have resulted in the publication of a peer-reviewed journal article [24].

Chapter 5: Effect of Post-Build Treatments on Surface Resistance

This chapter focuses on forming comparisons between 'as built' PBF samples and equivalent samples that have undergone a variety of post processing treatments. The LODR fixture is utilised for the measurement of surface resistance. Post-processing techniques investigated include silver plating, mirror finish polishing and various deburring methods.

The chapter concludes with use of the measured surface resistance values to create a finite element model of a C-band waveguide filter, thus highlighting the effect that different build orientations of individual internal surfaces can have on the overall microwave performance of a passive waveguide component.

Original Contributions arising from Chapter 5

- Silver plating reduces surface resistance of PBF samples to a value comparable with copper PCB. It also significantly improves the disparity between the surface resistance of horizontal and vertical orientated samples.
- Near-mirror finish polishing of horizontal and vertical orientated PBF samples produced surface resistance values comparable with each other, as well as that of an equivalent treated bulk aluminium sample; the increase in microwave loss of PBF samples is mainly attributed to the increased surface roughness.

These original contributions have resulted in the publication of a peer-reviewed conference paper [25].

Chapter 6: Microwave Evaluation of Thermal Expansion

The final experimental chapter aims to investigate thermal properties of PBF components by utilising a lesser known fractional-frequency shift microwave technique. Introductory details are given on the importance of understanding thermal expansion of PBF parts if uptake in applications such as satellite communications is to be further expanded, where parts are usually exposed to extreme variations in temperature. The theory behind the fractional frequency shift technique and how it enables the extraction of the thermal expansion coefficient is described in detail, along with the extraction of surface resistance for the microwave S-

Parameter data. The benefit of performing testing on a functional microwave component against traditional measurement methods is expressed. The measurement data presented included fractional frequency shift, coefficient of thermal expansion, Q factor and surface resistance; all as a function of changing thermal conditions.

Original Contributions arising from Chapter 6

- The coefficient of thermal expansion of AlSi10Mg produced by PBF is measured over an extreme temperature range (6 - 450 K); greater that the typical thermal cycling experienced by satellite components in space.

- A lesser known microwave technique is employed allowing for thermal characterisation of the PBF material using a passive microwave structure that could be adopted in a satellite communications system.

These original contributions have resulted in the publication of a peer-reviewed journal article [26].

CHAPTER 2
LITERATURE REVIEW AND BACKGROUND

This chapter presents a review of the current 'state of the art' for microwave devices produced by additive manufacturing, including summaries of the fundamental analysis of microwave loss and AM processes and parameters. An appraisal is conducted into the current methods presented in literature for assessing microwave performance of AM components, measurement the electrical and thermal properties of the formed material and the common post processing techniques required for microwave applications.

2.1 Additive Manufacturing for Microwave Applications

2.1.1 Additive Manufacturing Overview

Additive manufacturing, or '3-D printing' is a modern fabrication process that enables three-dimensional components to be built using multiple two-dimensional layers. This form of manufacturing is becoming increasingly common as technological developments allow for greater confidence in material performance, reduction in single-part build costs [27] and reduced time-to-market for new designs [28]. Many flavours of AM processes exist using a wide range of materials. One of the earliest forms of AM consisted of cutting patterns from sheets of paper before layering them with adhesive into a three-dimensional part [29]. Modern technological advancement make this process seem rather primitive. The main categories of modern AM systems include 'Liquid Polymer', 'Molten Material' and 'Discrete Particle'. Liquid polymer systems, used in processes such as stereo-lithography, employ a vat of liquid resin which is cured by a source in a two-dimensional pattern before the build platform is moved vertically to allow the next layer of liquid resin to cover the three-dimensional part; a schematic

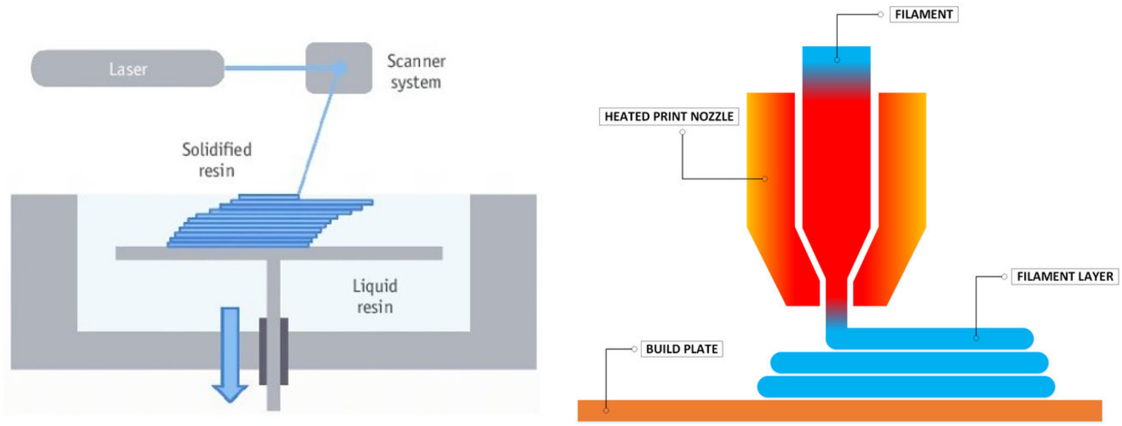

a) b)

Figure 2.1: Representation of a) Liquid Polymer and b) Molten Material additive layer manufacturing systems. Reprinted from [32] ©2016 Kim et al. (CC-BY-NC), and [33] ©2020 Cao et al. (CC-BY), respectively.

of the process is shown in Figure. 2.1a. Molten material systems use a material extrusion design and have recently found a new market amongst hobbyists. In fact, fusion deposition modeling, one form of Molten material system, is currently the most popular AM technology in use [30]. These systems often use polymer filaments, but some are capable of using bound metal [31], melted through a heated print nozzle and deposited on the build plate. The process is repeated over successive layers to build the three-dimensional part. A schematic of molten material system principles is shown in Figure. 2.1b.

With relation to this thesis topic, passive microwave applications, several studies have used polymer AM with an additional post-process metalisation. Geterud et al. [35] utilized an electroless plating procedure where upwards of 5μm thickness of copper is deposited on polymer waveguide sections produced through various types of AM, leading to conductive and functional components with drastically reduced weight. Genc et al. [34] used fused deposition modeling to fabricate a series of pyramidal horn antennas, shown in Figure. 2.2, plating each with a different metal coating. Copper, Chromium and Nickel were investigated and whilst all metalisations produced working antennas, perhaps unsurprisingly the copper plated version showed highest achieved gain of the

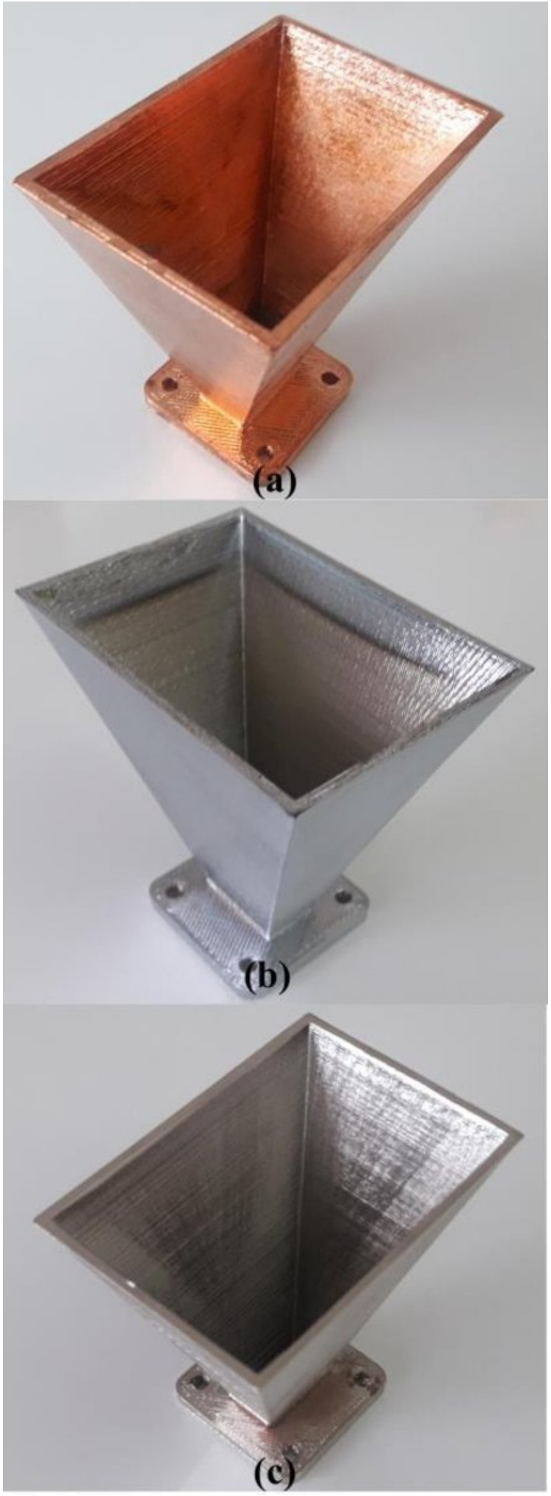

Figure 2.2: Genc et al. antenna horn manufactured by fused deposition modeling. Coated with a) copper, b) chromium and c) nickel. Reprinted from [34] ©2017 IEEE.

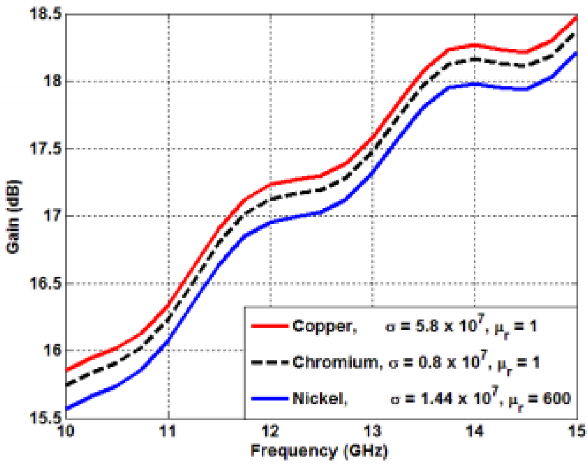

Figure 2.3: Genc et al. additive manufactured antenna horn gain results. Reprinted from [34] ©2017 IEEE.

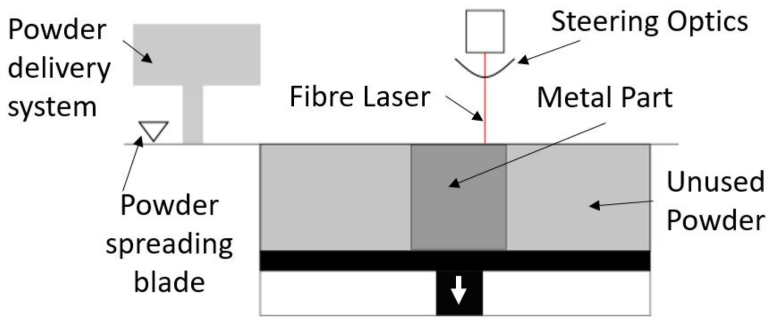

Figure 2.4: Representation of a powder bed fusion process; A discrete particle additive layer manufacturing system. Reprinted from [26] ©2019 Gumbleton et al. (CC-BY).

three materials, as shown in Figure. 2.3. However, these studies and others [36, 37, 38], have not compared the measured performance to current commercially available alternatives or considered the power handling and thermal properties of the polymer base in extreme operating conditions; as might be expected in aerospace applications.

Perhaps the largest area of interest for AM in passive microwave application is the discrete particle systems mentioned above. One example of this AM process is metal powder bed fusion (PBF), where layers of atomised metal powder are consecutively melted using a high powered laser into two-dimensional patterns, with each layer contributing to the three dimensional build; a representation is shown in Figure. 2.4. The potential of PBF for the production of passive microwave devices is exciting due to possibility of producing near full density (99.8%) parts while offering upto 50% weight reduction over traditionally manufactured alternatives [10]. PBF processes have also opened up new possibilities for the manufacture of novel three-dimensional, passive, microwave devices with previously un-realisable design freedom.

2.1.2 Application to Passive Microwave Devices

Amongst the early adopters of AM outside of academia, Airbus Defence and Space have been at the forefront of research into AM for microwave components. Early publications by Booth et al. described the use of AM to simplify the manufacture of Ortho Mode Transducers (OMT), which are some of the most complex feed chain components to manufacture [39]. The increased surface roughness present due to AM was somewhat offset by applying a silver plating process post-build. Additionally, through the monolithic design, the removal of flanges and multiple interconnects where losses tend to occur. Photographs of the traditional manufactured part and its AM equivalent are shown in Figure. 2.5. This is one example where AM has been used to improve the manufacturing of an existing component design. More recently, Kilian et al. have published several further studies utilising the design freedom of AM to create increasingly complex monolithic assemblies [40], incorporating the OMT into a single part build with multiple other components. Perhaps the presented build that best summarises the opportunities realised through AM is a Ku-band feed cluster [41], shown in Figure. 2.6.

This assembly consists of 18 feed chains, each comprising an antenna horn, OMT, transition segment and waveguide routers, including flanges; replacing upwards of 72 individual components with a single piece. Each section was designed for additive manufacture; for example the traditional rectangular waveguide routers have been replaced with elliptical sections, which have similar wave propagation properties but have been shown to exhibit lower ohmic loss, as

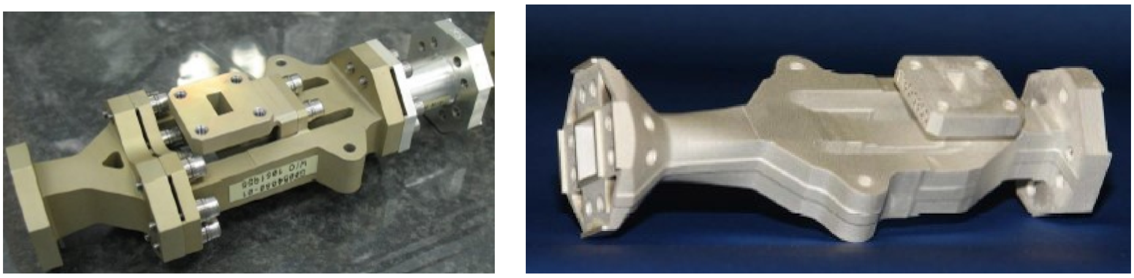

a) b)

Figure 2.5: Ortho Mode Transducers produced by a) multi part traditional manufacturing and b) monolithic additive manufacturing. Reprinted from [39] ©2017 IEEE.

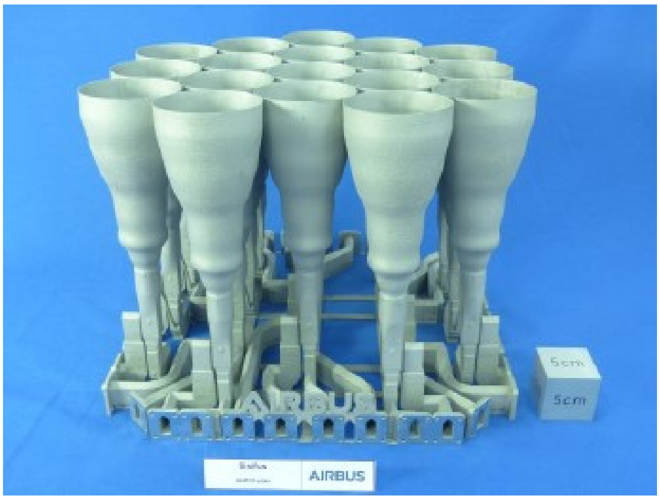

Figure 2.6: Single-part Ku-band Tx/Rx feed cluster. Reprinted from [41] ©2017 IEEE.

found by Booth et al. [42, 43] and Lorente et al. [44], and are easily produced through AM. Additionally, the whole assembly is orientated within the AM build chamber to minimise the area of downward facing surfaces, which would require supporting structures and often exhibit the highest surface roughness.

Underpinning the advances in complex assemblies are more fundamental investigations into optimised design geometries. Again Airbus have been a major contributor to this knowledge base through studies such as Kilian et al. [45] and the development of near free-form waveguide sections, as shown in Figure. 2.7. These developments allow for mass and quantity of components to be reduced and enables complex structures to be realised with minimal routing. Few other commercial companies share advancements in AM in the same manner as Air-

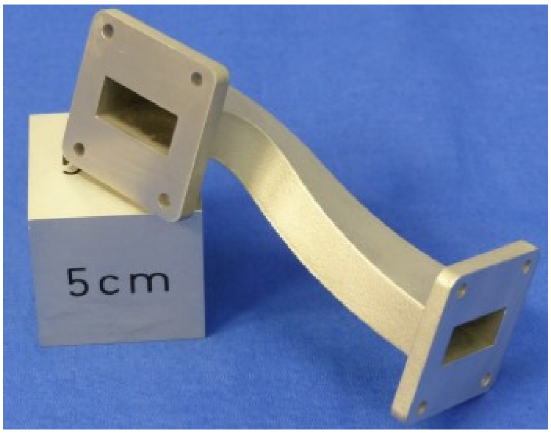

Figure 2.7: Near free-form waveguide section. Reprinted from [45]. ©2017 The Institute of Engineering and Technology.

Figure 2.8: Optimised Spline antennae horn produced by additive manufacturing. Reprinted from [46] ©2018 IEEE.

bus, but another exception is Thales, who have also published details of their AM manufactured components. Cailloce et al. have published studies on the the performance of spline horn antennas using aluminium and titanium alloys, optimised for low mass by thin walls and mesh structures, as shown in Figure. 2.8, as well as advanced single part clusters produced by AM [46]. Talom et al. also investigated different processing materials for microwave components in AM. This study found that the surface roughness of titanium built part was significantly lower that the aluminium equivalent and thus had a smaller influence on frequency shift in waveguide filters. However, the lower electrical conductivity meant that titanium built parts experience more loss [47]. Other contributing companies include Optisys, who have also developed novel iterations on the OMT using metal PBF and single part design [48] and The Mitre Corporation, building a frequency scaling, ultra-wideband phased array for satellite applications [49].

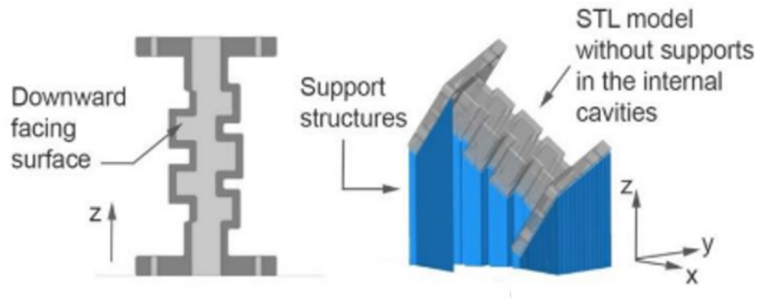

a)

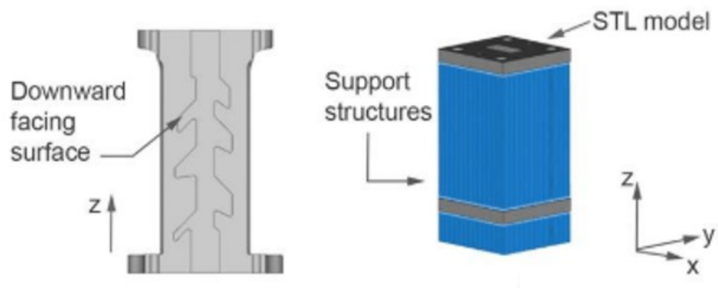

b)

Figure 2.9: Waveguide filter designs for production by additive manufacturing. a) traditional filter design, b) tilted downward facing surfaces. Reprinted from [50] ©2019 Calignano et al. (CC-BY).

From an academic perspective, there are several research groups investigating AM for microwave components. Perhaps the largest group of studies have been conducted by researchers at the Politecnico di Torino. Peverini et al. performed assessments of fundamental electromagnetic performance on standard waveguide filters produced by AM before optimising the design as to minimise the downward facing surfaces, which suffer increased roughness [51]. This design change is shown in Figure. 2.9, where each filter sub is 'tilted' and the part is manufactured vertically. The initial measurements were promising in that aluminium alloy could provide sufficiently low loss as to not require additional plating if correct decisions are made on the build orientation, although many studies still apply this additional, post-processing plating step to improve electrical performance. The possibility of foregoing plating is also observed by Hollenbeck et al., who compared waveguide attenuation values for commercial waveguides, AM and CNC equivalents [52]. As expected, the commercial waveguides were far superior in performance; however, the CNC and AM sections were relatively close in terms of attenuation, which is perhaps due to the requirement for the CNC section to be made in two pieces, such that the loss associated with surface roughness in the AM section is of the same order of magnitude as the loss associated with a seam along the H-plane of the CNC part. Calignano et al. further developed the 'tilted' filter design through a weight optimisation processes, achieving a 50% reduction in weight whilst maintaining filter performance [50].

Other microwave research groups have also performed studies using AM to implement their designs. Salek et al. fabricated rectangular waveguide filters using 'micro' laser sintering, where the laser spot size is $\sim$30 μm (much smaller than in typical PBF manufacturing systems). This increase in manufacturing accuracy enabled their design reach into the mm-wave regime, operating at approximately 100 GHz and with the use of copper plating a very good insertion loss was measured [53]. The additional plating was required in the first instance to offset the lower conductivity of the steel power used for the base manufacture but also, even with the reduced surface roughness ($\sim 5\mu$m), at such high frequencies the microwave loss is heavily dependent on the presence of surface features. This is consistent with other high frequency / millimeter wave studies utilising AM [54, 55]. Millimeter wave applications are becoming more relevant commercially, through for example collision avoidance, advanced communications and radar systems. However, the critical dimensions for such high frequency components is difficult to manufacture to a high quality with current commercially available AM systems. While at lower microwave frequencies AM has been used as an enabler for novel designs, such as 'quasi' elliptical inline filters presented by Rao et al. [56] or the 'slotted spherical resonator' filters proposed by Zhang et al. [57].

A significant theme of these studies is that the possibility for AM to enhance the aerospace supply chain is great, and this is not only for novel, ground breaking geometries, which are not necessarily achievable by traditional manufacturing methods; it is also for the simplification, reduction of lead time and the decrease in weight and physical size of more traditional components. In particular, despite the rough surface finish exhibited by AM components, the attenuation of waveguide structures is not drastically enhanced, at least in low microwave frequency applications (up to Ku band), as may have been expected (no more than a factor of two worse than traditional alternatives [58]). This leads to the prospect of improving performance through process optimisation and the desirable properties of requiring little or no post-processing between build and utilisation.

Within the Centre for High Frequency Engineering at Cardiff University, an alternative model for investigating microwave performance in AM parts has been initiated; to assess individual surfaces, as they would appear in 3D structures, using microwave cavity resonator techniques rather than measuring whole transmission line components in the 'macro approach' adopted by the studies mentioned above. Clark, Hefford and Porch have pioneered this approach and in the first instance examined the microwave loss exhibited by flat metal samples built in horizontal or vertical orientations [59]. Titanium alloy (Ti6Al4V), aluminium alloy (ALSi10Mg) and cobalt chrome alloy (CoCr) were investigated. Interestingly, all material samples built in a vertical orientation showed higher loss compared with an ideally flat, bulk metal, approximation (by a factor of $\sim$ 2-3), while the horizontal samples exhibited only slightly increased loss (by a factor of $\sim$ 1.1-1.5). This methodology has been extended and used throughout this thesis. A significant finding from Clark's work, which is discussed in more detail later in this chapter, was a deviation from the traditionally accepted correlation of microwave loss to RMS surface roughness. Rather, microwave performance is attributed to the distribution of roughness feature geometry and size, as opposed to the averaged peak-peak roughness height alone.

2.2 Surface Roughness and Microwave Loss

Surface resistance (R_S) is a key parameter when assessing the performance of conductive metal surfaces at microwave frequencies. Measurement and understanding the origin of enhanced R_S over the theoretical values for specific metals is important in the optimisation for low-loss microwave applications. In practice the manufacturing process alone will introduce surface features, which have been shown to strongly correlate with microwave loss and hence R_S [60, 61, 62, 63, 64, 59, 65]. R_S is defined as the real part of the ratio of tangential components of electric and magnetic fields at a metal surface; equivalently (and importantly for evaluating the performance of passive microwave devices) it is the power dissipated per unit area per unit parallel magnetic field at the surface of a metal. Electromagnetic (EM) wave analysis using the fourth of Maxwell's equations yields the following equation for Rs that demonstrates its dependence on key variables such as frequency f and conductivity σ (assuming the metal to be non-magnetic)

$$R_S = \sqrt{\frac{\pi f \mu_0}{\sigma}} \tag{2.1}$$

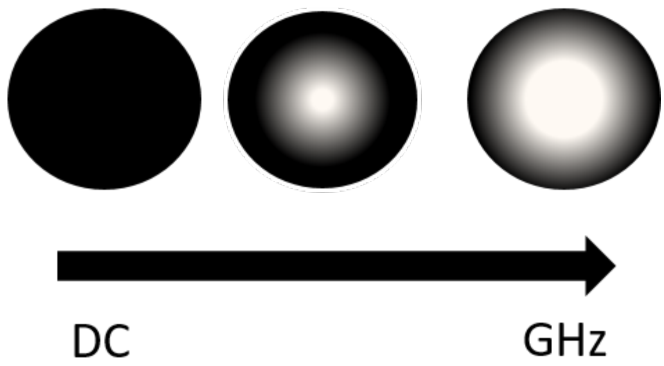

Figure 2.10: Current flow in a circular wire at different frequencies. Current flows in an increasing narrow layer at the extremities of the wire as frequency increases.

where μ_0 is the permeability of free space (H/m), f is the operating frequency (Hz) and σ is the electrical conductivity of the material. It should be noted that although R_S shares the same units (Ω) as the bulk resistance (R) of a material, these are two separate quantities. The DC value of R arises as the result of current flow over the whole cross-section of a metal component, but Rs arises owing to current flow very near the surface in a region called the skin depth (δ). The significance of R_S at microwave frequencies is due to the non-uniformly distributed alternating current within the conductor, where a high current density is concentrated near the surface. This phenomenon is known as the skin effect and the depth at which the majority of current (1 - 1/e = 63%) is carried is calculated as

$$\delta = \sqrt{\frac{1}{\pi f \mu_0 \sigma}} \tag{2.2}$$

For aluminium alloy AL6082 (of bulk conductivity $\sigma = 2.63\times10^7$ S/m) at a nominal frequency 5.3 GHz, it is calculated that $\delta = 1.96$ μm. Therefore, the majority of current will be carried in the outermost ≈ 2 μm of the material; we expect the surface roughness to be on a scale an order of magnitude larger than this and can have a significant impact on power loss. A simplistic representation of the skin depth in a cylindrical wire as a function of frequency is shown in Figure. 2.10. The current density associated with the skin effect decays

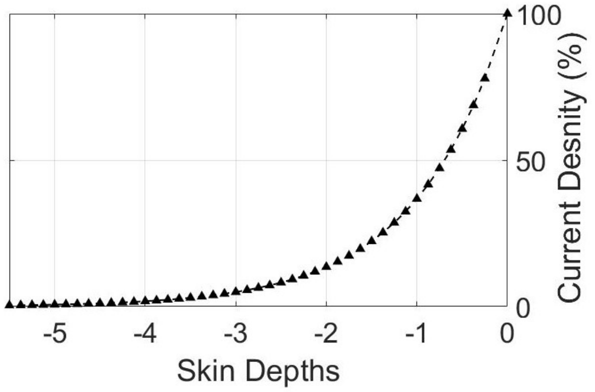

Figure 2.11: Current density decay as a function of skin depths into a conductor from its surface.

exponentially from the surface as a function of depth y into the conductor by

$$J_s(y) = J_0 e^{-y/\delta} \tag{2.3}$$

where J_0 is the current density at the surface ($y = 0$). This decay is shown graphically in Figure. 2.11, where one skin depth represents the distance into the material at which point the current density is $1/e$ or 37% of its surface value. When y=4δ into the conductor, 98% of current is flowing within this region of material.

2.2.1 Roughness and Performance

There is widespread acknowledgment that the presence of rough surfaces in microwave devices leads to an increase in resistive losses. Historically, the drive to understand and quantify this link lead to surface roughness being modeled as repeated, uniform, corrugations of arbitrary shape. Morgan, acknowledging that effective resistance had already been linked to the surface treatment of the material, was the first to present such a model directly linking surface roughness to microwave loss [63]. His work concluded that surface features (triangular or square profile) transverse to current flow have the effect of significantly increasing losses when the features are on the same scale as the skin depth. Hammerstad and Jenson adapted Morgan's results to present perhaps the most widely accepted and adopted surface roughness model for microwave loss estimations [66]. This was the first model to introduce a correction factor employed to the attenuation coefficient of transmission lines to account for surface roughness in a practical sense. Both Morgan's, and Hammerstad and Jeson's models use the ratio of RMS surface roughness to the skin depth to quantify excess losses. Hammerstad and Jenson's model is given by Equation. 2.4.

$$\alpha_{rough} = \alpha_{smooth} \times K \tag{2.4a}$$

where α_{smooth} is the calculated attenuation constant for a smooth conductor and K is the Hammerstad and Jenson correction factor

$$K = 1 + \frac{2}{\pi} tan^{-1} \left(1.4 \left[\frac{R_q}{\delta} \right] \right) \tag{2.4b}$$

where R_{q} is the RMS surface roughness.

Several later models proposing similar concepts are reported in literature, however, in all of these models the excess R_{S} tends to saturate at a correction factor of two as the ratio R_{q} / δ increases [67], so limiting their effectiveness to frequency ranges below around 5 GHz [68]. These important works on the effects of surface roughness on microwave loss have been seminal in the advancement of modeling and simulation tools [69] for EM applications; however, all rely on the RMS surface roughness in some form as the indicator for increased loss. Curran et al. [70] went someway further with this modeling to include edge effects and proximity effect in a unified model and introduced a "broad methodology" for analysis of resistive loss mechanisms, while still approximating roughness as idealised triangular corrugations. Many other works have also attempted to model roughness with this geometrical corrugation approach in various forms; conducting rigorous calculations on field magnitudes [71], adjusting the physical representation away from solid pyramid geometries [72] and developing three dimensions simulations of uniform periodic structures [73, 74], as well as showing

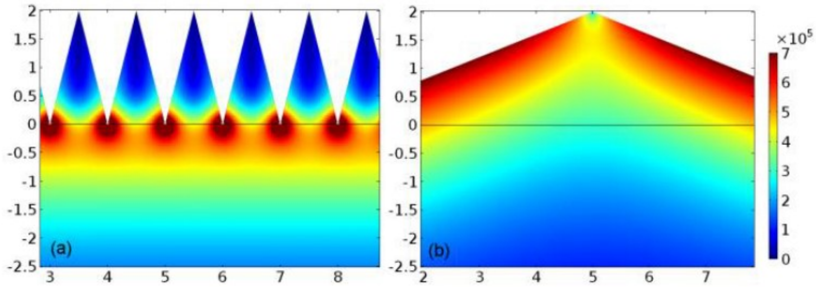

Figure 2.12: Simulation of induced current density (A/m^2) at 5,7 GHz for a) feature width = 1 μm and b) feature width = 10 μm. Reprinted from [59] ©2017 IEEE.

that the ×2 saturation of loss is a significant underestimation of experimental results [61, 75]. However, it may be observed that real-world roughness profiles are not simply constructed of uniform, homogeneous arbitrary geometries, but modeling of random roughness is not usually practical or indeed possible with the simulation tools we currently have at our disposal.

Clark et al. performed relatively simple 2D finite element model simulations, also on triangular grooves perpendicular to current flow, while adjusting not only the roughness peak height but also the feature width [59]. The simulated current density for the extremes of feature width are shown in Figure. 2.12. This current density profile shows that at these extremes current flow is not significantly impeded by the roughness peaks. Further to this, analysis of relative loss, displayed in Figure. 2.13, shows a clear relationship between roughness width (b) and skin depth. Specifically, when roughness peaks are approximately three times the skin depth maximum in loss is observed. Conversely, at the extremes of roughness width, microwave loss approximates to ideally flat surfaces. This study goes some way to understanding that, in reality, roughness profiles will have a variety of features sizes and perhaps it is a cumulative distribution rather than an RMS surface roughness that should be the key modeling parameter for high frequency loss estimation.

It should also be noted that in a transmission line structure that is generic to all of the passive components considered in this thesis, the information signal

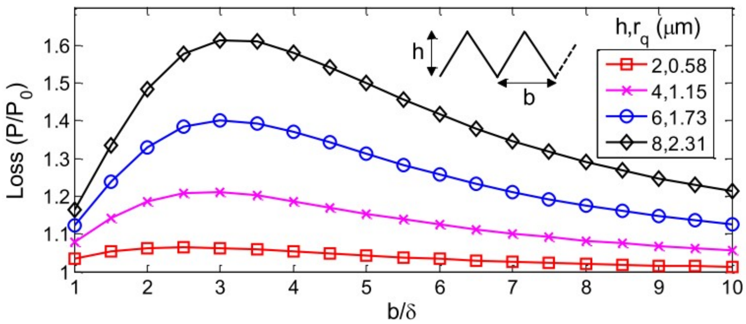

Figure 2.13: Simulated relative surface losses as a function of feature width relative to skin depth. Reprinted from [59] ©2017 IEEE.

is carried in the propagating EM wave confined by conducting boundaries. The conducing boundaries give rise to the attenuation of the EM fields penetrating into them such that roughness present on these boundaries serves to increase the surface area on which EM penetration occurs and hence leads to higher loss. The current flow shown in Figure.2.14, which follows the conductor profile, is a common assumption used in many loss models and describes the roughness peaks as discontinuities to current flow; this is perhaps misleading, as Figure.2.14 suggests that there is an increased current path length with increased roughness height at high frequencies (relative to the DC path length)[76]. Gold and Helmreich highlight the fundamental oversight that comes with modeling roughness as 2D grooves perpendicular to current flow by taking a 3D approach of the same problem [77], by assuming a current flow in a rough cylindrical conductor, where roughness peaks prolong the conductor length (l) by a factor K to give an effective conductor length (l_{eff}), the width (w_{eff}) and circumference (ζ_{eff}) of the conductor are also increased by K. In this case, the resistance per unit length is unchanged from that of a smooth conductor

$$R_{\text{rough}} = \frac{l_{\text{eff}}}{\sigma A_{\text{eff}}} = \frac{l_{\text{eff}}}{\sigma \delta \zeta_{\text{eff}}} = \frac{l}{\sigma \delta \zeta} \frac{K}{K} = R_{\text{smooth}} \tag{2.5}$$

Furthermore, Huray et al. [78, 79] state that the Fermi velocity of electrons in a good conductor (Copper) is $\approx 1.5 \times 10^6\ m/s$ whereas the EM wave propagating in the contained dielectric (or vacuum) is propagating at a speed of $v_{\text{p}} = c/\sqrt{\varepsilon_{\text{eff}}}$;

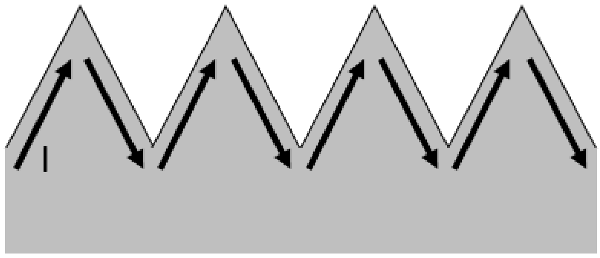

Figure 2.14: 2-D corrugated surface assumption behind the Hammerstad-Jenson model. Black arrows represent surface current flow at high frequencies.

where c is the speed of light in vacuum (3×10^8 m/s) and ε_{eff} is the relative permittivity of the media. This means that the propagating wave is traveling much faster than any charged particle could possibly move. Thus in order to sustain the propagating wave there must exist localised charge densities. Currents flowing the in the z direction transverse to roughness peaks in Figure. 2.14 are localised eddy currents rather than a signal current linked to the propagating EM wave in the adjacent media and as such the notion of roughness peaks acting as discontinuities to current flow is somewhat misleading.

2.2.2 Loss Measurement Techniques

Several methods for the evaluation of R_{S} using cavity resonance already exist and are represented well in literature; two main techniques have been established for this cause. The 'end wall' replacement of a resonant cavity structure [80, 81] and the use of dielectric resonator (DR) fixtures in various forms [82, 83, 84], perhaps most well known in the Hakki-Coleman implementation [85], shown in Figure. 2.15. In the 'end wall' replacement technique, the Q factor of the TE or TM mode of a cylindrical cavity resonator (usually manufactured of copper or aluminium) is measured. An end wall is then replaced with a planar sample of the study material and the change in Q factor can be used to extract R_{S}, relative to that of a reference sample. In the DR fixture approach, a low loss dielectric resonator material (e.g. sapphire) is suspended within a conductive shielding cavity with one wall replaced for the sample. When the dielectric is in close proximity to the sample the loss influence of the sample Q factor is greatest

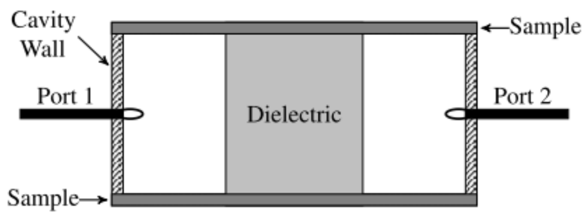

Figure 2.15: Illustration of the two-plate Hakki-Coleman dielectric setup. Where two parallel samples are measured simultaneously Reprinted from [86] ©2019 Hefford.

since it relies on the tangential magnetic field at the conductor surface

$$Q_c = \frac{\omega \mu_0 \iiint H^2 dv}{R_\mathrm{S} \iint H_t^2 ds} \tag{2.6}$$

where Q_c is the quality factor associated with conductive surfaces and ω is the angular frequency (Rad/s). DR fixtures with very high Q factors have been used for measuring superconducting films [90], which present the greatest challenges for R_S measurement owing to the extremely small R_S values for superconductors at microwave frequencies (around 0.1 mΩ for high temperature superconductors at 10GHz and 77K) and recently a modern lift off DR approach for additive manufactured parts with a high precision [59, 91, 25]. In both techniques resonant modes are chosen such that the induced current in the sample only has only azimuthal components [90, 82], appropriate for maximising sensitivity by avoiding current flow through the intersection of two pieces metal making up the outer cavity walls [92].

Although appropriate for maximising sensitivity, this means that only isotropic samples can be measured accurately. Owing to the layered nature of AM parts, and any anisotropy introduced as result of the laser scan pattern or build orientation used in their production. An alternative technique (described in Chapter. 3) is proposed within this thesis and is based upon the adaptation of a parallel plate resonator (PPR). PPR variations have been previously employed by Reible and Wilker [87], Gao et al. [88] and Taber [89] in studies on superconducting materials. These PPR methods involve dielectric spacers sandwiched between

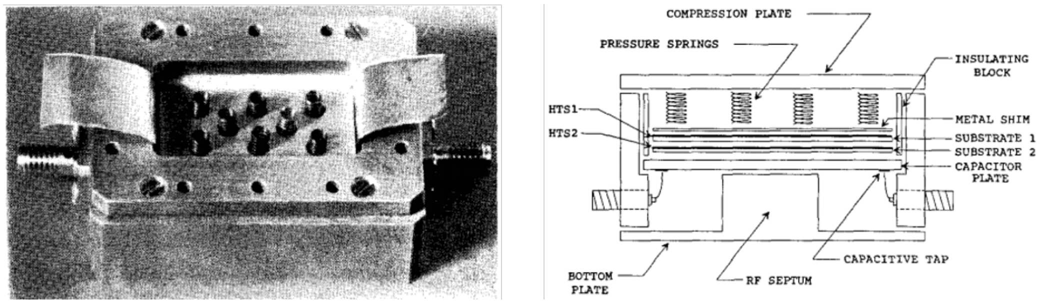

a)

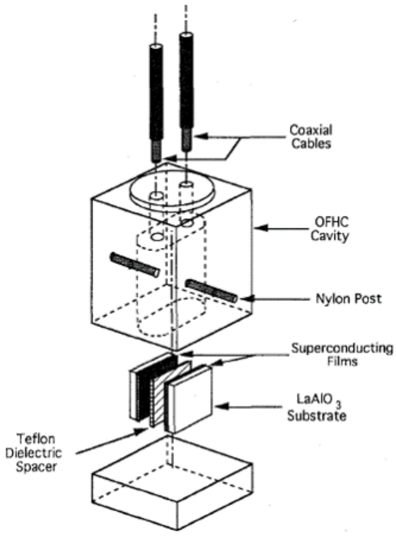

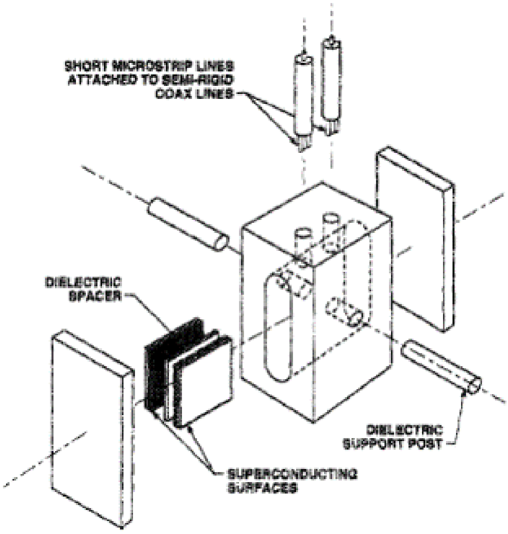

b) c)

Figure 2.16: Various parallel plate resonator implementations. a) Reible and Wilker, b) Gao et al. and c) Taber. Reprinted from [87] ©1991 IEEE, [88] ©1996 IEEE and [89] (with the permission of AIP Publishing), respectively.

superconducting films, which are compressed intimately together through a set of springs / rods external to the cavity as shown in Figure. 2.16. These versions necessitate highly complex and sensitive setups but are capable of generating uniform, directional current flow for measurement of HF losses. These structures will form the basis of the alternative PPR described in Chapter. 3.

2.3 Powder Bed Fusion: Process Parameters and Machine Data

Whilst discussing the use of AM for passive microwave applications, it is important to consider the mechanisms and parameters that define the manufacturing process itself. For the studies within this thesis, metal additive manufacturing is utilised in the form of powder bed fusion. Discussed below are the key parameters that may effect the outermost surfaces of built parts in which microwave currents will flow.

Throughout this thesis two Renishaw PBF systems are used; AM250 and RenAM500Q, shown in Figure. 2.17. There are some significant differences in the hardware between the two systems, outlined in Table. 2.1, however the fundamental process parameter considerations remain the same.

2.3.1 Powder Properties

The material of interest in this thesis is the commonly used AlSi10Mg Aluminium alloy powder. Its nominal chemical composition is shown in Table. 2.2. The

Feature	AM250	RenAM500Q
Laser	1 × 200/400 W	4 × 500 W
Focal Diameter (μm)	70	80
Build Volume (mm)	250 × 250 × 300	250 × 250 × 350
Max. Deposition Rate (cm^3/hr)	20	150

Table 2.1: Summary of key difference between Renishaw AM250 and RenAM500 metal additive manufacturing systems.

a) b)

Figure 2.17: Renishaw plc metal additive manufacturing systems. a) AM250 and b) RenAM500Q. Reprinted from from [93] ©2021 Renishaw plc.

Element	**Al**	**Si**	**Mg**	**Fe**	**N**	**O**	**Ti**	**Zn**	**Mn**	**Ni**	**Cu**	**Pb**	**Sn**
Mass%	Bal	10	0.35	0.25	0.20	0.20	0.15	0.10	0.10	0.05	0.05	0.02	0.02

Table 2.2: Nominal chemical composition of AlSi10Mg aluminium alloy powder for additive manufacturing applications.

material comprises aluminium with up to 10% mass fraction of silicon and small quantities of other elements such as magnesium. The silicon present helps to improve the fluidity of the melt pool while the addition of magnesium makes the alloy both harder and stronger than pure aluminium [94]. The metal powders used in PBF are manufactured through a process called atomisation, the most common of which is gas atomisation, where a stream of falling, molten, metal is acted upon by inert gas jets. Disrupting the metal flow into small spherical particles of molten metal which cool as they fall and are ultimately collected as powder. A generic representation of this process is shown in Figure. 2.18.

In general, the powder diameters for PBF applications are within the range of 15 - 45 μm [96] for 'raw' powder. The raw powder however is very expensive and unused powder from a build is generally recycled for economic reasons. It is accepted that re-used power will generally have a different size distribution than

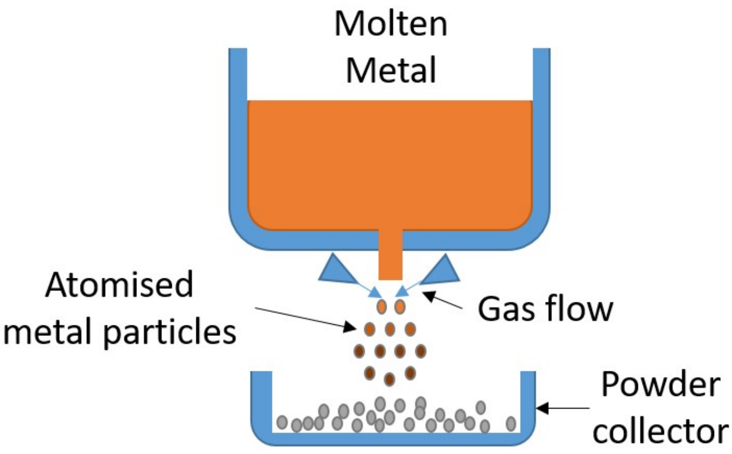

Figure 2.18: Gas atomisation process.

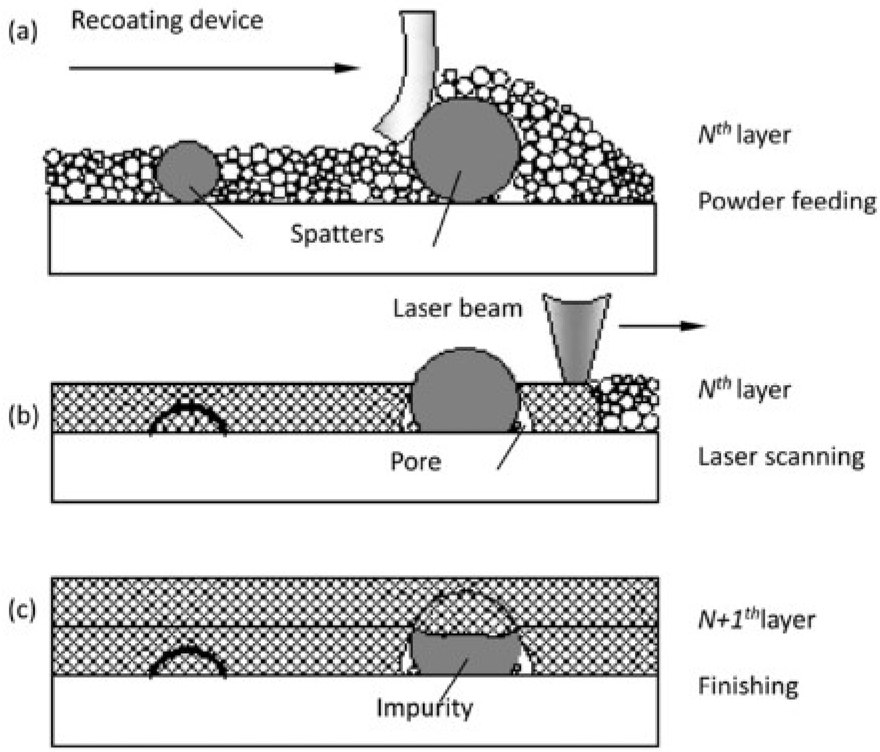

Figure 2.19: Illustration of the influence of spattering particles defect generation in powder bed fusion. Where spatter particles can generate pores within the bulk of a manufactured component. Reprinted from [95] ©2017, with permission from Elsevier.

raw powder and in the case of AlSi10Mg shape deformation is also experienced, as shown by Cordova et al. [97]. A significant mechanism for these differences is the generation of spatter, where particles are ejected from the melt pool and are deposited elsewhere on the powder bed [98]. Depending on the laser parameters, scan strategy and inert gas properties in the chamber, the spatter particles can combine to varying degrees with the loose powder atop of which they land, creating unusual shapes and altering the size distribution. Reuse of powder in this form can impact the quality of the final component, as illustrated in Figure. 2.19. Recycled powder undergoes treatment to sieve out any undesirable particles and, recently, novel methods of characterising particle size distribution have been proposed to aid the reuse of powder in PBF processes [99]. The particle size distribution will have an effect on the minimum layer thickness achievable and subsequently lead to changes in the characteristics of the built part.

2.3.2 Layer thickness

The layer thickness parameter is defined by the height at which a spreading blade is run relative the the previous layer. The choice of this value is relative to the average particle size being used; a layer thickness much less that the average diameter will mean few particles are actually processed, while a larger layer thickness can mean the laser energy may not fully fuse the particles to the layer below. From an economical perspective, a larger layer thickness leads to reduced build times and hence lower per-unit cost [100]. Figure. 2.20 shows the layer preparation when layer thickness (t) is slighting larger than the average particle diameter. The layer thickness can also affect the accuracy of manufacture, where for angled faces a 'staircase' effect is observed (and shown in Figure. 2.21). The smaller the layer thickness is in these circumstances, the more accurate the manufacturing can be to the designed geometry.

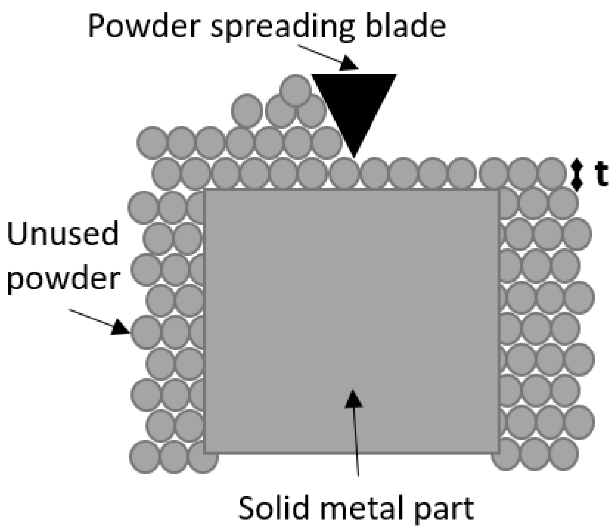

Figure 2.20: Representation of PBF layer thickness t.

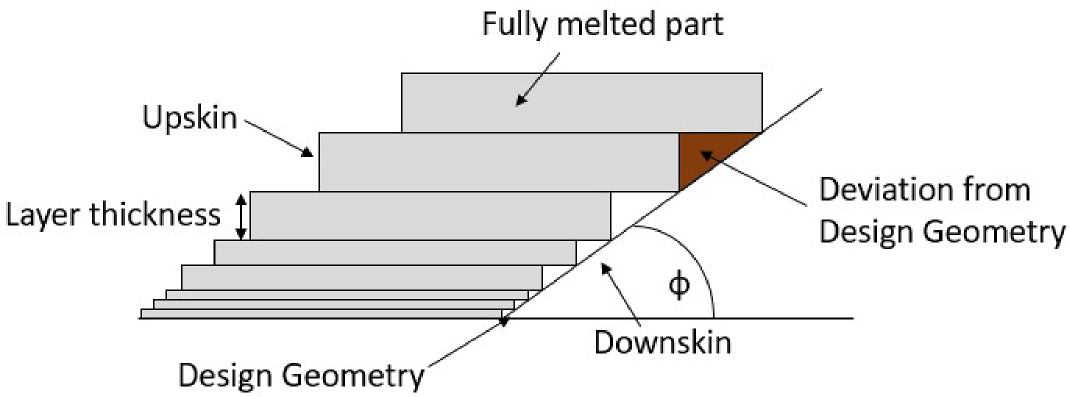

Figure 2.21: Graphic highlighting the effect of layer thickness on the accuracy of powder bed fusion manufacturing. Large layer thickness produces an equally large deviation from the design geometry.

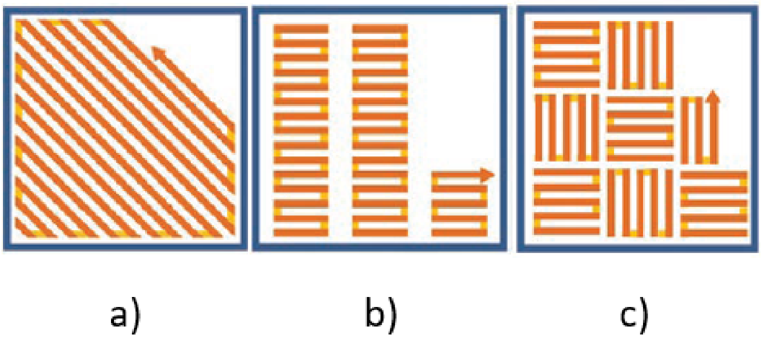

Figure 2.22: Three common scan strategies used by Renishaw additive manufacturing systems. a) Meander, b) Stripe and c) Chessboard. Adapted from [101] ©2017 Renishaw plc.

2.3.3 Scan Strategy

The scan strategy is the hatch path that the laser takes in melting each layer of a component. The three main strategies employed by Renishaw systems are (a) Meander; shown in Figure. 2.22a as straight line vectors directly between the borders of the part; this can be done in a unidirectional manner by returning the unpowered laser optic to the original boarder before scanning the next path, or a bidirectional manor which is significantly faster; meander is, in general, the quickest and most efficient strategy and is the one used throughout this thesis. (b) Stripe; shown in Figure. 2.22b where the processing area is split into thin stripes and the Meander pattern is used within each stripe; with typical stripes in the range of 5-10 mm, this strategy can become slow for large build areas but it ensures a more uniform residual temperature distribution than the Meander strategy. (c) Chessboard; shown in Figure.2.22c where the stripe pattern is divided into smaller, square areas in which the Meander path is employed; this strategy has little benefit over Stripe and its additional complexity leads to slow build times.

For each scan strategy, the direction of laser scan path is defined by the start angle and the rotation angle increment between layers, as shown in Figure. 2.23. The default value of rotation per layer is 67^o, ensuring that the same scan direction is not repeated for 180 layers, which helps to ensure a uniform fusing of

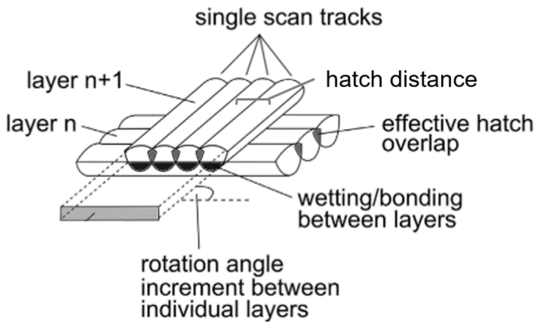

Figure 2.23: Layer-wise manufacturing in powder bed fusion. Adapted from [102], ©2018 WILEY-VCH Verlag GmbH & Co. KGaA.

layers. Other parameters, such as hatch distance shown in Figure. 2.23, will have an effect of the density and porosity of the final part. This parameter should be set such that there is a small overlap between adjacent tracks, which will be marginally smaller than the size of the effective melt pool.

2.3.4 Laser Properties

For both the AM250 and RenAM500Q systems, ytterbium fibre lasers are employed for powder melting. The default wavelength is between 1070-1080 nm, in the regime of high absoptivity for commonly used PBF metals [103]. The laser focal diameter is approximately $70 - 80$ μm and the maximum laser power for the AM250 system is 200 W, while for the RenAm500Q (which employs four independent lasers) the maximum power is 500 W. Laser power, during a given exposure time, determines the energy penetration into the powder bed; this must be sufficient to encourage good wetting between successive layers, however too high a power can result in cracking due to excessive thermal gradients [104]. Laser power also has a major role in determining the surface quality of a PBF component and its value subsequently will differ depending on which part of the component is being processed. Particularly when processing unsupported, overhanging, sections the laser power will determine how much energy penetrates previous layers and as such the level of partially melted powered adhered to the surface.

2.3.5 Build strategy

For any three dimensional component built by additive layer manufacturing, there will be some surfaces that have to be orientated at a finite angle relative to the build plate. Figure. 2.24 shows three common orientations for surfaces in three dimensional builds; Horizontal (parallel to build plate), Vertical (perpendicular to build plate) and 45^o; the latter is considered the lowest possible build angle achievable without the requirement for additional supporting structures [105]. This is significant because for any microwave part produced by additive manufacture, the presence of support structures within the internal volume of the component will severally effect performance. The removal of support structures often requires line of sight access for mechanical removal, one method of which is shown in Figure. 2.25a, which is often not achievable for internal volumes. as detailed in Figure. 2.25b. Furthermore, even if the supports can be removed, there will be powder residue and unwanted features on the surface, which could have negative impacts on the microwave performance. Therefore, the 45^o build orientation is significant for the production of microwave components via additive layer manufacturing.

The presence of surfaces of different build orientation within a microwave component necessitates consideration of the different surface features presented by each orientation. By classifying the upward facing and downwards facing sur-

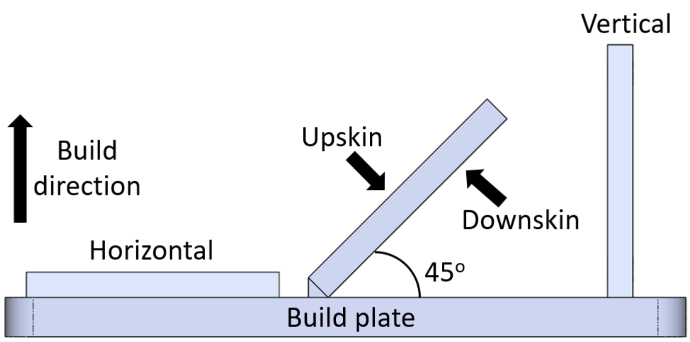

Figure 2.24: Additive manufacturing build strategy. a) Three commonly used build orientations and b) representation of the staircase effect. Reprinted from [24] ©2021 Gumbleton et al. (CC-BY).

a)

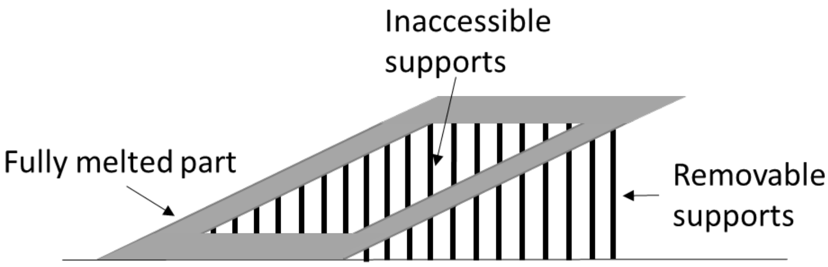

b)

Figure 2.25: Problematic support structures. a) Manual removal of support structures, reprinted from [106] ©2020 Conteo AG and b) schematic of inaccessible, internal supports.

faces of an angled build orientation as the 'upskin' and 'downskin', respectively, their individual properties can be explored. In the context of PBF, 'downskin' is used to refer to a scan path which is not directly on top of a previously processed layer. The downskin applies to any downwards facing surface at an angle below the set activation angle, 60° as default, relative to the build plate. Conversely, an 'upskin' refers to any laser path that does not have a proceeding layer directly above; each case has a different set of process parameters for manufacture. The different surface roughness properties of upskin and downskin surfaces are summarised in Figure. 2.26. There have been many studies performed on the manufacturability of the downskin (unsupported) surfaces, with a common concluding theme that these surfaces exhibit relatively low quality surface finishes [107, 108]. Others, such as Chen et al. [109], have sought to improve the sur-

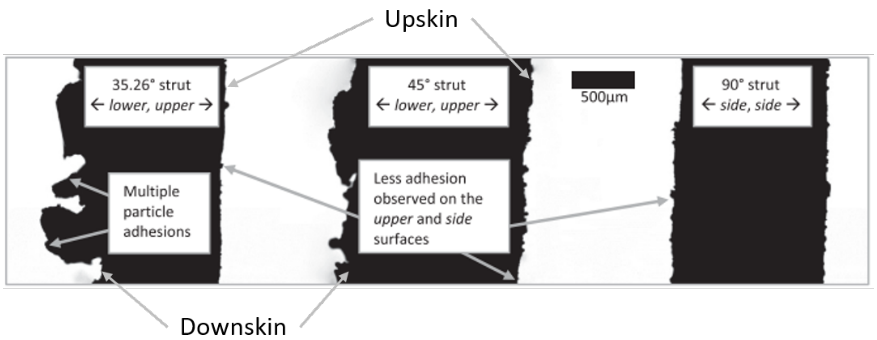

Figure 2.26: Optical microscope image of representative roughness profiles on AlSi12Mg lattice struts built at various angles relative to the build plate. Reprinted from [107] ©2016, with permission from Elsevier .

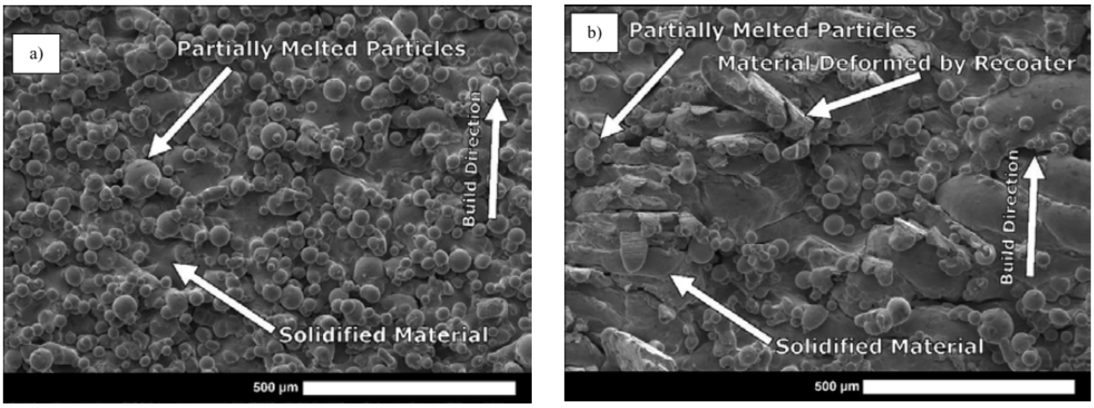

a) b)

Figure 2.27: SEM imaged of stainless steel surfaces produced by powder bed fusion at 60^o build angle. a) Laser power = 40 W and b) laser power = 195 W. Adapted from [110] ©2016 Fox et at (CC-BY).

face finish of overhanging surfaces on AlSi10Mg parts through adaptation of the downskin process parameters, specifically the laser energy density defined as

$$LED = \frac{P}{v} \tag{2.7}$$

where P (W) is the laser power and v (m/s) is the laser scan speed. It was shown that via changes to the LED through v, it was possible to reduce the surface roughness of overhanging surfaces by nearly 50%.

Fox et al. [110] performed similar investigations using the stainless steel alloy GP1, while also varying the input laser power. Figure. 2.27 shows the result of this work, where the differing dominant surface features are obvious. Figure. 2.27a shows that the lower laser power is not sufficient to fully melt some of the power, leading to high levels of dross formation where partially melted powders adhere to the surface, while in Figure. 2.27b the level of dross is significantly reduced. Han et al. [111], Xiang et al. [112], and Staub et al. [113] have performed additional studies on the optimisation of downskin parameters for improved surface quality. An interesting study by Han et al. [114] on the manufacture of overhanging surfaces suggested that it is the low thermal conductivity of loose, un-melted powder, that causes the dross defects and excess roughness. The slow dissipation of heat leads to a larger meltpool than that in a fully supported region. This increased size and the surface tension force of the melt pool, combined with gravity, leads to dross formation, a finding also supported by Dong et al. [115].

It is clear that opportunities to optimise the PBF process for improved surface finish are available. Given the link between microwave loss and surface roughness established above, there are also opportunities to develop the process for passive microwave devices.

2.4 Post-Processing Treatments

The current state of PBF applied to microwave components still necessitates for post-processing treatments to be applied. There are several processes available for the improvement of PBF in terms of both mechanical and electrical properties.

2.4.1 Heat Treatment

A common process that even manufactured parts of bulk metals may be be exposed to is heat treatment. In subtractive metals parts, heat treatment such as annealing will drive out dislocations close to the surface of the metal, thus increasing the electrical conductivity in the region where microwave currents will preferentially flow. In the case of metal PBF components, heat treatment in the

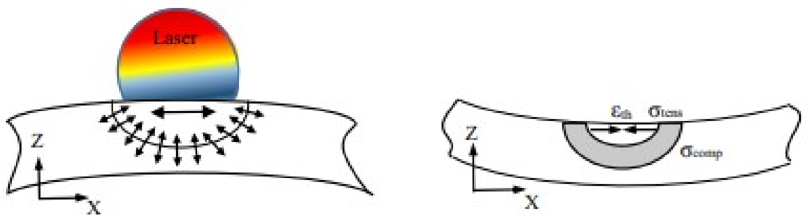

Figure 2.28: The evolution of residual stress in the powder bed fusion. Left is when the laser is interacting with the powder bed during heating and right when the heat source is removed in the cooling phase. Reprinted from [119] ©2018 Springer-Verlag London Ltd.

first instance is used to relive residual stress before removal from the AM build plate. The build up of residual stress in PBF parts is mainly caused, according to Salmi and Atzeni, by "*high spatial temperature gradients that are generated in the produced part as a result of the laser interaction with the metal powder, the thermal expansion, due to the heating and cooling by the laser source, and the plasticity and flow stress of the processed material*" [116]. The phenomenon is graphically represented in Figure. 2.28. Renishaw plc treat all aluminium parts made by PBF with a one hour heating ramp up to 320° C, held there for a further three hours, before a natural air cool to room temperature in an argon furnace [117]. The treatment of residual stress relief can help to prevent cracks and distortions in AM build parts. Beyond stress relief, heat treatment in used for aluminium to improve the electrical conductivity properties. In PBF, heat treatment brings about a coarsening of the microstructure[13, 118], which leads to less boundary discontinuities for electric current relative to the fine microstructure of untreated parts.

2.4.2 High Conductivity plating

As previously mentioned earlier in the chapter, the use of plating material of high electrical conductivity on PBF surfaces is a common way to overcome the excess loss exhibited compared to traditional manufactured alternatives [42, 51]. Plating microwave devices has two beneficial outcomes; firstly, due to the skin effect microwave currents will flow in only the outer most layers, so that if the plating is sufficiently thick then the entire microwave current can flow within the higher conductivity material; secondly, the fluid nature of the plating processes inevitably leads to the roughness valleys being filled, which lowers the overall surface roughness of the part [120]. Plating itself does have some drawbacks which need to be considered. Besides the obvious additional cost, financial and time, reliability is also a concern when operating in extreme environments, as might be expected in space or aerospace applications. Specifically, plating is subject to discrepancies between the coefficient of thermal expansion (CTE) of different materials, for example, silver has a CTE of approximately 18×10^{-6}K $^{-1}$ while the CTE of bulk aluminium alloy 6063 is approximately 23×10^{-6} K^{-1} (between 293 and 393 K) [121, 122]. In extreme instances, the plating material can disassociate from the AM surface and result in failure [123]. This scenario can be significantly worse with some polymer AM materials. Furthermore, the selection of processing techniques can result in differing mechanical properties from the same raw material, for example PBF processed AlSi10Mg exhibits a higher tensile strength than cast AlSi10Mg [124]. So although properties of the raw material may be known, the use of AM as a processing technique can bring about different property values.

2.4.3 Deburring Methods

A burr is defined, by Franke, as "*a material accumulation, which is created on the surface during the manufacturing of a workpiece. It extends over the intended and actual workpiece surface and has a slightly higher volume in comparison with the workpiece*" [125]. Although this definition actually relates to rough edges produced by traditional manufacturing tools, it could equally be applied to the non-uniform material accumulation 'beyond the intended workpiece' on additive manufactured surfaces, thus leading to poor surface finish. This terminology is adopted throughout this thesis.

The main deburring methods available for PBF parts include CNC machine

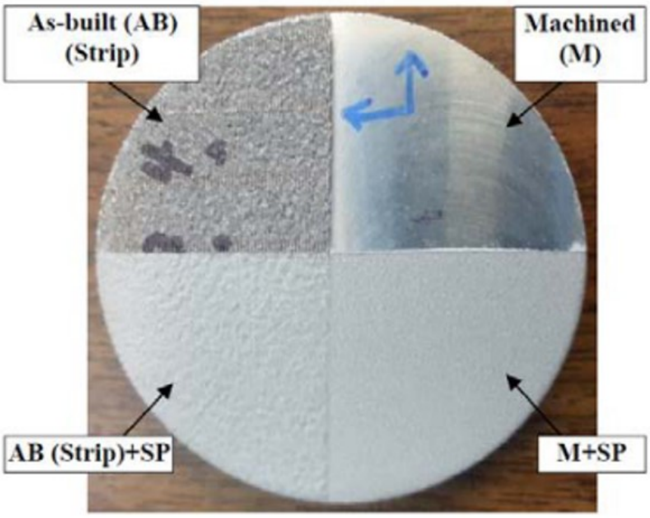

Figure 2.29: Photograph of an AlSi10Mg powder bed fusion sample plate treated by different deburring methods. Reprinted from [126] ©2018 Maamoun et al. (CC-BY).

finishing, where the PBF part is fixed to a traditional milling machine and the outer layer exhibiting the roughness is removed. This machining can be taken to extremes to leave a mirror-like finish on aluminium parts with RMS surface roughness lower than 1μm [127, 128]. Bead blasting / shot peening is a commonly implemented process, where small particles are fired at high velocity towards the PBF surface. The particles impacts with loose power and other protrusion on the surface, the kinetic energy forces such protrusions to break away leaving a smother finish [126]. A photograph of a PBF sample having under gone shot peening and machining is shown in Figure. 2.29. It has also been shown that shot peening can reduce the size of surface layer pores [129]. In a similar context, media tumbling / centrifugal finishing uses particle impact on the sample to perform surface modifications. Parts and abrasive media are mixed together and rotated in a 'barrel'. Although this process can produce very good result for surface smoothing, it tends to round corners on the sample parts and so they have to be very robust[130]. Furthermore, mechanical polishing type methods are likely to degrade the conductivity near the surface owing to increased dislocations and residual stress.

CHAPTER 3

MICROWAVE MEASUREMENT OF SURFACE RESISTANCE

3.1 Introduction

As discussed in Chapter 2, the relatively good performance of single-piece AM components [42, 41, 51, 131, 52] such as waveguide filters is somewhat surprising, given the average surface roughness is much higher than in CNC alternatives. Evaluating microwave performance in this way requires large, costly and time consuming sample preparation, while not allowing for assessment of microwave loss associated with individual surfaces. Rather than fabricating large samples, several methods for the evaluation of R_S for smaller samples already exist. Two main techniques are established for this purpose, 'end wall' replacement of a resonant cavity structure [80, 81] and the use of dielectric resonator (DR) fixtures in various forms [82, 83, 84, 85], each with its own advantages and disadvantages (see section 2.2).

Presented here is a background to microwave resonance measurements and loss quantification, followed by the description of two alternative / adapted measurement methods designed specifically for the investigation of AM samples. Firstly, an overview is given of a novel 'lift-off' DR (LODR) fixture which has been developed with N. Clark, S. Hefford and A.Porch [68, 91, 86] and employed in the measurement of additive manufactured parts throughout this work and in external publication [25]. Secondly a novel resonator based upon parallel plate transmission line principles is described, where one-directional induced current flow is controlled by the excitation of orthogonal resonant modes. Aspects of this chapter have been published in peer reviewed journal articles by this author [23, 91], with some figures and text having been reprinted (with relevant permissions where this author no longer hold the copyright).

3.2 Microwave resonance and loss

As previously outlined in section 2.2, microwave surface currents flow predominately in the outermost extremities of a conductor. The thickness of this current carrying area is called the skin depth δ. Analytically, the skin depth of microwave induced surface currents can be derived by examining the solutions to the wave equations for a good conductor; a full derivation can be found in [132]. A brief overview starts with Maxwell's time dependent equations in phasor form

$$\nabla \times \vec{E} = -j\omega\mu\vec{H} \tag{3.1a}$$

$$\nabla \times \vec{H} = j\omega\epsilon\vec{E} + \vec{J} \tag{3.1b}$$

where $\vec{E}$ and $\vec{H}$ are sinusoidal electric and magnetic fields, respectively, $\vec{J}$ is the conduction current density ($\sigma\vec{E}$), ω is the angular frequency ($2\pi f$), μ is the magnetic permeability, ϵ is the electric permittivity and σ is electrical conductivity. Solving for $\vec{E}$ by taking the curl of 3.1a and using 3.1b produces the wave equation as

$$\nabla^2\vec{E} + \omega^2\mu\epsilon\left(1 - j\frac{\sigma}{\omega\epsilon}\right)\vec{E} = 0 \tag{3.2}$$

Here we also define the propagation constant γ

$$\gamma = \alpha + j\beta = j\omega\sqrt{\mu\epsilon}\sqrt{\left(1 - j\frac{\sigma}{\omega\epsilon}\right)} \tag{3.3}$$

where α (dB/m) is the attenuation constant and β (Rads/m) is the phase constant or wave number. Equation 3.2 has solutions for $\vec{E}$, with basic plane wave assumptions that $\vec{E}$ has only an x component, is uniform in x and y and (along with $\vec{H}$) is perpendicular to the direction of propagation (z), as

$$E_x(z) = E^+e^{(-\gamma z)} + E^-e^{(\gamma z)} \tag{3.4}$$

omitting the $e^{j\omega t}$ term common to both terms.

Solutions for the $\mathrm{H_y}(z)$ field are computed in the same way. The attenuation as a function of distance z into the conductor is given by an exponential decay linked to α. For a good conductor, where $\sigma \gg \omega\epsilon$, γ approximates to $(1+j)\sqrt{(\omega\mu\sigma/2)}$ with $\alpha = \mathrm{Re}(\gamma)$. The skin depth is defined at the point the decay in field magnitude and hence conduction current is equal to $1/e$, such that $\delta = 1/\alpha$ ($e^{-\alpha z} = e^{-\alpha\delta} = e^{-1}$) and takes the form of equation 2.2.

R_S becomes a key figure of merit in microwave performance when considered in the context of power dissipation at a conductor surface in the presence of an electromagnetic (EM) field, as given by equation 3.5

$$\langle P_c \rangle = \frac{R_S}{2} \iint_S |H_S|^2 dS \tag{3.5}$$

where S is the surface on which the current flows (m^2) and H_S is the tangential magnetic field at the metal surface (A/m). The frequency dependence of R_S shows that for any given metal sample, resistance and hence power dissipation will increase as $\sqrt{f}$. Excess conductor loss associated with surface finish is encompassed within R_S as effective conductivity σ_eff. Loss in a conductor can therefore be seen as being directly proportional to R_S, with R_S being the quantifying metric for ohmic losses at microwave frequencies. Understanding and improving R_S is important in the optimisation of materials for low-loss microwave applications.

3.2.1 Microwave Resonance

Throughout this thesis the concept of resonance is used to investigate loss in additive manufactured samples. Measurements at resonance can provide a much more sensitive surface resistance characterisation than waveguide measurements, for example, while using compact, efficient and relatively simple to use structures with dimensions on the scale of fractions of wavelengths.

A resonance condition in microwave cavity systems occurs when the electric and magnetic stored energies are equal, such that the resulting input impedance is purely real and hence can be utilised to extract R_S of the resonator material. The fundamental measurement quantities for microwave resonance is the Quality (Q) factor. The unloaded Q factor of a resonant system relates stored energy to power loss as

$$Q = \omega_0 \frac{\text{Average Stored Energy}}{\text{Energy loss / sec}} = \omega_0 \frac{\langle W \rangle}{\langle P \rangle} \tag{3.6}$$

assuming any dielectric material within the cavity as lossless, the energy loss is given by Equation. 3.5 for the conductive cavity walls. The average energy stored is defined as

$$\langle W \rangle = \langle W_m \rangle + \langle W_e \rangle \tag{3.7a}$$

where,

$$\langle W_m \rangle = \frac{1}{4}\, \mu \iiint_V |H_V|^2 dV \tag{3.7b}$$

$$\langle W_e \rangle = \frac{1}{4}\, \varepsilon \iiint_V |E_V|^2 dV \tag{3.7c}$$

$\langle W_m \rangle$ is the average magnetic stored energy and $\langle W_e \rangle$ is the averaged electric energy stored. These energies are stored in the electromagnetic field of a standing wave formed within a hollow conductive cavity. The resonant condition is achieved when $\langle W_e \rangle = \langle W_m \rangle$. For a given system, a higher Q factor at resonance will indicate a lower level of real (resistive) impedance R_S.

3.2.1.1 Rectangular Cavity Resonator

For some simple shapes, it is convenient to view a cavity resonator as a waveguide transmission line which is shorted at both end. The standing wave is then described as the interference between forward and reverse travelling waves. An example of a microwave resonant structure is the rectangular cavity resonator. While the Q factor can be deduced through the equations above. The natural

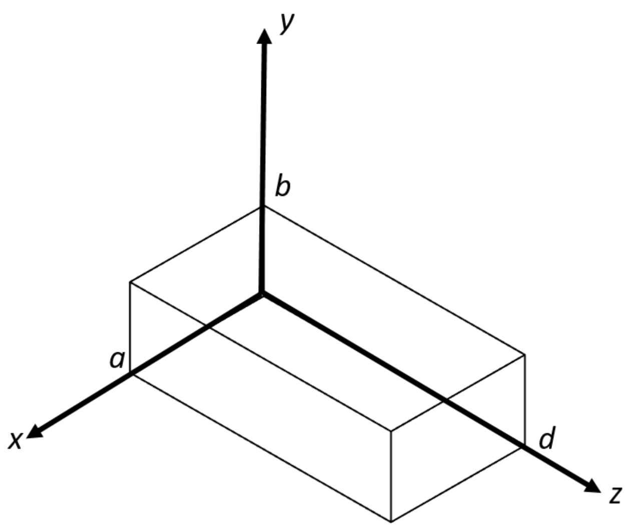

Figure 3.1: Geometric representation of a rectangular cavity resonator, of internal dimensions a, b and d.

resonant frequency for a given mode (f_{nml}) is determined by the cavities physical geometry. Treating the cavity as a shorted rectangular waveguide section allows the use of the propagation constant for a given waveguide mode (β_{nm}) to establish an expression for f_0; given that the boundary conditions at the side walls the rectangular waveguide are identical to those in the rectangular cavity.

$$\beta_{nm} = \sqrt{k^2 - {\frac{m\pi}{a}}^2 - {\frac{n\pi}{b}}^2} \tag{3.8}$$

Where a and b are the cavity geometry as illustrated in Figure. 3.1, $k = \omega\sqrt{\mu\varepsilon}$ is the wave number and m and n are the mode integers. The additional boundary conditions required for the cavity resonator are $E_{\mathrm{x}} = E_{\mathrm{y}} = 0$ on the end walls at $z = 0$ and d. The transverse electric field has a sinusoidal dependence on (β_{nm}); therefore the boundary conditions are met when $\sin(\beta_{\mathrm{bm}}d) = 0$ at integer multiples of a half wavelength along the waveguide length. The resonant frequency of the a rectangular cavity of length d is thus given by

$$f_{nml} = \frac{c}{2\pi\sqrt{\mu_r\varepsilon_r}}\sqrt{{\frac{m\pi}{a}}^2 + {\frac{n\pi}{b}}^2 + {\frac{l\pi}{d}}^2} \tag{3.9}$$

where c is the speed of light in a vacuum (approximately 3×10^8 m/s).

3.2.2 Microwave Measurements

Microwave resonant structures, as mentioned above, allow for losses associated with R_S on surfaces exposed to the parallel microwave H field to be measured with high sensitivity. For this to be realised however, information is needed about all other elements in the system, such as dielectric materials present in the cavity and the electromagnetic coupling to the external circuitry, to allow both excitation of the cavity modes and their measurement.

3.2.2.1 Electromagnetic coupling

In order for a resonant cavity to act as measurement systems they must first be connected to external circuitry for excitation. The connection takes the from of coupling to the electric or magnetic field within the cavity. The coupling method used will depend on several factors such as the geometry of the cavity, measurement application and field distribution of the target mode.

For this thesis, two port measurement are taken employing two main coupling methods; capacitive (probe) and inductive (loop) formed of lengths of coaxial cable in the forms depicted in Figure. 3.2. Capacitive coupling is achieved through an open circuit coaxial line protruding into the interior of the cavity volume, where the voltage formed by the open circuit leads to an electric field radiating from the probe. The probe is placed in an area of high electric field magnitude and orientated such to align with the direction of electric field in the target cav-

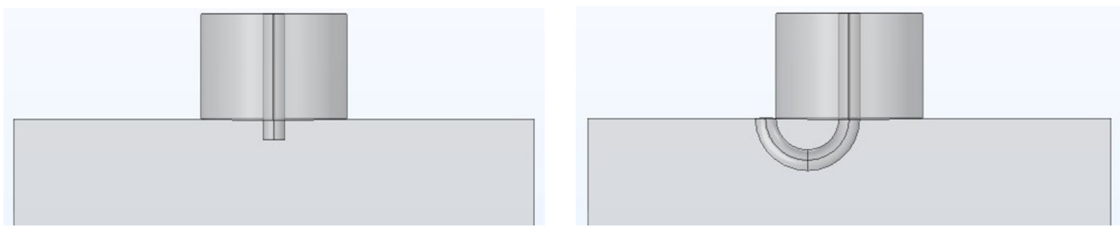

a) b)

Figure 3.2: CAD representation of a) capacitive coupling probe (to the E field) and b) inductive coupling loop (to the H field) created from coaxial transmission line.

ity mode. Alternatively, inductive coupling is achieved through a short circuited loop of coaxial cable protruding into the cavity volume. The generated magnetic field is perpendicular to the plane of the loop but tangential to the wall of the cavity, thus coupling to all cavity modes that have a component of surface magnetic field in this orientation.

The cavity must be matched to the external circuit in order to achieve maximum power transfer into the resonant system, such that the characteristic impedance of the feed line Z_0 then equals the input impedance of the cavity at resonance Z_{in}; generally, we can write $Z_{\mathrm{in}} = g \times Z_0$, where g is the coupling coefficient, which equals 1 in the case of critical coupling for maximum power transfer. In this condition, we define coupling coefficient $g = 1$ and is considered critically coupled. For $g < 1$ (under coupled) and $g > 1$ (over coupled), some degree of reflection is taking place at the coupling port and preventing full power transfer to the system.

For passive measurement techniques, this may not necessarily be a problem and can be accounted for in the scattering (S) parameter analysis. More importantly for two port measurements is the condition that the coupling coefficients for each port are equal; $g_1 = g_2$. This allows for a simplification of the analysis to give the peak power transfer as

$$P_0 = |S_{21}|^2 = \left(\frac{2g}{1+2g}\right)^2 \tag{3.10}$$

where S_{21} is the two port S parameter forward transmission coefficient. The effect of coupling is to increase the measured 3dB bandwidth, and hence reduce the measured (i.e. 'loaded') Q factor $\mathrm{Q_L}$ compared to unloaded Q factor $\mathrm{Q_0}$ (as set by the material properties of the cavity alone) by

$$Q_L = \frac{Q_0}{1+g_1+g_2} = \frac{Q_0}{1+2g} \tag{3.11}$$

when the coupling is symmetric; combining Equation. 3.11 with 3.10 yields

$$Q_L = Q_0 \left(1 - |S_{21}|\right) \tag{3.12}$$

where the unloading process simply requires measurement of the peak power at resonance, i.e. the insertion loss. Typically insertion loss at resonance should be in the range of -30dB to -20dB, i.e. g in the range 0.02 to 0.05. In this weakly coupled limit, there is still sufficient signal to noise ration (SNR) for accurate measurement, but the low value of g means that that the unloading process for $\mathrm{Q_0}$ from $\mathrm{Q_L}$ does not require highly accurate calibration of all cable and connector losses. A full analysis for coupling coefficients can be found in Appendix. A [133]. $\mathrm{Q_L}$ can be determined through measurement using the 3dB method where

$$Q_L = \frac{f_0}{BW} \tag{3.13}$$

where f_0 the resonant frequency and BW is the 3dB bandwidth, corresponding to the difference between the upper and lower frequencies at which the maximum amplitude of insertion loss is reduced by 3dB. This method relies only on three measurement points, making it a relative simple procedure if not the most precise. More advanced analysis can be done on measurement sweep data through Lorentizian or circle curve fitting operations [134]. The Lorentzian curve fitting method uses Equation. 3.10 in Lorentzian form and expressing in term of fitting parameters a_0, a_1 and a_2

$$P(f) = |S_{21}|^2 = \frac{P_0}{1 + 4Q_L^2 - 8Q_L^2\left(\frac{f}{f_0}\right) + 4Q_L^2\left(\frac{f}{f_0}\right)^2} = \frac{a_0}{1 + a_1 f + a_2 f^2} \tag{3.14}$$

the returned curev fitting parameters can be used to find values for Q_0, f_0 and P_0.

3.2.2.2 Surface Resistance and Dielectric Loss

Having established the unloaded quality factor (Q_0) of the cavity at resonance the parameters of interest can be investigated. For an ideal air filled cavity consisting of only conductive walls

$$Q_0 = Q_c \tag{3.15}$$

where Q_c is the contribution to Q_0 from the conductive walls. For some of the cavities used in these thesis, however, there are also dielectric elements present that contribute to overall loss and have a contribution to Q_0 (via their finite loss tangents) as

$$\frac{1}{Q_0} = \frac{1}{Q_c} + \frac{1}{Q_d} \tag{3.16}$$

where Q_d is the dielectric contribution to overall Q_0. Therefore, Q_0 can be further analysed by breaking up Q_c and Q_d into components associated with their geometry and those associated with their loss

$$\frac{1}{Q_0} = GR_S + p_{ed}\tan\delta \tag{3.17}$$

where G (Ω^{-1}) is the geometric factor of the conductive elements and p_ed, the dielectric filling fraction, are the geometric components defined as [132]

$$G = \frac{1}{\omega}\frac{\iint_S H_t \cdot H_t^* ds}{\iiint_V \mu H \cdot H^* dv} \tag{3.18a}$$

$$p_{ed} = \frac{\iiint_{Vd} \varepsilon_d E \cdot E^* dv}{\iiint_V \varepsilon_v E \cdot E^* dv} \tag{3.18b}$$

where S is the surface integral for each conductive surface, V_d is the volume integral for the dielectric volume and V is the volume integral for the whole of the host cavity. μ_0 is the permeability of free space, and ε_d and ε_v are the permittivity of the component material and the material filling the cavity, respectfully. The

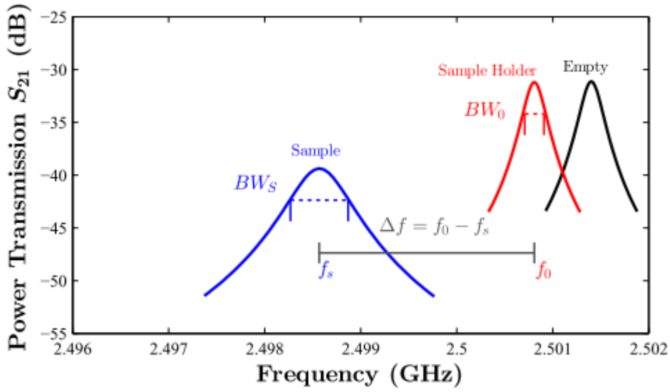

Figure 3.3: Example of traces for microwave cavity perturbation measurements.Changes in resonant frequency and Q factor can be related to properties of the material placed within the cavity volume. Reprinted from [139]

loss components are: tanδ, which is the dielectric loss tangent, and R_S which is the surface resistance of the conducting walls. tanδ and ε_d can be found through well documented cavity perturbation methods [135, 136, 137, 138]. An overview of the perturbation technique is given below. While G and p_ed can be found analytically for some simple structures, modern finite element modeling software can provide solution for complex geometries. Solving these quantities leaves only R_S to be found through measurement of Q_0.

3.2.3 Cavity Perturbation

Microwave cavity perturbation is a characterisation techniques suitable for dielectric materials. The technique involves placing a sample into a hollow cavity in the presence of an electromagnetic standing wave (at resonance). The change in the measured frequency and Q factor due to the sample can be used to infer its complex permeability and permittivity values. An illustration is shown in Figure. 3.3. Complex permittivity is defined as

$$\varepsilon = \varepsilon_r \varepsilon_0 = \left(\varepsilon_r' - j\varepsilon_r''\right) \varepsilon_0 \tag{3.19}$$

where ε_r' is the relative dielectric constant which is related to the ability to store electric field energy and ε_r'' is the relative dielectric loss. We can also define the loss tangent of a material as the ratio tanδ=$\varepsilon_r''/\varepsilon_r'$. In a similar way complex permeability is given by

$$\mu = \mu_r \mu_0 = \left(\mu_r' - j\mu_r''\right)\mu_0 \tag{3.20}$$

where μ_{r}' is the relative magnetic permeability which is related to the ability of the material to store magnetic field energy and μ_{r} is the relative magnetic loss. Assuming that a measurement sample does not drastically change the field distribution within the cavity, we can sue a simplified perturbation equation to find the complex material properties above. For complex permittivity [68]

$$\varepsilon_r' \approx -2\,\left(\frac{\Delta f}{f_0}\right)\frac{V_{\text{Cavity}}}{V_{\text{Sample}}}\,G_{\text{nmp}} + 1 \tag{3.21a}$$

$$\varepsilon_r'' \approx \frac{V_{\text{Cavity}}}{V_{\text{Sample}}}\left(\Delta\frac{1}{Q}\right)\,G_{\text{nmp}} \tag{3.21b}$$

where V_{Sample} and V_{Cavity} are the sample and cavity volumes, respectively, and G_{nmp} is the mode dependent scaling constant which is a representation of the fraction of the cavity volume is filled with electromagnetic fields. It is clear here that changes in resonant frequency relate to to stored energy and changes in Q factor relate to loss.

G_{nmp} can be found for common measurement modes of cylindrical cavities analytically, through simulation or with a sample of known properties (for permittivity). Common cavity modes for permittivity measurement are the $\text{TM}_{0\text{mp}}$ modes in which there is a minimum of magnetic field immediately at the centre of the axis, essential for electric field perturbation. The simplest method for determining G_{nmp} for permittivity measurements is to use a calibration sample such as PTFE with well know dielectric properties [140].

3.3 Lift Off Dielectric Resonator: Overview

The LODR fixture previously developed by by N.Clark, S.Hefford and A.Porch has been used to measure samples reported in Chapter. 5. Full details on the measurement technique can be found in [68, 86], while a summary and presentation of measured R_S results are published in [91, 25]. The LODR improves on existing open-ended dielectric resonator methods of measuring R_S through the use of a novel calibration procedure designed to accurately account of loss contributions from each section of the fixture.

3.3.1 Measurement Theory

The fundamental principle of measurement is the same as in the PPR fixture, in much as much as the evaluation of Equations. 3.16 and 3.17 allows for Q_0 to be separated into loss contributions from conductive surfaces and dielectric volumes. Equations. 3.18a and 3.18b provide a method of generating G and p_{ed} values from the electric and magnetic field distributions within the cavity. The measurement theory diverges from PPR in both the physical practice and calibration technique, such that the loss contributions are evaluated at a number or small incremental distances from the samples plate and curve fitting is used to accurately asses contributions from each section of the fixture. A schematic

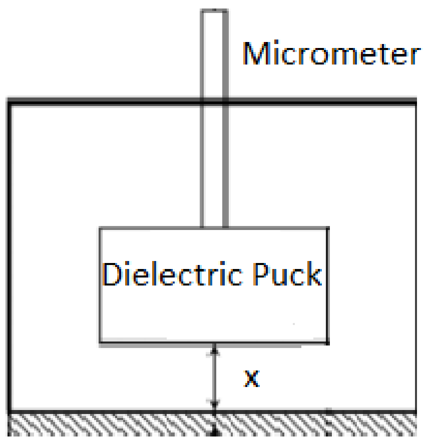

Figure 3.4: Schematic of the lift-off dielectric resonator fixture. Reprinted from [59] ©2017 IEEE.

of the dielectric resonator fixture is shown in Figure. 3.4. The measurement equation in terms of the dielectric puck, supporting rod, cavity walls and the sample plate as a function of lift off position x becomes

$$\frac{1}{Q_0(x)} = G_w(x)R_{Sw0}\sqrt{\frac{f(x)}{f_0}} + G_s(x)R_{Ss0}\sqrt{\frac{f(x)}{f_0}} + \frac{p_{ed_d}(x)\tan\delta_{d0}}{f_0/f(x)} + \frac{p_{ed_r}(x)\tan\delta_{r0}}{f_0/f(x)} \tag{3.22}$$

where f_0, R_{Sw0}, R_{Ss0}, $tan\delta_{\mathrm{d0}}$ and $tan\delta_{\mathrm{r0}}$ are the resonant frequency, surface resistance of the cavity walls, surface resistance of the sample, loss of the dielectric puck and loss of the supporting rod, respectively, at position $x = 0$. $Q_0(x)$, $f(x)$, $G_W(x)$ and $G_S(x)$, and $p_d(x)$ and $p_r(x)$ are the total unloaded Q factor, resonant frequency, geometric factors for the conductive surfaces and energy filling fractions for the dielectric volumes, respectively; all have been given a dependency on position x.

Figure 3.5: Photograph of the lift off dielectric resonator fixture. Reprinted from [91] ©2021 IEEE.

3.3.2 Resonator Design

A photograph of the dielectric resonator fixture is shown in Figure. 3.5. The device operates in the $TE_{01\delta}$ resonant mode at 7.5 GHz. This mode is chosen due to the field patterns generating only azimuthal induced currents on the sample plate, while also tightly confining the electric and magnetic field to the dielectric owing to the high relative permittivity of sapphire. Therefore the optimal measuring height for maximising the loss contribution from the sample is $x = 0$, where the magnetic field is highest at the sample surface. The relative loss contributions for each element in the fixture in shown in Figure. 3.6, where it can seen that the majority loss contributor is the sample for lift-off positions $x < 1$ mm. Increasing the lift off position above 1 mm alters the field distribution and leads to higher relative losses from the cavity walls and dielectric itself. Subsequently the error in measurement of sample R_{S} increases as x is increased as the sample becomes a minor loss contributor.

The internal cavity is produced of aluminium with a radius of 15 mm and a height of 22.5 mm. The dielectric puck is made of single-crystal c-plane sapphire of $\tan\delta$ approximately 2×10^{-5} at room temperature, whereas the supporting rod is made of PTFE of $\tan\delta \approx 1\times10^{-4}$. Microwave coupling for the desired mode is achieved through the use of inductive coupling loops orientated with their planes perpendicular to the tangential magnetic field at the cavity wall. The electric and magnetic field patterns for $TE_{01\delta}$ mode are shown in Figure. 3.7.

3.3.3 Calibration Results

As previously stated, the advantage of this implementation of the open-ended dielectric resonator is a novel calibration procedure for determining parasitic system losses. Q_0 is measured at discrete vertical positions (x) from the reference plate of the same material as the cavity walls (therefore $R_{\mathrm{Sw0}} = R_{\mathrm{Ss0}}$). Least squares curve fitting is then used to fit the calibration equation (3.23) for the

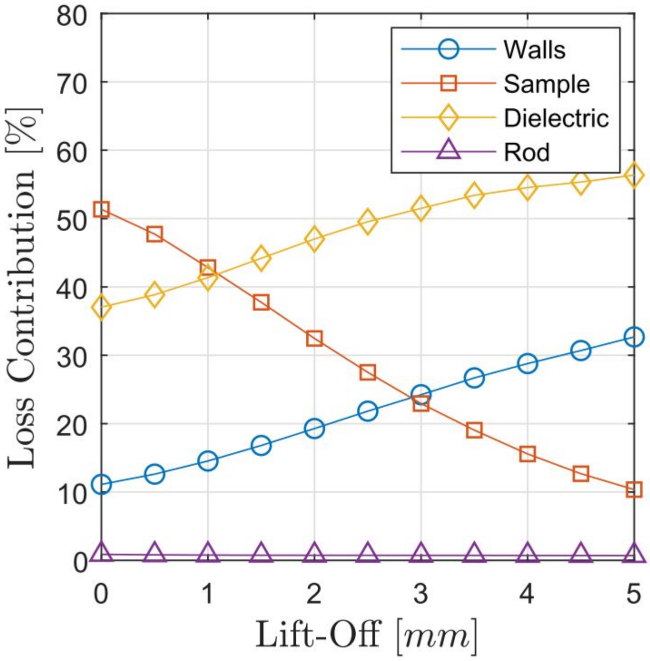

Figure 3.6: Graph of the relative loss contribution against measurement position (x) for the lift-off dielectric resonator fixture. Reprinted from [86] ©2019 Hefford.

three unknown variables R_{Sw0}, $tan\delta_{\mathrm{d0}}$ and $\tan\delta_{\mathrm{r0}}$ while minimising error.

$$\frac{1}{Q_0(x)} = \Big(G_w(x) + G_s(x)\Big) R_{Sw0} \sqrt{\frac{f(x)}{f_0}} + \frac{p_{ed_d}(x) tan\delta_{d0}}{f_0/f(x)} + \frac{p_{ed_r(}x) tan\delta_{r0}}{f_0/f(x)} \quad (3.23)$$

Measured quality factor data and the corresponding least squares curve fit is shown in Figure 3.8. This curve fitting result shows a good agreement with the measured quality factor data. Once calibration is complete and the unknown variables are found, measurement can be performed at any value of x (ideally when x <1 mm) within the calibrated range by replacing the reference plate with a sample under test. Q_0 is measured and Equation 3.22 is solved for R_{Ss0} in the usual way.

3.3.4 Initial Results and Discussion

A set of samples consisting of copper PCB and Al6082 aluminium alloy plates have been measured, along with PBF samples produced of AlSi10Mg and Ti6Al4V. The PBF samples in this section have been produced on a Renishaw RenAM500

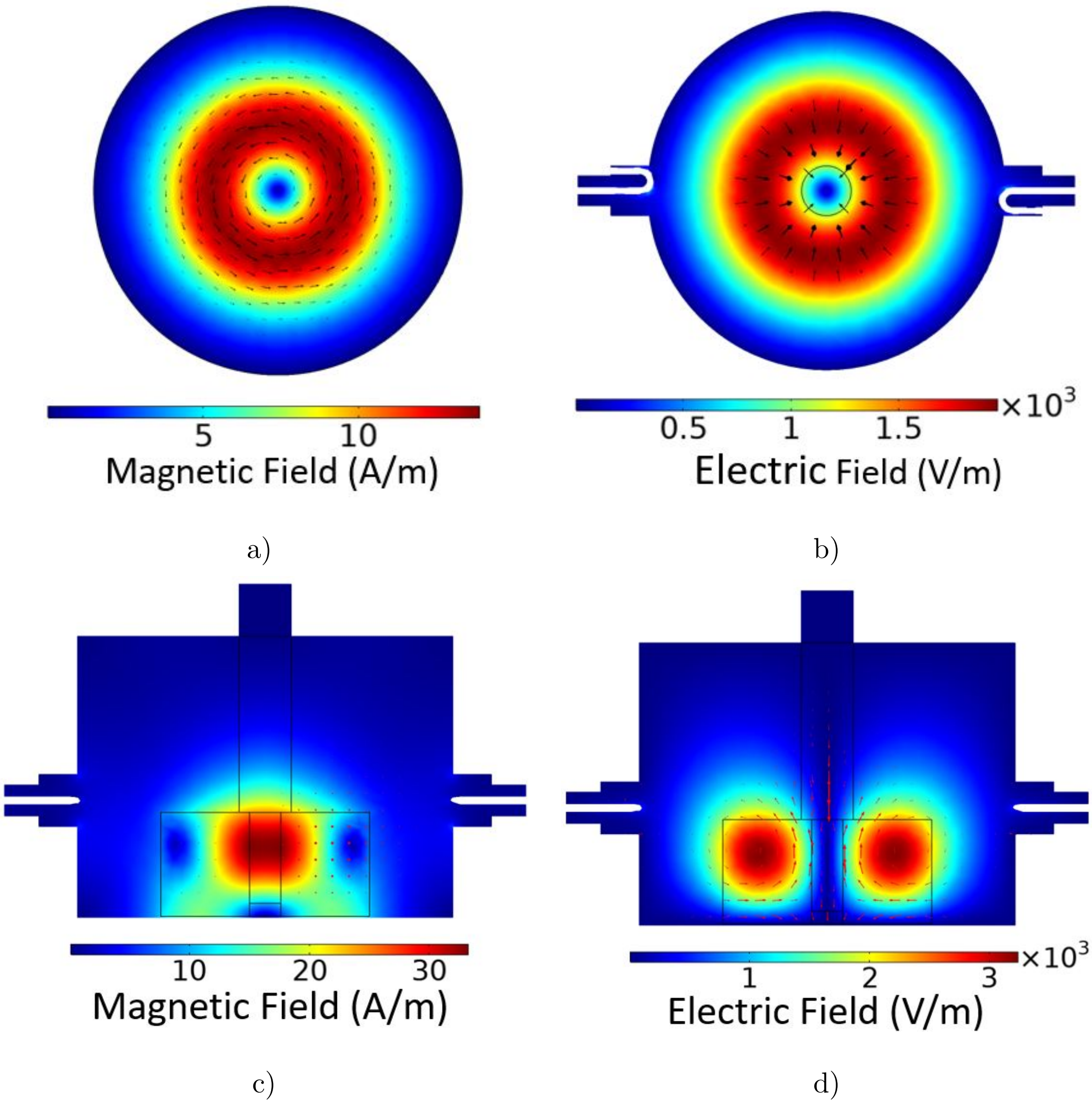

Figure 3.7: Electromagnetic field simulations for the Lift-off dielectric resonator fixture operating in $TE_{01\delta}$ mode at 7.5 GHz when $x = 0.1$ mm. a) Top view of the sample surface. Magnetic field (A/m) magnitude is shown as a colour gradient while the azimuthal surface current density is represented by the black arrows. b) Cross sectional view from the top of the dielectric puck. Electric field (V/m) is shown by the color gradient while magnetic field is represented by the black arrows. c) Cross sectional view from the side of the fixture. Magnetic field (A/m) is shown by the colour gradient while the electric field (V/m) is represented by the red arrows. d) Cross sectional view from the side of the fixture.Electric field (V/m) is shown by the colour gradient while the magnetic field (A/m) is represented by the red arrows. Adapted from [86] ©2019 Hefford.

laser powder bed fusion manufacturing system. For planar metal reference plate of PCB and Al6082, the measured values of R_S are shown in Figure. 3.9. The effective conductivity calculated from these results (4.99×10^7 S/m for the PCB and 2.26×10^7 S/m for Al6082) are realistic when considering the 'book value' of DC conductivity for pure copper is 5.7×10^7 S/m and for aluminium Al6082 is 2.63×10^7 S/m. The 20% difference is likely to be degraded electrical conductivity due to alloying, dislocations or internal stress near the surface, and indeed surface roughness. This is the best that can be usually achieved when performing such a measurement. Figure. 3.10 shows the measured R_S values for AlSi10Mg and Ti6Al4V samples. As expected, the choice of operating mode means that there is no EM leakage from the gaps present when measuring PBF samples and the method is able to distinguish between metals of different conductivity. This

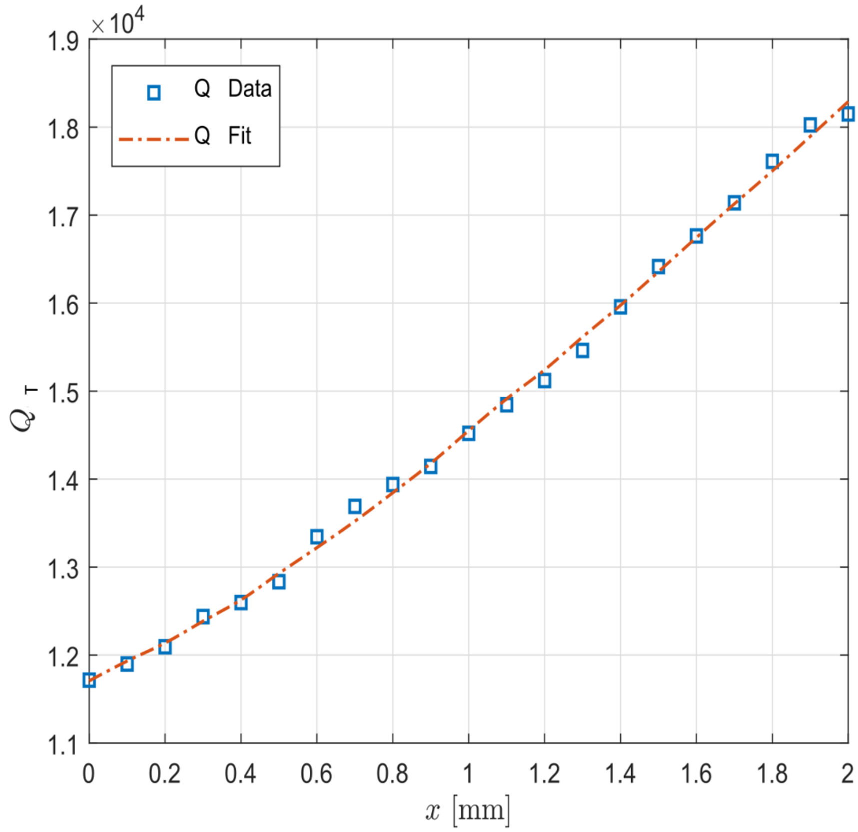

Figure 3.8: Calibration result for the lift-off dielectric resonator fixture. Graph showing the measured quality factor (Q_0) and corresponding least-squares curve fit. Reprinted from [91] ©2021 IEEE.

method is used extensively for sample measurements in Chapter. 5 and more detailed theory and results are published in [25, 68, 91, 86].

3.4 Parallel Plate Resonator

In both the 'end wall replacement' and DR methods mentioned in Section.3.1, including the lift-off dielectric resonator in Section.3.3, resonant modes are chosen such that the induced currents on the sample surfaces only have only azimuthal components [90, 82]. Although appropriate for maximising sensitivity to the sample plate, this means that only isotropic materials can be measured accurately. Owing to the layered nature of AM parts, and any anisotropy introduced as result of the laser scan pattern used in their production, it would be beneficial to have access to a technique to measure R_S which would enable one-dimensional currents to flow on metal surfaces, and for the current flow direction to be easily rotated by 90 degrees without having to reassemble the fixture. The technique proposed here provides such a method through the adaptation of an enclosed parallel plate resonator system. The induced currents flow in linear, orthogonal directions on a small study sample through the excitation of separate resonant modes.

3.4.1 Measurement Theory

The resonant cavity design is based upon an enclosed parallel plate transmission line structure, where current flows equally on the upper and lower surfaces. In this implementation, the upper surface of the cavity is the sample under test, while the lower surface is formed of a small metal plate held on a PTFE frame. We choose this adaption since then the sample does not need to be cut to a precise size or thickness, it just has to overlap the end of the shielding cavity. Furthermore, the requirement for screw holes on the sample is not strictly necessary as a simple clamp would ensure the required electrical contact. The metal plate is used as a reference and is common to all measurements, as its dimensions

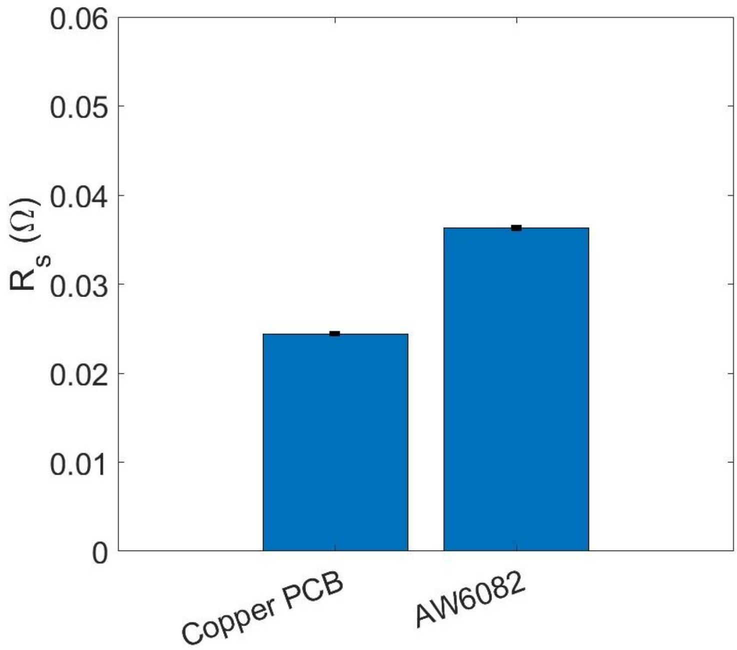

Figure 3.9: Surface resistance measurements for planar reference samples. Measurements taken using a lift-off dielectric resonator fixture operating in $TE_{01\delta}$ resonant mode at 7.5 GHz. Standard error is given by the error bars as 3.3×10^{-4} Ω and 3.1×10^{-4} Ω for copper PCB and Aluminium AW6082, respectively, for 10 repeated measurements.

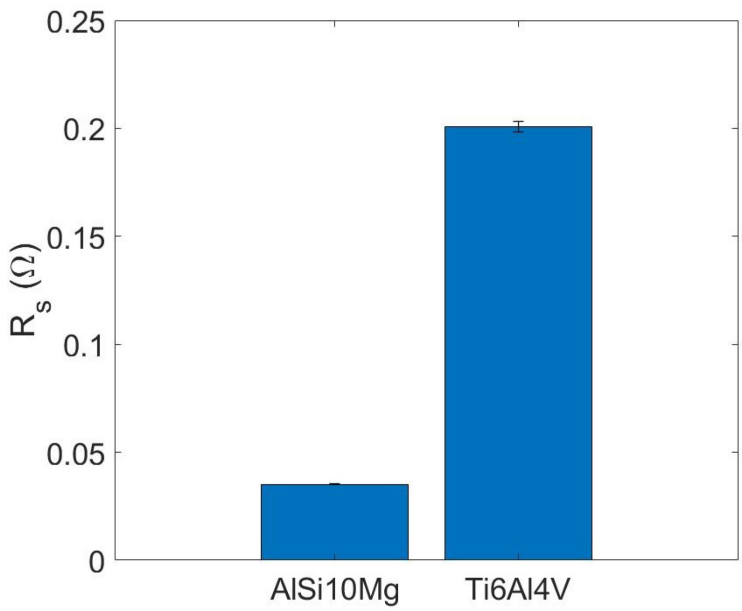

Figure 3.10: Surface resistance measurements for powder bed fusion produced samples. Measurements taken using a lift-off dielectric resonator fixture operating in $TE_{01\delta}$ resonant mode at 7.5 GHz. Standard error is given by the error bars as 1.9×10^{-4} Ω and 4.6×10^{-3} Ω for copper PCB and Aluminium AW6082, respectively, for five repeated measurements.

fix the resonant frequencies. Importantly, this means that only the sample is to be replaced, leaving the delicate coupling and metal plate as constants for each measurement. Provided that the walls of the cavity are sufficiently distant to the sample, induced currents and hence ohmic loss are equally distributed between the resonant structure and the sample, with only minor currents induced in the walls of the host cavity. Measurement of Q factor is used to asses the power loss of the system where, after calibration, differences in measured Q factor can be attributed to R_S values and form a comparison between various study samples. A CAD rendering of the parallel plate resonator is shown in Figure. 3.11.

3.4.1.1 Parallel Plate Transmission Line Theory

Simple analytic expressions for Q factor and resonant frequency of an idealised parallel plate resonator can be derived based on a half-wavelength section of parallel plate transmission line, as shown in cross section in Figure 3.12. Here, we assume that the current distribution on the cross section is uniform and also that the EM field magnitudes are uniform and contained wholly within the space between the plates (this becoming a better approximation as the aspect ratio h/W tends to zero).

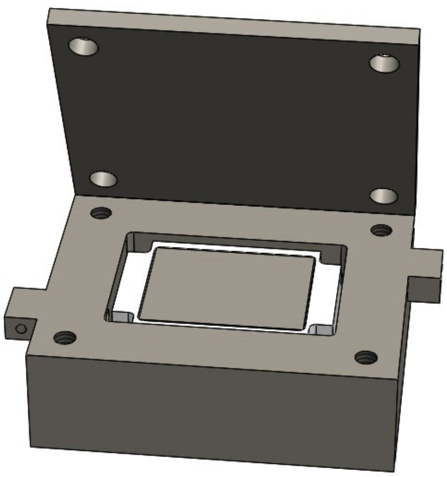

Figure 3.11: CAD rendering of a parallel plate resonator fixture for measurement of quality factor and evaluation of microwave surface resistance.

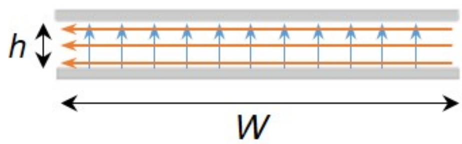

Figure 3.12: Schematic diagram showing the idealised, uniform electric (blue) and magnetic (red) fields in the space between the plates of a parallel plate transmission line. Current flow in the parallel plates is perpendicular to the magnetic field and opposite in each plate. Reprinted from [23] ©2021 IEEE.

Resonant Frequency Equation

The resonance condition is that the line length satisfies $l = p\lambda/2$, where λ is the wavelength along the line and p is an integer (> 0), the longitudinal mode number. The resonant frequencies are then

$$f_0 = \frac{pc}{2\sqrt{\varepsilon_{eff}}l} \tag{3.24}$$

where ε_{eff} is the effective dielectric constant of the line. Although mostly air spaced, the presence of a finite electric field in the PTFE sample frame will cause ε_{eff} to be slightly larger than 1, and the fringing fields at the open edges of the parallel plate structure mean that the length of the structure should be replaced by an effective value l_{eff} which is slightly bigger than the geometric length l, which increases approximately linearly as the plate separation h increases, assuming that the condition $h \ll l$ is maintained; the combined effects of ε_{eff} and l_{eff} are to reduce f_0 below the simple prediction from Equation 3.24. The resonant frequencies of the orthogonal TEM_{001} and TEM_{010} modes of interest in our fixture are then found by replacing l with b = 25 mm and a = 20 mm, respectively, giving frequencies of 6.0 and 7.5 GHz (in practice reduced to 5.3 and 6.4 GHz, respectively, owing to the effects mentioned above).

Q Factor Equation

For a simple analysis of the Q factor, we first consider the conductor quality factor Q_{c}. With the usual assumption that $h \ll W$, the resistance per unit length of a parallel plate line is $R \approx 2R_{\mathrm{S}}/W$, in terms of which its conductor attenuation constant is $\alpha_{\mathrm{c}} = R/2Z_0$. Assuming the characteristic impedance is $\mathrm{Z}_0 \approx \eta_0 d/W$ ($\eta_0 \approx 377\ \Omega$ is the free space wave impedance), these results can be combined with Equation 3.24 to give the following simple expression

$$Q_{\mathrm{c}} = \frac{p\pi}{2\alpha_{\mathrm{c}} l} \approx p\frac{\eta_0}{R_{\mathrm{S}}}\frac{d}{l} \approx 2p\sqrt{\varepsilon_{\mathrm{eff}}}\frac{d}{\delta} \tag{3.25}$$

where δ is the skin depth (defined by Equation. 2.2) and $p = 1$ for the TEM_{001} and TEM_{010} modes of interest here. Although greatly simplified, Equation 3.25 predicts the important dependency that Q_{c} is proportional to the plate separation h but independent of the plate width W. This assumes that the sample plate is parallel to the reference plate [141] and any deviation will change d and hence Q_{c}. In the case of planar metal samples, this error is accounted for during calibration. However for AM samples, any tilt present may rise from local non-uniform irregularities, quantified by the range in RMS surface roughness ($\mathrm{R_q}$) across the sample. From the AM samples investigated here, the maximum deviation in $\mathrm{R_q} = \pm 4.5\ \mu$m; this could have an effect of raising the quality factor through altering the effective plate separation, leading to an overall underestimate of R_{S} with an error of $\sim 0.45\%$. The dielectric quality factor Q_{d} is very high since the vast majority of the electric field energy is stored in the air space (by design), but can be written in the usual manner as $Q_{\mathrm{d}} = 1/\tan\delta_{\mathrm{eff}}$.

Q Factor Equation: PPR Calibration

Finite element modeling using modern computer simulation package COMSOL Multi-Physics generates accurate solutions in a non-idealised system such as ours. Whilst the approximate analytic analysis predicts the correct dependencies on key variables, simulation is needed for further refinement in order to extract more precise values of R_{S} from experimental data. The following, more rigorous approach starts with the well known equation for quality factor [132], expressed as a total value for the whole cavity resonator in Equation. 3.6. Different loss contributions can be isolated from Q_0 through

$$\frac{1}{Q_0} = G_s R_{Ss} + \sum_{m=1}^{i} G_{w_m} R_{Sw_m} + \sum_{p=1}^{j} p_{ed_p} \tan\delta_p \tag{3.26}$$

where Q_0 is the total unloaded Q factor of the system, R_{Ss} and G_{s}, R_{Sw} and G_{w} are the surface resistances and geometric values associated with the sample and the summation of i remaining conductive walls of the cavity and sample plate respectively. While p_{ed} is the dielectric filling fraction for j dielectric volumes present in the fixture (e.g PTFE frame and Nylon_{66} screws). The geometric factors and dielectric filling fractions are defined in equations 3.18a and 3.18b.

The numerical value of these geometric factors and geometric filling fraction will alter for operation in different resonant modes. The values of the definite integrals for G and p_{ed} can be accurately found through modern three-dimensional simulation packages (e.g COMSOL Multi-physics). tanδ is found for the dielectric material through cavity perturbation while R_{Sw} and R_{Sr} are found through calibration using a sample of the same material as the cavity walls (R_{Sw}=R_{Ss}). This leaves the sample R_{Ss} the only unknown variable from Equation. 3.26 to be analysed when measuring a study sample. Correction for fractional changes in frequency between measurement samples is achieved by assuming $\mathrm{R}_S \propto \sqrt{f}$ and tan$\delta \propto f$: the latter is a commonly accepted feature of dielectric loss, often quoted as $Q_{\mathrm{d}} * f$ = constant.

$$R_s(f) \approx Rs(f_0) \times \sqrt{\frac{f}{f_0}} \tag{3.27a}$$

$$\tan\delta(f) \approx \tan\delta(f_0) \times \frac{f}{f_0} \tag{3.27b}$$

A final calibration step is performed by measuring a PCB sample (with measured electrical isotropy, see Figure. 3.35) and weighting the results to known values found through an alternative evaluation technique [25]. This final calibration step is required to account for the current accumulation on the corners of the reference plate, shown in Figure. 3.19; this is the common "current crowding" that appears at the edges of planar transmission lines such as this. We find via COMSOL simulation that this non-uniform current distribution in the reference plate is constant across all measured samples of different electrical conductivity, which is discussed in more detail in Section. 3.4.3.3, therefore the final calibration step only needs to be completed once.

3.4.2 Resonator Design

The parallel plate resonator has undergone several iterations. To create the required orthogonal resonant modes, a metal plate of 25 x 20 x 1 mm^3 must be present within a rectangular cavity. The method for holding such a item has been investigated below.

3.4.2.1 PTFE Frame Design

The choice of shape for the supporting PTFE frame is critical to ensure the lowest possible dielectric loss contribution and highest physical stability to maximise reproducibility. Early iterations of PPR used the resonant structure as the study sample, placed on top of a pedestal attached to the lower surface of the rectangular cavity. A variety of frame shapes are shown in Figure 3.13. The rectangular editions on the the left introduced too much error associated with the placement of the sample, as there was no physical restraint for the sample. Furthermore the dielectric material is in an area of high electric feild, so will reduce Q_d significantly. The cross design, shown in Figure 3.14, was an improvement in terms of reproducibility while also removing the PTFE material as much as possible from areas of high electric field, to maintain a high value of Q_d. However, an

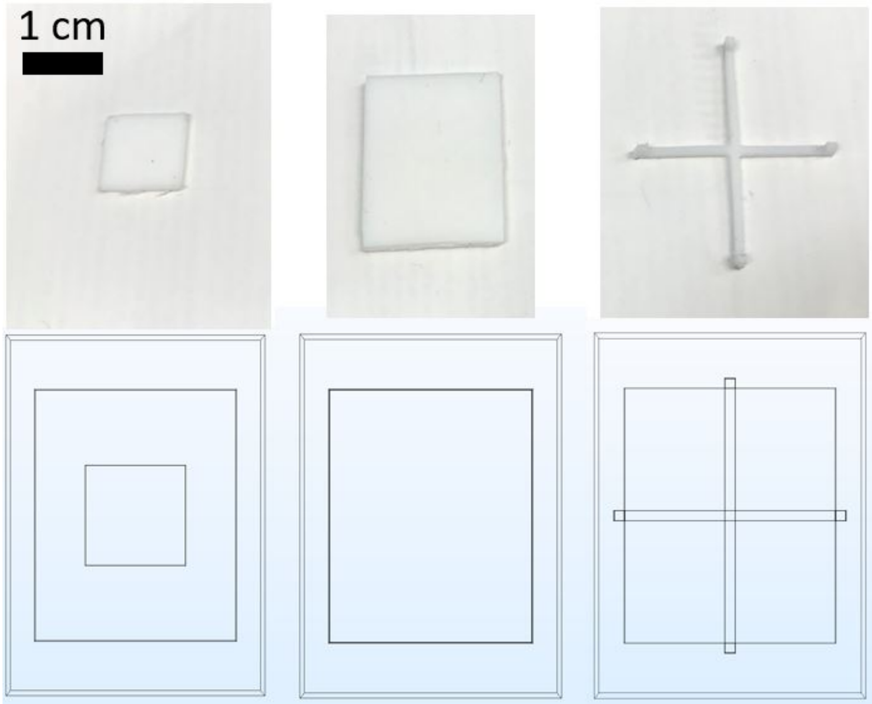

Figure 3.13: Photographs and CAD geometries of preliminary PTFE frame designs for securing samples within the Parallel Plate Resonator structure.

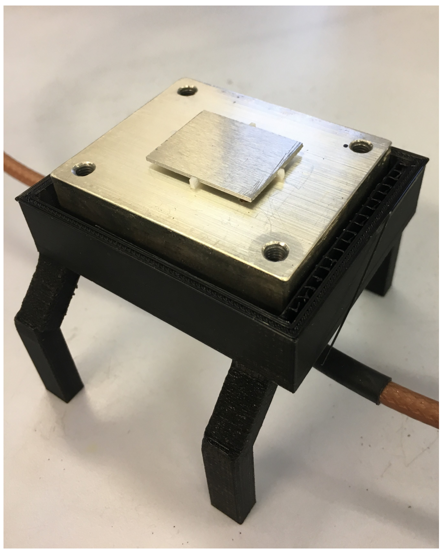

Figure 3.14: Photograph of a cross shaped PTFE frame in place holding an Silver plated calibration sample for the Parallel Plate Resonator structure (Mk1).

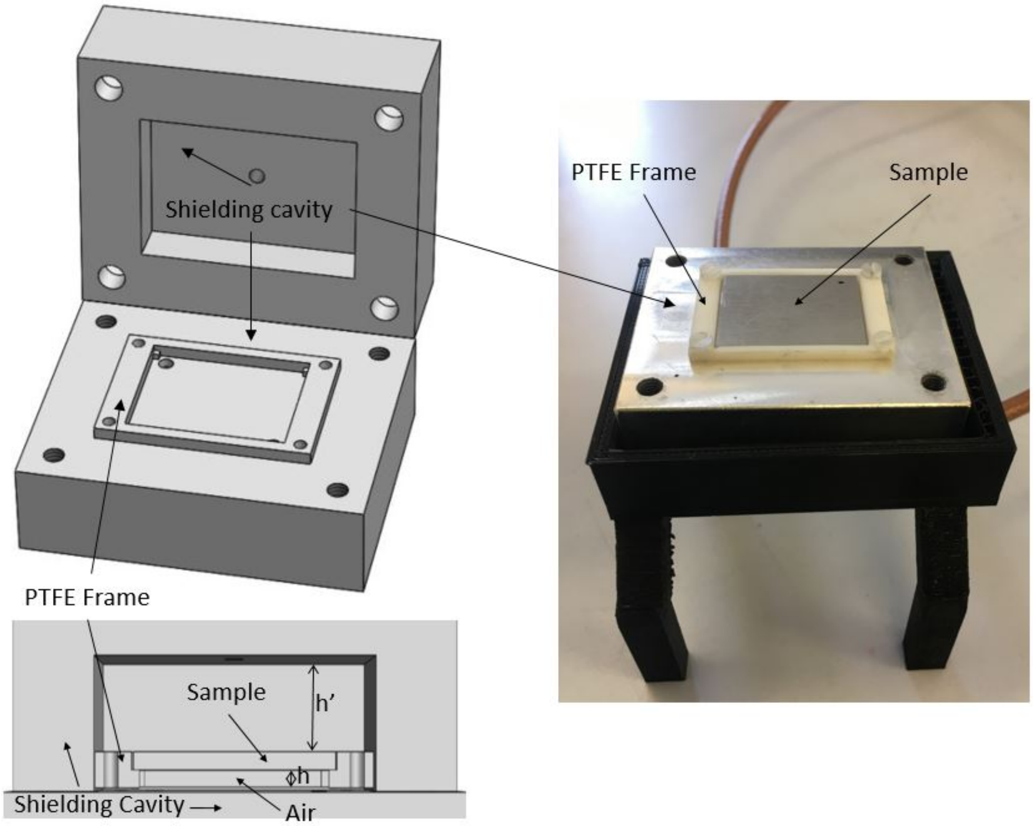

Figure 3.15: CAD renderings and photograph of the initial parallel plate resonator design (Mk2). A small PTFE frame holds a sample 1 mm from the bottom surface of the shielding cavity.

adhesive was required to hold the frame in place on the bottom surface of the cavity. The adhesive chosen for this purpose was First Contact optical cleaning fluid [142]. Although good for its intended optical purposes, the solution acts as a heavy microwave absorber within this resonant cavity and drastically reduced the measured Q factor, via a low value of Q_d. Such a low Q factor and an obvious source of high microwave loss not associated with the sample makes it difficult to extract accurate R_S values with any degree of certainty.

The second iteration used a cut out PTFE block, attached with $Nylon_{66}$ screws on the four corners. This design can be seen in Figure. 3.15 as part of the resonator CAD renderings and photograph. This PTFE frame iteration avoids the need for lossy adhesives within the cavity and initial measurements on bulk metal alloy samples were encouraging. Figure. 3.16 shows the measurements of Q factor and evaluated R_S for samples using the parallel plate resonator Mk2

Table 3.1: Table of sample geometries measured with a digital caliper.

Sample ID	Length (mm)	Width (mm)	Thickness (mm)	Error (mm)
Ag	25.33	20.15	1.05	± 0.05
Cu	25.30	20.40	1.01	± 0.05
Brass	25.23	20.13	1.01	± 0.05
Al	24.97	19.91	1.04	± 0.05

shown in Figure. 3.15. The measured Q factor values show a distinct separation in values between various metal samples, successfully distinguishing between materials of different electrical conductivity. Evaluating Q factor for R_S, it is shown that the copper (Cu) sample has the lowest surface resistance in both resonant modes, followed by the silver plated aluminium (Ag) sample with aluminium being the most resistive, as is expected.

However several other issues were found during the commissioning. The $Nylon_{66}$ screws used to secure the PTFE frame introduce an additional dielectric loss to factor into the analysis, although through cavity perturbation these loss factors can be accurately modeled and accounted for. A more significant issue is noted with the accuracy of manufacturing the geometry of the samples. A study by Haefner formally identified that changes in physical geometry of rectangular transmission lines can alter the high frequency resistance seen on the line [143]. A series of prepared samples produced of different materials for the parallel plate resonator have been measured for physical geometry and the results can be seen in Table. 3.1. The range in width values is around 0.5 mm. To illustrate the impact changes in geometry can have on evaluated R_S values, graphs of simulated R_S and resonant frequencies are shown in Figure. 3.17. For a ± 1mm range in sample width, evaluated R_S shows a range of values of $\sim \pm 1.5$ mΩ around an average R_S around 23.2 mΩ. This is expected when the shift in resonant frequency is taken into account, where wider samples exhibit lower R_S values as explained by the relationship $R_S \propto \sqrt{f}$. For the measured

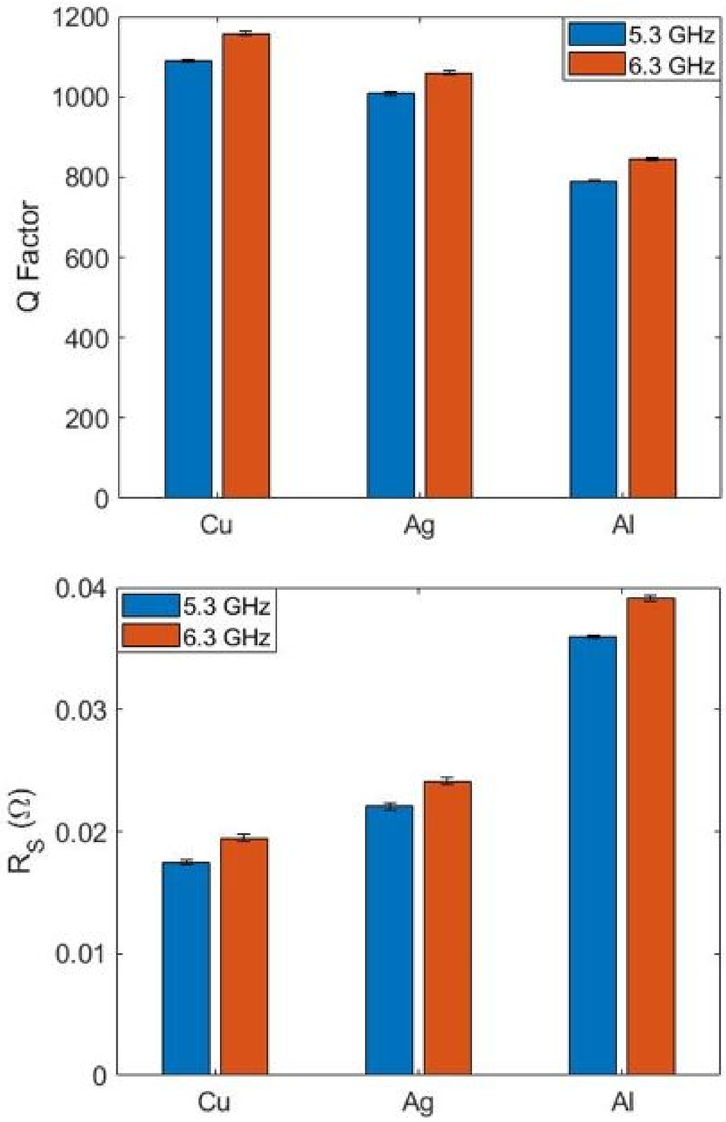

Figure 3.16: Graphs of measured Q factor and evaluated surface resistance (R_S) from the parallel plate resonator (Mk2) fixture. The standard error is given by the error bars for five repeat measurements

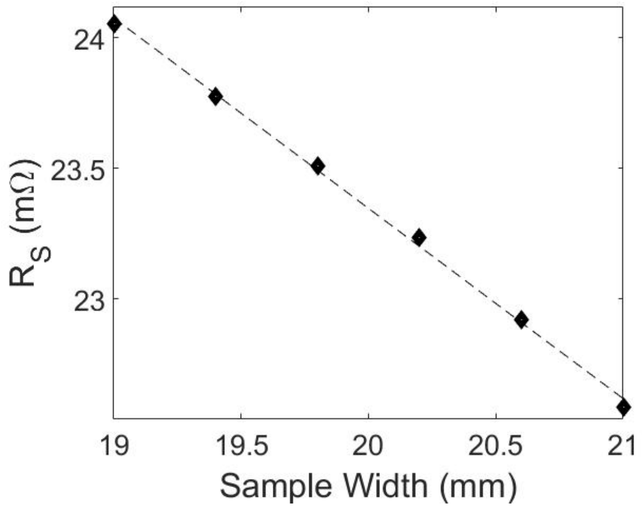

a)

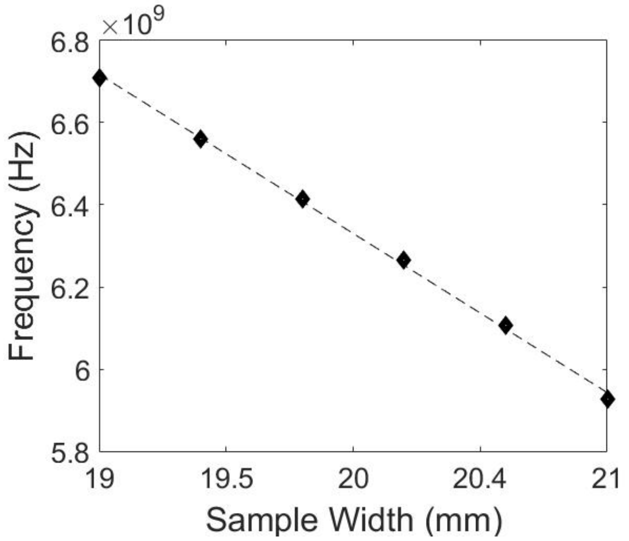

b)

Figure 3.17: Graphs of a) simulated surface resistance (R_S) and b) resonant frequency as a function of sample width for a silver plated sample. Width varied $\pm$ 1 mm from the design specification of 20 mm around an R_S value of 23.25 mΩ

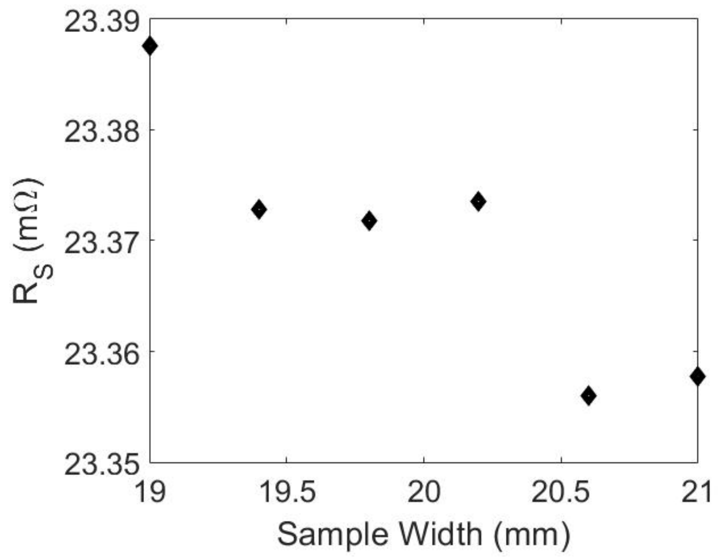

Figure 3.18: Graph of frequency corrected surface resistance (R_S). Corrected to 6.4 GHz (20mm width).

samples in Table. 3.1, this would equate to a difference of 0.4 mΩ for the range of measured geometries, if produced of the same material, generating roughly a ±2% error from geometry alone. The shift in resonant frequency and changing G factor values brought about by changes in length and width can be accounted for by meticulous and painstaking physical measurement and simulation for every sample. A demonstration of this is shown in Figure. 3.18, where R_{S} values are separated by only 32 $\mu\Omega$ after correction. However, the uncertainty introduced by the physical geometry measurement using a set of calipers means that the error is large.

Further to geometric uncertainties in this design, an investigation into surface current density in the small rectangular sample highlights an uneven distribution. Specifically, due to the corners present on the sample there is a high density of current concentrated on the extremities of the sample, where the radius of curvature is greatest. The technical term for this effect is current crowding. Figure. 3.19 shows the surface current distribution along the length of the sample while the resonator is operating TEM_{010} mode at 6.4 GHz. The current density peaks at the edges of the sample, suggesting that the sensitivity of the measure-

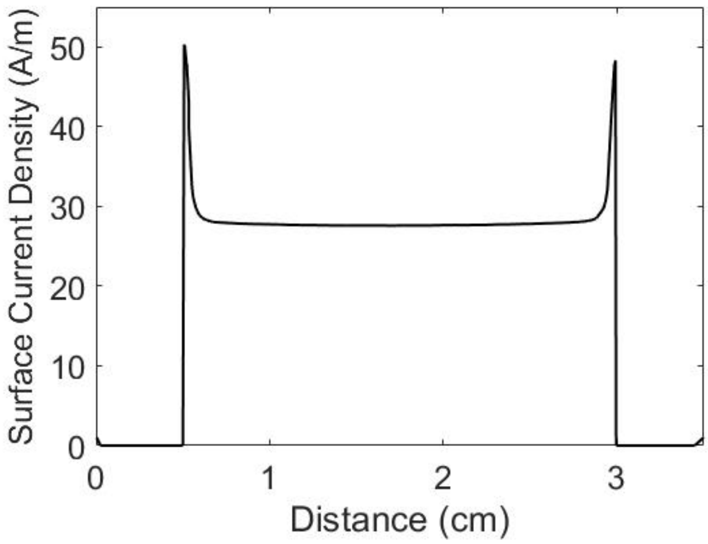

Figure 3.19: Simulated surface current density (A/m) along the length of the sample, while current flows across the samples width, operating in TEM_{010} mode at 6.4 GHz. The slight asymmetry in the peaks is due to limitations in the resolution of the FEM mesh.

ment is focused on these areas extreme to the peripheral of the surface rather than an average across the whole surface of the sample. The uneven sensitivity brought about by the current distribution means that this particular design, using the central rectangular plate as the sample is desirable. This current crowding phenomena is discussed further in the final design section of this chapter.

However, when assessing the technique for PBF samples a more fundamental problem is encountered. Producing of a sample in a PBF process requires a series of support structures to elevate it from the build platform; this is to allow effective removal of the part from the build platform. Cutting these support structures away is the first post processing step in achieving a finished part. However, when the samples are thin, and built in a horizontal orientation, it can be difficult to obtain sufficient purchase as to secure the sample while the support structures are removed. An example of the resultant part facing this issue is shown in Figure. 3.20, where the support structures have not successfully been removed. This renders the sample not fit for testing as it no longer meets the 1 mm thickness specification so the microwave cannot be accurately accounted for from the ‘support structure’ face. It is clear that to effectively evaluate PBF

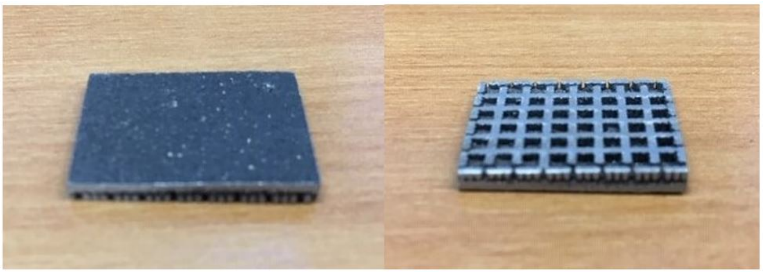

Figure 3.20: Photographs of a sample produced of AlSi10Mg on a Renishaw AM250 Powder Bed Fusion additive manufacturing system. The thin samples made it difficult to effectively remove support structures from horizontally built samples.

samples, the resonator fixture must be designed so that only a single face of the sample is measured at any one time.

3.4.2.2 Final Cavity Design

Figure. 3.21 shows schematic images and photograph of the final cavity design. Silver plating has been utilised to increase the electrical conductivity of the cavity walls and reference plate, and hence ensure that the maximum relative loss contribution is focused on the measurement sample. We choose silver as silver has the highest electrical conductivity of any material at room temperature, leading to the lowest possible surface resistance for the reference plate, which has to be subtracted in the method to find the surface resistance of the sample under test. The base material used was aluminium for the cavity and reference plate, PTFE for the reference plate support structure and Nylon_{66} for the securing screws. The internal dimensions of the cavity structure are 35 x 25 x 7 mm^3, while the resonant structure is 25 x 20 x 1 mm^3. This reference plate is held on a frame of PTFE which provides an air spacing h of ∼1 mm between it and the sample, which together act as half-wave resonators in orthogonal orientations (width and length). The ratio between length and width is such that sufficient separation of around 20% (∼ 1 GHz) is present between the centre frequencies of the two desired, parallel plate associated resonant modes; this separates them sufficiently spectrally to allow independent measurements of their resonant fre-

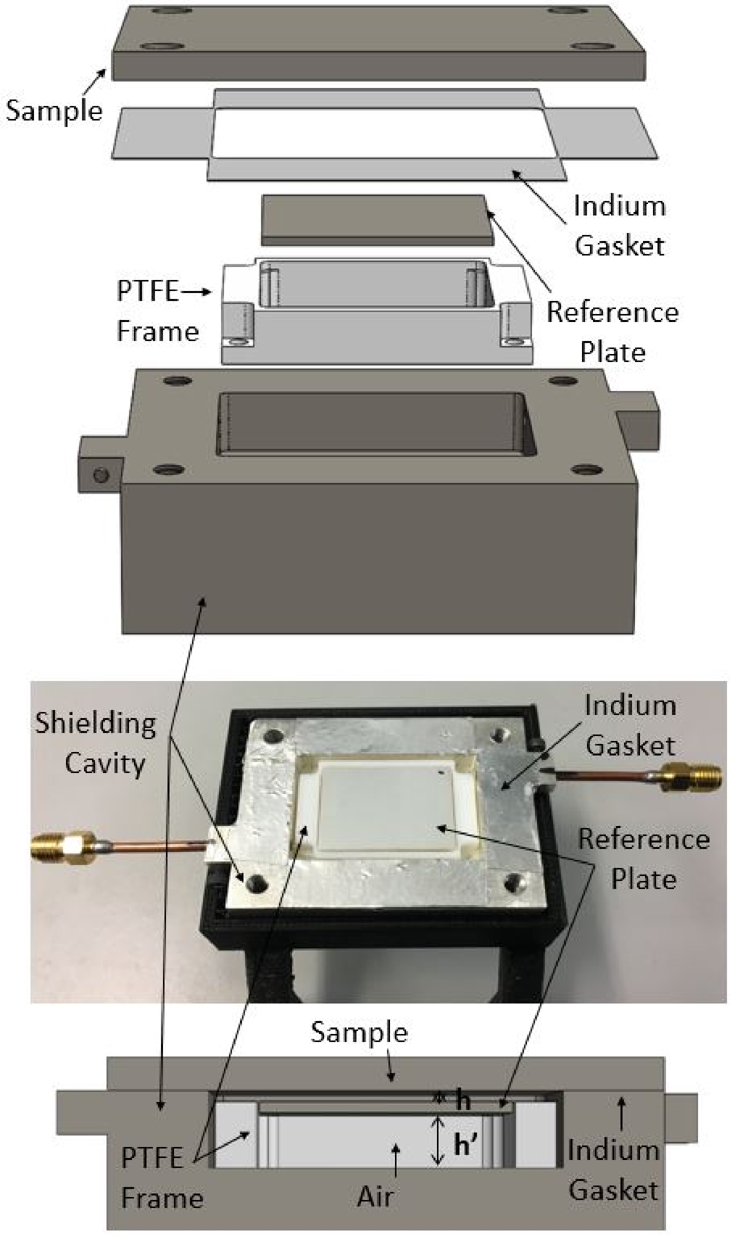

Figure 3.21: Enclosed Parallel Plate Resonator (Mk3). A PTFE frame suspends the small reference plate below the sample within the shielding cavity. Resonant frequency and Q factor are analysed to evaluate R_S of the sample. Top) Exploded CAD image, Middle) Photograph of the parallel plate resonator, Bottom) CAD Cross section of the assembled fixture. Reprinted from [23] ©2021 IEEE.

quencies and Q factors via the S21 parameters. The half wavelength resonant frequency associated with the reference plate is defined in Equation. 3.24.

It is accepted that when the distance between the lower conducting surface of the reference plate and the lower wall of the host cavity (h') is greater than five times the height of the substrate (h), the loss contribution from the top wall of the cavity becomes comparatively small [144], as shown in Figure. 3.27. In addition, the proximity of the side walls of the cavity to the sample must be such as to create a sufficient separation between the parallel plate associated modes and cavity associated modes, in doing so also reducing the stray capacitance between the resonant structure and the cavity walls. In this design the dominant mode of the rectangular cavity TE_{101} is around 7 GHz while the half wave resonator frequencies of the parallel plate sample are TEM_{001} at around 5.3 GHz and TE_{010} at around 6.4 GHz.

To further increase the influence of the conductors on the total system loss, the dielectric spacer is removed from areas of high electric field, resulting in minimal dielectric loss. To ensure a good electrical connection and avoid EM leakage from the fixture, an electrically conductive gasket made of 100 μm thick indium foil of electrical conductivity $\sigma = 1.2 \times 10^7$ S/m was placed around the edges of the cavity structure. The extremely pliable metal deforms to fill the voids between peaks of rough surfaces at the metal-to-metal joints. This is of particular importance when measuring samples produced of metallic additive manufacturing, where roughness peaks can be $\pm$ 100 μm high from the mean surface plane. A schematic of the problem is shown in Figure. 3.22. The gasket enables a good electrical contact with as large of an area of the rough surface as possible, effectively reducing any loss associated with radiation through any gaps between roughness peaks while maximising the loss contribution from the ohmic properties of the sample itself.

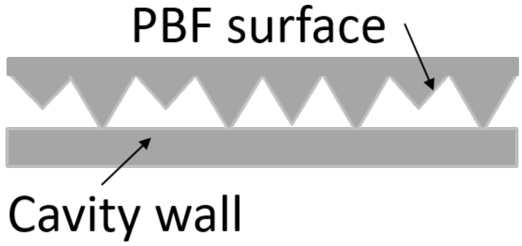

Figure 3.22: Schematic of the interface between a rough PBF sample and the smooth, machined, aluminium cavity wall. Air pockets / gaps are formed between the cavity wall and smaller protrusion of roughness on the PBF surface.

3.4.3 Simulation

The electric field distribution for TEM_{001} and TEM_{010} can be seen in Figure. 3.23a. The corresponding magnetic field induces current flow on the sample. The simulated surface currents for both TEM_{001} and TEM_{010} resonant modes are shown in Figure. 3.23b, where the current on the surface of the sample flows in a uniform pattern, having a directional dependence on the operating mode. Also shown on Figure. 3.23 is the positioning of the coupling probes, in opposing corners of the cavity volume where electric field is high for both resonant modes. Using COMSOL Multi-physics simulation tool combined with cavity perturbation measurements for ε_{r} and $\tan\delta$, the loss contribution for each section of the fixture can be evaluated. The parameters used for simulation at 6.4 GHz are: relative permittivity of the PTFE frame ($\varepsilon_{\mathrm{r_P}}$) = 2.1 and Nylon securing screws ($\varepsilon_{\mathrm{r_N}}$) = 3.9, dielectric loss for PTFE ($\tan\delta_{\mathrm{P}}$) = 1.0×10^{-4} and Nylon screws ($\tan\delta_{\mathrm{N}}$) = 1.3×10^{-2} and $\sigma = 4.9 \times 10^{7}$ S/m of the silver plating used on the cavity walls, reference plate and calibration sample. This value for the silver plating material is around 20% lower than the recorded DC book value for pure silver and is typical of values seen at microwave frequencies [145, 146, 147].

The forward transmission coefficient (S_{21}) traces from both simulation and measurement are shown in Figure. 3.24 and are in good agreement. Evaluating the field integrals from equations 3.18a and 3.18b, and combining with Q_0 given through simulation, Equation. 3.26 can be solved for R_{S}. The total simulated

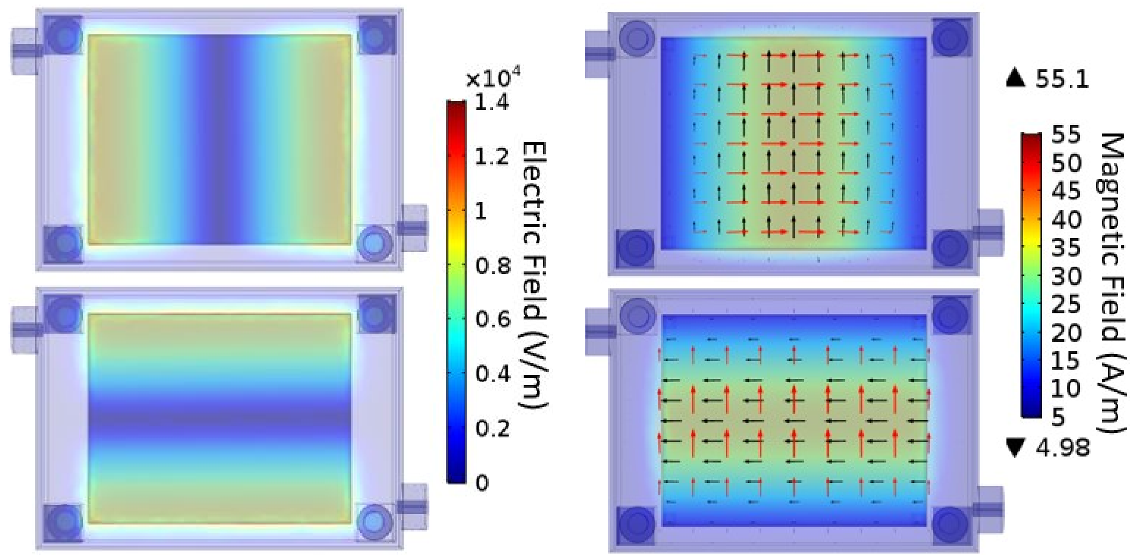

a) b)

Figure 3.23: Top view of simulation results for the parallel plate resonator. a) Simulated electric field distribution and magnitude, b) Simulated induced surface currents (red arrows), magnetic field (black arrows) and magnetic field distribution and magnitude, for TEM_{001} (Top) at 5.3 GHz where current flow along the length of the sample and TEM_{010} (Bottom) at 6.4 GHz where current flows along its width. Simulations are performed using COMSOL Multiphysics software with an arbitrary input power of 1 W. Adapted from [23] ©2021 IEEE.

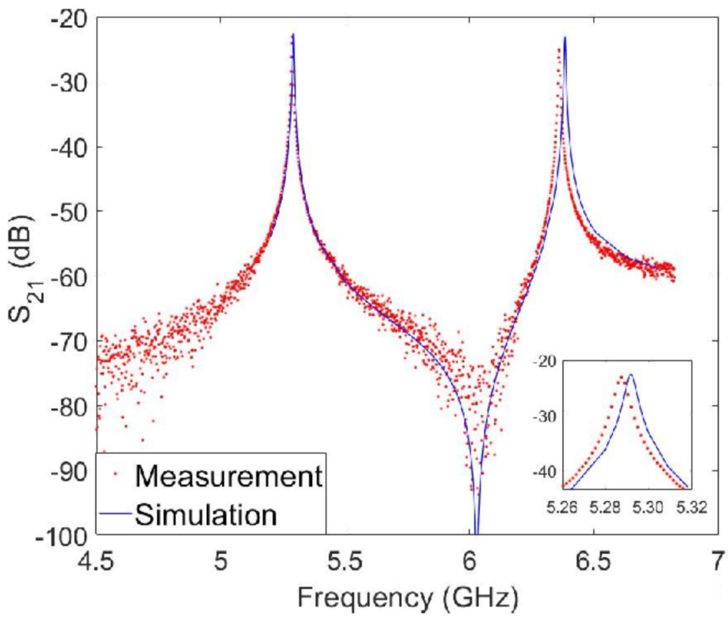

Figure 3.24: Graph of the magnitude of S_{21} transmission coefficient for the parallel plate resonator. Red dots are the measured values using a Keysight N5232A PNA. Blue line is the simulated trace using COMSOL multi-physics. Inset is a magnified view of the measured and simulated S_{21} transmission coefficient traces for TEM_{001}. Reprinted from [23] ©2021 IEEE.

Table 3.2: Simulated loss contribution within the parallel plate resonator fixture operating in TEM_{010} mode at 6.4 GHz. Silver plated aluminium is used as the material for the cavity walls, sample and reference plate.

Fixture Section	Loss contribution (%)
Sample	44.1
Reference plate	43.9
Host Cavity Walls	9.6
$Nylon_{66}$ Screws	1.4
PTFE Frame	1.0

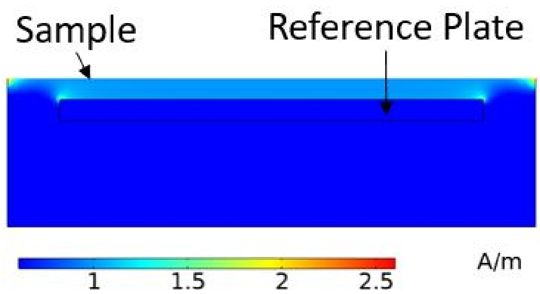

Figure 3.25: Simulated magnetic field magnitude (A/m) at 1 MHz in a cross section of a rectangular conductor geometry similar to that of the parallel plate resonator. Current is flowing into the page in this example.

loss contribution from each section of the fixture is shown in Table. 3.2.

3.4.3.1 Corner Effects on Current Distribution at Microwave Frequencies

When considering the resistance of a conductor in a transmission line, an important factor is the cross sectional area in which current is flowing, as explained by equation 3.28, derived from Pouillet's law [148].

$$R = \frac{\rho}{A} \approx \frac{\rho}{2\delta(W+t)} \approx \frac{R_s}{2(W+t)} \tag{3.28}$$

where ρ is the resitivity of the material, A is the current carrying cross sectional area, δ is the skin depth and W and t are the width and thickness of the conductor respectively. Sharp corners on a rectangular conductor lead to a localisation of magnetic field and thus a high current density at the edges of the conductor, as well as concentration of the electric fields. This localisation of magnetic field is shown in Figure. 3.25. These simulations have been performed at lower MHz frequencies for better computational efficiency, however they portray the same principles apply at GHz frequencies. In addition, the skin effect at microwave frequencies forces current to flow on the extremities of the conductor geometry. Figure. 3.26 shows the effect that increasing frequency has on the current density of a rectangular conductor. With an opposing current flowing in the sample (upper cavity wall in Figure. 3.26), and the ratio W/h designed to be large, the current in the reference plate is concentrated on the surface closest to the sample, particularly at the corner areas, with only minor currents flowing on the lower and side surfaces [149]. The inset to Figure. 3.26 is a close up view of the corner and upper surface of the reference plate showing this uneven current distribution, which is more exaggerated at higher frequencies.

The simulated surface current densities for the reference plate (upper surface), sample and cavity wall are shown in Figure. 3.27. The non-uniform current distribution in the reference plate effectively means that current is flowing in a smaller cross sectional area. At high frequencies this current carrying area becomes very small due to a decrease in skin depth. According to equation 3.28, this small current carrying area at the corners will lead to a higher overall resistance value of the reference plate. The increase in resistance due to these corner effects is quantified by a correction factor of approximately 1.2 [150] for an isolated conductor, even higher when there is a opposing current in the parallel ground plate (sample) [149]. It is important to note here that the current density in the sample under test remains uniform, owing to the absence of any corners.

Multiple scholarly articles have been published concerning singularity conditions for electric field and magnetic field at sharp edges [151, 152, 153] and the current density associated with magnetic field singularities [154]. These are mainly concerned with analytic solutions for cases where ideally sharp corners

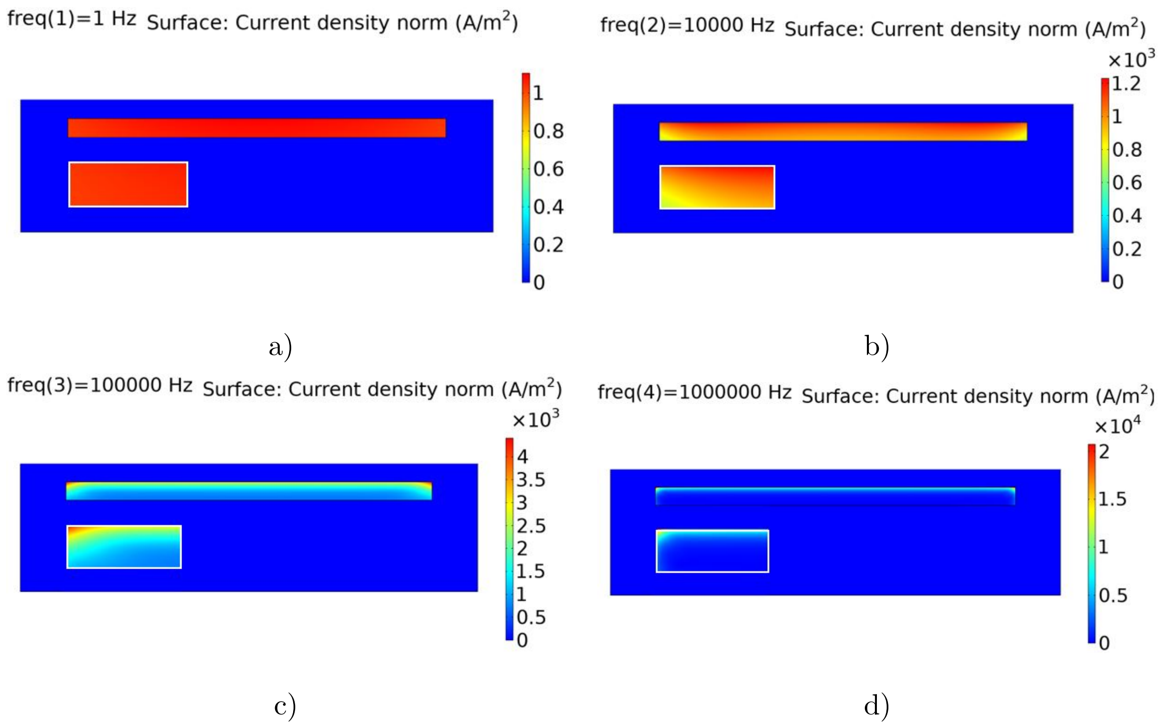

Figure 3.26: Simulation results showing the effect of frequency on the current density (A/m^2) on the cross section of rectangular conductor. Inset is a magnified view of the corner, an area of high current density at high frequencies, flowing out of the page on the reference plate. Simulation performed at a) 1 Hz, b) 10 kHz, c) 100 kHz, d) 1 MHz.

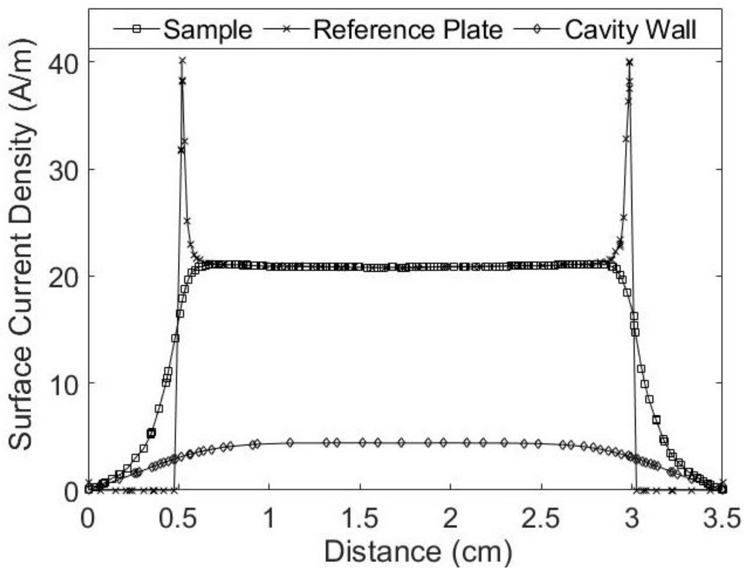

Figure 3.27: Simulated surface current density along the length of the cavity, for current flow along its width. This is shown for the surface of the reference plate and surface of the sample, which make a parallel plate resonator. Also shown is surface current density of the cavity wall parallel to the sample. Results are for the TEM_{010} resonant mode at 6.4 GHz, where surface currents flow perpendicular to the cut line. Reprinted from [23] ©2021 IEEE.

exist in material of infinite conductivity. However, when assessing a material of finite conductivity and non-ideal corners, as produced by any manufacturing technique, these singularities cease to exist [149, 155]. The field magnitude growth seems to obey a $R^{-\frac{1}{3}}$ rule in many cases, where R is the distance from the conductor edge [149, 152], leading to the uneven current density shown in Figure. 3.27.

3.4.3.2 Effect of Corner Radius

The current density due to corners in rectangular conductors can be reduced through the introduction of a corner radius, something present in most common manufacturing processes. Figure. 3.28 displays the current density of a rectangular conductor at 100 MHz with various corner curvatures. As the corner radius increases, the current density is lower and is distributed more evenly along the upper surface and side walls the conductor. This spreading will have the effect of reducing the overall resistance of the conductor. In the absence of an accurate measurement of corner radius for the reference plate, an a-priory calibration process is implemented for the PPR; where a PCB sample of know R_{S}, measured with an alternative method, is used to calibrate the PPR setup.

3.4.3.3 Effect of Sample conductivity

To ensure that the uneven current distribution in the reference plate does not prevent the PPR fixture from accurately measuring study samples, a simulation sweep of electrical conductivity has been performed for the sample surface. Figure. 3.29 shows the simulated surface current density in the reference plate when electrical conductivity value of the sample-under-test are swept from 1.0 $\times$ 10^5 S/m to 1.0 $\times$ 10^8 S/m i.e. to above the conductivity of Ag at room temperature, to take the range to absolute extreme for practical circumstances. Figure. 3.30 shows the surface current density along the length of the sample-under-test for the same simulation parameters. The simulated results show no

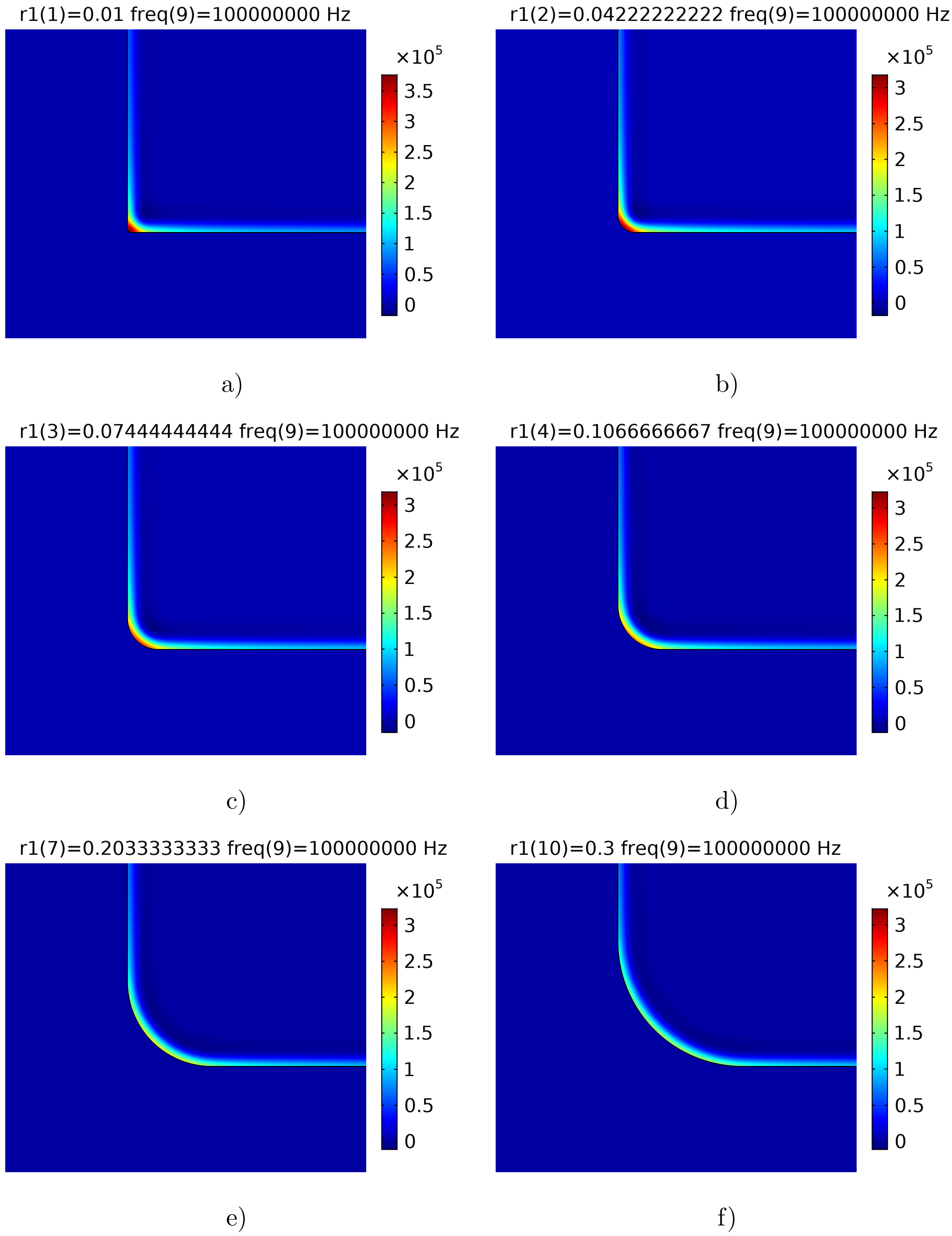

Figure 3.28: Simulation results showing the effect of corner radius on the current density (A/m^2) within a rectangular conductor at 100 MHz. Corner radius a) 0.01 mm, b) 0.04 mm, c) 0.07 mm, d) 0.11 mm, e) 0.20 mm, f) 0.30 mm.

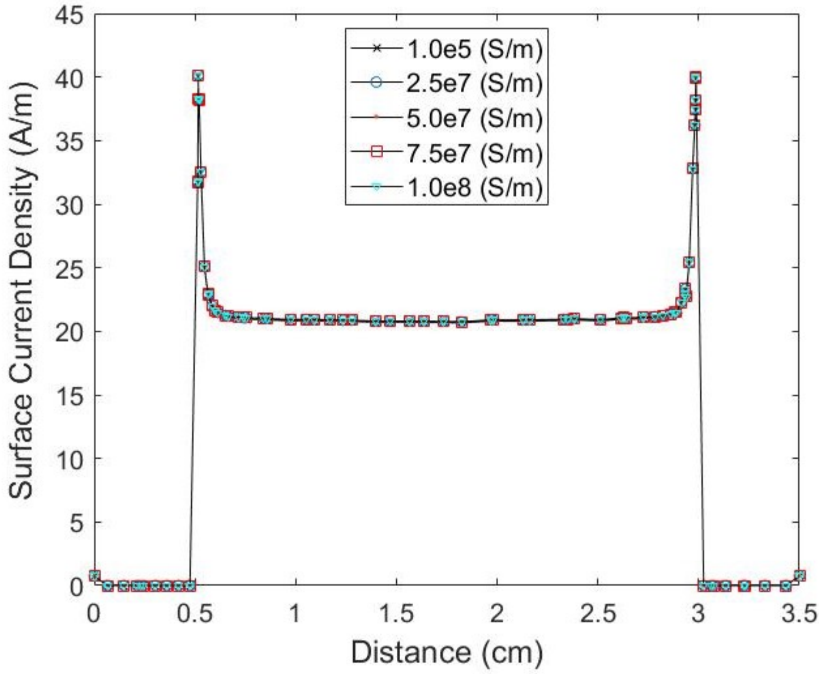

Figure 3.29: Simulated surface current density along the length of the cavity. This is shown for the surface of the reference plate at various electrical conductivity values for the sample surface.

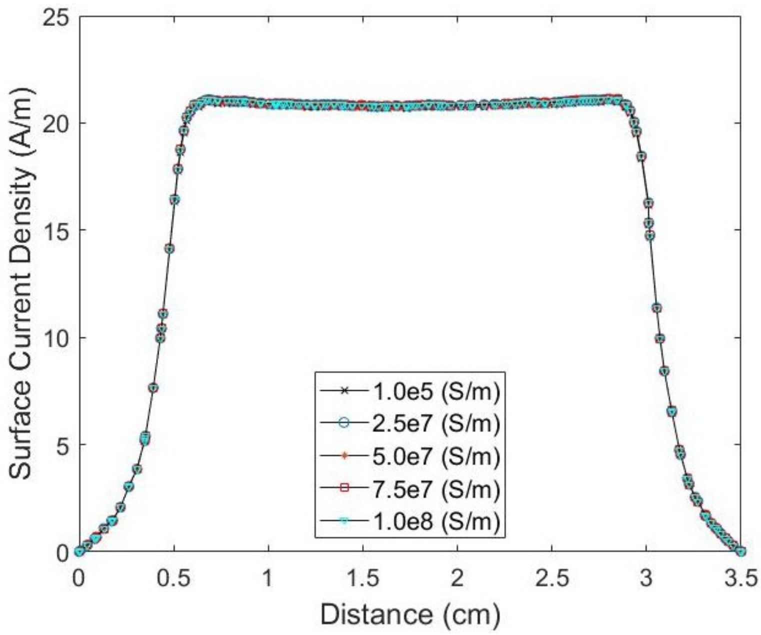

Figure 3.30: Simulated surface current density along the length of the sample, while current is flowing along the width. This is shown for a variety of electrical conductivity values.

discernible difference in current density distribution on the reference plate with changing (sample) conductivity. This distribution can therefore be considered a constant for any sample-under-test (within these electrical conductivity values) and is calibrated out of the final analyses for sample R_S through the use of a copper PCB calibration plate of known surface resistance.

3.4.4 Microwave Coupling

Microwave coupling is achieved through capacitive probes in opposing corners of the cavity volume, orientated parallel to the cavity wall as to align with the electric field between the sample and reference plate. The coupling probes are manufactured from RG405 coaxial cable, where the inner conductor protruded into the cavity volume by approximately 3 mm. They are placed near the corners of the rectangular reference plate, in areas of high electric field for both modes of interest. This placement is chosen to be sufficiently distant as to provide a low coupling coefficient (S_{21} below -20dB) and decrease systematic error when unloading Q factor [133]. The system insertion loss (S_{21}) from simulation and measurement are shown in Figure. 3.24. The inset to Figure. 3.24 is a simulated cross section of the coupling probe geometry, which is shown in greater detail in Figure. 3.31. Return losses (S_{11} and S_{22}) for TEM_{001} and TEM_{010} are shown in Figures. 3.32 and 3.33 respectively. The close match between S_{11} and S_{22} losses (for both resonant modes of interest) allows for the conclusion to be drawn that symmetrical coupling is achieved in this implementation, facilitating the

Figure 3.31: Cross section of the parallel plate resonator geometry, showing the coupling probe orientated parallel to the cavity wall as to align with electric field between the reference plate and the sample. Reprinted from [23] ©2021 IEEE.

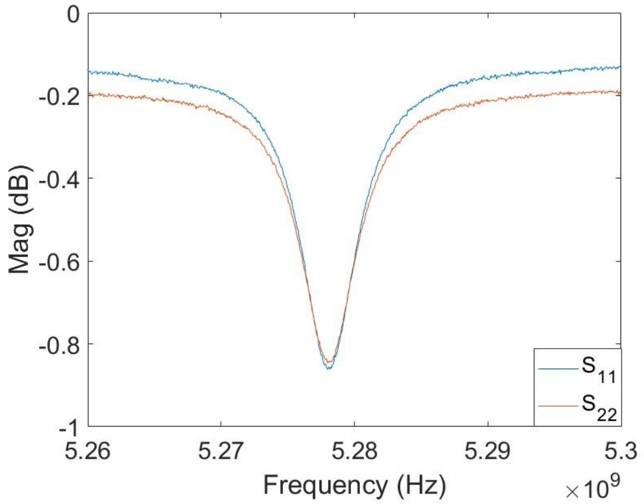

Figure 3.32: S Parameters for the electromagnetic coupling of TEM_{001} mode at 5.3 GHz in the parallel plate resonator.

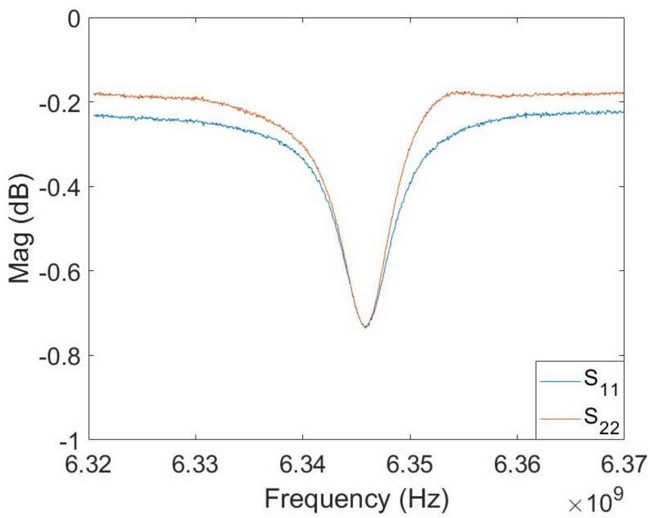

Figure 3.33: S Parameters for the electromagnetic coupling of TEM_{010} at 6.4 GHz in the parallel plate resonator.

evaluation of unloaded Q factor to be performed using the simplified technique described in Chapter 1.1.

3.4.5 Calibration Results

In order to accurately account for the additional losses associated with the crowding of the current density at the edges of the rectangular reference plate described in section 3.4.3, a calibration procedure is outlined here using a sample of copper PCB of known R_S. The value of R_S considered as 'known' is taken from a previous set of measurement results using the dielectric resonator fixture described in Section. 3.3 and published in [25, 91, 86]. This provides the best measurement of R_S by any means that we can access, and should be considered to be a "gold standard" value.

3.4.5.1 PCB Samples

On microscopic inspection of the Rogers Corp. RT/duroid 6002 sample plates, evidence of a directional surface pattern can be seen and is shown in Figure. 3.34, generated by the electro-depositing process of the copper foil manufacturing process [156]. As highlighted, the DR measurement technique (used for the 'known' R_S value) makes use of azimuthal currents induced in the sample. This current

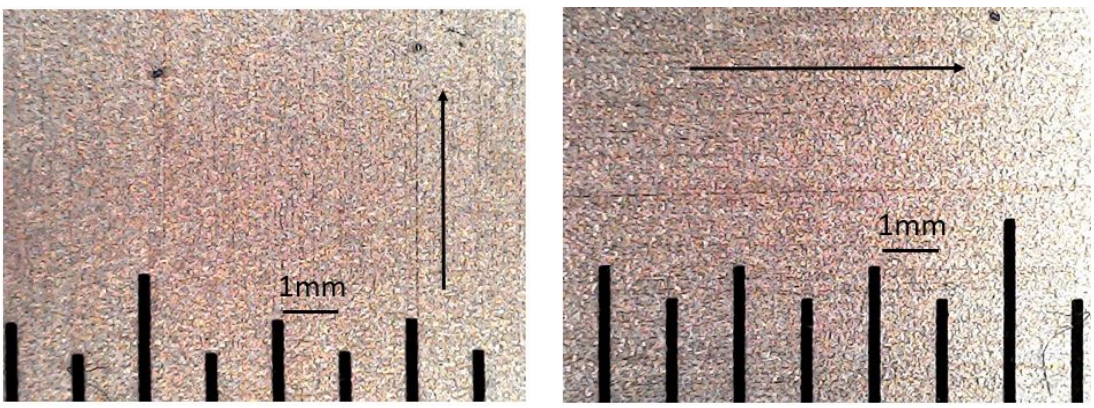

a) b)

Figure 3.34: Microscope image of PCB (Rogers Corp. RT/duroid 6002) samples. Samples where the rolling direction can be seen along the sample a) length and b) width. Black arrows indicate the direction of patterning.

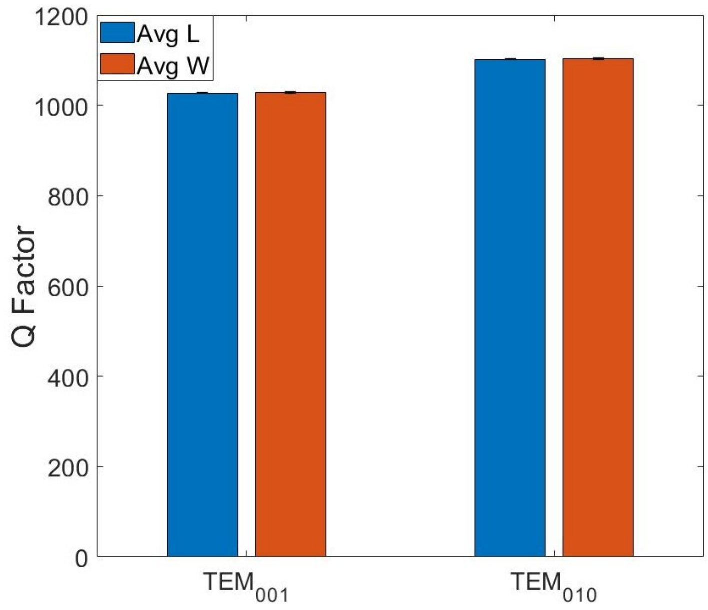

Figure 3.35: Average quality factor measurements for PCB samples with orthogonal surface patterns, using both resonant modes for each sample set. Standard error is shown in the error bars.

pattern gives an orientationally averaged value for R_S of the sample. In the case of the PCB samples where there exists directional surface patterns, the DR method alone cannot be used to asses the influence of these directional patterns on the surfaces resistive properties. To ensure isotropy in R_S and hence the reliability of the calibration, samples were produced such that these surface patterns are orientated in perpendicular directions (i.e. three sample plates where the pattern runs along the length and three sample plates where the pattern runs across the width). These samples were measured using the parallel plate resonator fixture and their Q factor values are shown in Figure. 3.35.

The measurements show only around 0.1% difference between the average Q factor values for each sample set. This very low value is of the same magnitude as the random error seen for individual samples, due to the high accuracy of the Keysight PNA used to measure Q factor and frequency. This is compared to a random error of approximately 1% across all measurements (equating to a variation in Q factor of 12 about an average value of around 1100, for 24 measurements across six sample plates measured in TEM_{010}), arising from the manual placement and fixing of the sample to the fixture.

3.4.5.2 Correction factor for evaluating R_{Ss}

As stated in [150], sharp corners on rectangular conductors require a correction factor to properly account for the current crowding. Therefore the COMSOL generated solutions are used in conjunction with a known sample to find an appropriate correction factor. Since the contribution to loss from the cavity walls is low (around 2%) it is combined with the reference plate to give an average R_{SwCal} value for the silver plated conductive surfaces of the test fixture (minus the sample plate). This is unchanged by the replacement of various samples and defined as

$$R_{SwCal} = \frac{\frac{1}{Q_0} - G_{Cu}R_{S_{Cu}} - \sum_{p=1}^{N} p_{ed_p}\tan\delta_p}{G_{Sw}} \tag{3.29}$$

where $R_{\mathrm{S_{Cu}}}$ and G_{Cu}, and $R_{\mathrm{Sw_{Cal}}}$ and G_{Sw}, are the surface resistance and geometric factors for the 'known' reference PCB sample and remaining conductive surfaces in the fixture, respectively. Having established the isotropic nature of the PCB samples through Q factor measurements, shown in Figure. 3.35, $R_{\mathrm{S_{Cu}}}$ is found by scaling the measured value from [25](24.2 mΩ) using Equation. 3.27a to be 22.3 mΩ at 6.39 GHz. Inserting this value into Equation. 3.29 gives R_{SwCal} = 31.35 mΩ.

Through evaluation of Equation. 3.26, when R_{Ss} is set equal to R_{Sw} as in the Section 3.4.1.1, R_{SwAvg} is evaluated to be 27.58 mΩ, as an average value for every silver plated conductive surface in the fixture. Therefore, using the value gained from Equation. 3.29 we can calculate the correction factor as;

$$k = \frac{R_{Sw_{Cal}}}{R_{Sw_{Avg}}} = \frac{31.35m\Omega}{27.58m\Omega} = 1.14 \tag{3.30}$$

This correction factor can be applied to R_{Sw} in Equation. 3.26 to produce accurate values for R_{Ss} of any measured sample in the TEM_{010} mode at 6.4 GHz, without the need for additional PCB calibration sample. Equation. 3.26 in terms

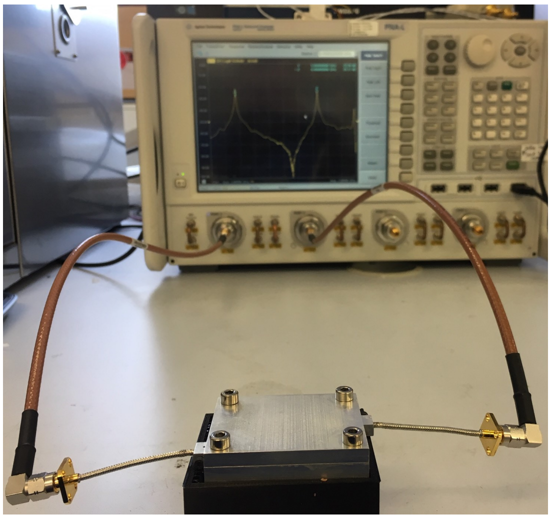

Figure 3.36: Photograph of the experimental setup of the parallel plate resonator connected to Keysight N5232A network analyser. Display showing the S21 trace for frequency spanning both resonant modes (TEM_{001} at 5.3 GHz and TEM_{010} at 6.4 GHz). Reprinted from [23] ©2021 IEEE.

of R_{Ss} of the sample then becomes

$$R_{Ss} = \frac{\frac{1}{Q_0} - \sum_{m=1}^{M} G_{w_m} k R_{SwAvg} - \sum_{p=1}^{N} p_{ed_p} \tan\delta_p}{G_{s_n}} \tag{3.31}$$

R_{Ss} for the silver plated aluminium reference plate is found to be 23.15 mΩ at 6.39 GHz.

3.4.6 Initial Results and Discussion

Measurements of Q factor were taken for flat metal samples of semi-bright-silver plated aluminium and Rogers Corp. RT/duroid 6002 PCB calibration samples, bulk metal alloys of aluminium AL6082 and brass CZ121, as well as samples produced of AlSi10Mg and Ti6Al4V, by means of PBF. Q factor and frequency were measured through 2-port S-parameters using a Keysight N5232A network analyser. A photograph of the measurement setup is shown in Figure.3.36.

3.4.6.1 Planar Metal Samples

The evaluated R_{S} values for measured samples can be seen in Figure. 3.37, from which we can deduce that R_{S} values measured in both resonant modes follow the

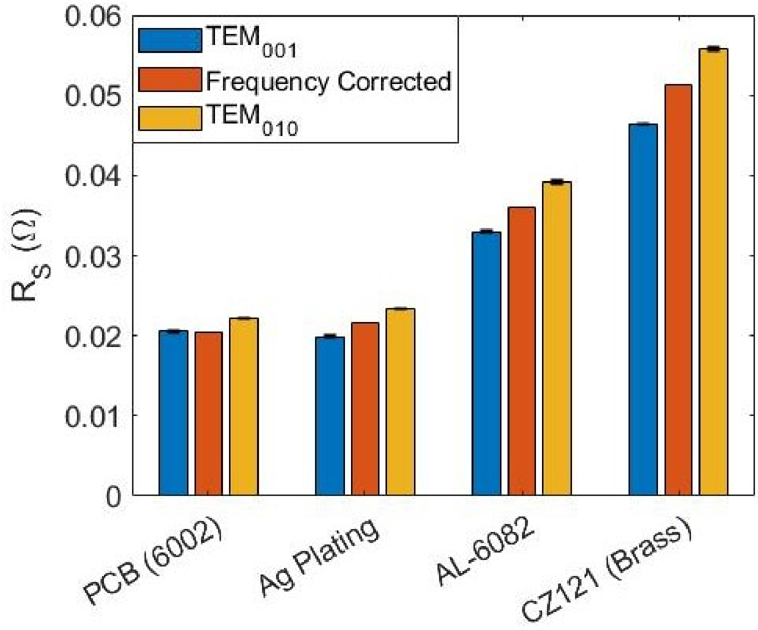

Figure 3.37: Surface resistance values of various metal plates. Measurements taken using a parallel plate resonator fixture operating in TEM_{001} at 5.3 GHz and TEM_{010} at 6.4 GHz. Standard error values are shown via error bars, values of which are: in TEM_{001} $\pm 4.4\times10^{-5}\Omega$, $\pm 1.3\times10^{-4}\Omega$, $\pm 1.1\times10^{-4}\Omega$, $\pm 8.8\times10^{-5}\Omega$ and in TEM_{010} $\pm 4.3\times10^{-5}\Omega$, $\pm 8.8\times10^{-5}\Omega$, $\pm 2.6\times10^{-4}\Omega$, $\pm 1.8\times10^{-4}\Omega$ for Rogers Corp. RT/duroid 6002 PCB, silver plated aluminium, aluminium alloy (AL6082) and brass alloy (CZ121), respectively. Also shown is the frequency corrected R_S values for TEM_{010} scaled down to 5.3 GHz. Reprinted from [23] ©2021 IEEE.

expected trends when compared with commonly known bulk metal resistances, namely that silver and copper PCB exhibit the lowest electrical resistance and brass the highest (out of metals studied here). The standard error for ten measurements (per sample) are shown as error bars on Figure. 3.37. For all study samples, R_S is higher in the TEM_{010} mode at 6.4 GHz than in TEM_{001} at 5.3 GHz. This is expected due to the skin effect, where the majority of current is contained in thinner surface layers as frequency increases, and so becomes more susceptible to loss from micro-surface roughness features. Also shown is the scaled R_S value from 6.4 GHz to 5.3 GHz. This scaled approximation is more closely matched with the value measured in TEM_{001} for Rogers Corp PCB sample, where the surface is expected to be smooth and isotropic.

However the increased loss seen at higher frequencies due to micro-roughness features cannot be separated or accounted for in the bulk metal samples, where

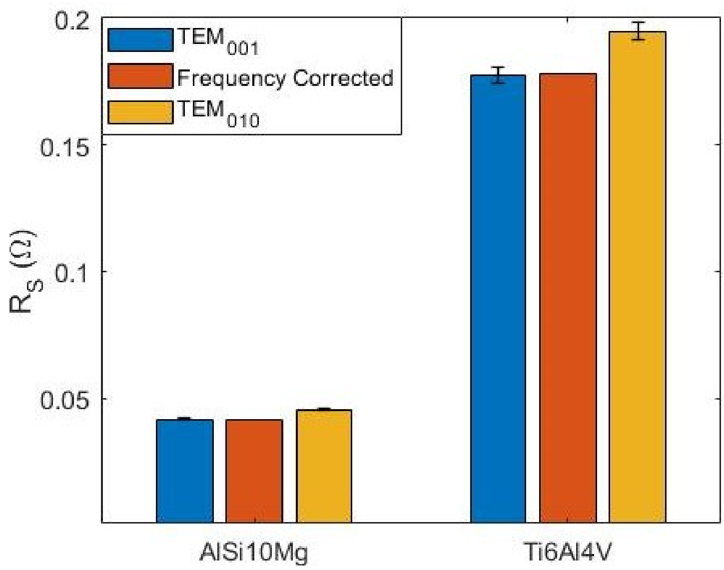

Figure 3.38: Surface resistance values for measured samples produced of AlSi10Mg and Ti6Al4V by means of powder bed fusion additive layer manufacturing. Measurements taken using a parallel plate resonator fixture operating in TEM$_{001}$ at 5.3 GHz and TEM$_{010}$ at 6.4 GHz. Standard error values are shown via error bars, values of which are: in TEM$_{001}$ $\pm 2.0 \times 10^{-4} \Omega$ and $\pm 3.4 \times 10^{-3} \Omega$, in TEM$_{010}$ $\pm 2.8 \times 10^{-4} \Omega$ and $\pm 3.5 \times 10^{-3} \Omega$ for AlSi10Mg and Ti6Al4V, respectively. Also shown is the frequency corrected R_{S} values for TEM$_{010}$ scaled down to 5.3 GHz. Reprinted from [23] ©2021 IEEE.

machining has introduced micro-surface roughness feature or dislocations, increasing loss at higher frequencies. Alternatively it has produced an anisotropic finish on the surface, increasing or reducing R_{S} in one orientation. Because the induced current flow in the two operating modes flow in orthogonal directions, close matching of values using the simple scaling formula in Equation.3.27a can be used to predict isotropic behaviour in R_{S} of a sample. As shown in the error bars on Figure. 3.37, the standard error is very small for all sample plates, although this does increase when measuring samples of lower electrical conductivity such as brass.

3.4.6.2 Additive Manufactured Samples

Samples produced by PBF are evaluated for R_{S} and shown in Figure. 3.38. As expected, the R_{S} value for titanium alloy Ti6Al4V is much higher than that of aluminium alloy AlSi10Mg due to its significantly lower electrical conductivity.

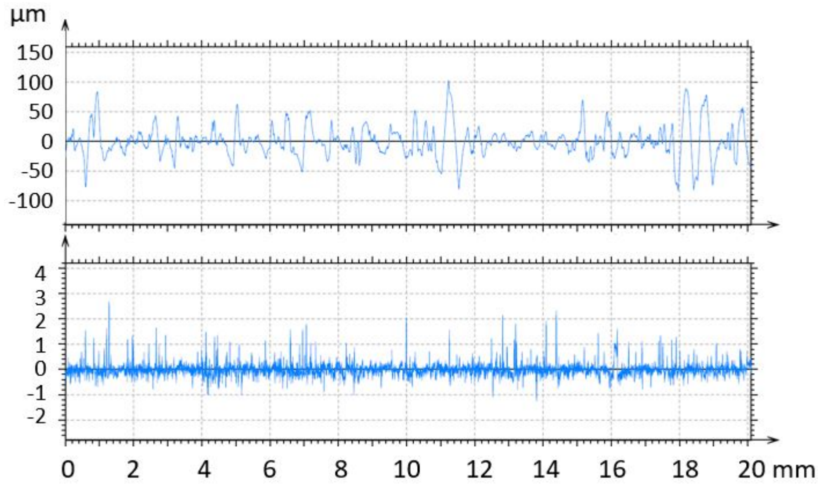

Figure 3.39: Roughness profiles of additive manufactured AlSi10Mg (top) and Ag plated aluminium samples (bottom). The profiles have been recorded using a Talysurf series 2 drag profiler and analysed with a 0.8mm cutoff filter. Reprinted from [23] ©2021 IEEE.

The PBF produced aluminium alloy samples showed a slightly larger R_S value (46.4 mΩ at 6.4 GHz) than a bulk aluminium alternative AL6082 (39.2 mΩ at 6.4 GHz). The difference between these samples can be ascribed to the excess roughness present from the laser melting process, which has been well documented to lead to an increase in microwave loss [59, 157, 44]. RMS surface roughness for the PBF samples was measured as $R_q \approx 16.5$ μm whilst for the bulk aluminium alloy sample $R_q \approx 0.66$ μm. These roughness profiles are shown in Figure. 3.39 and were measured on a Talysurf series 2 drag profiler and analysed with a 0.8mm cutoff Gaussian low pass filter. In both materials, the frequency scaled values suggest an isotropic behaviour in terms of R_S. Again, the standard error in measurement is much higher for lower conductivity samples of Ti6Al4V.

3.5 Conclusion

This chapter presents two methods for evaluating the microwave surface resistance of flat metal samples. An overview of a previously published dielectric resonator fixture [68, 86, 91, 25] featuring a novel 'lift-off' calibration process is given as background methodology to the results presented later on in Chapter. 5. The DR technique is also used as a reference to provide a sample of known R_S

for use in the second measurement technique presented here, the parallel plate resonator.

The parallel plate resonator fixture has been shown to effectively measure flat metal samples of bulk metal material, as well as samples produced by laser powder bed fusion, suggesting a reasonable robustness in the measurement technique. The random errors associated with the measurement are very small, around 0.1% and are associated with the measurement equipment, such is the accuracy of the PNA used to measure Q factor and frequency. In addition, there exists a approximately 1% error associated with the removal and re-fixing of the sample plate to the fixture. This low error provides a high level of confidence when directly comparing two measured sample plates. However a larger error is seen when measuring samples of low electrical conductivity (around 2%). Overall accuracy is achieved through the use of a known sample as a calibration piece, in an a-prior calibration process. This is particularly important due to the absence of an accurate corner radius value for the reference plate. Through this calibration process, and due to the nature of the induced orthogonal current flow in two resonant modes, the isotropic and low loss nature of Rogers Corp. RT/duroid 6002 PCB (in terms of R_{S} in the xy plane) has been confirmed. Additionally, samples produced of AlSi10Mg and Ti6Al4V by means of powder bed fusion also exhibit this xy plane isotropy in R_{S}. This result could have great significance in the design for manufactured of microwave components using PBF.

PBF samples produced of AlSi10Mg show only a small increase in surface resistance as compared to bulk aluminum alternative AL6082. This difference is explained partly by the roughness profiles of the two materials. It is worth noting that the PBF samples presented here were produced in the horizontal build orientation (parallel to the build plate). Therefore no conclusion can be drawn yet about vertical surfaces, with complex layer boundaries and adhered (partially melted) powders. This aspect is however investigated further in Chapters 4 and 5.

The PPR measurement technique presented here is unique in that it allows excitation of two resonant modes, inducing currents in orthogonal, one-directional patterns in the sample-under-test without the need for removal and re-fixing of the sample. These orthogonal modes allow for measurement of R_S at two discrete, but close, frequencies and for the estimation of isotropic surface properties.

CHAPTER 4
EFFECT OF PBF PROCESS PARAMETERS ON SURFACE RESISTANCE

4.1 Introduction

The physical properties of components produced by powder bed fusion can be affected significantly by the selection of process parameters during the build. In many cases, the default parameter setups for aluminium-silicon alloys are chosen in order to overcome the material's high reflectively and thermal conductivity [158]. These essential conditions then provide a parameter window in which to optimise for the desired component material properties. Often in the literature these optimisations are performed for mechanical properties such as creep, elongation and porosity [159], as well as tensile strength [160] and relative density [161], to name a few. Surface roughness is another substantial research theme, with motivations that include aesthetics, corrosion resistance, fatigue performance [162] and geometric tolerance [163]. Aspects of these surface roughness studies may also be useful in the optimisation of PBF to microwave applications, since the link between roughness and microwave loss is well established [63, 70].

Of particular interest is the improvement of surface finish for overhanging / downwards facing surfaces [110, 108, 164], which are often unavoidable in three-dimensional microwave components such as waveguides, and which experience dross formation (discussed in Section. 4.2.2 and shown in Figure. 4.1), thus generating significantly higher roughness than in other orientations [50, 165]. To the author's knowledge there is currently no published literature on optimised parameter sets specifically for the microwave performance of overhanging surfaces.

The electrical properties of PBF components are still inferior to machined alternatives [42, 166], however, the overall positive performance is surprisingly good given the poor surface finish apparent on PBF surfaces. The main techniques used in the literature to assess microwave PBF structures take a macro approach by measuring a complete waveguide component, with some studies comparing performance to a traditional manufactured equivalents or simulated component responses [55, 167]. In this chapter a more fundamental approach is taken, where individual surfaces of different build orientations are assessed for microwave surface resistance (R_S). Investigation is performed on the influence of process parameters, in the form of laser power, on the R_S of PBF surfaces. In addition, a study is undertaken on the influence of the laser scan path on microwave performance of horizontally built surfaces. No post-processing is performed on any samples in this chapter. All R_S measurements are performed using the parallel plate resonator technique described in Section. 3.4. Elements of this chapter have been previously published in peer reviewed journal articles [23, 24], with some figures and text having been reprinted (with relevant permissions where this author no longer hold the copyright).

4.2 Sample Preparation

To assess the microwave performance of PBF produced components, a series of flat planar samples have been made in three common build orientations; horizontal, vertical and 45^o with reference to the plane of the build plate. Samples were built in each orientation using the Renishaw default process parameter setup (see Table. 4.1) as reference samples, with other samples manufactured using a variety of laser powers for the border scan, upskin and downskin parameters for vertical, upfacing (45^o) and downfacing (45^o) surfaces, respectively. Furthermore, in Section. 4.2.3, an investigation is performed into anisotropy brought about the laser scan path on horizontal surfaces. To achieve this, the laser scan path was oriented to generate uniform roughness corrugations either parallel or perpendicular to current flow, representing the best and worst cases, respectively, for microwave loss [63].

Table 4.1: Key default process parameters for horizontal, vertical and 45^o surfaces produced from AlSi10Mg by powder bed fusion using a Renishaw RenAM500 system.

	Laser Power (W)	Point Distance (μm)	Exposure time (μs)
Horizontal & 45^o (Upskin)	100	60	90
Vertical (Border)	350	60	40
45^o (Downskin)	100	40	70

4.2.1 Build Orientations

For the comparison of build orientations with respect to microwave performance, as well as to provide reference samples in the optimisation study, a set of sample plates have been produced using the default process parameter setup. The orientations selected are common in the design of 3D microwave components and will each have different losses (quantified by their R_S values) associated with their surface profiles. These samples are manufactured from AlSi10Mg powder on a Rensiahw RenAM500 additive manufacturing system and the key process parameter levels for each orientation are detailed in Table. 4.1.

4.2.2 Process Parameter Optimisation

A major microwave loss contributor in over hanging surfaces of PBF parts are partially melted powder sphere caused by the laser energy penetrating below the desired layer. An simplified schematic of the problem, known as 'dross formation', is shown in Figure. 4.1.

Down and up facing surfaces are treated differently in the PBF build process to the core of the part, through the application of up/ downskin process parameters. Both parameter sets often consist of multiple laser passes over the same area / layer, so that any optimisation of these surfaces should focus on the the up/downskin parameters rather than the core. Specifically, at 45^o incline and 25 μm layer thickness, the step/overhang will be 25 μm. With a laser diameter

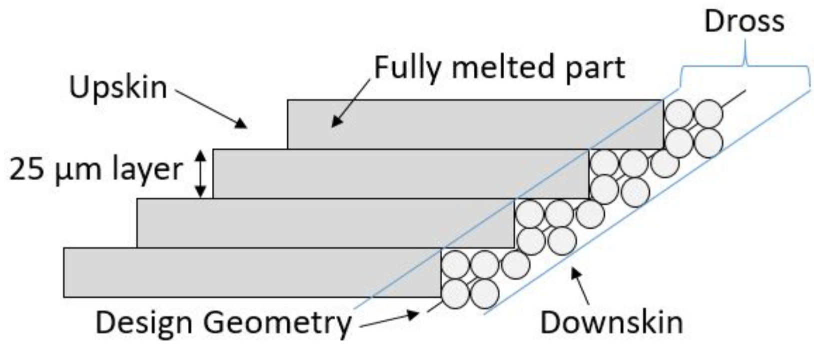

Figure 4.1: Schematic of the dross formation process in powder bed fusion manufacturing. Reprinted from [24] ©2021 Gumbleton et al. (CC-BY).

Table 4.2: Key process parameters for horizontal, vertical and 45^o surfaces produced in AlSi10Mg by powder bed fusion using a Renishaw RenAM500 system.

Laser Power (W)	
Vertical (Border)	45^o (Upskin & Downskin)
250, 270, 290, 310, 350, 370, 410, 430, 450, 470	0, 60, 80, 100, 120, 140, 160, 180

of 70 μm generating a melt pool diameter of approximately 120 μm, only the upskin/downskin border scan will be performed. Similarly in the case of vertical samples, the volume border scan will define the properties of the first approximately 120 μm of the surface. Further to this, from a microwave perspective, the skin depth (described by Equation. 2.2 and discussed in detail in Section. 2.2) tends to be much smaller than the layer thickness and the laser diameter. Therefore, the majority of microwave current will be flowing in the region defined by the border parameters for all parameter setups investigated here.

As discussed in Section. 2, several studies have shown a link between laser energy density (LED) and surface roughness [110, 109, 168], with LED defined using the simple expression

$$LED = P/v \tag{4.1}$$

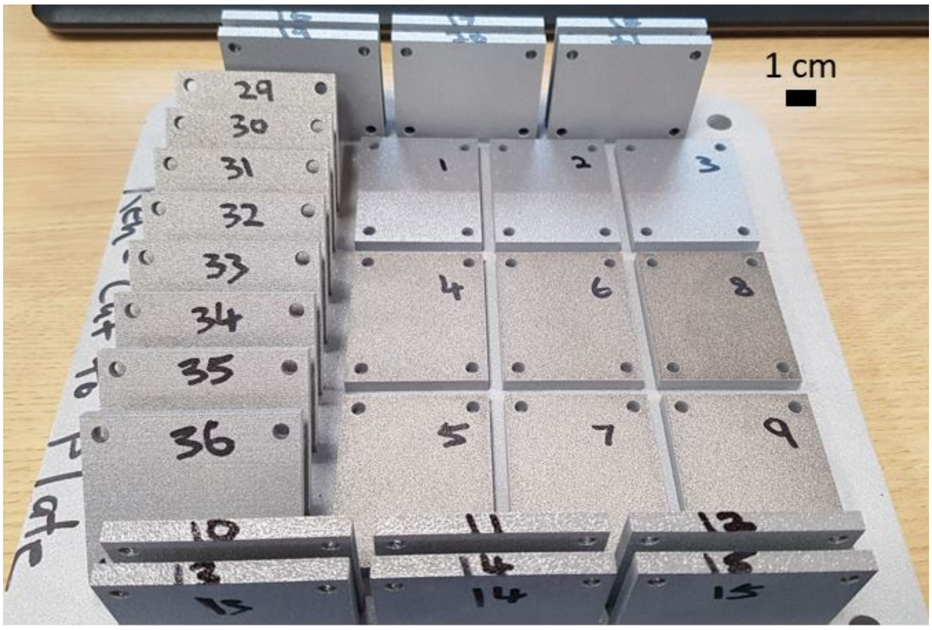

Figure 4.2: Photograph of Renishaw RenAM500 build plate layout and AlSi10Mg samples produced by powder bed fusion. Samples are created in horizontal, vertical and 45^o orientations using a variety of laser powers. Reprinted from [24] ©2021 Gumbleton et al. (CC-BY).

where P is the laser power (W) and v (m/s) is the scan speed. In this study the scan speed is kept constant at the machine default setup while a sweep of energy density, via changes in laser power, is performed to investigate the affects on microwave loss. The laser powers investigated for each surface orientation are detailed in Table. 4.2. A photograph of a RenAM500 build plate populated with the samples described above is shown in Figure. 4.2.

4.2.3 Orthogonal Roughness profiles

An additional set of horizontal samples have been manufactured, in which a uniform roughness profile is generated deliberately to emulate the best and worst cases scenarios for microwave loss. Morgan [63] presented theoretical calculations that showed that roughness (modeled as grooves), orientated perpendicular to current flow, will severely inhibit current and thus increase resistance. Hammerstad's [66] model remains the main and most widely accepted model for

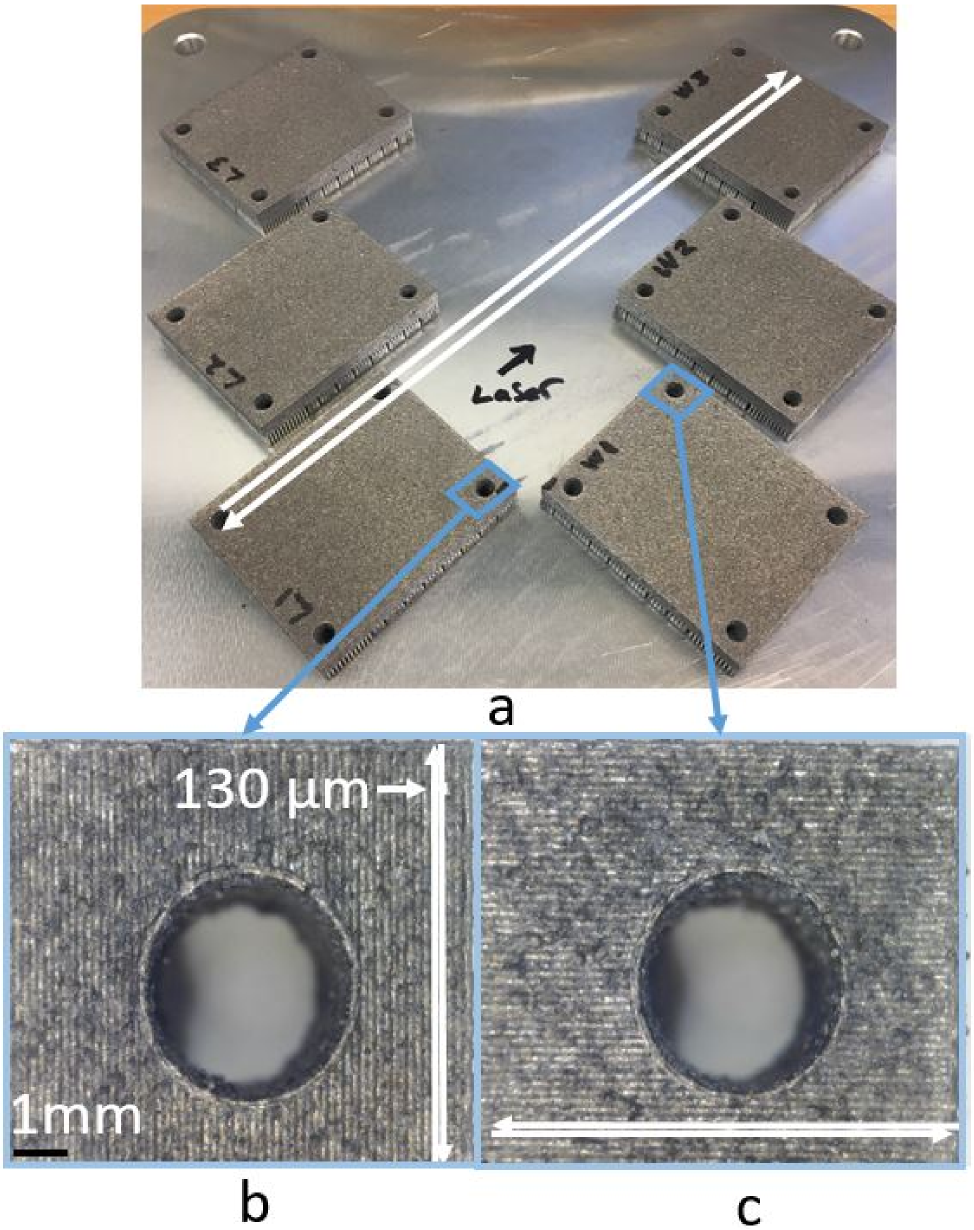

Figure 4.3: Photograph of Renishaw AM250 build plate layout and AlSi10Mg samples produced by powder bed fusion. White arrows indicate the laser scan path. a) Layout for sample set so that the laser scan path is parallel to the width or length of the sample. Directional roughness features have been generated along b) the length of the sample and c) the width of the sample. Reprinted from [23] ©2021 IEEE

quantifying loss due to roughness. Using a series of grooves to model roughness, the model generates a correction factor based on the ratio of RMS surface roughness height (R_q) and skin depth. Subsequent studies have used the saw-tooth roughness profile in modeling techniques but it is accepted that it is difficult to accurately model real-world roughness [76]. These samples, created from AlSi10Mg using a Renishaw AM250 additive manufacturing system, are designed to generate grooves / corrugations parallel and perpendicular to current flow in different resonant modes. The default process parameters are used for the core of the samples and the upskin parameters are disabled, such that the laser scan path is exposed. The main process parameters for these samples are: laser power = 200W, hatch distance = 130 μ m, layer thickness = 25 μm, exposure time = 140 μs and point distance = 80 μ m. The starting angle of the laser scan, which rotates by 67° each consecutive layer, is calculated so that the final layer scan path is parallel to the edges of the samples. A photograph of the populated build plate with the laser path annotated is shown in Figure. 4.3a. Figure 4.3b and c shows a close up view of the roughness corrugations parallel to the sample length and width, respectively. This sample set allows an investigation into anisotropy that may be induced in the PBF by the laser itself and is intended to exploit the orthogonal resonant modes that can excited in the PPR measurement fixture; each sample will have a roughness profile that is parallel to current flow in one mode while perpendicular in the second (orthogonal) mode.

4.3 Results and Discussion

4.3.1 Build Orientations

Samples produced using default build parameters in different orientation have been measured to evaluate R_S and the results are shown in Fig. 4.4. The standard error reported on Fig. 4.4 is very small due to the high precision frequency measurement equipment used (Keysight N5232A network analyser), with less than 0.1% random error and the described cavity resonator fixture providing approx-

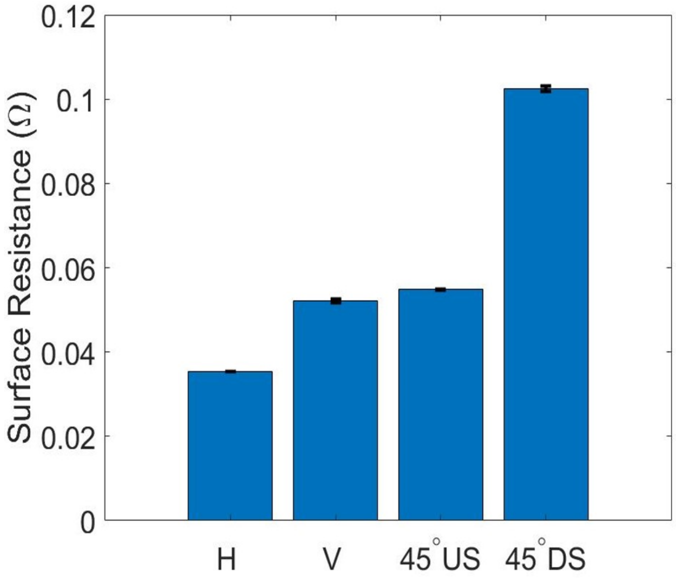

Figure 4.4: Measured surface resistance values for samples of different build orientation manufactured using default process parameters. Measurements were taken at 6.4 GHz using the parallel plate resonator fixture, with 5.3 GHz data scaled to this standard frequency. Standard error is shown by error bars. Reprinted from [24] ©2021 Gumbleton et al. (CC-BY).

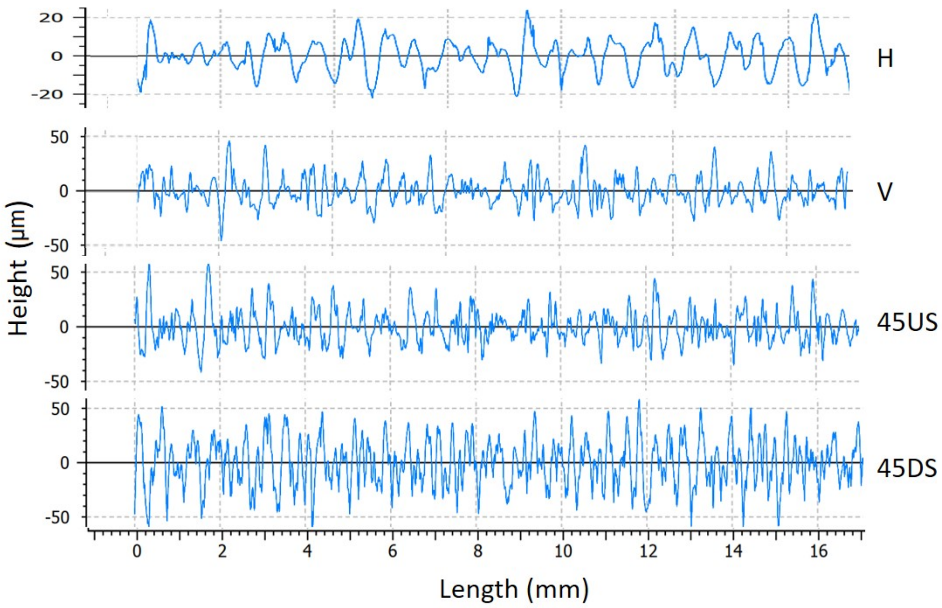

Figure 4.5: RMS surface roughness R_{q} profiles from a Talysurf 2 drag profiler using a 0.8mm filter. The profiles are for powder bed fusion samples produced in horizontal, 45° upskin and downskin, and vertical build orientations.

imately 1% systematic error from the removal and replacement of samples. The 45° downskin surface, perhaps predictably, performs significantly worse in terms of microwave loss than other build orientations. Specifically, R_{S} is nearly two times higher than that of the equivalent samples for vertical and upskin surfaces. Horizontally built plates exhibit the lowest loss of all samples, a result that supports previous measurements by this author [25], while there is only a marginal difference between vertical and 45° upskin surfaces. RMS surface roughness (R_{q}) measurements have been performed using a TalySurf Series 2 drag profiler fitted with a tip of 2 μm radius and analysed with a 0.8mm cutoff low pass filter. Rq

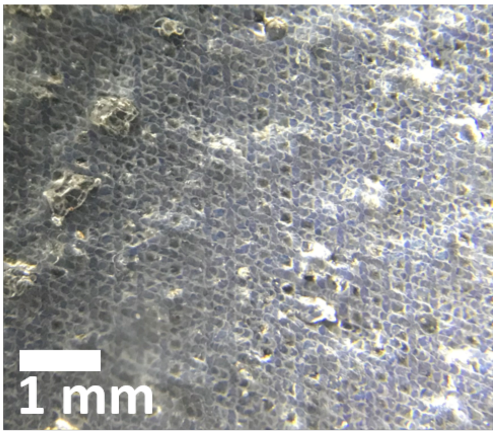

a)

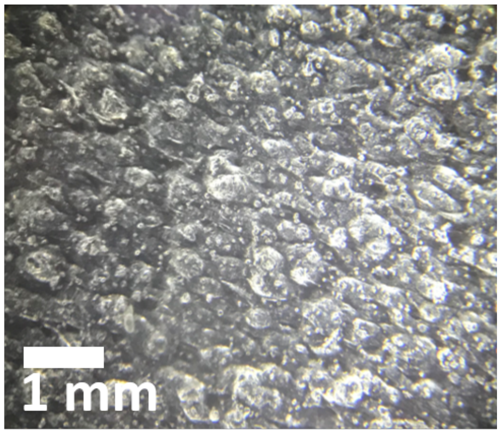

b)

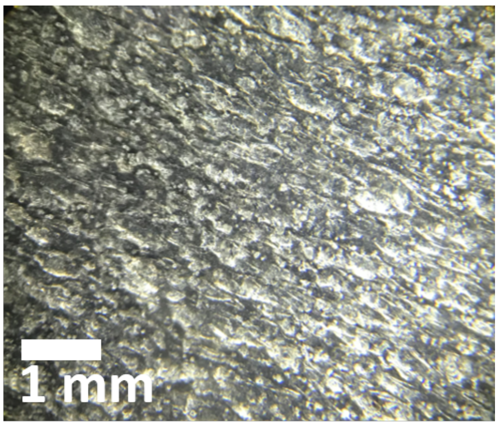

c)

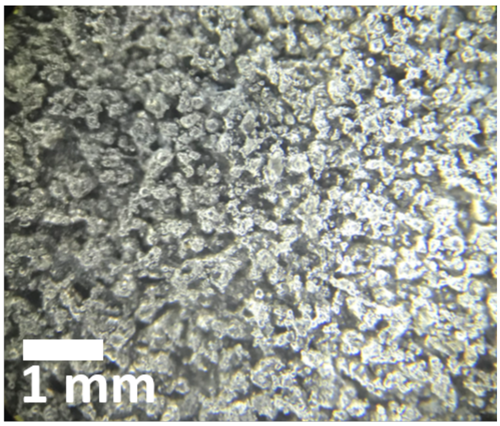

d)

Figure 4.6: Microscope images of a) horizontal, b) vertical c) 45° upskin and d) 45° downskin surfaces. All surfaces are manufactured using the default parameter set for each scenario. Scale bar is set at 1 mm.

for the default parameter set (~6 μm for horizontal, ~12 μm for vertical, ~13 μm for 45° upskin and ~20 μm for 45° downskin orientations) correspond well with the measured R_S, which increases with increasing surface roughness. R_q profiles of different orientations in the default parameter set are shown in Figure. 4.5. The downskin R_q and R_S values are approximately two times higher than that of the vertical / upskin surface and approximately four times higher than the horizontal orientation. This is further supported by examining the surfaces microscopically, as shown in Figure. 4.6. Figure. 4.6a shows the horizontal surface as relatively smooth and uniform with only small balling and agglomerated spatter formations [95, 169, 170]. In contrast, Figure. 4.6d shows a surface nearly entirely formed of small isolated protrusions of clustered particles. Very little contact is made between protrusions, which would be expected to inhibit microwave current flow significantly.

From the measurement results of different build orientations, it is evident that the commonly utilised macro style approach of testing PBF microwave components is missing crucial information regarding the regions where loss contributions are greatest. This also suggests that the overall performance of waveguide components will be heavily dependent on the component orientation within the build process.

4.3.2 Laser Power Optimisation

Figures. 4.7, 4.8 and 4.9 show the measured R_S values and R_q of for samples built in a vertical orientation, 45° upskin and 45° downskin surfaces, respectively, against varying process laser power. In all cases R_S correlates well with observed changes in R_q. Figures. 4.7 and 4.8 show that there is no significant trend observed relating R_S to changes in laser power for vertical and 45° upskin orientations. This may be explained for the upskin through the core build process having sufficiently melted the layer prior to the upskin parameters being implemented. Similarly, for the vertical built samples, border scans are repeated

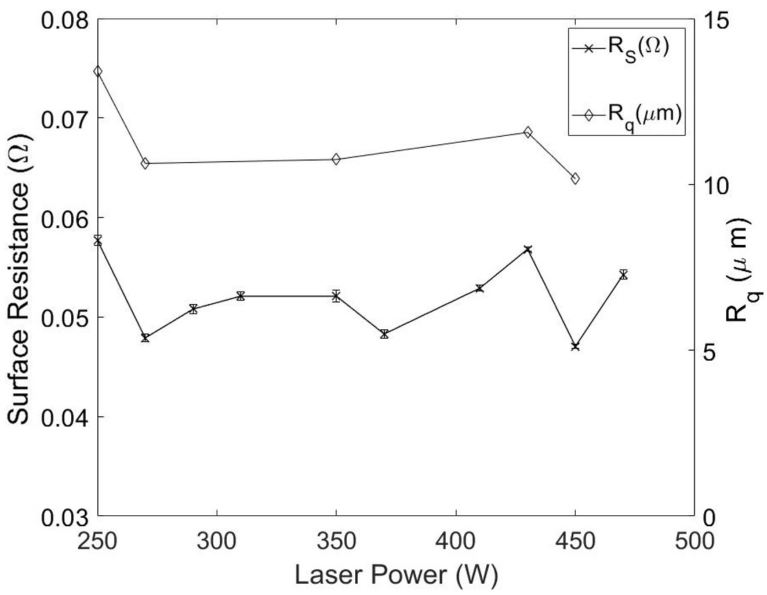

Figure 4.7: Measured surface resistance and RMS surface roughness (R_q) values for various border laser power levels in vertical built samples. Standard error is shown via error bars for five repeat measurements are on the order of $\sim 4\times10^{-4}\Omega$. Reprinted from [24] ©2021 Gumbleton et al. (CC-BY).

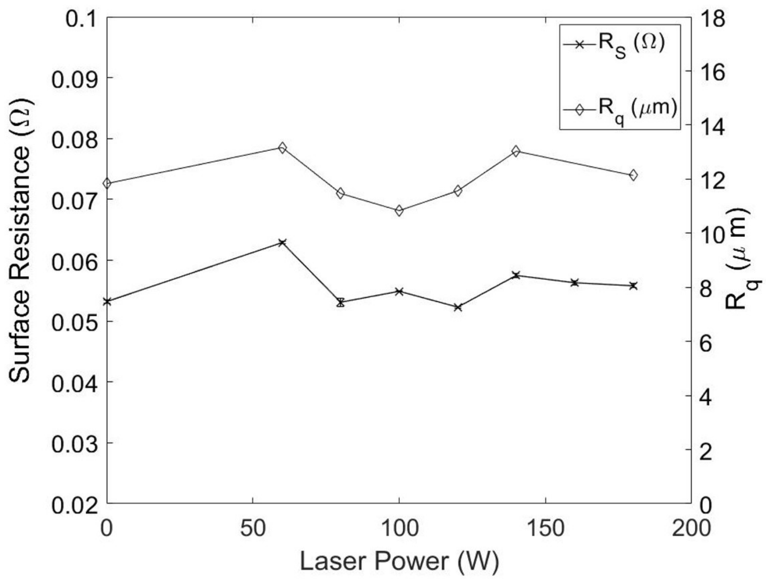

Figure 4.8: Measured surface resistance and RMS surface roughness (R_q) values for various laser power levels in the upskin parameter set for 45° orientated samples. Standard error is shown via error bars for five repeat measurements are on the order of $\sim 3\times10^{-4}\Omega$. Reprinted from [24] ©2021 Gumbleton et al. (CC-BY).

over successive layers, allowing for heat transfer through multiple layers such that a stable melt pool is generated, thus avoiding splutter and an excess of partially adhered powders.

Interestingly, the 45° downskin surfaces do exhibit a significant improvement in their R_S values with increasing laser power, shown in Figure. 4.9. This is quantified by low values of R_S and correlates with lower values of R_q. There is around a 40% relative reduction in R_S for the highest laser power 180 W (best case) against 60W (worse case), and around a 22% reduction in R_S for the best case compared to the default laser power result. Furthermore, the disparity (quantified by a percentage difference) seen between downskin and upskin/vertical surfaces, for the default reference cases, is nearly halved by applying the high laser power setup to the downskin parameter (from 93% to 52%).

Optical microscope images are shown in Figure. 4.10 for several downskin surfaces at different power levels and additional optical microscope images for other selected surfaces are shown in Appendix B. The surface of the 60 W sample (Fig. 4.10a) consists of an abundance of isolated satellites adhered only to the underlying surface. These partially melted powder spheres or satellites neither form a smooth surface nor a sufficiently good electrical connection, and so are a major microwave loss contributor. The adherence of partially melted powders is explained, at a fundamental level, by the surface energy of their spherical shapes. The surface area of a sphere is very high for a fixed volume, requiring less energy to form new bonds with other surfaces than to fully melt the powder [171]. In the 180 W sample (Fig. 4.10b), however, these satellites appear to have formed into larger agglomerates with surrounding particles, creating a more effective network of electrical connections and a more coherent layer. This is explained by the additional laser energy density penetrating deeper into this layer and more fully melting a greater proportion of the particles.

Due to the layer-wise nature of PBF, there is a concern that the layer boundaries could have an adverse effect on microwave performance. Exploiting the

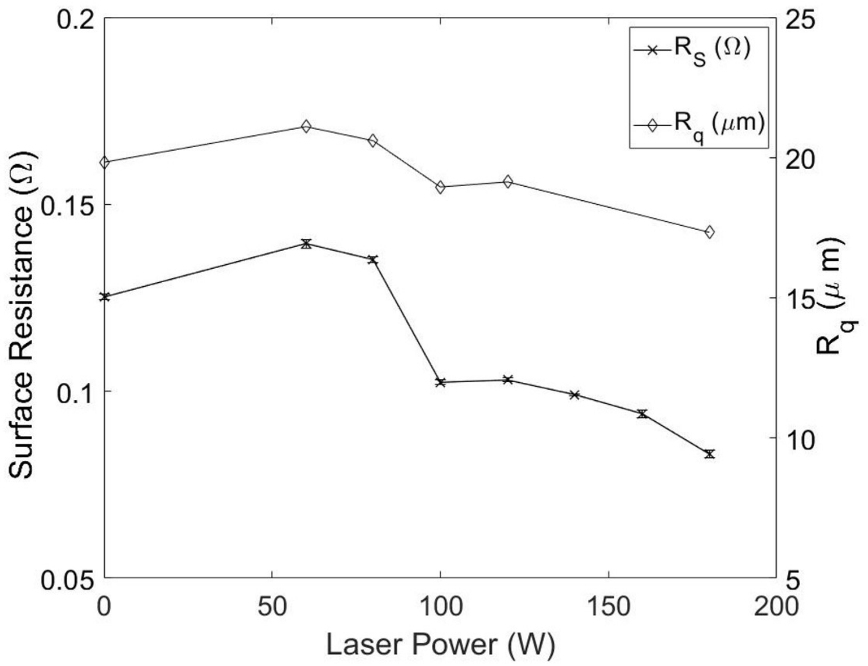

Figure 4.9: Measured surface resistance and RMS surface roughness (R_q) values for various laser power levels in the downskin parameter set for 45° orientated samples. Standard error is shown via error bars for five repeat measurements are on the order of $\sim 4\times10^{-4}\Omega$. Reprinted from [24] ©2021 Gumbleton et al. (CC-BY).

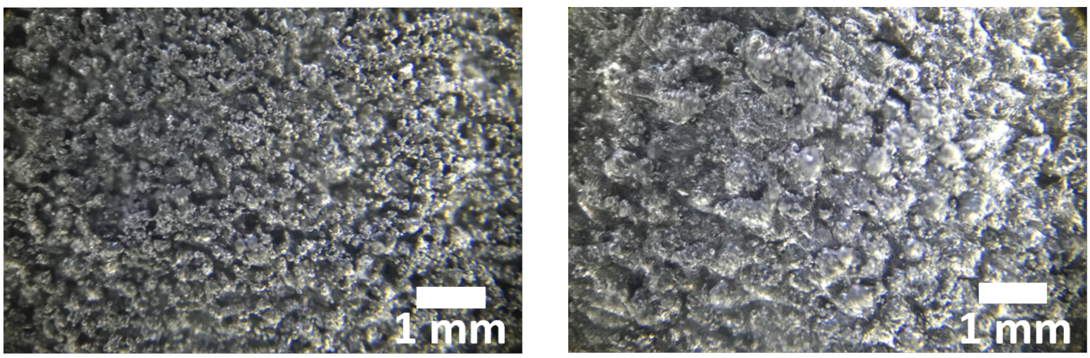

a) b)

Figure 4.10: Microscope images of 45° downskin surfaces manufactured with laser powers of a) 60 W and b) 180 W. Scale bar is set at 1 mm. Reprinted from [24] ©2021 Gumbleton et al. (CC-BY).

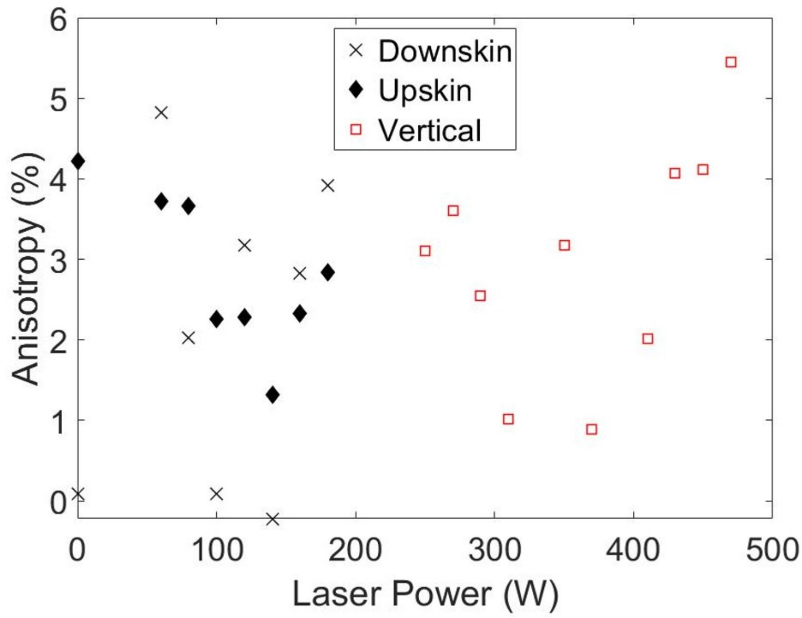

Figure 4.11: Percentage difference between surface resistance values measured in TEM_{001} at 5.3 GHz, where current flows parallel to layer boundaries, and TEM_{010} at 6.4 GHz, where current flows perpendicular to layer boundaries.

PPR fixture's orthogonal resonant modes allows currents to be excited both along and across layer boundaries for 45^o and vertical samples. A simple scaling approximation (from Equation. 3.27a) allows the difference in R_S to be evaluated perpendicular and parallel to layer boundaries. The general trends seen in R_S and laser power correlations in measurement mode TEM_{001} at 5.3 GHz are also seen in TEM_{010} at 6.4 GHz. After scaling, anisotropy is expressed as a percentage difference from the measured value in TEM_{001} at 5.3 GHz and is shown in Figure. 4.11. There is a range of around +5 % anisotropy across all samples of 45° and vertical orientations. The positive sign means that higher R_S values are measured when current is flowing in the direction perpendicular to layer boundaries. The spread, however, suggests that further work needs to be done on this topic, specifically testing a larger sample set.

4.3.3 Application to Waveguide Components

Using the results from the previous sections, several X-band waveguide components have been produced with different downskin laser parameters to investigate the optimisation effects on real systems. The components are shown prior to removal from the build plate in Figure. 4.12. The build orientations are such that two internal surfaces of each waveguide are upwards facing and use the default parameter setup, while the remaining downward facing surfaces are swept for each waveguide section using the following laser powers; ALM1 = 100 W (default), ALM2 = 0 W and ALM3 = 180 W. The resulting differences in electrical performance of the waveguide sections can then be attributed to the downskin surfaces. Figure. 4.13 shows one of these waveguide sections connected to a vector network analyser, through magnetic coupling loops, by using blank end flanges; this converts the waveguide transmission line section into a waveguide resonant cavity, allowing loss to be measured more reliably through Q factor than

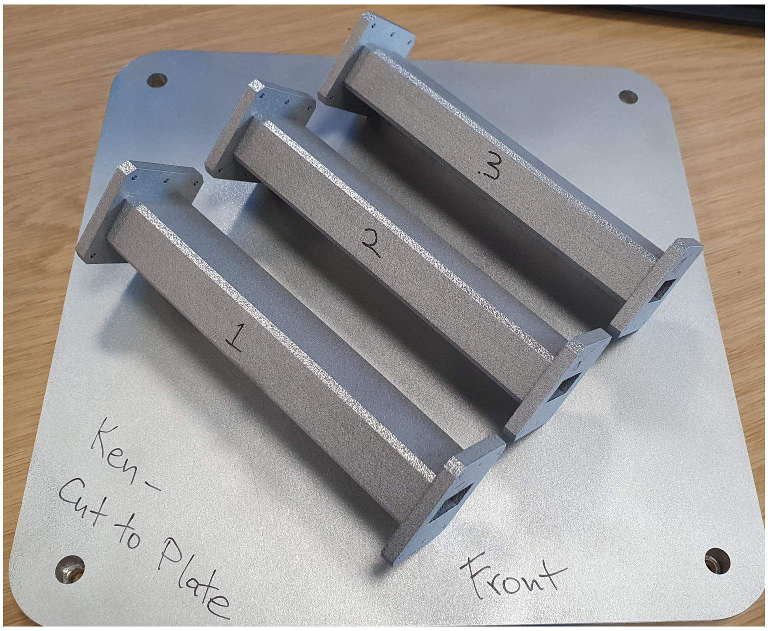

Figure 4.12: Three straight waveguide sections on a Renishaw RenAM500 build plate. Each section is produced with different downskin laser parameters. Reprinted from [24] ©2021 Gumbleton et al. (CC-BY).

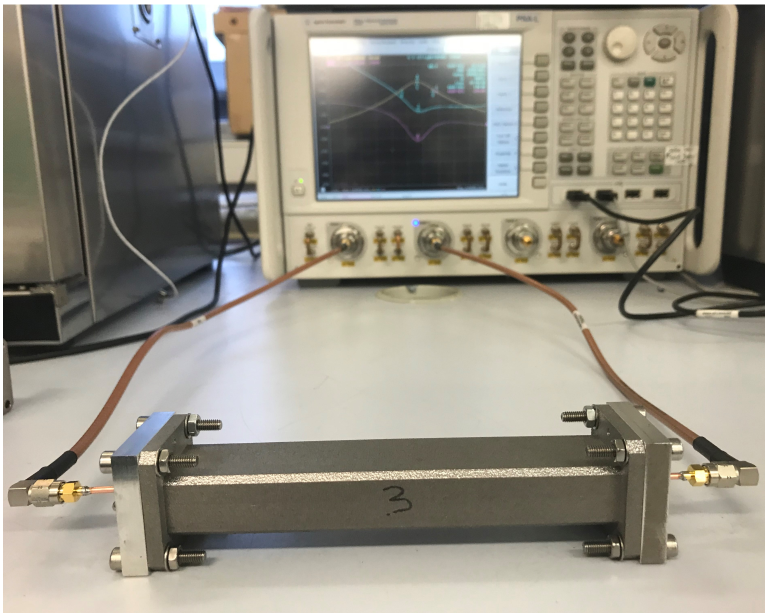

Figure 4.13: Additive manufactured AlSi10Mg waveguide section connected as a cavity resonator to a vector network analyser. Reprinted from [24] ©2021 Gumbleton et al. (CC-BY).

the attenuation from the measurement of attenuated power of a travelling wave; for example a typical waveguide may have an attenuation coefficient of approximately 0.5 dB/m, for a section of length = 154 mm the attenuation would be too small to accurately measure. Q factor and hence R_{S} are measured through the forward transmission S parameter S_{21}. These traces are shown as an inset to Figure. 4.14. The resonant frequency of the dominant TE_{101} mode of this air filled cavity is 6.62 GHz, a similar frequency to the PPR measurements for consistency of results and dictated by the internal geometry of the cavity; 22.9±0.06 mm × 10.2±0.1 mm × 154.0±0.1 mm. R_{S} for the cavity geometry is found by

$$R_S = \frac{1}{G\,Q_0} \tag{4.2}$$

where the geometry constant G is found through simulation using COMSOL Multi-physics software to solve the field integrals in Equation. 3.18a. The measured R_{S} values for each waveguide section are shown in Figure. 4.14. There is a clear reduction in R_{S} for sample ALM3, arising from the use of 180 W for the

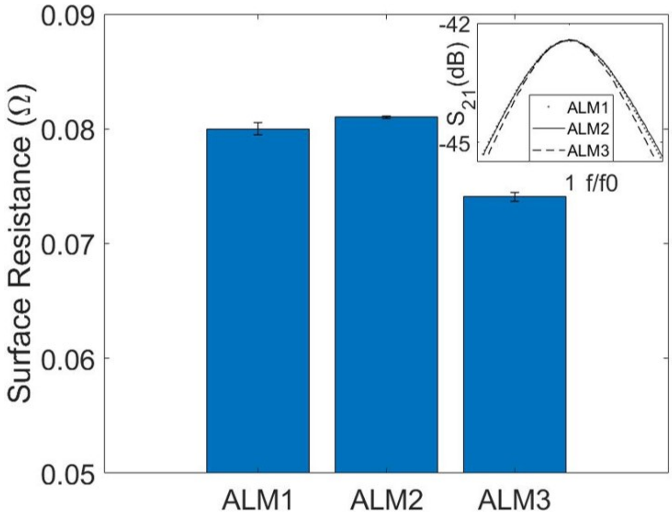

Figure 4.14: Measured surface resistance values for additive manufactured rectangular waveguide resonators produced using various down skin laser powers. Standard error is shown via error bars. Inset is the forward transmission S parameter traces for each waveguide resonator. Reprinted from [24] ©2021 Gumbleton et al. (CC-BY).

downskin laser power when compared to the default value (ALM1 : 100 W) and the absence of a downskin layer (ALM2: 0 W). These results are promising for the optimisation of PBF produced parts for microwave applications.

To assess how the reduction in R_{S} will translate into a waveguide transmission line system, attenuation has been calculated using the measured resonator R_{S} (R_{Sr}) values over the X-band frequency range. Conductor attenuation (α_c) due to the surface conduction losses of a uniform, rectangular waveguide in the TE_{10} mode is assessed by [172]

$$\alpha_c = \frac{R_{\mathrm{Sr}}(f)}{b\eta_0\sqrt{1-x^2}}\left[1+\frac{2bx^2}{a}\right] \tag{4.3}$$

where a and b are the long and short internal dimensions of the waveguide, respectively, and η_0 is is wave impedance of free space. The dimensionless parameter x is defined as the ratio $x = f_{\mathrm{c}}/f$, where $f_{\mathrm{c}} = c/2a$ is the cut-off frequency of the TE_{10} mode and f is the frequency of single mode operation (i.e in the range

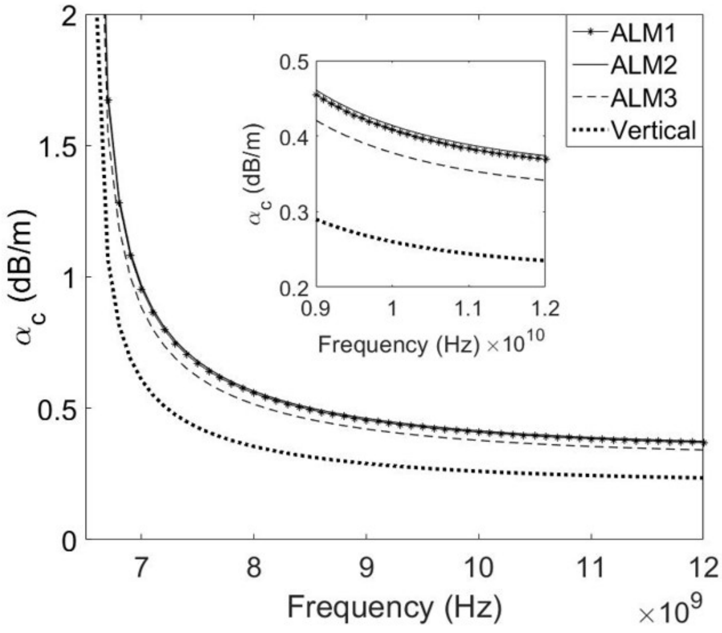

Figure 4.15: Calculated attenuation for TE_{10} mode of three rectangular waveguides produced by additive manufacturing using various downskin laser powers. Also included is a calculated value for an equivalent waveguide consisting of vertical surfaces. Inset is a magnified view of the calculated attenuation. Reprinted from [24] ©2021 Gumbleton et al. (CC-BY).

$c/2a < f < c/2b$). For calculation of α_c over the X-band frequency range, R_{Sr} is scaled from the cavity resonator measured value by

$$R_S(f) = R_{Sr}\sqrt{\frac{f}{f_r}} \tag{4.4}$$

Figure. 4.15 shows the calculated α_c values for each waveguide section over the X-band frequency range. The reduced R_{S} value for ALM3 provided a modest ~0.05 dB/m improvement in conductor loss. For completeness, and to show the effect of build orientation on attenuation, a calculated value for an equivalent rectangular waveguide built in a vertical orientation is included on Fig. 4.15; the R_{S} value for this is taken from Fig. 4.4. Attenuation is significantly lower (~0.13 dB/m) in the absence of downward facing surfaces. The results presented here are promising for the continued improvement in performance, and subsequent industrial uptake, of PBF components for microwave applications, where the design of three-dimensional parts, such as waveguide filters, will inevitably necessitate for one or more downward facing surfaces.

4.3.4 Orthogonal Roughness Profiles

4.3.4.1 Simulation

Current analytical models for roughness effects on microwave performance tend to rely on R_q as an input, essentially considering only the average height profile of roughness. Modern, full wave simulation software however enables roughness to be modelled in a variety of shapes, including discontinues and varying roughness widths. To further understand how current flows in the skin depth layer relative to different roughness profiles, a series of simulations have been performed, extending the previous published work of the Cardiff group [59] and emulating the roughness profiles generated using the laser scan path; here, roughness is simulated via a set of grooves of various peak heights (h) and, importantly, peak-peak widths (b), perpendicular to current flow, which allows for the evaluation of loss associated with the surface profile.

Figure. 4.16 shows the simulated surface current density for a variety of roughness profiles, simulated at 5.3 GHz with a skin depth of ~ 2 μm. In all simulations h is fixed arbitrarily at 6 μm while b is varied. In the extreme cases where b much larger (Figure. 4.16c and d) than the skin depth, the current can be seen to follow the profile as it would in a flat surface. Interestingly, when b is much smaller (Figure. 4.16a) than the skin depth, current flows underneath the protrusions, again effectively behaving like a flat surface. However, when b is of the magnitude of a few skin depths, current flow is significantly impeded leading to higher resistive loss. This is confirmed when normalised power loss is expressed as a function of b (in skin depths), as shown in Figure. 4.17. High R_{q} values alone do increase loss compared a perfect flat surface; however, maximum loss is exhibited when b is around three times the skin depth. For very large or very

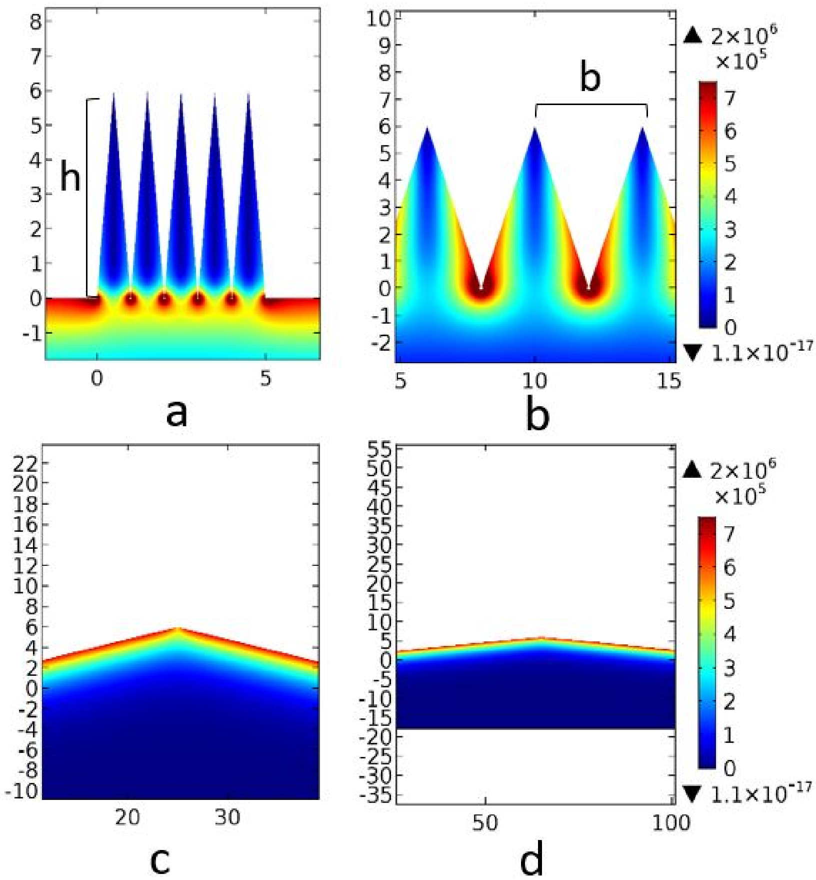

Figure 4.16: Two-dimensional simulated current density in aluminum at 5.3 GHz, where roughness peak height (h) = 6 μm. a) Peak-peak distance (b) = 1μm, b) b = 4μm, c) b = 50 μm and d) b = 130 μm. Dimensional axis labeled in μm and the current density legend in A/m^2.

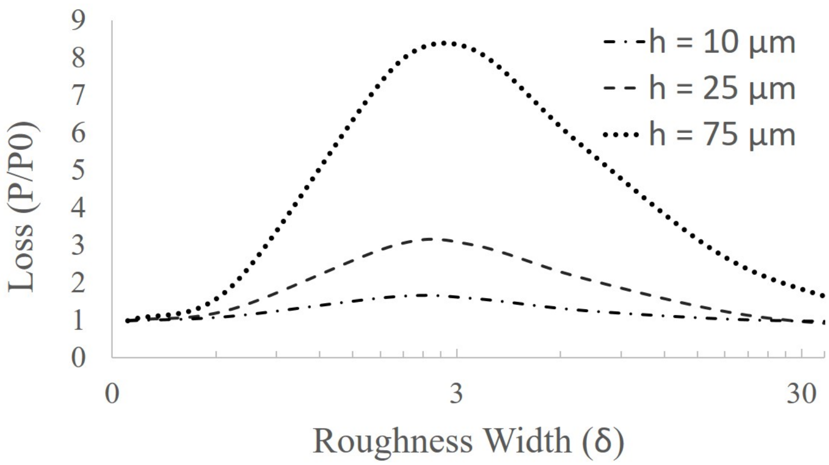

Figure 4.17: Simulated normalised power dissipation as a function of roughness width (expressed in skin depths).

small feature widths (relative to three skin depths), relatively small increases in loss are observed compared to ideally flat surfaces.

4.3.4.2 Measurement Results

By exploiting the orthogonal current flow generated by two resonant modes of the PPR (Chapter. 3.4), the influence of the laser scan path on R_S can be investigated. Three samples of each laser scan orientation have been measured in the PPR for Q factor and subsequently evaluated for R_s. Each measurement consisted of exciting both resonant modes in turn, so as to effectively produce simultaneous measurements on the same sample, where current will be flowing both perpendicular and parallel to roughness, corresponding to the theoretical best and worst cases, respectively, for microwave loss [63].

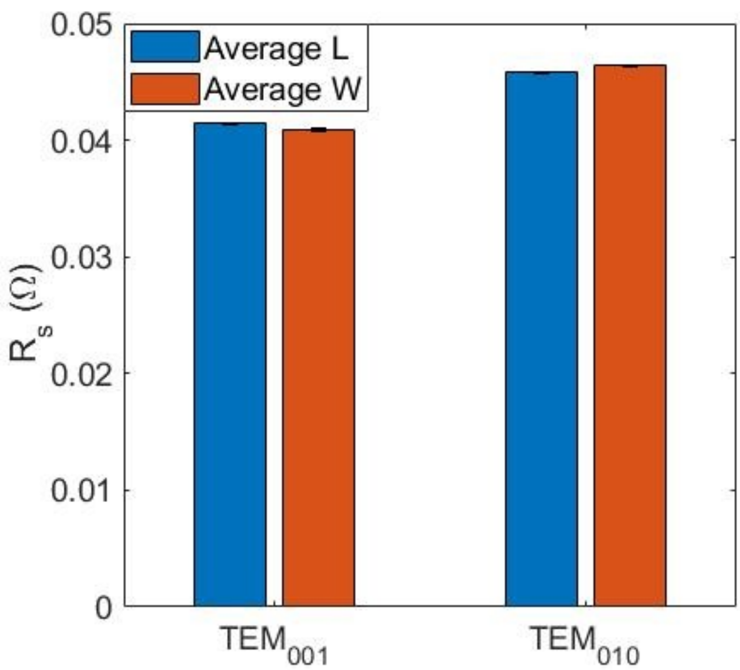

Figure 4.18: Average surface resistance values for AlSi10Mg samples produced with the laser scan path along the length or across the width of the sample. Measurement taken using the parallel plate resonator operating in TEM_{001} mode at 5.3 GHz and TEM_{010} mode at 6.4 GHz. Standard error values for 10 measurements per sample are shown via error bars. Reprinted from [23] ©2021 IEEE.

The averaged evaluated R_S values for both sample sets are shown in Fig.4.18. The difference in the averaged values of R_S due to directional roughness features, in both resonant modes, is less than 0.5 mΩ, while the range of R_S values for all samples is around 1.5 mΩ. These measurements were repeated 10 times on each of the six samples and standard error is calculated to be much less than 1%. The systematic error in very low owing to the high measurement precision of the VNA used, while a larger error exists attributed to small positional errors arising from the manual replacement of the samples. These results suggest that the R_S value, for the PBF surfaces tested, is not dependent on the laser scan path and is effectively isotropic. This result is perhaps not surprising given the simulation results above, when feature width of the deliberately induced roughness is considered.

Figure. 4.19 shows a three-dimensional surface profile of one of the PBF samples measured, taken using a Taylor Hobson Talysurf 2 drag profiler. The scan paths are clearly seen, and are also shown in Figure. 4.3 b and c. The width of the features produced by the laser scan on the AlSi10Mg PBF samples here

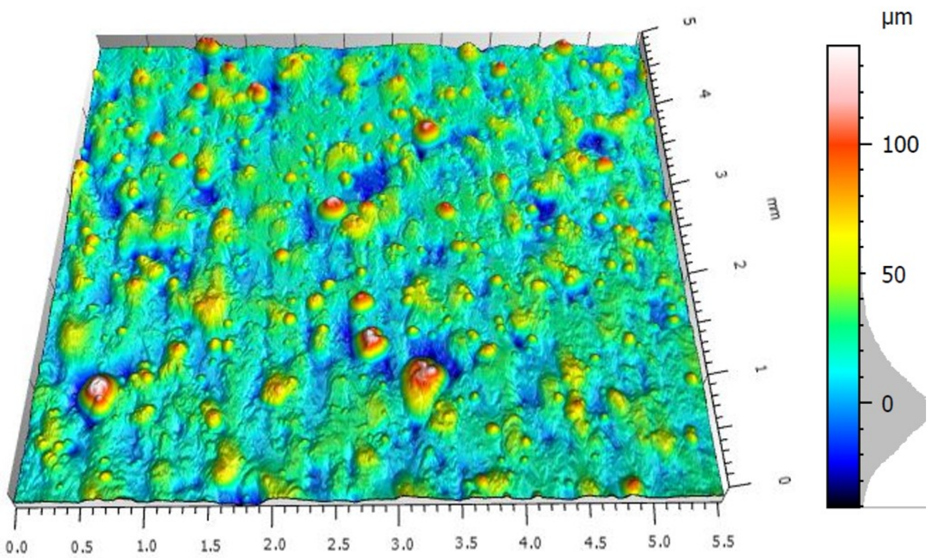

Figure 4.19: Three-dimensional surface profile of a powder bed fusion plate with laser induced roughness features. Measured on a Taylor Hobson Talysurf 2 drag profiler. Axis scale is in mm while color scale for height is in μm.

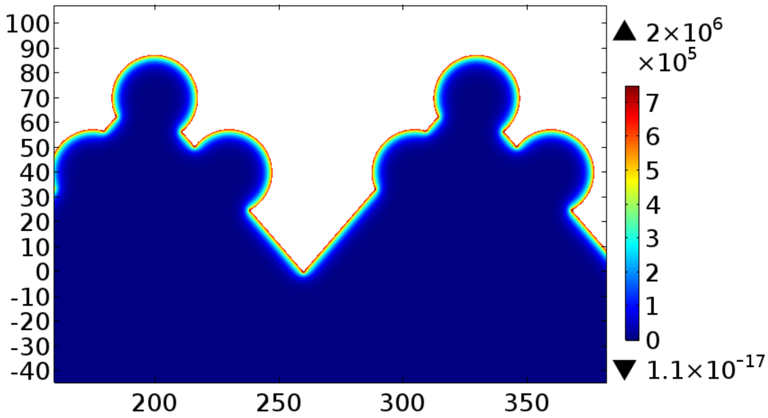

Figure 4.20: Simulation of surface current density. The model geometry consists of roughness peaks with partially melted powder adhered to the surface. The axes have units of μm and current density (A/m) is shown via color scale.

are large enough ($\approx 130\ \mu$m) as to be approximated as a near flat surface, given that the skin depth at the operating frequencies is around 2 μm. Figure. 4.19 also shows a large quantity of non-uniform roughness features such as balling and spatter (identified by the extreme profile heights and rounded geometries). To demonstrate the effect of such features, a simple extension to the simulations above is performed.

Fig.4.20 shows rudimentary simulation results for a roughness profile that includes partially melted powders. The simulation is based on the roughness heights and feature widths measured on the PBF samples, while the partially melted power is based on a particle radius of 35 μm. The value of P/P_0 (i.e. loss normalised to an ideally flat surface) based on this simulation is recorded as 1.77 for triangular roughness peaks and 2.13 for roughness with partially melted powder. This result suggests that the partially melted powder present on the surface of the samples can contribute significantly to loss. This simulation however does not take into account the fact that the powder adhered to the surface is often not fully melted, so the electrical contact may be worse than the simulation suggests, perhaps underestimating its loss contribution.

4.4 Conclusions and Further Work

This chapter has investigated the effect that process parameters can have on the microwave performance of metal PBF samples. A significant finding, through experimentation, is the reduction in R_S of downward facing surfaces through an increase in downskin laser power, which represents an important improvement for the adoption of PBF in the production of microwave components. The underside of the material is essentially made up of powder rather than a solid material, which understandably produces different behaviours and properties. The increased laser energy melts more of the isolated powder particles into a more coherent layer of solid metal and hence starts to perform as such. Downward facing surfaces are often unavoidable in passive microwave devices and measurements of plates in various build orientations have shown a significant difference in loss contributions from each surface. This leads to a conclusion that the commonly utilised macro approach of testing whole waveguide components is missing important information on on the precise surfaces the loss is occurring. This knowledge can be used in the design - for - additive manufacture process to ensure critical surfaces (i.e. areas of high current flow) are oriented in the most efficient way; where downward facing surfaces must be present, the laser power parameters can be optimised accordingly to minimise excess roughness and hence microwave loss.

A second set of interesting results is seen in the investigation of the influence of laser scan path. This work has shown that loss in PBF produced microwave components is not associated with natural groves created by the laser scan pattern. These grooves are on a scale too large to contribute significantly to loss. With a laser diameter of 70 μm and melt pool of $\sim$130 μm, it would be difficult to produce roughness on the scale of $\sim$ 5 μm necessary for maximum loss at the C band frequencies used here. This suggests that the laser scan path should not be a major concern to microwave designers working with ALM products, with horizontal surfaces being effectively isotropic in terms of R_S. Rather, excess loss over machined parts maybe be due to micro-surface roughness such as partially adhered particles, voids and splutter. this finding may become less valid as freq is increased and new studies are ongoing to investigate this.

These findings suggests that the correct selection of process parameter can bring about improvements in performance of passive microwave components produced by PBF, not only through the physical reduction in surface roughness but also through the advancement in design knowledge for component orientation.

Further work is required to determine what effect the variation in laser power has on the sub-surface properties of downward facing surfaces. The influence that increased laser power may be having on the mechanical properties of the surfaces has not been investigated here and would be a useful further study in the drive for increased industry uptake. Additional imaging studies would also be interesting to investigate the variation in microsructure size and shape due to different laser powers.

CHAPTER 5
EFFECT OF POST-BUILD TREATMENTS ON SURFACE RESISTANCE

5.1 Introduction

The additional treatment of PBF parts post manufacturing is, in many applications, a necessary step to achieve the desired properties. A range of treatments are available for the enhancement of mechanical properties, such as hot isostatic pressing to reduce interior porosity [173, 174], annealing and other heat treatments for relieving residual stress and increasing hardness [118] and shot penning to improve the surface finish [68, 126, 129]. This chapter investigates the use of post processing techniques specifically for the improvement of microwave performance, quantified by low surface resistance (R_{S}), of metal powder bed fusion (PBF) samples. The main categories of treatments investigated include the removal of loose, semi-melted powder from the material surface, coating with a material of high electrical conductivity and polishing to remove the surface roughness profile. Treated PBF sample measurements are then compared with 'pre-treatment' equivalent samples to evaluate the effect of the post-processing treatment on R_{S}. All PBF samples discussed within this chapter have been manufactured of AlSi10Mg using a Renishaw RenAM500 laser PBF additive manufacturing system, unless otherwise stated.

Quality factor measurements and subsequent evaluation for R_{S}, are performed using the lift-off dielectric resonator fixture described in Section. 3.3 operating in the $\mathrm{TE}_{01\delta}$ mode at 7.5 GHz. The measurement fixture and several sample plates are shown in Figure. 5.1. Parts of this chapter have been published in a peer-reviewed conference paper [25] with some figures and text having been reprinted (with relevant permissions where this author no longer hold the copyright).

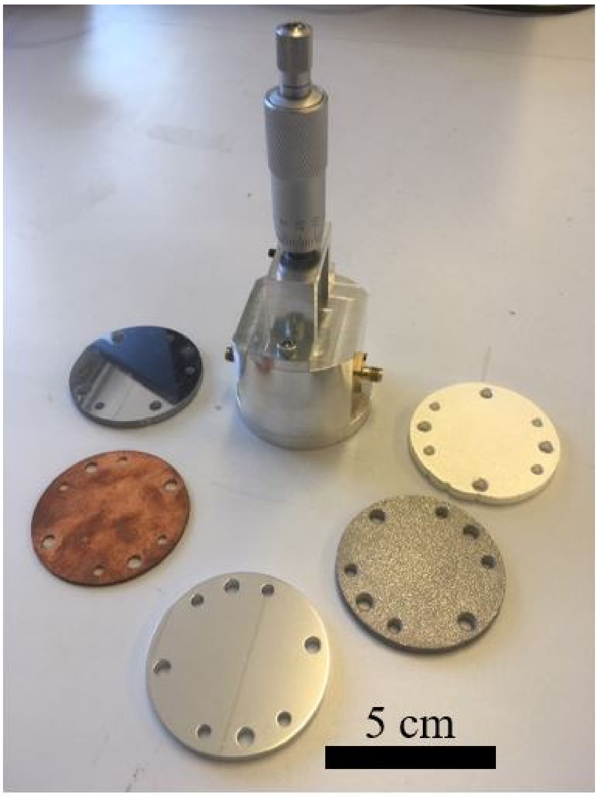

Figure 5.1: Photograph of the lift-off dielectric resonator fixture with samples plates of copper PCB and polished aluminium along with powder bed fusion samples treated by silver plating, media tumbling and machine polishing. Adapted from [25] ©2019 IEEE.

5.2 Sample Preparation

Surface resistance is measured for a variety of samples with various post-processing techniques having been implemented. These techniques include silver plating, bead blasting, media tumbling and machine polishing in various combinations. In addition, samples of copper PCB, machined bulk AL6082 aluminium alloy and 'as built' samples of AlSi10Mg are used for reference. The reference samples of copper PCB and Al6082 are shown in Figure. 5.2. PBF samples have been produced using the process parameters detailed in Table. 5.1 in both vertical and horizontal orientations prior to receiving selected post-processing treatments. The build plate containing the PBF study samples (AlSi10Mg) in their 'as built' form is shown in Figure. 5.3.

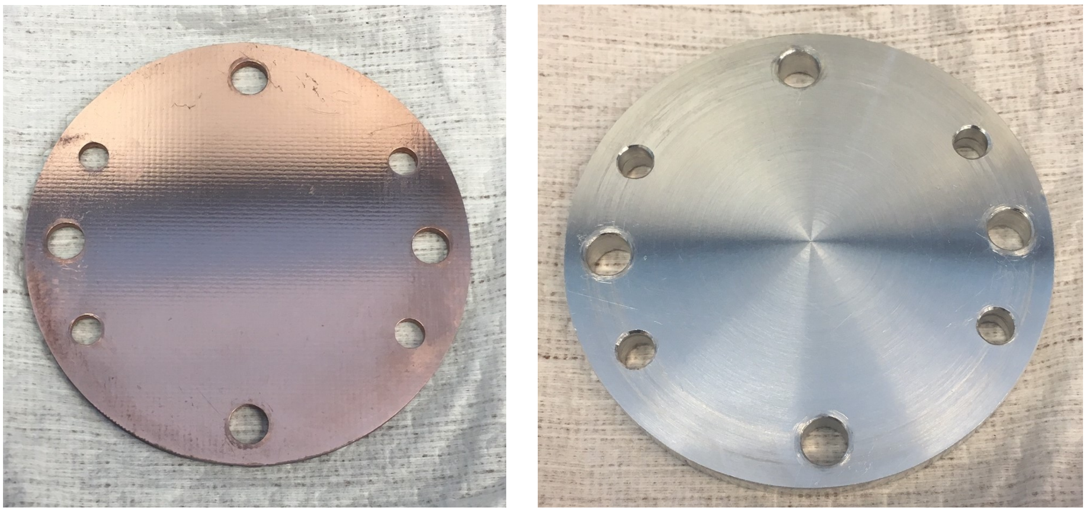

a) b)

Figure 5.2: Photographs of the reference samples a) copper PCB (35 μm thickness) b) Al6082 aluminium alloy.

Figure 5.3: Photograph of the build plate containing AlSi10Mg samples produced by laser powder bed fusion prior to post processing treatments.

Table 5.1: Process parameters used to produce AlSi10Mg Samples on a Renishaw RenAM500 laser powder bed fusion system.

	Laser Power(W)	Point Distance (μm)	Exposure Time (μm)	Hatch Distance (μm)
Volume	350	60	40	90
Upskin	100	60	90	130

5.2.1 Silver Plating

Due to the skin effect, where the majority of current is carried in the outermost few microns of material, an obvious improvement method would be to introduce an additional layer of material which exhibits the desired properties, i.e. high electrical conductivity. In practice this is easily implemented through various plating techniques for copper or precious metals such as silver and gold. In this study, silver (Ag) is chosen as the plating material owing to its high electrical conductivity compared to available alternatives. A plating layer of sufficient thickness is required to encompass the majority of current flow; at four skin depths thickness $\sim$ 98% of current will flow within the silver material. For silver of nominal electrical conductivity (σ) of 6×10^7 S/m, using Equation. 2.2 the skin depth (δ) at 7.5 GHz is calculated to be $\sim$0.75 μm. The silver plating employed in this study is a semi-bright silver solution of between 5.0 and 7.5 μm in thickness, equating to between six and ten skin depths, and can therefore be

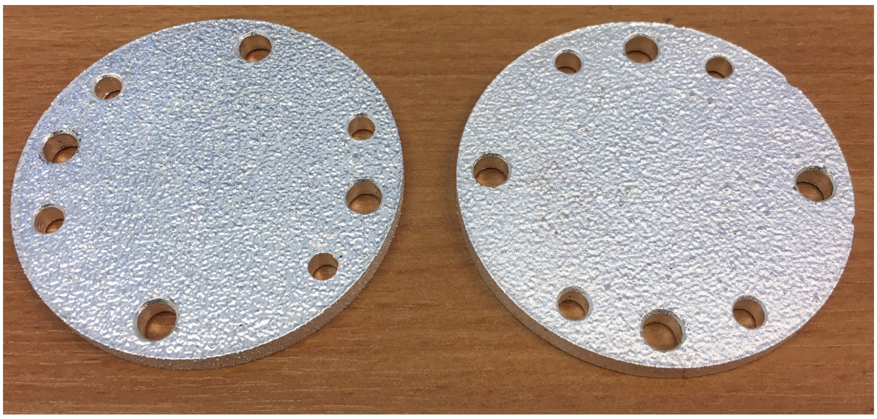

Figure 5.4: Silver Plated AlSi10Mg samples produced by laser powder bed fusion in a horizontal orientation. The sample on the left is ‘as built’ with silver plating layer whilst the right sample has also been bead blasted.

considered sufficiently thick to carry the majority of current flow. Due to the oxidising nature of the aluminium alloy, a nickel sub-layer is required to ensure good adhesion of the silver plating and this nickel sub-layer is around 3.0-5.0 μm thick. However, the measurement techniques features an 'end wall replacement' approach and as such the absolute thickness of the sample is not a concern, , as long as the base layer is effectively screened by the highly conducting coating above it. In addition, the silver plating technique goes someway to reducing surface roughness, as the liquid plating solution will partially fill the valleys of the roughness profile. Several silver plated samples are shown in Figure 5.4

5.2.2 Deburring

Deburring methods for the smoothing of sample surfaces are investigated by means of bead blasting / shot peening and media tumbling. These methods are employed to remove any loose or partially melted powder from the surface. The bead blasting process is a manual post processing technique that uses spherical ceramic beads fired at pressure towards the sample. In this study, the ceramic material used comprised of $\sim$ 65% Zirconia (ZrO_2), $\sim$ 30% glass and the remainder alumina (Al_2O_3) with an average diameter of 400 μm. The tumbling process, in contrast, is more controlled and consists of media being continually

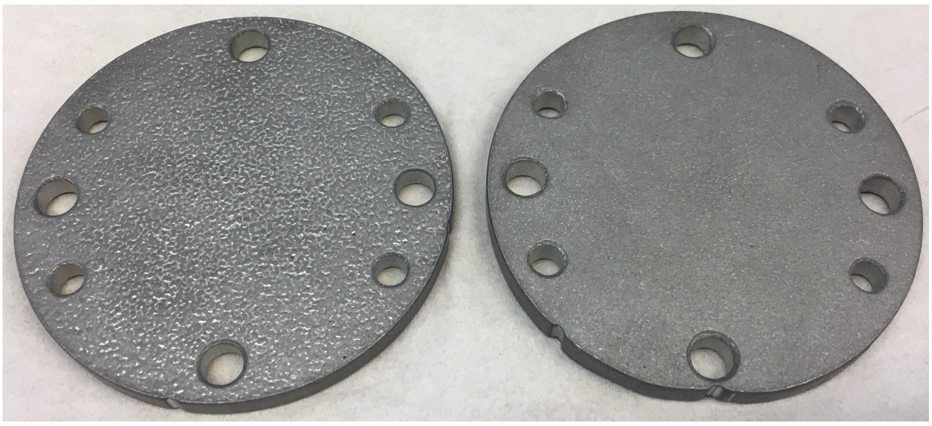

Figure 5.5: Photograph of AlSi10Mg samples manufactured by laser powder bed fusion and treated by media tumbling with Rosler RM06/06 triangular media. The left hand sample is built in a horizontal orientation. The right hand sample is built in the vertical orientation.

rolled (tumbled) across the sample surface through centrifugal force. Speed of rotation fixes the input energy size of media influences the possible surface finish. The media used for this purpose is a ceramic material of size 6 $\times$ 6 $\times$ 6 mm^3 in a pyramid geometry. The samples are fixed in place while the media is excited by the rotational / vibrational motion of the machine; the contact between sample and media causes the raised peaks(burrs) and partially melted powder adhered on the sample to be knocked off. A photograph of horizontal and vertical orientated samples, treated by media tumbling, is shown in Figure. 5.5.

5.2.3 Polishing

Machine polishing is used to remove the influence of surface roughness on R_S completely. The process involves repeated polishing and buffeting to the sample surface to remove extrusions until a mirror-like finish is produced [127, 128]. Polishing has been performed on the 'as built' samples of AlSi10Mg (horizontal and vertical build orientation) and the reference plate of Al6082, all of which have been measured for R_S prior to treatment. The mirror-like finish of the treated plates exhibit values for RMS surface roughness (R_q) of ~ 20 nm. The roughness value for these surfaces is much lower than one skin depth in aluminium at 7.5 GHz ($\sim 1\mu$m) and can be considered flat for microwave current. The machine

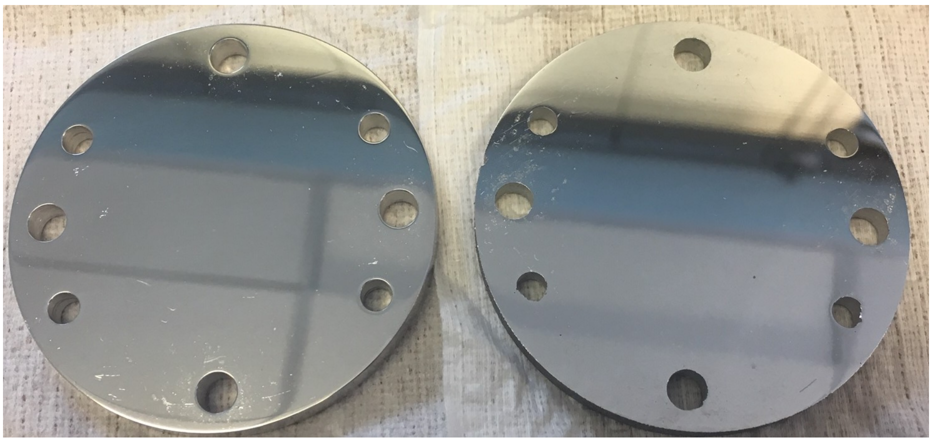

Figure 5.6: Photograph of two polished (mirror finish) samples. The left hand sample is produced of Al6082 Bulk Aluminium Alloy. The right hand sample is produced of AlSi10Mg manufactured by laser powder bed fusion in a horizontal orientation.

polished Al6082 and horizontally built AlSi10Mg samples are shown in Figure 5.6. Practically this method would not be suitable for internal surfaces, however it is used here to assess the influence of surface finish on R_{S}.

5.2.4 Summary of Measurement Protocol

A series of PBF sample plates have been produced and treated by silver plating, polishing and deburring in various combinations, along with reference samples of 'as built' AlSi10Mg, PCB and Al6082 plates. For PBF samples, plates have been produced in both vertical and horizontal orientations for all treatment methods. Samples were manufactured in two batches, with the media tumbled and machine polished samples tested in separate measurement sessions to the as-built, silver plated and bead blasted samples. During each measurement session, common samples were repeatedly re-measured to ensure the consistency of results, giving rise to a standard error of two percent between measurements of batches (for 10 measurements). A summary of the sample ID and description for all measured samples is shown in Table. 5.2.

5.3 Results and Discussion

Measurement of each sample plate has been performed a minimum of six times over two discrete measurement sessions using the DR fixture described in Section. 3.3 at 7.5 GHz. Presented here are the average measured R_{S} and calculated σ_{eff} (see Equation. 2.1 in Chapter. 2) for each plate, which form a comparison with the reference samples. The σ_{eff} values are utilised in COMSOL simulations of a C band waveguide filter in Section. 5.3.2 to examine the performance of 3D components comprising both horizontal and vertical surfaces.

5.3.1 Surface Resistance Measurements

The averaged results for R_{S} and σ_{eff} are shown in Figure. 5.7. As is perhaps expected given the rough surfaces on the Ag plated samples, the copper PCB

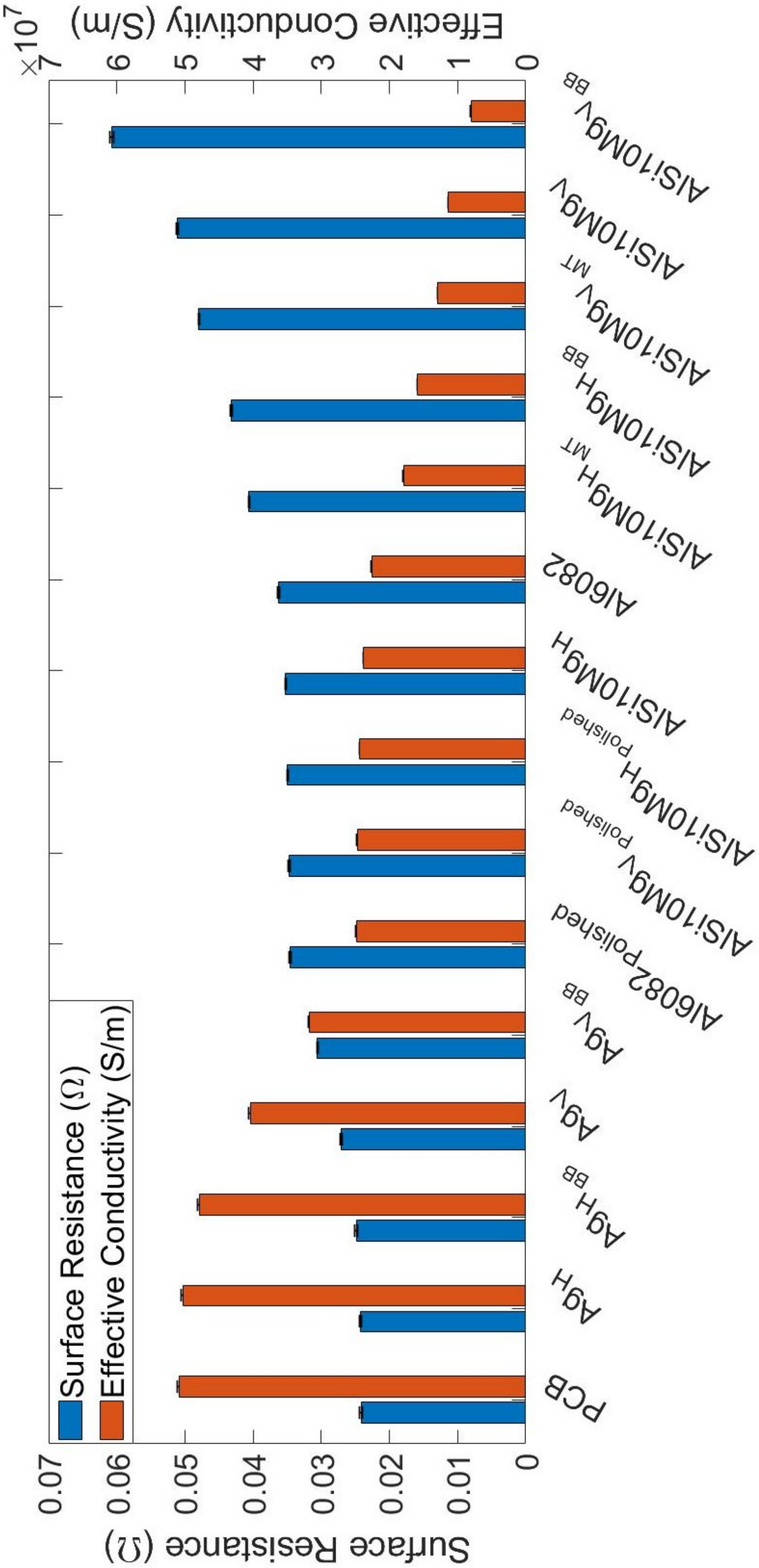

Figure 5.7: Graph of surface resistance (blue) and effective conductivity (orange- calculated from (Equation.2.1)) at 7.5 GHz. Standard error is shown for each sample as an error bar, typically in the range of $1\times\ 10^{-4}\Omega$ for R_{S}. Reprinted from [25] ©2019 IEEE.

Table 5.2: Measurement Sample Description

Sample ID	Post Processing Treatment
PCB	Copper PCB reference sample
Al6082	Bulk aluminium alloy Al6082 (CNC machined) reference sample
Ag_{H}	Silver plated AlSi10Mg PBF sample (Horizontal build orientation)
Ag_{V}	Silver plated AlSi10Mg PBF sample (Vertical build orientation)
$Ag_{H_{BB}}$	Silver plated PBF sample (Horizontal build orientation) with bead blasting
$Ag_{V_{BB}}$	Silver plated PBF sample (Vertical Build Orientation) with bead blasting
$AlSi10Mg_{H}$	AlSi10Mg PBF sample 'as built' (Horizontal build orientation)
$AlSi10Mg_{V}$	AlSi10Mg PBF sample 'as built' (Vertical build orientation)
$Al6082_{Polished}$	Bulk aluminium alloy Al6082 with machine polished finish
$AlSi10Mg_{H_{Polished}}$	AlSi10Mg PBF sample (Horizontal build orientation) with machine polished finish
$AlSi10Mg_{V_{Polished}}$	AlSi10Mg PBF sample (Vertical build orientation) with machine polished finish
$AlSi10Mg_{H_{BB}}$	AlSi10Mg PBF sample (Horizontal build orientation) with bead blasting
$AlSi10Mg_{V_{BB}}$	AlSi10Mg PBF sample (Vertical build orientation) with bead blasting
$AlSi10Mg_{V_{MT}}$	AlSi10Mg PBF sample (Horizontal build orientation) with media tumbled finish
$AlSi10Mg_{V_{MT}}$	AlSi10Mg PBF sample (Vertical build orientation) with media tumbled finish

sample exhibited the lowest R_{S} value of all samples studied here.

The notably poor performance of samples built in a vertical orientation opposed to horizontal is shown in Figure. 5.8. The disparity between the two orientations studied is greatest for the 'as built' samples, where vertical samples exhibit an R_{S} of approximate 1.5 times higher. For the machine polished samples, where the influence of surface roughness has been minimised, there is only negligible differences between the two build orientations. For the deburring treatments, the ratios in Figure. 5.8 are perhaps misleading as the disparity between orientations is reduced through a larger increase in the R_{S} value of the horizontal samples rather than a reduction in the vertical samples. These treatments are discussed in more detail later in this section.

Focusing on the silver plating process, R_{S} is reduced significantly compared to the 'as built' AlSi10Mg sample and becomes similar in value to the PCB sample. Furthermore the plating also goes some way to reducing the disparity in R_{S} between vertical and horizontal build orientations, as shown in Figure. 5.7. The

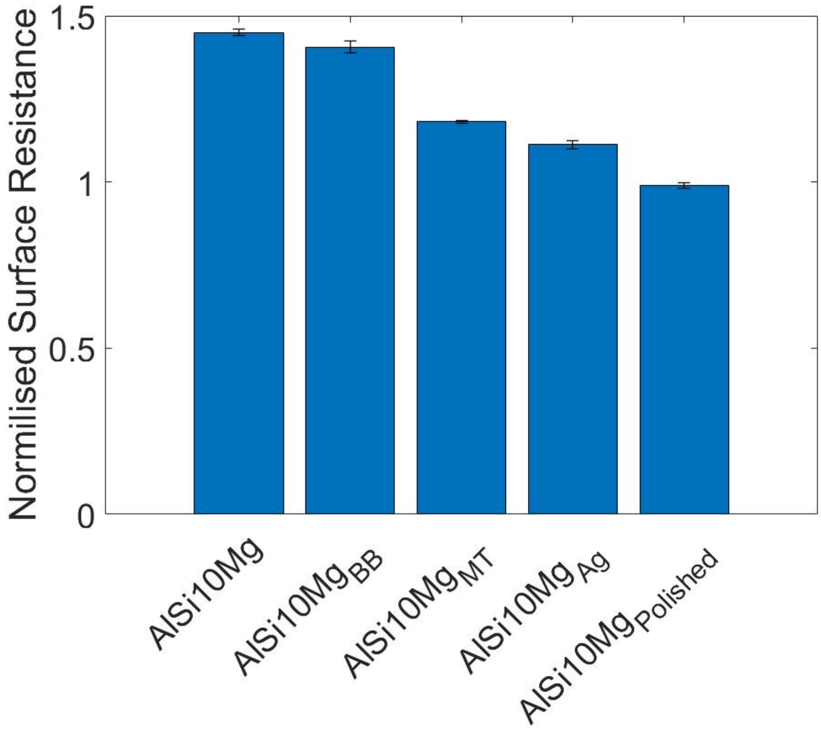

Figure 5.8: Surface resistance values for vertically built samples as a ratio with equivalent horizontal built samples. Standard error is shown in the error bars, typically for 10 measurements.

effect of silver plating on R_S, through a ratio to equivalent 'pre-plating' surfaces, is shown in Figure. 5.9. In all cases silver plating has reduced R_S. The largest improvement is seen for the vertically built surfaces, where a $\sim 50\%$ reduction in R_S is evident after silver plating for both the 'as built' and bead blasted samples. This may be due to the current being nearly entirely contained within the silver layer, as such avoiding the additional complexities associated with current flow in partially melted powders or across layer boundaries in the PBF material. The horizontally built samples also exhibit a significant improvement, of at least 30%, as compared to the equivalent 'pre-treatment' samples. This result is not surprising, given the high electrical conductivity of silver, as well as removing current in near its entirety from the PBF material.

The deburring methods employed here have increased R_S for the majority of samples. The exception to this is the vertical orientation treated with media

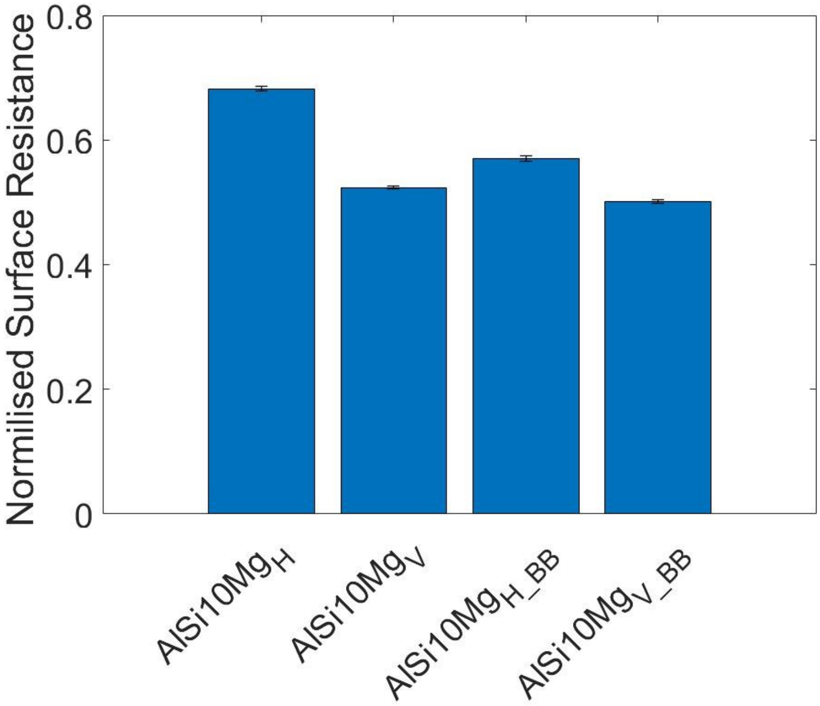

Figure 5.9: Silver plating effect on surface resistance. Each averaged sample R_{S} is shown as a ratio with the equivalent 'pre-treatment' sample. Standard error is shown by the error bars.

tumbling, where a marginal improvement of $\sim 6\%$ is observed. The comparison of R_{S} results for the media tumbling process are shown in Figure. 5.10a through a ratio with an equivalent 'pre-treatment' sample. The process does however increase the R_{S} value for the horizontally built sample. R_{S} results for the bead-blasted samples are shown in Figure. 5.10b as a ratio with an equivalent 'pre-treatment' sample. Marginal increases in R_{S} is observed for the samples treated with both bead-blasting and silver plating, whilst a more significant negative impact is seen in the samples without silver plating. Again, the higher conductivity and the skin effect make this result not entirely surprising. The overall trend of these deburring methods of increasing R_{S} is however somewhat unexpected. The measured surface roughness values, detailed in Appendix. C, do not correlate directly with R_{S}. For example, the bead-blasting process was successful in lowering the overall roughness R_{q} by approximately 45% for the vertical built sample, however simultaneously increasing its R_{S} value by approx-

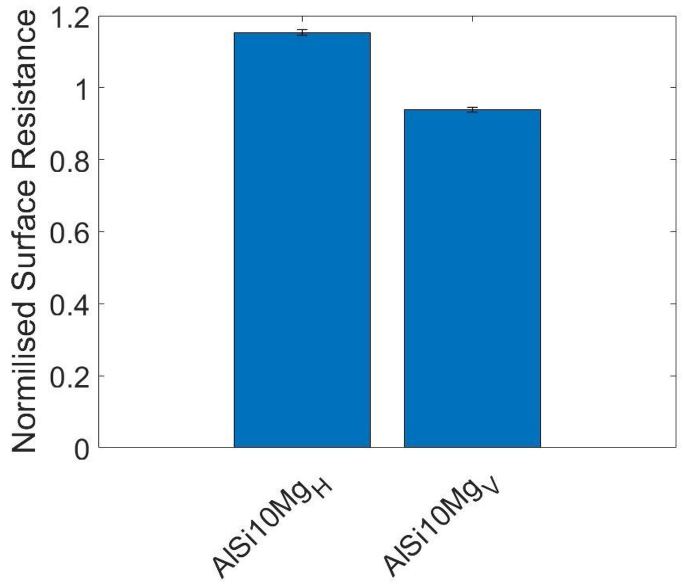

a)

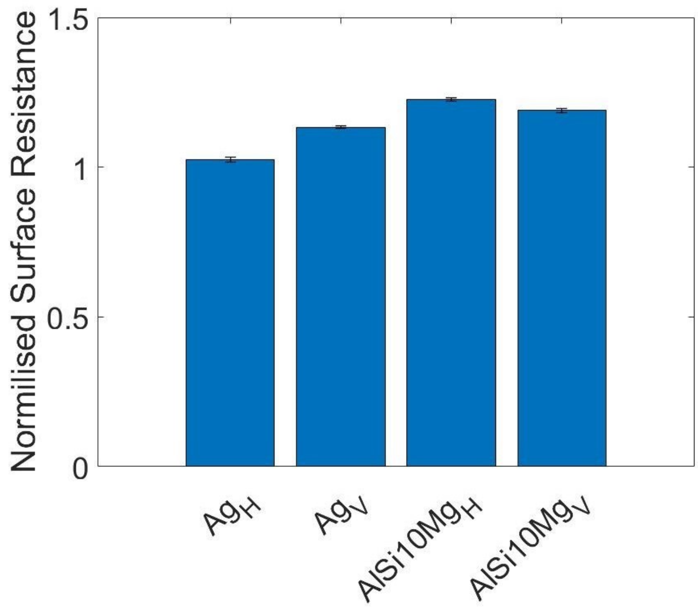

b)

Figure 5.10: Effect of a) media tumbling and b) bead blasting treatment on the microwave surface resistance of powder bed fusion produced samples. Values are shown as a ratio with the equivalent 'pre-treatment' R_S values. Standard error is shown by the error bars.

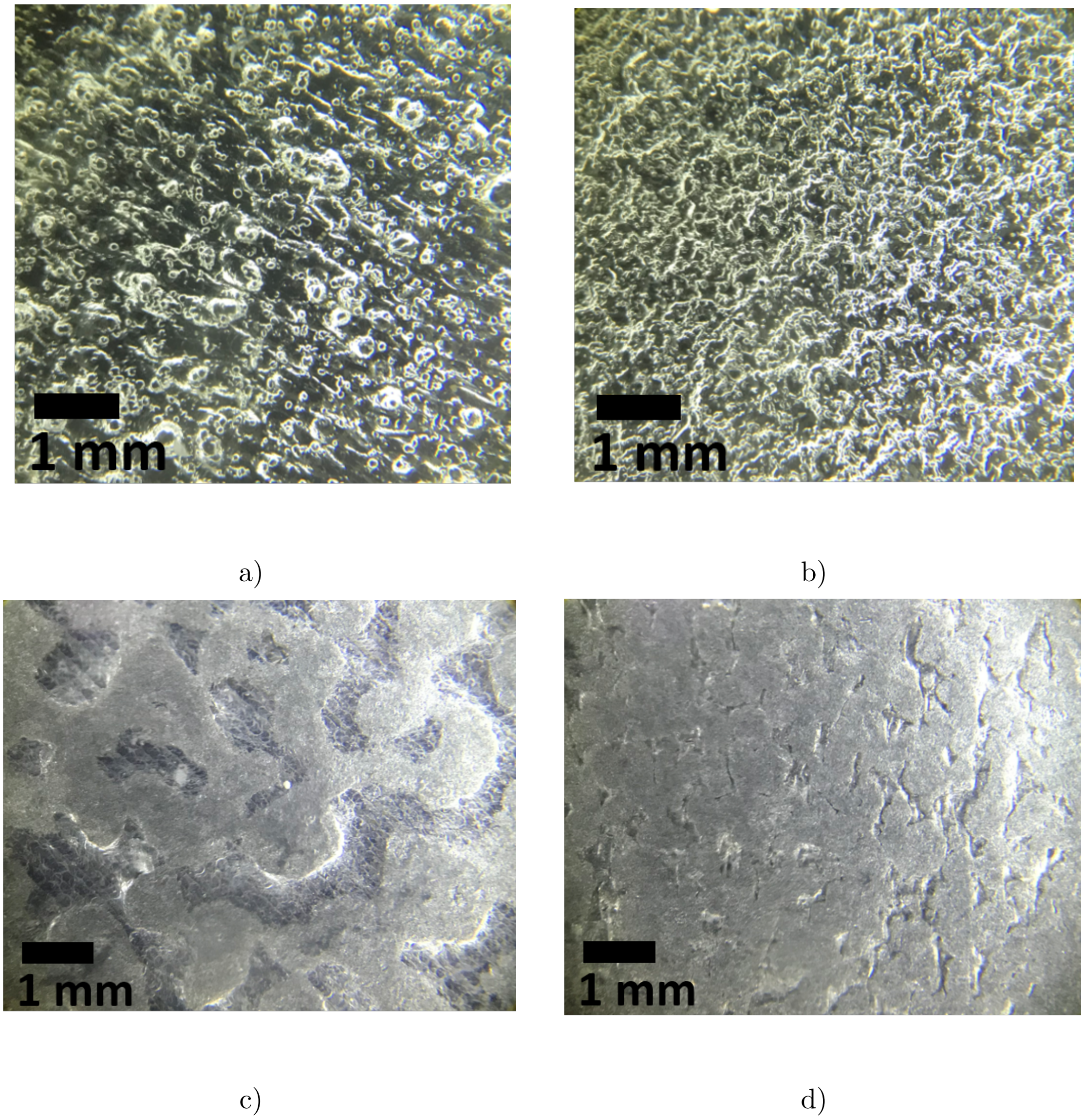

Figure 5.11: Optical microscope images of bead blasting and media tumbling post-processing treatments. Silver plated, vertical build orientation a) ‘as built’ and b) bead blast. Media Tumbling c) horizontal orientation and d) vertical orientation.

imately 20%. This suggests that although the partially melted powders and protrusions may have been removed, the process of particle impacts is deforming the metal surface in other ways [175]. This assumption is confirmed through optical microscope images shown in Figure. 5.11. Figure. 5.11 a and b shows ’as built’ and bead blasted surfaces, respectively, of silver plated samples built in a vertical orientation. The large roughness features present on the ‘as built’ surface are replaced by an increased number of smaller indentations. Figure. 5.11 c and d show media tumbled surfaces of samples produced in horizontal and vertical orientations, respectively. This unusual surface texture appears to be the result of flattening roughness protrusions by compression rather than the removal of loose particles. In Figure. 5.11c, the scan path can be seen under the features. Although the surface in Figure. 5.11d looks smooth by visual inspection, the media tumbling process is causing some other effect on the surface that is increasing R_S values over those seen in 'as built' samples.

The machine polishing process removed the surface roughness almost entirely, leaving a surface finish of less than 0.02μm on all study samples. The influence of this treatment on samples in both build orientations is shown in Figure. 5.12a through the ratio to equivalent 'pre-treatment' PBF samples. There is a large improvement in R_S, of $\sim 35\%$, for the vertically built sample while only a modest improvement ($\sim 2\%$) is observed for the horizontal orientation. This is expected given the 'pre-treatment' vertical surfaces exhibit R_q three times higher than in the horizontal orientation (see Appendix. C) and although R_q is not the only parameter to influence loss, it does give some indication as to a surfaces' microwave performance. Interestingly, when the absolute R_S values for the polished surfaces are compared, no significant difference can be seen between the horizontal and vertical PBF samples, or indeed with the Al6082 aluminium alloy sample, which has undergone the same treatment. The averaged R_S values for all polished samples are shown in Figure. 5.12b, where < 1 % differences are seen between the PBF and bulk Al6082 aluminium alloy samples. This result is significant because it highlights that the excess conductor loss associated with PBF components can be entirely attributed to the surface finish. It also suggests that the layer boundaries formed within the vertically built samples, which are still present after removing roughness, are not contributing significantly to the inhibition of current flow.

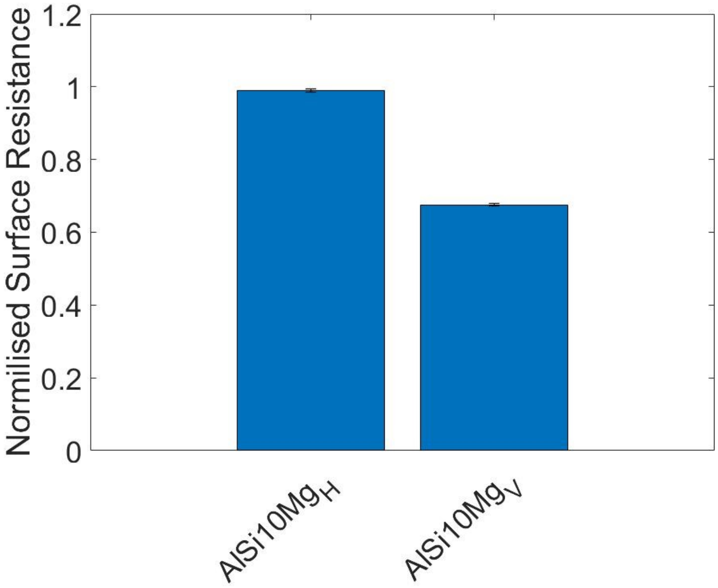

a)

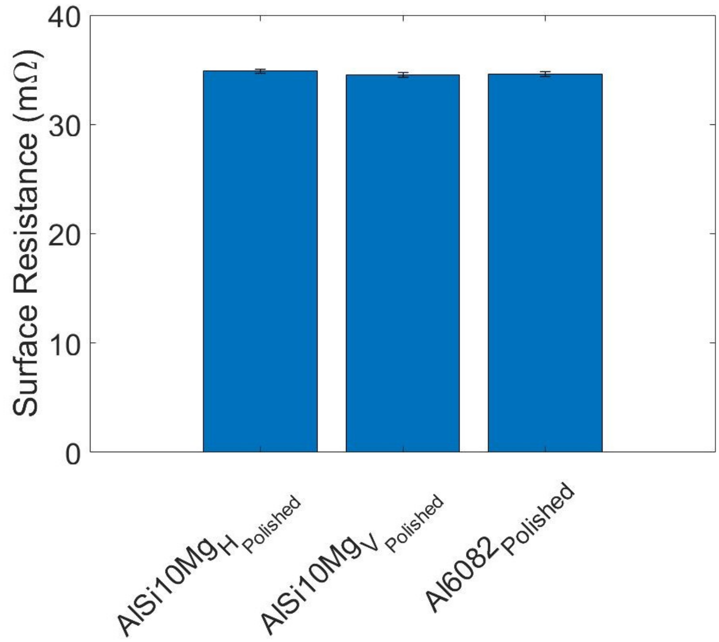

b)

Figure 5.12: Effects of mirror-finish polishing on surface resistance. a) Ratio of surface resistance for the polished sample against their 'pre-treatment' equivalents and b) absolute surface resistance. Standard error is shown by the error bars.

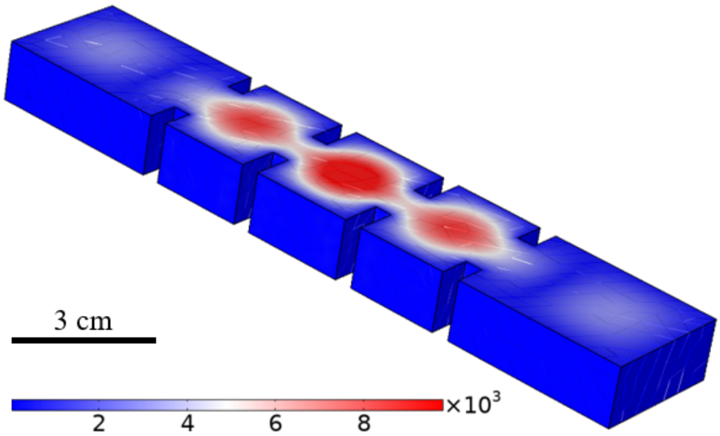

Figure 5.13: CAD model of a C band rectangular waveguide filter using (using COMSOL Multiphysics). Simulated electric field magnitude (V/m) from a 1 W input power at the centre of the passband is shown by the colour gradient. Reprinted from [25] ©2019 IEEE.

5.3.2 Simulated Waveguide Filter

The measured R_S values can be converted into an effective conductivity (σ_eff) through Equation. 2.1 and are shown in Figure. 5.7. σ_eff can then be used in almost any EM simulation package to account for the losses associated with surface roughness [77]. Horizontal built PBF samples have exhibited surprisingly good performance when compared to traditionally machined alternatives, which is a very positive result for microwave devices that can be manufactured in only one plane, such as some patch antennas [176, 177]. However, many passive microwave components will have a three-dimensional nature and as such, for PBF produced parts, will be subject to the loss properties of more than one build orientation.

To examine how the presence of both horizontal and vertical surfaces affect the overall microwave performance, a rectangular waveguide filter has been implemented in COMSOL multiphysics for simulation of the band-pass insertion loss. The model is based on [178] and adapted for operation in the C band with a passband between 7.25 and 7.55 GHz (consistent with the DR measurement frequency). The three-pole, air filled component consists of cascaded cavity resonators coupled by inductive irises of dimensions 9.4 × 4 mm^2 and 7.2 × 4 mm^2

. This study uses S-parameters for the dominant TE_{10} propagating mode of the waveguide to asses loss. Individual surfaces of the component can be attributed a relevant σ_{eff} value, such that the measured horizontal and vertical surfaces can be incorporated into the model. The σ_{eff} values used for each surface are taken from Figure. 5.7. A representation of the model and its electric field distribution within the passband is shown in Figure. 5.13. The simulated S_{21} traces are shown in Figure. 5.14. S_{21} in this case corresponds to the insertion loss, IL=-20log$|S_{21}|$,in the usual way, such that the more negative an S_{21} value the higher the loss that is exhibited. Included for completeness is a hypothetical scenario where all walls of the waveguide are made from the copper PCB material, as would be expected this setup produces the lowest loss value of all combinations investigated, however the silver plated and silver plated bead blasted devices were comparable. Polished AlSi10Mg and Al6082 parts performed similarly, with 24% increase in passband

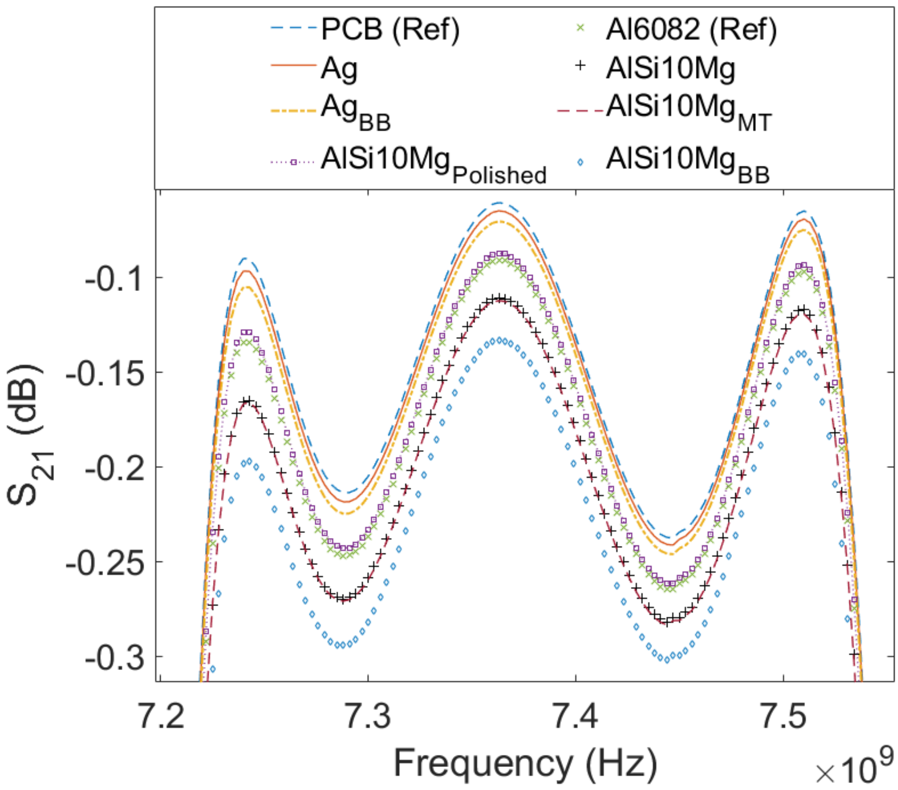

Figure 5.14: Simulated S_{21} traces for a C band waveguide filter. Modeled with different σ_{eff} values for vertical and horizontal surfaces. Adapted from [25] ©2019 IEEE.

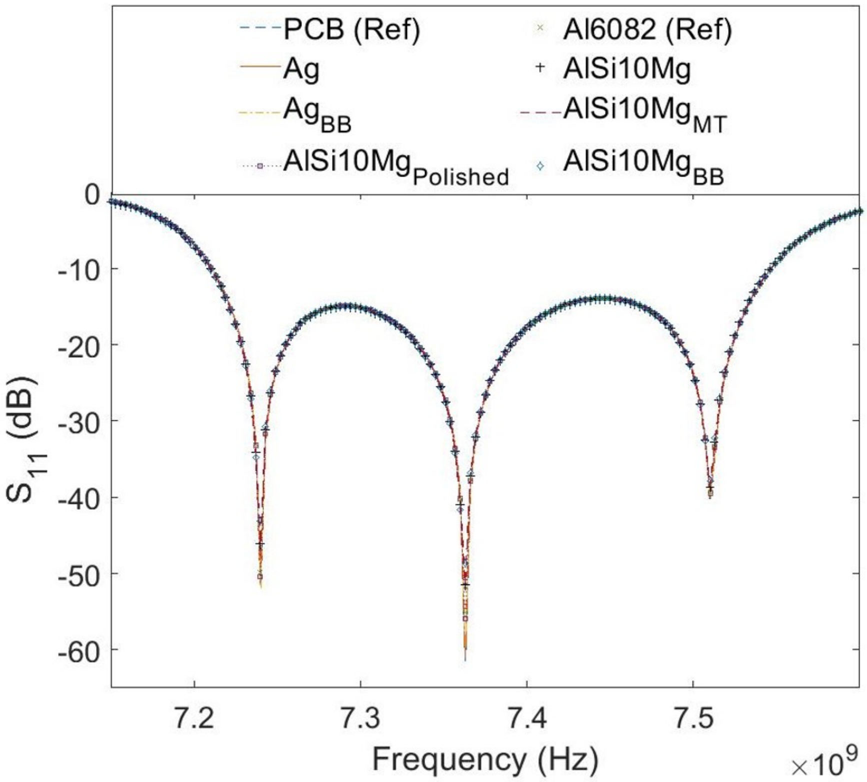

Figure 5.15: Simulated S_{11} traces for a C band waveguide filter. Modeled with different σ_{eff} values for vertical and horizontal surfaces.

insertion loss over PCB values. Although the 'as built' horizontal AlSi10Mg sample performed well in comparison to Al6082 in isolation, when the vertical surface is included the overall performance is significantly worse that the equivalent simulation for an Al6082 filter. This results highlight the negative impact the vertical surfaces have on EM component performance. It is with noting here that this model is somewhat simplified as it does not account for overhanging surfaces that would be present on a real component build, however it is of some use in evaluating the impacts of different build orientations combined into three-dimensional components. Furthermore, some of the treatments examined here would not be realisable for internal surfaces of three-dimensional components, for example the mirror-finish polishing and bead blasting processes. Included for completeness are the simulated S_{11} traces (corresponding to return loss) for each scenarios shown in Figure. 5.15, where there is no significant variance between materials and in all cases values are below the normally acceptable -15 dB level.

5.4 Conclusions and Further Work

The most influential of the post-process surface treatments investigated here is the use of silver plating. The improvement in R_S seen in these samples is in the range of 30% to 50%. This can be attributed to the increased conductivity value of silver over aluminum as the primary conductor and the removal of nearly all current from the PBF material. Although the 'book value' conductivity of silver is higher than that of copper, the surface finish of PFB parts are considerably worse than those of the PCB sample. Furthermore, the electrical conductivity plated metals tends to be significantly less (as low as 25%) than that of its bulk metal equivalent [179]. The combination of these properties result in silver plated PBF parts exhibiting a lower effective conductivity than copper PCB.

As suspected, vertical built surfaces perform significantly worse than parts built in a horizontal orientation. Specifically, when 'as built' parts were investigated in a three-dimensional simulation of the C-band bandpass filter. The vertical surfaces degraded the overall performance to a level much lower than that of traditionally machined aluminium (Al6082). However, the silver plating process has been effective in reducing the disparity between vertical and horizontal surfaces. This makes the silver plating process the most viable option as a single treatment of three-dimensional components for use in microwave applications, at least in the low GHz frequency range. It should be noted that downwards facing surfaces in PBF parts may not provide similar R_S values to those of upward facing surfaces, and have not be considered in this study.

The results from bead blasted and media tumbled samples are surprising in that they lead to an increase in R_S. This may suggest that they are influencing the surface topology of the sample, which dominates over the intended removal of loose particles. There are a number of influential variables in both processes that have not be considered in this study. These include particle size and blast pressure, as well as media shape and material, all of which merit further investigation.

By machine polishing of the PBF samples, so effectively reducing the surface roughness, it has been shown that the underlying aluminum alloy can perform comparably with the traditionally machined alloy. This suggests that the inclusion of silicon in the starting powder does not have a significant negative effect on its microwave performance, as might not have been suspected from the outset. Furthermore, the crystalline structure of the PBF samples is perhaps similar to traditional alloys and requires further studies using advanced characterisation techniques. However, due to the nature of this finishing process, it is not suitable for the internal faces of three-dimensional PBF structures.

An interesting technique not investigated here but reported in the literature is chemical machining. Using solutions of Nitric and Hydrofluoric acids, it is possible to significantly reduce roughness in PBF parts without changing the chemical composition of the alloy [180]. This techniques warrants proper consideration in future work related to optimising R_{S}.

CHAPTER 6
MICROWAVE EVALUATION OF THERMAL EXPANSION

6.1 Introduction

Thermal expansion can be problematic in many areas of engineering, not least during the PBF process itself, where higher silicon content in aluminium alloy powders can help lower thermal expansion and prevent crack formation [118] during the rapid melting and solidification process. In metallic solids, the crystalline structure of atoms is relatively compact at very low temperatures, but as temperature increases the potential energy and spacing between atoms increases and forces the solid to expand [181]. In one extreme, modern bridges allow for expansion through the use of specially placed expansion joints, where structural restraining forces of the order of 4×10^6 N would otherwise be required to prevent loss of support in the presence of only a 10 K temperature rise [182]. Similarly, thermal expansion can have detrimental effects during precision engineering. High frequency waveguides and filters, for example, have critical dimensions which are sensitive to temperature, which results in deviations in their desired operating frequencies. Large enough shifts in frequency can render a device inadequate for its intended purpose. This phenomenon is particularly worrisome when operating in harsh temperature environments, such as in space and aerospace applications where, for example, typical thermal cycling between 98 K – 433 K is experienced by components of satellite systems [183]. For example, a thermal cycle of 300K could cause a component made from aluminium alloy (coefficient of thermal expansion $\sim 23\times10^{-6}$ K^{-1}) to change its length by around 0.7%, i.e. 0.7 mm for a component of length 10cm; this could have a major effect on the performance of a high precision part like a microwave filter. It is therefore apparent that accurate information about the building materials is essential in order to make considered judgments regarding safety and suitability. The metric for quantifying geometrical changes due to changes in temperature is the coefficient of thermal expansion (CTE).

AM enables advancements in component manufacture in many fields of engineering, but it is still a relatively new technology where the thermal properties of the melted powder alloys need to be explored. Furthermore, the selection of processing techniques can deliver differing properties from the same raw material, as shown in Chapter.2. So although properties of the raw material may be known, the use of AM as a processing technique can bring about different values of material properties compared with the 'book' values. In addition, metallic AM parts currently exhibit inferior electrical properties when compared to traditional bulk metals, as described in proceeding chapters, leading to anomalously high values of surface resistance at microwave frequencies, and so high losses. To overcome these losses, post processing techniques such as machine polishing [184] and silver plating are often employed [42, 51, 176]. Machine polishing of three dimensional structures is not always possible and silver plating has become the most commonly used treatment. Silver plating, as mentioned in Chapter.2, is affected by the CTE of different materials where, in these instances, the plating material can disassociate from the host surface and result in failure [123].

Thus, the investigation of thermal expansion in AM parts is of major interest, and the added advantage of being able to machine complex geometries opens up opportunities to use less conventional, but potentially more precise, methods to examine the materials used. This study uses a fractional frequency shift method to evaluate the true CTE of an aluminium cylindrical microwave cavity produced through PBF over a wide temperature range (6 – 450 K) without the need for strict calibration. To the author's knowledge, this is the first time that CTE for AM materials has been assessed over a wide range of temperature, as is appropriate for space-based components, using a passive microwave structure (produced by PBF) that can be adopted in a satellite communications system.

Parts of this chapter have been published in a peer-reviewed journal paper [26], with some figures and text having been reprinted.

6.1.1 Linear Coefficient of Thermal Expansion

The metric for quantifying geometrical changes due to changes in temperature is the linear CTE. A common form of CTE described in literature is the 'mean' CTE [185], a linear average of the expansion of a material over a specified temperature range expressed as

$$\alpha_m = \frac{1}{L_0}\frac{L_1 - L_0}{T_1 - T_0} \tag{6.1}$$

where L and T are length and temperature, respectively, while 0 and 1 denote the initial and final values, respectively. Limiting Equation. 6.1 to small changes in length and temperature, we can define the true coefficient of thermal expansion as

$$\alpha_c \approx \frac{1}{L_0}\frac{dL}{dT} \tag{6.2}$$

where dL/dt is the gradient of the curve of length against temperature and is expressed at one temperature point. Figure 6.1 highlights the difference between the two CTE definitions.

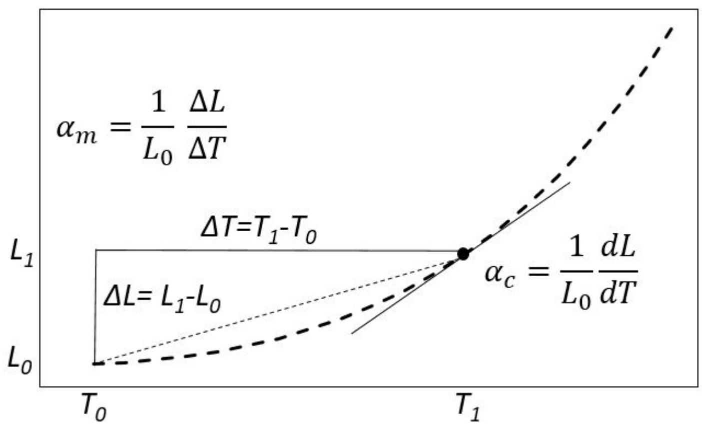

Figure 6.1: Representation of mean and true coefficient of thermal expansion.

6.1.1.1 Approximation for the Coefficient of Thermal Expansion

In metallic solids such as aluminium alloys, thermal expansion has contributions arising from ionic lattice vibrations as well as the free electron density. Since it is accepted that thermal expansion of solids will follow the same temperature dependence as the material's specific heat capacity [186], an expression for thermal expansion can be formulated from the use of the Debye and Somerfeld-Drude models.

The ionic contribution to specific heat capacity ($C_{\mathrm{v_i}}$), and therefore thermal expansion, can be expressed using the Debye model as [186]

$$C_{v_i} = 9 n_i k_b \left(\frac{T}{\Theta_D} \right)^3 D \tag{6.3a}$$

where D is the Debye function

$$D = \int_0^{\frac{\Theta_D}{T}} \frac{x^4 \; e^x}{(e^x - 1)^2} \; dx \tag{6.3b}$$

k_b is Boltzmann's constant (1.38 $\times 10^{-23}$ J/K)Θ_D is the Debye Temperature (nominally 390 K for aluminium [186]), T is temperature (K), and n_i is the density of ions ($\sim 6 \times 10^{22}/\mathrm{cm}^3$ for aluminium [186])

$$n_i = 6.022 \times 10^{23} \; \frac{\rho_m}{A} \tag{6.3c}$$

where ρ_m is the mass density (2.7g/cm^3 for aluminium) and A is the atomic mass (27 u for aluminium). This model predicts that the specific heat capacity (hence thermal expansion) will follow a T^3 dependence at temperatures well below the Debye temperature and follows the Dulong-Petit law constant at high temperature, in which specific heat tends to a constant over high temperatures.

However, when considering metallic solids, the electronic contribution to specific heat must also be accounted for as this becomes important at very low temperatures. The Sommerfeld-Drude model approximates the electronic contribution to specific heat ($C_{\mathrm{v_e}}$) as [186]

$$C_{v_e} = \frac{\pi^2}{2} n_e k_b \left(\frac{T}{T_f} \right) \tag{6.4a}$$

where T_f is Fermi temperature ($\sim$ 14 $\times 10^4$ K for aluminium) and n_e is the free electron density

$$n_e = Z n_i \tag{6.4b}$$

where Z is the nominal valance (three for aluminum). The Sommerfeld-Drude model predicts that specific heat capacity from electronic contributions will follow a linear temperature dependence. Due to the extremely high T_f value, the electronic contribution is very small compared to the ionic contribution and is only appreciable at very low temperatures. Therefore low temperature specific heat capacity in metals varies as $\alpha T + \beta T^3$, where α and β are constants. However the linear term from the electronic contribution is only observed when $T < T_0$ [186], which is defined by

$$T_0 = 0.145 \left(\frac{Z \Theta_D}{T_f} \right)^{1/2} \Theta_D \tag{6.5}$$

The ionic contribution exceeds the electronic contribution to specific heat at $T > T_0 \approx 12.55\ K$.

The approximate models described above lead to the formulation of an expression for CTE [186]

$$\alpha_c = \frac{1}{3B} \left(\gamma C_{V_i} + \frac{2}{3} C_{V_e} \right) \tag{6.6}$$

where B is the bulk modulus (76 GPa) and γ is Grüneisen parameter (it value found through curve fitting to experimental data). Both γ and B are very weakly temperature dependent and assumed to be constant for this analysis.

6.1.2 Temperature Dependent Resistivity

In an ideal metal, conduction electrons are able to migrate through the lattice without impediment. In a real metal, resistivity is introduced by a number of factors. For alloyed metals, a residual resistivity is present which is temperature independent and arises due to ions of the alloying material disrupting the lattice structure [181]. The temperature dependent contribution to electrical resistivity is associated with the lattice vibrations that also contribute to thermal expansion. The increasing lattice vibrations act as a source of resistance through the scattering of electrons known as electron-phonon interaction [187]. Resistivity can be therfore be expressed as

$$\rho = \rho_0 + \rho(T) \tag{6.7}$$

where ρ_0 is the residual resistivity and $\rho(T)$ is the temperature dependent electron-phonon contribution to resistivity.

The Bloch-Grüneisen model has been used successfully in several studies to fit experimental temperature dependent resistivity data for metal solids [188, 189, 190]. The model is expressed as [191]

$$\rho(T) = A\left(\frac{T}{\Theta_R}\right)^5 \int_0^{\frac{\Theta_R}{T}} \frac{t^5}{(e^t - 1)(1 - e^{-t})} dt \tag{6.8}$$

where A is a constant associated with the material, Θ_R is the characteristic temperature (usually close to the Debye temperature of a material) and T is the temperature at measurement.

6.2 Measurement Theory

The microwave cavity resonator method allows calculation of CTE via evaluating the derivative of resonant frequency over temperature. The metallic material of interest must be machined to contain a hollow cavity of known dimensions. The method is based on the microwave resonant frequency response of this cavity being directly dependent on the internal geometry. The equation for the resonant frequency, f, of transverse-magnetic (TM) modes in a cylindrical air spaced cavity is given by [132]

$$f_{nml} = \frac{c}{2\pi}\sqrt{\left(\frac{p_{nm}}{a}\right)^2 + \left(\frac{l\pi}{d}\right)^2} \tag{6.9}$$

where c is the speed of light, m, n and l are the mode integers, i.e p_{nm} is m^{th} root of the n^{th} order Bessel function $J_n(x)$ of the first kind, and l is the integer number of half wavelengths along the cavity axis. a and d are the cavity radius and height, respectively. In this study the test cavity is made of an aluminium alloy, as such it is subject to thermal expansion, making a and d temperature dependent and approximated to the first order as

$$a = a_0(T) \approx a_0(1 + \alpha_c \Delta T) \tag{6.10a}$$

$$d = d_0(T) \approx d_0(1 + \alpha_c \Delta T) \tag{6.10b}$$

where a_0 and d_0 are the initial radius and height, α_c is the linear CTE of the cavity walls and ΔT is the change in temperature. Evaluating the first order partial derivatives of (6.9) including the temperature dependence of (6.10a) and (6.10b), the fractional change in frequency due to changes in temperature can be expressed as [192, 193]

$$\frac{\Delta f}{f_0} \approx -\alpha_c \left(\frac{c}{2\pi f_0}\right)^2 \left(\frac{p_{nm}^2}{a_0^2} + \frac{l^2\pi^2}{d_0^2}\right)\Delta T \approx -\alpha_c \Delta T \tag{6.11}$$

where α_c is

$$\alpha_c \approx -\frac{1}{f_0}\frac{\Delta f}{\Delta T} \approx \frac{1}{f_0}\frac{df}{dT} \tag{6.12}$$

for small shifts in f and T. The fractional frequency shift, df, becomes analogous to dL from (6.2). Hence small shifts in resonant frequency can be directly attributed to the CTE of the cavity material.

6.3 Experimental Method

The microwave cavity resonator used for this study [68] was produced on a Renishaw AM250 laser powder bed fusion additive manufacturing system. The material used in this study, aluminium alloy (AlSi10Mg), comprises aluminium with up to 10% mass fraction of silicon and small quantities of other elements such as magnesium. The silicon present helps to improve the fluidity of the melt pool while the addition of magnesium makes the alloy both harder and stronger than pure aluminium [94]. The main PBF process parameters used to produce this cavity include: laser power = 200W, hatch distance = 130 μm, layer thickness = 25 μm, exposure time = 140 μs and point distance = 80 μm and each layer is orientated at 67° to the previous layer. The chamber is vacuumed with a flow of argon to avoid oxidisation of the powder.

The TM_{010} mode of the cavity is used to measure the resonant frequency over the temperature range 6 – 450 K. The TM_{010} mode of a cylindrical cavity is the lowest frequency (i.e. dominant) mode of such a structure when the radius is larger than the length. Its electromagnetic (EM) field distribution comprises a high electric field on its axis, and high azimuthal magnetic field near to its outer perimeter. Higher order modes, TM_{210} and TM_{310}, are also measured between 310 – 450 K to investigate the influence of EM field distribution on CTE.

The cavity used and the EM field distributions for each mode are shown in Figure 6.2. The cavity's internal dimensions were $a = 4.6$ cm and $d = 4$ cm while the resonant frequencies (at 310 K) of the three modes studied were TM_{010} at 2.522 GHz, TM_{210} at 5.343 GHz and TM_{310} at 6.643 GHz. The geometric factors (G) from Equation. 3.18a for TM_{010} is evaluated, through COMSOL Multiphysics simulation, for the temperature range between 210.5 Ω^{-1} at 6 K and 211.3 Ω^{-1} at 450 K.

To cover such a wide temperature range, the experiment was conducted in

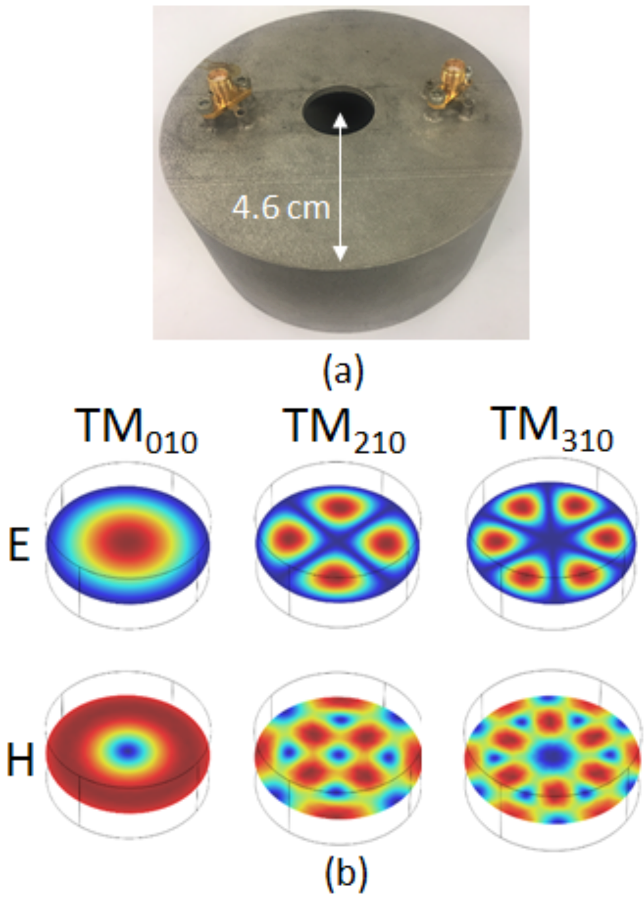

Figure 6.2: (a) Cylindrical cavity produced through powder bed fusion, (b) field distributions of TM_{010}, TM_{210} and TM_{310} modes. Reprinted from [26] ©2019 Gumbleton et al. (CC-BY).

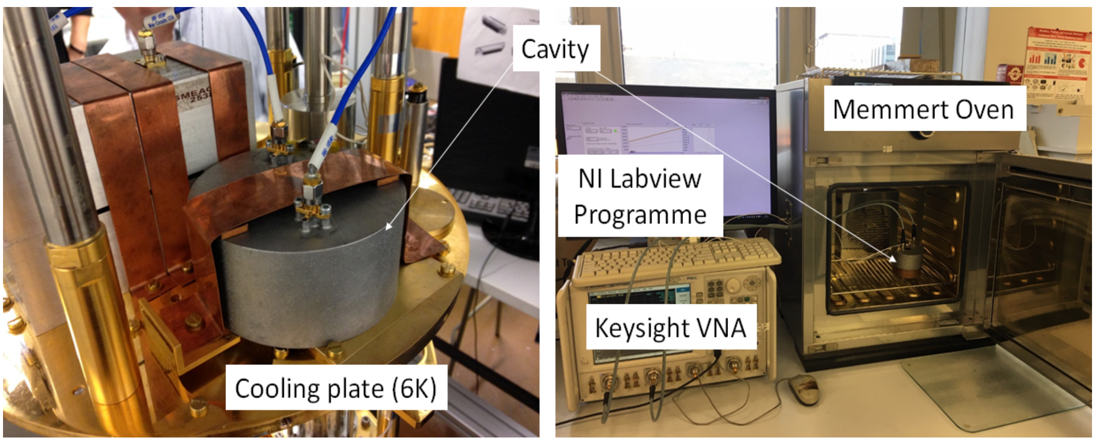

Figure 6.3: Photograph of the experimental setup for the dilution fridge (6 – 300 K) and oven ramps (310 – 450 K). Reprinted from [26] ©2019 Gumbleton et al. (CC-BY).

two parts: a cooling ramp between 6 – 300 K and a heating ramp between 310 – 450 K. Figure 6.3 shows the two experimental setups used for each section of the temperature range. The fractional frequency shift for both ramps was measured through 2-port S-parameters, with the cooling ramp using a Keysight Fieldfox N9914A portable vector network analyser (VNA) and the heating ramp using a lab based Keysight VNA. Due to a wider available frequency range in the heating ramp setup, higher order modes, TM_{210} and TM_{310}, were also observed between 310 – 450 K to investigate the influence of of a different EM field distribution on CTE.

The cooling system used for the low temperature range is a Bluefors dilution fridge with a cooling rate of 0.2 K/min. The AM microwave cavity resonator was clamped to an internal plate with copper straps and the temperature of the cavity was directly measured using a calibrated diode thermometer. To ensure good thermal contact with the plate, the rough as-manufactured surface of the cavity was polished until visually smooth. For the high temperature range, the cavity was heated in a Memmert UF 30 oven with a 1 K/min heating rate. A National Instruments (NI) NI-cDAQ-9171 was used to interface two temperature sensors and an NI LabVIEW program was used to record all measurements during the oven ramp. A comparison between the Keysight and Fieldfox VNAs was performed to ensure consistency in frequency measurements. S_{21} measurements taken under the same environmental conditions produced a deviation of $\approx$ 20 kHz between the resonant frequency of TM_{010} recorded by the two measurements systems, giving rise to a relative standard error of $< 0.1\%$.

6.4 Results and discussion

The resonant frequency of the PBF produced cylindrical cavity across the full temperature range is shown in Figure 6.4. At $\sim$310 K there is a deviation from the trend line in the absolute values of the resonant frequency when comparing the fridge and oven measurements. This is due to the design of the cavity con-

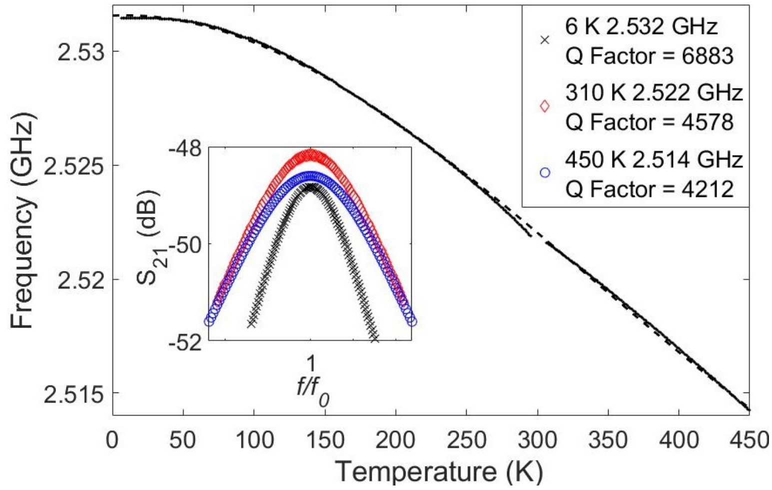

Figure 6.4: Resonant frequency shift of TM_{010} as a function of temperature. The dashed line is added as a guide to the eye. Inset plot of normalised S_{21} traces at different temperatures. Reprinted from [26]

taining a hole at the top and bottom. Since the electric field of the TM_{010} mode is central and parallel to the axis of the cavity, the electric field leaks from the hole. This fringing field will interact with materials external to the cavity, in this instance the copper strip attaching the cavity to the cold plate of the dilution fridge. The exact proximity and material was not replicated in the oven ramp and explains the deviation from the trend line. At temperatures above approximately 150 K, we observe that the resonant frequency is linearly proportional to the ambient temperature and follows (6.12). When cooled to temperatures lower than approximately 150 K, the resonant frequency starts to saturate and is no longer linearly dependent on temperature, while at temperatures below approximately 40 K this tends to a constant.

The inset of Figure 6.4 shows S_{21} traces at three temperature points with the corresponding Q factor values. We observe that at lower temperature the 3dB bandwidth is narrower, resulting in a higher Q factor, itself $\propto 1/R_{\mathrm{S}} \propto \sqrt{\sigma}$. Comparing the measured Q factor values to an equivalent cavity produced via traditional methods (Q $\approx 11,000$ at 310 K and Q $\approx 9,500$ at 450 K [194]), highlight the significant negative impact that poor surface finish associated with the AM manufacturing processes has on R_{S}.

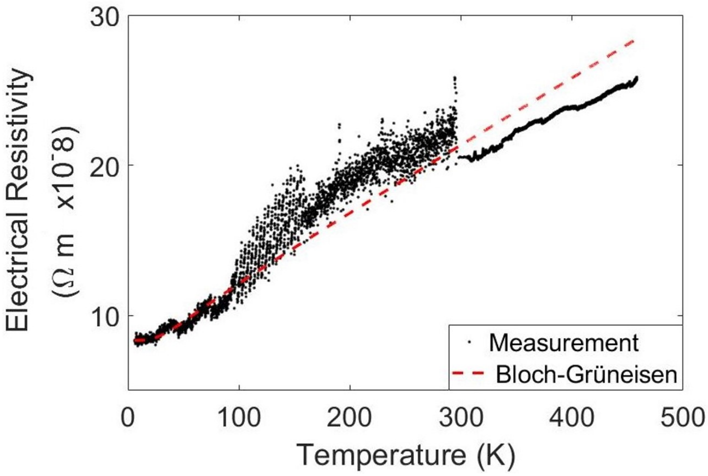

Figure 6.5: AC Electrical resistivity (at 2.5 GHz) of AlSi10Mg microwave resonant cavity as a function of temperature.

Figure 6.5 shows the microwave resistivity calculated from simulated G and measured Q factors. The error associated with measuring the bandwidth in our system can be as large as 1 KHz with a 2.5 GHz resonant frequency [192], which is on the same scale as the coefficient of resistivity, typically 3.9 $\times 10^{-3}$ K^{-1} for aluminium. Therefore extracting this coefficient is not possible. This error makes the Q factor data noisy, however Figure. 6.5 is able to show a general trend of increasing resistivity with increasing temperature. Also plotted on Figure 6.5 is the calculated Bloch-Grüneisen model for resistivity against temperature. In addition, this is a high frequency measurement of resistivity, so the poor surface finish is also contributing to the high resistivity values at low temperature compared with pure and machined aluminium.

Plotting the gradient of the frequency shift as per (6.12) produces a plot of the true CTE, displayed in Figure 6.6. The diamond markers indicate the value for CTE specified in the Renishaw PLC datasheet for AlSi10Mg [94], which matches closely with the recorded data and agrees well with the fitted Debye curve. Observed CTE values between 260 - 390 K deviate from the curve fit. In addition to the deviation arising from the cavity design, there is also uncertainty due to cooling / heating gradients at the start of each ramp, prior to the material reaching a thermal equilibrium. The volume of metal comprising the cavity

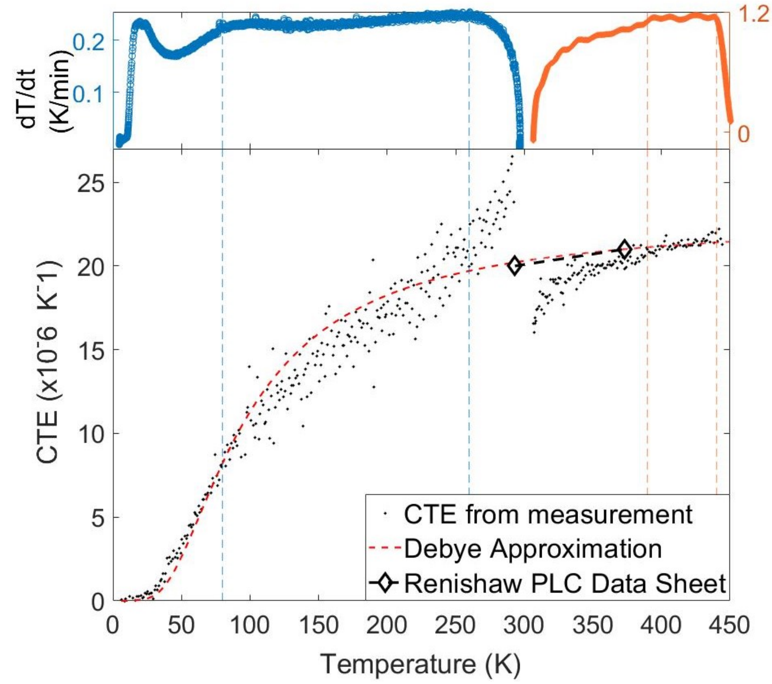

Figure 6.6: True coefficient of linear thermal expansion as a function of temperature, derived from the resonant frequency measurements of the PBF cylindrical cavity in TM_{010} mode. The curve fit uses the Debye approximation for thermal behaviour in solids [186]. Reprinted from [26] ©2019 Gumbleton et al (CC-BY).

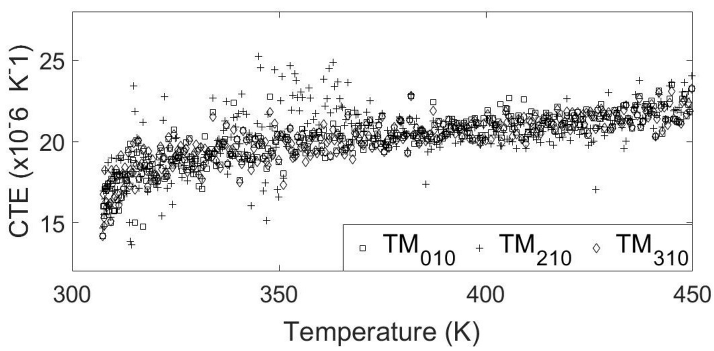

Figure 6.7: True Coefficient of thermal expansion. Derived from resonant frequency measurements for TM_{010}, TM_{210} and TM_{310} cavity modes. Reprinted from [26] ©2019 Gumbleton et al. (CC-BY).

experiences a thermal lag and takes some time to reach thermal equilibrium. The inset curves for temperature gradient with respect to time ($\mathrm{d}T/\mathrm{d}t$) show regions of non-linearity between 0 – 80 K, 260 – 300 K, and 310 – 390 K. However, the Debye model [186] provides a good fit despite the non-linear regions. CTE at low temperatures exhibits a T^3 thermal dependence and at very low temperatures the vibrations that relate to lattice energy levels, and hence to thermal expansion, starts to freeze out [186] causing CTE to tend to zero. While at high temperatures CTE becomes approximately constant, as per the Dulong-Petit law [186], where it can be observed that CTE values between 293 – 393 K are lower than those stated in literature for bulk aluminium alloy 6063 (23×10^{-6} K^{-1}) [195]. 6000 series aluminium alloys are commonly utilised in the manufacture of microwave resonant structures due to their high electrical conductivity [99].

Figure 6.7 shows the CTE for TM_{010}, TM_{210} and TM_{310} modes between 310 K and 450 K. Each measured mode produces a similar CTE curve. This suggests that field distribution within the cavity, at least for low power applications, does not have an affect on CTE and is a good indicator of material homogeneity.

The results outlined above show the utilisation of a little known microwave technique as an alternative to traditional methods of measuring CTE. The technique demonstrates the use of microwave cavity resonators made from the material under test since they are very susceptible to temperature. Previous studies [192, 193] have shown the extraction of CTE using this method for aluminium and copper has been achieved owing to the ability to measure frequency with very low error. While this approach requires that the metal be fabricated into a specific geometry, the advantage of AM is that such unconventional shapes can be easily realised.

Traditional CTE measurement techniques, such as push rod dilaometry and thermo-mechanical analysis, have also been successfully used to evaluate thermal expansion in PBF materials (Invar36, Stainless steel 316L and Ti-6Al-4V) between 280 – 1200 K [196, 197]. Push rod dilatometry [198] uses the linear displacement of a rod placed against the sample under test to evaluate CTE. Thermo-mechanical analysis [199] is closely related to dialometry, however, uses a force equalisation technique to measure changes in length. In both techniques, commercially available equipment can provide a resolution of ~10 nm [200]. A more precise CTE measurement technique is interferometry [201], an optical technique that uses changes in reflected 'fringe' patterns to infer changes in geometry. However, due to the requirement for highly reflective surfaces and complex alignment processes, interferometry is more often utilised to measure the rod displacement in dilalometry systems, culminating in resolutions as small as ~0.25 nm [202]. In all of the above mentioned traditional techniques, strict sample preparation criteria must be observed with sample volume normally required in low cm^3 range, while often requiring an additional material of known CTE for calibrating out the CTE of the measurement system itself. The main limitation of this study is the thermal lag present due to non-linear heating and cooling rates, where the cavity fails to reach a thermal equilibrium during the early stages of each temperature ramp. This may be overcome through finer control of the temperature gradients, but with much slower, linear heating/cooling profiles.

6.5 Conclusions and Further Work

This chapter has used a fractional frequency shift method to evaluate the true CTE for PBF AlSi10Mg metal, fabricated into a cylindrical microwave resonant structure. This technique has allowed the material to be characterised across an extreme temperature range as a functional component as appropriate for space-based components. In addition, the single part geometry negates the need for calibration pieces and small geometrical material samples. Measured CTE results for the cavity material are found to match well with the CTE value reported in the manufactures' data sheet $\sim 20\times10^{-6}$ K^{-1} over the specified temperature range.

Further work around this topic includes a study of the process parameters that can affect the CTE value of the material. Several studies have already shown that laser energy density [196] has an optimal level for low thermal expansion, while hatch spacing has an effect of the heat transfer characteristics [203] which may also affect CTE. Using the TM_{mn0} resonant modes means that only the radial expansion is evaluated, therefore CTE in various orientations can be observed through manufacturing a cavity at different angles from the base plate. This will allow exploration of the effects of layer boundaries on thermal expansion.

CHAPTER 7
FINAL SUMMARY AND FURTHER WORK

This work presents a focused investigation into the use of AlSi10Mg alloy within PBF process, specifically for microwave applications. A novel measurement fixture has been proposed and is utilised within several experimental studies relating to microwave surface resistance. Further studies on the effect of PFB process parameters and available post-processing treatments have been completed. Finally, a study is presented looking at the thermal expansion of AlSi10Mg produced by PBF within a scenario typical of satellite applications.

This final chapter provides a concise summary of the work completed and suggestions for additional studies that would be of interest to the wider PBF / microwave communities, based on the results presented in this thesis.

7.1 Measurement of Microwave Surface Resistance

This thesis presents a novel measurement fixture based upon a parallel plate waveguide resonator. The key feature of this implementation is its ability to excite two orthogonal resonant modes in which one directional surface currents are induced in a flat planar conductive sample. Analysis of the measured Q factors allows for extraction of the materials' R_{S}.

Several mechanical adaptations would be beneficial for the improvement of this fixture. In particular, the indium gasket required for PBF sample measurements can be time consuming and inconsistent in their implementation. A groove surrounding the cavity could be fitted to allow partial submersion of an indium wire. This would help speed up the gasket fitting process and provide a consistent finish. Additionally, the difference in hardness between the aluminium cavity and the steel screws has caused threads to wear and the fixing of PBF samples to become a relatively sensitive process. It would be better to replace these fittings with through-bolts to allow for the measured application of torque and increase the longevity of the fixture.

From a microwave perspective, further improvements could be gained by the redesign of the supporting frame such that the requirement for nylon screws could be avoided and further PTFE removed from areas of high electric field.

7.2 Process parameters Optimisation

Two studies are presented on the use of PBF process parameter to influence R_{S} values. A link has been established between laser power, surface roughness and surface resistance in AlSi10Mg for downward facing surfaces. This proves that the optimisation of these processes for microwave applications is possible, although much more work is still required. A second positive outcome is linked to the measured isotropy in R_{S} measured for AlSi10Mg, built in a horizontal orientation, whilst implementing artificially induced 'worst' and 'best case' roughness profiles.

Further work is required to investigate the influence of such elevated downskin laser power on the mechanical properties of the produced part. New copper alloy powders are now become more processable and also merit investigation into their use and optimisation for passive microwave components. Fundamentally there are many process parameters that have not been studied here, hatch distance and laser track speed for example, which may have a contribution to microwave performance.

7.3 Post Processing Treatments

A selection of post-processing treatments have been utilised and their effect on microwave loss measured for planar metal samples. Perhaps not surprisingly, silver plating of AlSi10Mg PBF parts brought the measured R_{S} to comparable levels with copper PCB, while treatments associated with deburring the rough PBF surfaces had mixed results. Bead blasting, for example, increased R_{S} in every case within this study, however previously publish literature had suggested the opposite. This highlights the uncontrolled nature of the process, where distance from the part, tool pressure and manual operation can all effect the final outcome. A significant finding is that the 'mirror' polishing of PBF samples are directly comparable with a traditionally machined Al6082 sample; this suggests that the inclusion of silicon in the chemical composition is not having a significant negative effect of electrical conductivity and that the excess loss exhibited by PBF microwave components is primarily due to the surface finish.

Further work would include the direct comparison to AlSi10Mg processed by other techniques, rather than comparing to the different alloy Al6082. There are also other post processing techniques that would be suitable for finishing internal walls that have not been explored here, including chemical polishing and abrasive slurry finishing.

7.4 Thermal Expansion coefficient

This thesis has presented the results for the true CTE of AlSi10Mg produced by PBF. The temperature range over which CTE was measured is extreme, much greater than the typical thermal cycling experienced by satellite components. Furthermore, CTE was measured using a passive microwave device, which could be incorporated into a satellite communication system, without the need for additional hardware or complex calibration.

To increment this work, studies could be performed on devices manufactured in different build orientations such that the radial CTE described in this thesis can be extracted. Additionally, there are several process parameters that have been reported to effect CTE, such as hatch spacing, and merit further investigation.

REFERENCES

[1] ASTM F2792-10, ‘Standard terminology for additive manufacturing technologies’, ASTM International, 2010.

[2] M. Schmidt et al., ‘Laser based additive manufacturing in industry and academia’, *CIRP Annals*, vol. 66, no. 2, pp. 561–583, 2017.

[3] A. Uriondo, M. Esperon-Migues, and S. Perinpanayagam, ‘The present and future of additive manufacturing in the aerospace sector: A review of important aspects’, *Proc. IMechE Part G: J. Aerospace Engineering*, vol. 229, no. 11, pp. 2132–2147, 2015.

[4] P. Unwin et al., ‘National strategy 2018-25’, Additive Manufacturing UK, 2017.

[5] Innovate UK, ‘A landscape for the future of high value manufacturing in the UK’, Technology Strategy Board, 2017.

[6] Materials KTN, ‘Shaping our national competency in additive manufacturing’, Additive manufacturing special interest group for Technology Strategy Board, 2014.

[7] M. Attaran, ‘The rise of 3-D printing: The advantages of additive manufacturing over traditional manufacturing’, *Business Horizons*, vol. 60, pp. 677–688, 2017.

[8] D. Böckin and A. Tillman, ‘Environmental assessment of additive manufacturing in the automotive industry’, *Journal of Cleaner Production*, vol. 226, pp. 977–987, 2019.

[9] D. E. Cooper, M. Stanford, K. A. Kibble, and G. J. Gibbons, ‘Additive manufacturing for product improvement at red bull technology’, *Materials Design*, vol. 41, pp. 226–230, 2012.

[10] N. T. Aboulkhair, N. M. Everitt, I. Ashcroft, and C. Tuck, ‘Reducing porosity in AlSi10Mg parts processed by selective laser melting’, *Additive Manufacturing*, vol. 1-4, pp. 77–86, Oct. 2014.

[11] C. Emmelmann, P. Sander, J. Kranz, and E. Wycisk, ‘Laser additive manufacturing and bionics: Redefining lightweight design’, *Physics Procedia*, vol. 12, pp. 364–368, 2011, Lasers in Manufacturing 2011 - Proceedings of the Sixth International WLT Conference on Lasers in Manufacturing.

[12] M. Javidani, J. Arrenguin-Zavala, J. Danovitch, Y. Tian, and M. Brochu, ‘Additive manufacturing of AlSi10Mg alloy using direct energy deposition: Microstructure and hardness characterization’, *J. Therm. Spray Tech.*, vol. 26, pp. 587–597, 2017.

[13] L. Zhou et al., 'Microstructure, precipitates and hardness of selectively laser melted AlSi10Mg alloy before and after heat treatment', *Materials Characterization*, vol. 143, pp. 5–17, 2018.

[14] M. Ghasri-Khouzani et al., 'Comparing microstructure and hardness of direct metal laser sintered AlSi10Mg alloy between different planes', *J. of Manufacturing Processes*, vol. 37, pp. 274–280, 2019.

[15] A. Bin Anwar and Q. Pham, 'Selective laser melting of AlSi10Mg: Effects of scan direction, part placement and inert gas flow velocity on tensile strength', *J. of Materials Processing Technology*, vol. 240, pp. 388–396, 2017.

[16] B. Chen et al., 'Strength and strain hardening of a selective laser melted AlSi10Mg alloy', *Scipta Materialia*, vol. 141, pp. 45–49, 2017.

[17] L. Hitzler et al., 'Direction and location dependency of selective laser melted AlSi10Mg specimens', *J. of Materials Processing Technology*, vol. 243, pp. 48–61, 2017.

[18] C. M. Laursen et al., 'Relationship between ductility and the porosity of additively manufactured AlSi10Mg', *Materials Science and Engineering: A*, vol. 795, p. 139 922, 2020.

[19] F. Nalli, L. Cortese, and F. Concli, 'Ductile damage assessment of Ti6Al4V, 17-4PH and AlSi10Mg for additive manufacturing', *Engineering Fracture Mechanics*, vol. In Press, 2020.

[20] H. Bian, K. Aoyagi, Y. Zhao, C. Maeda, T. Mouri, and A. Chiba, 'Microstructure refinement for superior ductility of Al−Si alloy by electron beam melting', *Additive Manufacturing*, vol. 32, p. 100 982, 2020.

[21] R. Sorrentino and O. Peverini, 'Additive manufacturing: A key enabling technology for next generation microwave and millimeter-wave systems', *Proc. of the IEEE*, vol. 104, no. 7, pp. 1361–1366, 2016.

[22] H. Williams and E. Butler-Jones, 'Additive manufacturing standards for space resource utilization', *Additive Manufacturing*, vol. 28, pp. 676–681, 2019.

[23] R. Gumbleton, J. A. Cuenca, S. Hefford, K. Nai, and A. Porch, 'Measurement technique for the microwave surface resistance of additive manufactured metals', *IEEE Transactions on Microwave Theory and Techniques*, vol. 69, no. 1, pp. 189–197, 2021.

[24] R. Gumbleton, R. Batson, K. Nai, and A. Porch, 'Effect of build orientation and laser power on the microwave performance of metal additive manufactured components', *IEEE Access*, vol. 9, pp. 44 514–44 520, 2021.

[25] R. Gumbleton, K. Nai, S. Hefford, and A. Porch, 'Effects of post-processing treatments on the microwave performance of additively manufactured

samples', in *2019 Proceedings of the 13th European Conference on Antennas and Propagation*, Krakow: IEEE, 2019.

[26] R. Gumbleton, J. A. Cuenca, G. M. Klemencic, N. Jones, and A. Porch, 'Evaluating the coefficient of thermal expansion of additive manufactured AlSi10Mg using microwave techniques', *Additive Manufacturing*, vol. 30, p. 100 841, 2019.

[27] E. Atzeni and A. Salmi, 'Economics of additive manufacturing for end-usable metal parts', *Int. J. Adv. Manuf. Technol.*, vol. 62, pp. 1147–1155, 2012.

[28] M. K. Niaki, S. A. Torabi, and F. Nonino, 'Why manufacturers adopt additive manufacturing technologies: The role of sustainability', *Journal of Cleaner Production*, vol. 222, pp. 381–392, 2019.

[29] I. Gibson, D. Rosen, and B. Stucker, *Additive Manufacturing Technologies*, 2nd ed. Springer, 2015.

[30] J. C. Najmon, S. Raeisi, and A. Tovar, 'Review of additive manufacturing technologies and applications in the aerospace industry', in *Additive Manufacturing for the Aerospace Industry*, Elsevier, 2019, pp. 7–31.

[31] Studio System Data Sheet, 'Printer specifications', Desktop Metal, 2019.

[32] G. B. Kim et al., 'Three-dimensional printing: Basic principles and applications in medicine and radiology', *Korean J Radiol.*, vol. 17, no. 2, pp. 182–197, 2016.

[33] L. N. Y. Cao and D. Y. H. Pai, 'Real-time measurements of particle geometric surface area by the weighted sum method on a university campus', *Aerosol and Air Quality Research*, vol. 20, pp. 1569–1581, 2020.

[34] A. Genc, I. Bahadir Basyigit, T. Goksu, and S. Helhel, 'Investigation of the performances of X-Ku band 3D printing pyramidal horn antennas coated with the different metals', in *Proceedings of the 10th International Conference on Electrical and Electronics Engineering*, Bursa: IEEE, 2017.

[35] E. G. Geterud, P. Bergmark, and J. Yang, 'Lightweight waveguide and antenna components using plating on plastics', in *Proceedings of the 7th European Conference on Antennas and Propagation*, Gothenburg: IEEE, 2013.

[36] V. Gjokaj, P. Chahal, J. Papapolymerou, and J. D. Albrecht, 'A novel 3D printed vivaldi antenna utilizing a substrate integrated waveguide transition', in *2017 IEEE International Symposium on Antennas and Propagation*, San Diego, 2017, pp. 1253–1254.

[37] S. Alkaraki et al., 'Compact and low-cost 3-D printed antennas metalized using spray-coating technology for 5G mm-wave communication systems', *IEEE Antennas and Wireless Propagation Letters*, vol. 17, no. 11, pp. 2051–2055, 2018.

[38] D. Helena, A. Ramos, T. Varum, and J. N. Matos, 'Inexpensive 3D-printed radiating horns for customary things in IoT scenarios', in *proceedings of 14th European Conference on Antennas and Propagation (EuCAP)*, Copenhagen, 2020.

[39] P. A. Booth, M. Skeen, and S. Stirland, 'Low cost, short lead-time feed chain components for multi-beam antennas', in *Proceedings of 3rd European Conference on Antennas and Propagation (EuCAP)*, Berlin, 2009, pp. 853–857.

[40] M. Kilian, A. Schinagl-Weiß, P. Kohl, A. Sommer, C. Hartwanger, and M. Schneider, 'Additive layer manufactured waveguide RF components', in *Proceedings of 49th European Microwave Conference (EuMC)*, Paris, 2019, pp. 790–793.

[41] M. Kilian et al., 'Ku-band sfb-cluster manufactured by additive manufacturing techniques', in *Proceedings of the 13th European Conference on Antennas and Propagation*, Krakow: IEEE, 2019.

[42] P. A. Booth and E. Valles Lluch, 'Enhancing the Performance of Waveguide Filters Using Additive Manufacturing', *Proceedings of the IEEE*, vol. 105, no. 4, pp. 613–619, Apr. 2017.

[43] ——, 'Realising advanced waveguide bandpass filters using additive manufacturing', *IET Microwaves, Antennas & Propagation*, vol. 11, no. 14, pp. 1943–1948, Nov. 19, 2017.

[44] J. A. Lorente, M. M. Mendoza, A. Z. Petersson, L. Pambaguian, A. A. Melcon, and C. Ernst, 'Single part microwave filters made from selective laser melting', in *Proceedings of 2009 European Microwave Conference (EuMC)*, Rome, 2009, pp. 1421–1424.

[45] M. Kilian, C. Hartwanger, M. Schneider, and M. Hatzenbichler, 'Waveguide components for space applications manufactured by additive manufacturing technology', *IET Microwaves, Antennas and Propagation*, vol. 11, no. 14, pp. 1949–1954, 2017.

[46] Y. Cailloce, P. Hourlay, F. Lebrun, and B. Palacin, 'Additive manufacturing of Ku band horn antennas for telecommunications space applications', in *Proceedings of 12th European Conference on Antennas and Propagation (EuCAP)*, London, 2018.

[47] F. T. Talom and S. Turpault, 'Additive manufacturing for RF microwave devices: Design, performances and treatments improvement evaluations', in *Proceedings of International Conference on Electromagnetics in Advanced Applications (ICEAA)*, Verona, 2017, pp. 1473–1476.

[48] M. Hollenbeck, R. Smith, C. Cathey, and J. Opra, 'X-band integrated printed antenna measurement', in *Proceedings of IEEE/MTT-S International Microwave Symposium (IMS)*, Philadelphia, 2018, pp. 149–151.

[49] M. W. Elsallal et al., 'An additively manufactured, all-metallic frequency-scaled ultra-wide spectrum element (AM-FUSE) active electronically scanned array (AESA) for space-borne applications', in *Proceedings of IEEE International Symposium on Phased Array System and Technology (PAST)*, Waltham, 2019.

[50] F. Calignano et al., 'High-performance microwave waveguide devices produced by laser powder bed fusion process', *Procedia CIRP*, vol. 79, pp. 85–88, 2019.

[51] O. A. Peverini, M. Lumia, F. Calignano, G. Addamo, M. Lorusso, E. P. Ambrosio, D. Manfredi, and G. Virone, 'Selective Laser Melting Manufacturing of Microwave Waveguide Devices', *Proceedings of the IEEE*, vol. 105, no. 4, pp. 620–631, Apr. 2017.

[52] M. Hollenbeck, K. Wamick, C. Cathey, J. Opra, and R. Smith, 'Selective laser melting aluminum waveguide attenuation at k-band', in *Proceedings of IEEE MTT-S International Microwave Symposium (IMS)*, Honololu, 2017, pp. 45–47.

[53] M. Salek, X. Shang, R. C. Roberts, M. J. Lancaster, F. Boettcher, D. Weber, and T. Starke, 'W-Band waveguide bandpass filters fabricated by micro laser sintering', *IEEE Transactions on Circuits and Systems II: Express Briefs*, vol. 66, no. 1, pp. 61–65, 2019.

[54] X. Shang, P. Penchev, C. Guo, M. J. Lancaster, S. Dimov, Y. Dong, M. Favre, M. Billod, and E. de Rijk, 'W-Band waveguide filters fabricated by laser micromachining and 3-D printing', *IEEE Transactions on Microwave Theory and Techniques*, vol. 64, no. 8, pp. 2572–2580, 2016.

[55] M. D'Auria et al., '3-d printed metal-pipe rectangular waveguides', *IEEE Transactions on components, packaging and manufacturing technology*, vol. 5, no. 9, pp. 1339–1349, 2015.

[56] J. Rao, K. Nai, and J. Hong, '3-d metal printed inline quasi-elliptic bandpass filter', in *Proceedings of 50th European Microwave Conference (EuMC)*, Utrecht, 2021, pp. 894–896.

[57] F. Zhang et al., '3-d printed slotted spherical resonator bandpass filters with spurious suppression', *IEEE Access*, vol. 7, pp. 128 026–128 034, 2019.

[58] P. A. Booth, R. Roberts, M. Szymkiewicz, and C. Hartwanger, 'Using additive manufacturing for feed chain and other passive microwave components', in *Proceedings of 11th European Conference on Antennas and Propagation (EuCAP)*, Paris, 2017, pp. 558–562.

[59] N. Clark, S. Hefford, and A. Porch, 'Effect of build orientation and surface finish on surface resistance in microwave components produced by Selective Laser Melting', in *2017 47th European Microwave Conference (EuMC)*, Nuremburg: IEEE, Oct. 2017, pp. 508–511.

[60] E. Hammerstad and F. Bekkadal, *Microstrip Handbook*. Univ. Trondhiem, 1975.

[61] L. Tsang, X. Gu, and H. Braunisch, 'Effects of random rough surface on absorption by conductors at microwave frequencies', *IEEE Microwave and Wireless Components Letters*, vol. 16, no. 4, pp. 221–223, 2006.

[62] T. Iwai, D. Mizutani, and M. Tani, 'Measurement of high-frequency conductivity affected by conductor surface roughness using dielectric rod resonator method', in *2015 IEEE International Symposium on Electromagnetic Compatibility (EMC)*, Dresden, 2015, pp. 634–639.

[63] S. P. Morgan, 'Effect of surface roughness on eddy current losses at microwave frequencies', *Journal of Applied Physics*, vol. 20, no. 4, pp. 352–362, 1949.

[64] F. Yu and P. Nagy, 'Numerical method for calculating the apparent eddy current conductivity loss on randomly rough surfaces', *Journal of Applied Physics*, vol. 95, no. 12, pp. 8340–8351, 2004.

[65] A. Sain and K. L. Melde, 'Characterizing the impact of conductor surface roughness on CB-CPW behavior via reduced computational complexity', in *Proceedings of IEEE 21st Conference on Electrical Performance in Electronic Packaging and Systems*, 2012, pp. 260–263.

[66] E. Hammerstad and O. Jensen, 'Accurate models for microstrip computer-aided design', in *IEEE MTT-S International Microwave symposium Digest*, Washington, DC, USA, May 1980, pp. 407–409.

[67] S. Groiss, I. Bardi, K. Preis, and K. A. Richter, 'Parameters of lossy cavity resonators calculated by the finite element method', *IEEE Transactions on Magnetics*, vol. 32, no. 3, pp. 894–897, 1996.

[68] N. Clark, 'Microwave Methods for Additive Layer Manufacturing', PhD Thesis, Cardiff University, 2017.

[69] *COMSOL multiphysics 5.1 release highlights*, `https://uk.comsol.com/release/5.1/rf-module`, Accessed: 5 Dec 2020.

[70] B. Curran, I. Ndip, S. Guttowski, and H. Reichl, 'A methodology for combined modeling of skin, proximity, edge, and surface roughness effects', *IEEE Transactions on Microwave Theory and Techniques*, vol. 58, no. 9, pp. 2448–2455, 2010.

[71] A. Matsushima and K. Nakata, 'Power loss and local surface impedance associated with conducting rough interfaces', *Electronics and Communications in Japan, Part 2*, vol. 89, no. 1, pp. 1–10, 2006.

[72] S. Hall et al., 'Multigigahertz causal transmission line modeling methodology using a 3-D hemispherical surface roughness approach', *IEEE Transactions on Microwave Theory and Techniques*, vol. 55, no. 12, pp. 2614–2624, 2007.

[73] X. Chen, 'EM modeling of microstrip conductor losses including surface roughness effect', *IEEE Microwave and Wireless Components Letters*, vol. 17, no. 2, pp. 94–96, 2007.

[74] M. V. Lukić and D. S. Filipovic, 'Modeling of 3-D surface roughness effects with application to $\mu-coaxiallines$', *IEEE Transactions on Microwave Theory and Techniques*, vol. 55, no. 3, pp. 518–525, 2007.

[75] A. F. Hall, J. W. Reynold, and J. C. Rautio, 'Conductor profile effects on the propagation constant of microstrip transmission lines', in *Proceedings of IEEE MTT-S International Microwave Symposium (IMS)*, Anaheim, USA: IEEE, 2010.

[76] B. Curran, I. Ndip, S. Guttowski, and H. Reichl, 'On the quantification and improvement of the models for surface roughness', in *2009 IEEE Workshop on Signal Propagation on Interconnects (SPI)*, Los Alamitos, CA, USA: IEEE Computer Society, 2009.

[77] G. Gold and K. Helmreich, 'A physical surface roughness model and its applications', *IEEE Transactions on Microwave Theory and Techniques*, vol. 65, no. 10, pp. 3720–3732, 2017.

[78] P. G. Huray et al., 'Fundamentals of a 3-D 'snowball' model for surface roughness power losses', *IEEE Electromagnetic Compatibility Magazine*, vol. 9, no. 2, pp. 62–65, 2020.

[79] P. G. Huray, *The foundations of signal integrity*. John Wiley & Sons, 2010.

[80] B. Tonkin and Y. G. Proykova, 'Modular system for microwave surface impedance measurements of high-temperature superconductors', *Superconductor Science and Technology*, vol. 6, pp. 353–359, 1993.

[81] D. Cooke et al., 'Surface resistance of $YBa_2Cu_3O_7$ films deposited on $LaGaO_3$ substrates', *Applied Physics Letters*, vol. 55, no. 9, pp. 914–916, 1989.

[82] M. J. Lancaster, *Passive Microwave Device Applications of High-Temperature Superconductors*. Cambridge University Press, 1997.

[83] R. Fletcher and J. Cook, 'Measurement of surface impedance versus temperature using a generalized sapphire resonator technique', *Review of Scientific Instruments*, vol. 65, no. 8, pp. 2658–2666, 1994.

[84] J. Mazierska and C. Wilker, 'Accuracy issues in the surface resistance measurements of high temperature superconductors using dielectric resonators', *Transactions on Applied Superconductivity*, vol. 11, no. 4, pp. 4140–4147, 2001.

[85] B. Hakki and P. Coleman, 'A dielectric resonator method of measuring inductive capacities in the millimeter range', *Trans. Micro. Theor. Tech.*, vol. 8, no. 4, pp. 402–410, 1960.

[86] S. Hefford, 'Microwave Processing in Additive Manufacturing', PhD Thesis, Cardiff University, 2019.

[87] S. A. Reible and C. W. Wilker, 'Parallel plate resonator for accurate RF surface loss measurements', *IEEE Trans. Magn.*, vol. 27, no. 2, pp. 2813–2816, 1991.

[88] F. Gao, M. V. Klein, J. Kruse, and M. Feng, 'Mode coupling in superconducting parallel plate resonator in a cavity with outer conductive enclosure', *IEEE Trans. Microw. Theor. Techn.*, vol. 44, no. 6, pp. 944–952, 1996.

[89] R. C. Taber, 'A parallel plate resonator technique for microwave loss measurements on superconductors', *Rev. Sci. Instrum.*, vol. 61, no. 8, pp. 2200–2206, 1990.

[90] J. Krupka and J. Mazierska, 'Improvement of accuracy in measurements of the surface resistance of superconductors using dielectric resonators', *Transactions on Applied Superconductivity*, vol. 8, no. 4, pp. 164–167, 1998.

[91] S. Hefford, N. Clark, R. Gumbleton, and A. Porch, 'Lift-off dielectric resonator for the microwave surface resistance measurement of metal plates', *IEEE Transactions on Instrumentation and Measurement*, vol. 70, p. 8 002 208, 2021.

[92] A. Porch, 'Microwave Impedance', in *Handbook of Superconducting Materials*, D. Cardwell and D. Ginle, Eds., vol. 2, Bristol: IOP Publishing, 2003, pp. 1415–1435.

[93] Renishaw PLC. (2021). Accessed: 31 Mar 2021, [Online]. Available: `https://www.renishaw.com/en/metal-additive-manufacturing-3d-printing-systems--37011`.

[94] ——, 'AlSi10Mg-0403 powder for additive manufacturing', 2015.

[95] D. Wang et al., 'Mechanisms and characteristics of spatter generation in SLM processing and its effect on the properties', *Materials and Design*, vol. 117, pp. 121–130, 2017.

[96] Renishaw PLC, *Metal powders for AM*, Accessed: 21 Feb 2021. [Online]. Available: `https://www.renishaw.com/en/metal-powders-for-am--31457`.

[97] L. Cordova, M. Campos, and T. Tinga, 'Revealing the effects of powder reuse for selective laser melting by powder characterization', *JOM*, vol. 71, pp. 1062–1072, 2019.

[98] N. T. Aboulkhair, I. Maskery, C. Tuck, I. Ashcroft, and N. M. Everitt, 'On the formation of alsi10mg single tracks and layers in selective laser melting: Microstructure and nano-mechanical properties', *Journal of Materials Processing Technology*, vol. 230, pp. 88–98, 2016.

[99] N. Clark, N. Jones, R. Setchi, and A. Porch, 'Particle size characterisation of metals powders for Additive Manufacturing using a microwave sensor', *Powder Technology*, vol. 327, pp. 536–543, Mar. 1, 2018.

[100] L. Rickenbacher, A. Spierings, and K. Wegener, 'An integrated cost-model for selective laser melting (SLM)', *Rapid Prototyping Journal*, vol. 19, no. 3, pp. 208–214, 2013.

[101] Renishaw PLC, 'Quantam material editor 2019 v5.1; quick start guide', 2019.

[102] L. Hitzler, M. Merkel, W. Hall, and A. Öchsner, 'A review of metal fabricated with laser- and powder-bed based additive manufacturing techniques: Process, nomenclature, materials, achievable properties, and its utilization in the medical sector', *Advanced Engineering Materials*, vol. 20, no. 5, p. 1 700 658, 2018.

[103] C. K. Chau, M. V. Matham, and Y. Kim, *Lasers in 3D Printing and Manufacturing*. World Scientific, 2017.

[104] W. Xiong et al., 'Effect of selective laser melting parameters on morphology, microstructure, densification and mechanical properties of supersaturated silver alloy', *Materials and Design*, vol. 170, p. 107 697, 2019.

[105] E. van de Ven, R. Mass, C. Ayas, M. Langelaar, and F. van Keulen, 'Continuous front propagation-based overhang control for topology optimization with additive manufacturing', *Structural and Multidisciplinary Optimization*, vol. 57, pp. 2075–2091, 2018.

[106] Swiss Plastics Platform, *Equipment for 3D print finishing*, Accessed: 28 Feb 2021. [Online]. Available: https://www.swissplasticsplatform.com/en/showcase/en/equipment-for-3d-print-finishing-np-2.

[107] M. Leary et al., 'Selective laser melting (SLM) of AlSi12Mg lattice structures', *Materials and Design*, vol. 98, pp. 344–357, 2016.

[108] D. Wang, Y. Yand, Z. Yi, and X. Su, 'Research on the fabricating quality optimization of the overhanging surface in SLM process', *Int. J. Adv. Manuf. Technol.*, vol. 63, pp. 1471–1484, 2013.

[109] H. Chen, D. Gu, J. Xiong, and M. Xia, 'Improving additive manufacturing processability of hard-to-process overhanging structure by selective laser melting', *Journal of Materials Processing Technology*, vol. 250, pp. 99–108, 2017.

[110] J. C. Fox, S. P. Moylan, and B. M. Lane, 'Effect of Process Parameters on the Surface Roughness of Overhanging Structures in Laser Powder Bed Fusion Additive Manufacturing', in *Procedia CIRP*, vol. 45, 2016, pp. 131–134.

[111] X. Han, H. Zhu, X. Nie, G. Wang, and X. Seng, 'Investigation on selective laser melting AlSi10Mg cellular lattice strut: Molten pool morphology,

surface roughness and dimensional accuracy', *Materials*, vol. 11, no. 3, p. 392, 2018.

[112] Z. Xiang, L. Wang, C. Yang, M. Yin, and G. Yin, 'Analysis of the quality of slope surface in selective laser melting process by simulation and experiments', *Optik*, vol. 176, pp. 68–77, 2019.

[113] A. Staub, A. B. Spierings, and K. Wegener, 'Selective laser melting at high laser intensity: Overhang surface characterization and optimization', in *Proceedings of Direct Digital Manufacturing Conference*, Berlin, Germany, Mar. 2018.

[114] Q. Han, H. Gu, S. Soe, R. Setchi, F. Lacan, and J. Hill, 'Manufacturability of AlSi10Mg overhang structures fabricated by laser powder bed fusion', *Materials Design*, vol. 160, pp. 1080–1095, 2018.

[115] Z. Dong, Y. Liu, W. Li, and J. Liang, 'Orientation dependency for microstructure, geometric accuracy and mechanical properties of selective laser melting AlSi10Mg lattices', *J. Alloys Compd.*, vol. 791, pp. 490–500, 2019.

[116] A. Salmi and E. Atzeni, 'Residual stress analysis of thin AlSi10Mg parts produced by laser powder bed fusion', *Virtual and Physical Prototyping*, vol. 15, no. 1, pp. 49–61, 2020.

[117] K. Nai, Personal Communication.

[118] A. H. Maamoun, M. Elbestawi, G. K. Dosbaeva, and S. C. Veldhuis, 'Thermal post-processing of AlSi10Mg parts produced by Selective Laser Melting using recycled powder', *Additive Manufacturing*, vol. 21, pp. 234–247, 2018.

[119] L. Wang, X. Jiang, Y. Zhu, X. Zhu, J. Sun, and B. Yan, 'An approach to predict the residual stress and distortion during the selective laser melting of AlSi10Mg parts', *Int. J. Adv. Manuf. Technol.*, vol. 97, pp. 3535–3546, 2018.

[120] A. Inberg, D. Ashkenazi, G. Kimmel, Y. Shacham-Diamand, and A. Stern, 'Gold-silver electroless plating on laser powder-bed fusion additively printed AlSi10Mg parts', *metals*, vol. 10, p. 557, 2020.

[121] C. Y. Ho and R. Taylor, *Thermal Expansion of Solids*. ASM International, 1998.

[122] Atlas-Steels, 'Aluminium alloy data sheet 6063', Atlas Steels, Datasheet, 2013.

[123] D. King, J. Middendorf, K. Cissel, T. Key, and C. Carney, 'Selective laser melting for the preparation of an ultra-high temperature ceramic coating', *Ceramics International*, vol. 45, pp. 2466–2473, 2, Part A Feb. 1, 2019.

[124] L. P. Lam, D. Q. Zhang, Z. H. Liu, and C. K. Chua, ‘Phase analysis and microstructure characterisation of AlSi10Mg parts produced by Selective Laser Melting’, *Virtual and Physical Prototyping*, vol. 10, no. 4, pp. 207–215, Oct. 2, 2015.

[125] V. Franke. (2018). ‘Burr’. Accessed: 01 April 2021, [Online]. Available: `https://doi.org/10.1007/978-3-642-35950-7_6393-4`.

[126] A. H. Maamoun, M. A. Elbestawi, and S. C. Veldhuis, ‘Influence of shot peening on AlSi10Mg parts fabricated by additive manufacturing’, *J. Manuf. Mater. Process.*, vol. 2, no. 3, p. 40, 2018.

[127] M. F. Da Silva, K. Shimizu, K. Kobayashi, P. Skeldon, G. Thompson, and G. Wood, ‘On the nature of the mechanically polished aluminium surface’, *Corrosion Science*, vol. 37, no. 9, pp. 1511–1514, 1995.

[128] H. Li, D. Walker, X. Zheng, G. Yu, C. Reynolds, W. Zhang, and T. Li, ‘Advanced techniques for robotic polishing of aluminum mirrors’, in *Proceedings of Optical Fabrication, Testing, and Metrology VI*, vol. 10692, Frankfurt: SPIE, 2018, pp. 152–163.

[129] J. Damon et al., ‘Process dependent porosity and the influence of shot peening on porosity morphology regarding selective laser melted AlSi10Mg parts’, *Additive Manufacturing*, vol. 20, pp. 77–89, 2018.

[130] M. Kahlin et al., ‘Improved fatigue strength of additively manufactured ti6al4v by surface post processing’, *International Journal of Fatigue*, vol. 134, p. 105 497, 2020.

[131] O. Addamo et al., ‘Experimental research activity on additive manufacturing of microwave passive waveguide components’, in *Proceedings of the 47th European Microwave Conference*, Nuremberg: IEEE, 2017.

[132] D. Pozar, *Microwave Engineering*, 3rd ed. Wiley, 1998.

[133] A. Porch, ‘Microwave resonator analysis’, 2012.

[134] P. J. Petersan and S. M. Anlaget, ‘Measurement of resonant frequency and quality factor of microwave resonators: Comparison of methods’, *Journal of Applied Physics*, vol. 84, no. 6, pp. 3392–3402, 1998.

[135] O. O. Klein, S. Donovan, M. Dressel, and G. Grüner, ‘Microwave cavity perturbation technique: Part I: Principles’, *International Journal of Infrared and Millimeter Waves*, vol. 14, no. 12, pp. 2423–2457, 1993.

[136] S. Donovan, O. O. Klein, M. Dressel, K. Holczer, and G. Grüner, ‘Microwave cavity perturbation technique: Part II: Experimental scheme’, *International Journal of Infrared and Millimeter Waves*, vol. 14, no. 12, pp. 2459–2489, 1993.

[137] M. Dressel, O. O. Klein, S. Donovan, and G. Grüner, 'Microwave cavity perturbation technique: Part III: Applications', *International Journal of Infrared and Millimeter Waves*, vol. 14, no. 12, pp. 2489–2517, 1993.

[138] R. G. Carter, 'Accuracy of microwave cavity perturbation measurements', *IEEE Transactions on Microwave Theory and Techniques*, vol. 49, no. 5, pp. 918–923, 2001.

[139] J. Cuenca, 'Characterisation of powders using microwave cavity perturbation', PhD Thesis, Cardiff University, 2015.

[140] J. Krupka, 'Measurements of the complex permittivity of low loss polymers at frequency range from 5 ghz to 50 ghz', *IEEE Microwave and Wireless Components Letters*, vol. 26, no. 6, pp. 464–466, 2016.

[141] C. A. Valagiannopoulos and N. K. Uzunoglu, 'Rigorous computation of green's function of a parallel-plate waveguide with a tapered wall', *Electromagnetics*, vol. 29, no. 3, pp. 203–219, 2009.

[142] Photonic-Cleaning, 'First contact polymer: Data sheet', Photonic-Cleaning, 2017.

[143] S. J. Haefner, 'Alternating-current resistance of rectangular conductors', *Proceedings of the Institute of Radio Engineers*, vol. 42, no. 4, pp. 434–447, 1937.

[144] K. Gupta et al., *Microstrip Lines and Slotlines*. Artech House, 1996.

[145] E. Maxwell, 'Conductivity of metallic surfaces at microwave frequencies', *Journal of Applied Physics*, vol. 18, no. 7, pp. 629–638, 1947.

[146] B. Benarabi, F. Kahlouche, B. Bayard, A. Chavanne, and J. Sautel, 'Microwave characterization of electrical conductivity of composite conductors by half-wavelength coplanar resonator', *Progress in electromagnetics research letters*, vol. 60, pp. 73–80, 2016.

[147] P. Dankov, S. Kamenopolski, V. Peshlov, and R. Traykov, 'Determination of equivalent conductivity of metallized plastic antenna elements in Ka band', in *in proceedings of 2016 Global Symposium on Millimeter Waves (GSMM) & ESA Workshop on Millimetre-Wave Technology and Applications*, Espoo, 2016, pp. 1–4.

[148] J. V. Manca et al., 'Localized monitoring of electromigration with early resistance change measurements', *Microelectronics Reliability*, vol. 38, no. 4, pp. 641–650, 1998.

[149] R. Faraji-Dana and Y. Leonard Chow, 'The current distribution and ac resistance of a microstrip structure', *IEEE Transactions on Microwave Theory and Techniques*, vol. 38, no. 9, pp. 1268–1277, 1990.

[150] ——, ‘Edge condition of the field and a.c. resistance of a rectangular strip conductor’, *IEE Proceedings H (Microwaves, Antennas and Propagation)*, vol. 137, pp. 133–140, 2 Apr. 1990.

[151] S. Marchetti and T. Rozzi, ‘Electric field singularities at sharp edges of planar conductors’, *IEEE Transactions on Antennas and propagation*, vol. 39, no. 9, pp. 1312–1320, 1991.

[152] R. De Smedt and J. Van Bladel, ‘Field singularities near aperture corners’, *IEE Proceedings A (Physical Science. Measurement and Instrumentation. Management and Education. Reviews)*, vol. 134, pp. 694–698, 8 Sep. 1987.

[153] S. Marchetti and T. Rozzi, ‘H-field and J-current singularities at sharp edges in printed circuits’, *IEEE Transactions on Antennas and propagation*, vol. 39, no. 9, pp. 1321–1331, 1991.

[154] J. Bladel, ‘Field singularities at the tip of a cone’, *Proceedings of the IEEE*, vol. 71, no. 7, pp. 901–902, 1983.

[155] T. Fawzi and P. Burke, ‘H-field and J-current singularities at sharp edges in printed circuits’, *IEEE Transactions on Magnetics*, vol. 10, no. 3, pp. 429–430, 1974.

[156] Advanced Connectivity Solutions, ‘Copper foils for high frequency materials’, Rogers Corporation, 2019.

[157] B. Zhang, Z. Zhan, Y. Cao, H. Gulan, P. Linner, J. Sun, T. Zwick, and H. Zirath, ‘Metallic 3-D printed antennas for millimeter and sub-millimeter wave applications’, *IEEE Transactions on Terahertz Science and Technology*, vol. 6, no. 4, pp. 592–600, 2016.

[158] K. Kempen, J. Van Humbeeck, and J. Kruth, ‘Processing AlSi10Mg by selective laser melting: Parameter optimisation and material characterisation’, *Materials Science and Technology*, vol. 31, no. 8, pp. 917–923, 2014.

[159] N. Read, W. Wang, K. Essa, and M. M. Attallah, ‘Selective laser melting of AlSi10Mg alloy: Process optimisation and mechanical properties development’, *Materials and Design*, vol. 65, pp. 417–424, 2015.

[160] K. Kempen, J. Thijs L Van Humbeeck, and J. P. Kruth, ‘Mechanical properties of AlSi10Mg produced by selective laser melting’, *Physics Procedia*, vol. 39, pp. 439–446, 2012.

[161] S. Bai, N. Perevoshchikova, Y. Sha, and X. Wu, ‘The effects of selective laser melting process parameters on relative density of the AlSi10Mg parts and suitable procedures of the Archimedes method’, *Applied Sciences*, vol. 9, p. 583, 2019.

[162] A. Lean and E. Aghion, ‘Effect of surface roughness on corrosion fatigue performance of AlSi10Mg alloy produced by selective laser melting’, *Materials Characterization*, vol. 131, pp. 188–194, 2017.

[163] S. Marimuthu, A. Triantaphyllou, M. Antar, D. Wimpenny, H. Morton, and M. Beard, 'Laser polishing of selective laser melted components', *Int. Journal of Machine Tools & manufacture*, vol. 95, pp. 97–104, 2015.

[164] W. Shi, P. Wang, Y. Liu, and G. Han, 'Experiment of process strategy of selective laser melting forming metal nonhorizontal overhanging structure', *Metals*, vol. 9, p. 385, 2019.

[165] A. Charles, A. Elkaseer, L. Thijs, V. Hagenmeyer, and S. Scholz, 'Effect of process parameters on the generated surface roughness of down-acing surfaces in selective laser melting', *Applied Sciences*, vol. 9, no. 6, p. 1256, 2019.

[166] C. Garcia, R. Rumpf, H. Tsang, and J. Barton, 'Effects of extreme surface roughness on 3d printed horn antenna', *Electronics Letters*, vol. 49, no. 12, pp. 734–736, 2013.

[167] B. Zhang and H. Zirath, 'A metallic 3-D printed e-band radio front end', *IEEE Microwave and Wireless Components Letters*, vol. 26, no. 5, pp. 331–333, 2016.

[168] T. Yang et al., 'The influence of process parameters on vertical surface roughness of AlSi10Mg parts fabricated by selective laser melting.', *Journal of Materials Processing Tech.*, vol. 266, pp. 26–36, 2019.

[169] M. Lutter-Gunther, M. Broker, T. Mayer, S. Lizak, C.Seidel, and G. Reinhart., 'Spatter formation during laser beam melting of AlSi10Mg and effects on powder quality', in *Procedia CIRP*, vol. 74, elsevier, 2018, pp. 33–38.

[170] M. T. Andani, R. Dehghani, M. R. Karamooz-Ravari, R. Mirzaeifar, and J. Ni, 'A study on the effect of energy input on spatter particles creation during selective laser melting process', *Additive Manufacturing*, vol. 20, pp. 33–43, 2018.

[171] R. M. German, *Sintering Theory and Practice*. Wiley, 1996.

[172] S. Ramo, J. R. Whinnery, and T. van Duzer, *Fields and Waves in Communication Electronics*. Wiley, 1994.

[173] C. Chen et al., 'Effect of hot isostatic pressing (HIP) on microstructure and mechanical properties of Ti6Al4V alloy fabricated by cold spray additive manufacturing', *Additive Manufacturing*, vol. 27, pp. 595–605, 2019.

[174] W. Tillmann et al., 'Hot isostatic pressing of IN718 components manufactured by selective laser melting', *Additive Manufacturing*, vol. 13, pp. 93–102, 2017.

[175] W. Possart, C. Bockenheimer, and B. Valeske, 'The state of metal surfaces after blasting treatment part I: Technical aluminium', *Surface and Interface Analysis*, vol. 33, no. 8, pp. 687–696, 2002.

[176] T. Chio, G. Huang, and S. Zhou, 'Application of Direct Metal Laser Sintering to Waveguide-Based Passive Microwave Components, Antennas, and Antenna Arrays', *Proceedings of the IEEE*, vol. 105, no. 4, pp. 632–644, Apr. 2017.

[177] K. A. Nate et al., 'A fully printed multilayer aperture-coupled patch antenna using hybrid 3d / inkjet additive manufacturing technique', in *Proceedings of the 45th European Microwave Conference*, Paris: IEEE, 2015.

[178] COMSOL. (2018). 'Waveguide iris bandpass filter'. Accessed: 18 Sep 2018, [Online]. Available: `https://uk.comsol.com/model/waveguide-iris-bandpass-filter-12737`.

[179] E. S. Rosker et al., 'Approaching the practical conductivity limits of aerosol jet printed silver', *Applied Materials and Interfaces*, vol. 12, pp. 29 684–29 691, 2020.

[180] F. Scherillo, 'Chemical surface finishing of alsi10mg components made by additive manufacturing', *Manufacturing Letters*, vol. 19, pp. 5–9, 2019.

[181] R. Smallman and R. Bishop, *Modern Physical Metallurgy and Materials Engineering*. Butterworth-Heinemann, 1999.

[182] D. Lee, *Bridge Bearings and Expansion Joints*. Chapman and Hall, 1994.

[183] J. C. Yang and K. K. de Groh, 'Materials Issues in the Space Environment', *MRS BULLETIN*, vol. 35, p. 10, 2010.

[184] D. L. Creedon, M. Goryachev, N. Kostylev, T. B. Sercombe, and M. E. Tobar, 'A 3D printed superconducting aluminium microwave cavity', *Applied Physics Letters*, vol. 109, no. 3, p. 032 601, Jul. 18, 2016.

[185] J. D. James, J. A. Spittle, S. G. R. Brown, and R. W. Evans, 'A review of measurement techniques for the thermal expansion coefficient of metals and alloys at elevated temperatures', *Measurement Science and Technology*, vol. 12, no. 3, R1–R15, Mar. 1, 2001.

[186] N. Ashcroft and N. Mermin, *Solid State Physics*. Brooks/Cole, 1976.

[187] J. Ziman, *Electrons and Phonons*. Oxford University Press, 1963.

[188] Z. Cheng, L. Liu, S. Xu, M. Lu, and X. Wang, 'Temperature Dependence of Electrical and Thermal Conduction in Single Silver Nanowire', *Scientific Reports*, vol. 5, no. 1, p. 10 718, Sep. 2015.

[189] A. D. Cahill, A. Fukasawa, and J. B. Rosenzweig, 'Measurements of Copper RF Surface Resistance at Cryogenic Temperatures for Applications to X-Band and S-Band Accelerators', in *Proceedings of International Particle Accelerator Conference (7th)*, Busen, Korea, May 2016, pp. 487–490.

[190] A. Bid, A. Bora, and A. K. Raychaudhuri, 'Temperature dependence of the resistance of metallic nanowires of diameter 15 nm : Applicability of

Bloch-Gruneisen theorem', *Physical Review B*, vol. 74, no. 3, p. 035 426, 2006.

[191] D. Cvijovic, 'The Bloch-Gruneisen function of arbitrary order and its series representations', *Theoretical and Mathematical Physics*, vol. 166, no. 1, pp. 37–42, Jan. 1, 2011.

[192] J. A. Cuenca, D. R. Slocombe, and A. Porch, 'Temperature Correction for Cylindrical Cavity Perturbation Measurements', *IEEE Transactions on Microwave Theory and Techniques*, vol. 65, no. 6, pp. 2153–2161, Jun. 2017.

[193] ——, 'Corrections to "temperature correction for cylindrical cavity perturbation measurements"', *IEEE Transactions on Microwave Theory and Techniques*, vol. 65, no. 12, pp. 5078–5078, Dec. 2017.

[194] N. Clark, G. Shaw, and A. Porch, 'Effect of Surface Stresses on Microwave Surface Resistance and Its Impact for Cavity Perturbation Measurements', *IEEE Microwave and Wireless Components Letters*, vol. 27, no. 10, pp. 939–941, Oct. 2017.

[195] Atlas-Steels, 'Alluminium Alloy Data Sheet 6063', Atlas Steels, 2013.

[196] M. Yakout, M. Elbestawi, and S. C. Veldhuis, 'A study of thermal expansion coefficients and microstructure during selective laser melting of Invar 36 and stainless steel 316L', *Additive Manufacturing*, vol. 24, pp. 405–418, Dec. 2018.

[197] A. Mertens, S. Reginster, H. Paydas, Q. Contrepois, T. Dormal, O. Lemaire, and J. Lecomte-Beckers, 'Mechanical properties of alloy ti6al4v and of stainless steel 316l processed by selective laser melting: Influence of out-of-equilibrium microstructures', *Powder Metallurgy*, vol. 57, no. 3, pp. 184–189, Jul. 2014.

[198] ASTM E289-17, 'Standard Test Method for Linear Thermal Expansion of Rigid Solids with Interferometry', ASTM International, 2017.

[199] ASTM E228-17, 'Standard Test Method for Linear Thermal Expansion of Solid Materials With a Push-Rod Dilatometer', ASTM International, 2017.

[200] TA Instruments, 'Dilatometry -L90016.000', TA Instruments, 2013.

[201] ASTM E831-14, 'Standard Test Method for Linear Thermal Expansion of Solid Materials by Thermomechanical Analysis', ASTM International, 2014.

[202] M. Okaji, N. Yamada, K. Nara, and H. Kato, 'Laser interferometric dilatometer at low temperatures: Application to fused silica SRM 739', *Cryogenics*, vol. 35, no. 12, pp. 887–891, Dec. 1995.

[203] Z. Dong, Y. Liu, W. Wen, J. Ge, and J. Liang, ‘Effect of Hatch Spacing on Melt Pool and As-built Quality During Selective Laser Melting of Stainless Steel: Modeling and Experimental Approaches’, *Materials*, vol. 12, no. 1, p. 50, 2018.

Appendices

APPENDIX A

MICROWAVE RESONATOR ANALYSIS

Microwave Resonator Analysis

Prof. Adrian Porch, November 2012

1. Introduction and Main Results

Microwave resonators can be coupled either ***capacitively*** (using an open circuit transmission line, which couples to the resonator's electric field) or ***inductively*** (using a short circuit line, which couples to the magnetic field). The equivalent circuit of an inductively-coupled resonator is shown in Fig. 1. The input and output lines are terminated in ***coupling loops***, forming a pair of mutual inductances m_1 and m_2 at ports 1 and 2, respectively, of the resonator. Each mutual inductance depends only on geometry, i.e. the loop area, its orientation and position relative to the resonator. Identical loops give symmetric coupling, with a single mutual inductance $m = m_1 = m_2$. In Fig. 1 (and in the following analysis) we ignore the self-inductances of the loops, which is a usually a good approximation in practice.

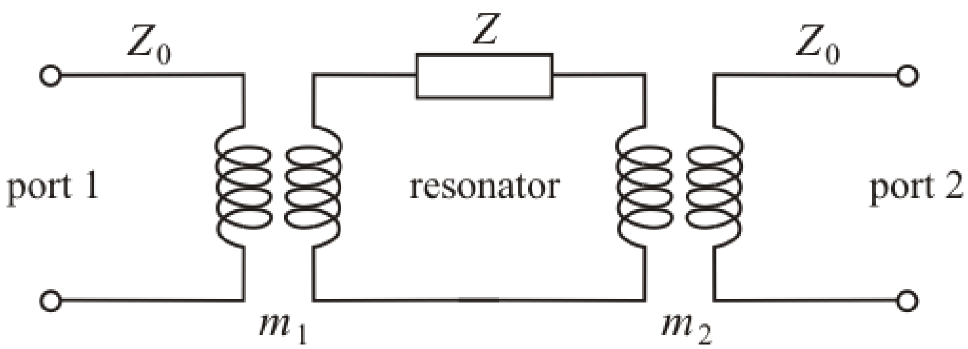

Figure 1: *The equivalent circuit of a two port, loop-coupled resonator. The resonator is modelled as a series LRC circuit, of impedance Z.*

The resonator is modelled as a series LRC circuit whose resonant frequency, impedance and (unloaded) quality factor are given by

$$\omega_0 = \frac{1}{\sqrt{LC}}, \qquad Z = R + j\omega L + (j\omega C)^{-1}, \qquad Q_0 = \frac{\omega_0 L}{R}$$

As we'll show below, circuit analysis of the loop-coupled resonator of Fig. 1 in the limit of high Q_0 gives the following results for the forward voltage transmission coefficient S_{21} and the resulting power transmission coefficient $P(f)$ in the frequency domain ($f = \omega / 2\pi$)

$$S_{21}(f) = \frac{2\sqrt{g_1 g_2}}{1 + g_1 + g_2 + 2jQ_0 \dfrac{f - f_0}{f_0}}$$

$$\rightarrow \; P(f) = |S_{21}|^2 = \frac{4 g_1 g_2}{(1 + g_1 + g_2)^2 + 4Q_0^2 \left(\dfrac{f - f_0}{f_0} \right)^2}$$

The dimensionless ***coupling coefficients*** are defined by

$$g_1 = \frac{\omega_0^2 m_1^2}{Z_0 R} = \frac{\omega_0 m_1^2 Q_0}{L}, \qquad g_2 = \frac{\omega_0^2 m_2^2}{Z_0 R} = \frac{\omega_0 m_2^2 Q_0}{L}$$

where Z_0 is the characteristic impedance of the input/output lines (usually 50 Ω). Note that $g \propto m^2 Q_0$, so that stronger coupling (and greater power transmission at resonance) is obtained by increasing m, by increasing Q_0, or by increasing both.

Usually we assume ***symmetric coupling*** (i.e. $g = g_1 = g_2$, identical coupling loops), which simplifies the analysis somewhat, though by measuring $|S_{11}|^2$ and $|S_{22}|^2$ we can determine both coupling coefficients independently (see Appendix A).

Writing $P_0 = \left(\frac{2g}{1+2g}\right)^2$ and $Q_L = Q_0\left(1-\sqrt{P_0}\right)$ $\rightarrow$ $P(f) = \dfrac{P_0}{1+4Q_L^2\left(\dfrac{f-f_0}{f_0}\right)^2}$ (1)

where P_0 is the peak power at resonance and Q_L is called the ***loaded quality factor***, which is smaller than Q_0 due to the loading effects of the coupling.

2. Circuit Analysis of Microwave Resonator Circuits

The microwave resonator and each of the two coupling loops can be assigned its own transfer matrix. The coupling loops behave like transformers and have the transfer matrices shown in Fig. 2.

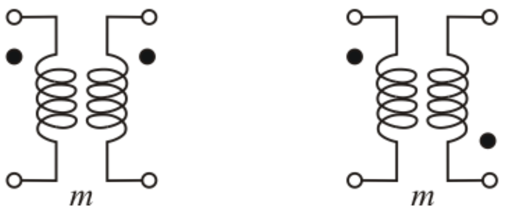

$$\begin{pmatrix} 0 & -j\omega m \\ \frac{1}{j\omega m} & 0 \end{pmatrix} \qquad \begin{pmatrix} 0 & j\omega m \\ -\frac{1}{j\omega m} & 0 \end{pmatrix}$$

***Figure 2**: Transfer matrices for the magnetic coupling loops, which act as transformers with one arm representing the coupling loop, the other the resonator. Note the sign change depending on the sense (i.e. phase) of the loop windings.*

The transfer matrix of the full equivalent resonator circuit of Fig. 1 is found using

$$\begin{pmatrix} a & b \\ c & d \end{pmatrix} = \pm \begin{pmatrix} 0 & -j\omega m_1 \\ \frac{1}{j\omega m_1} & 0 \end{pmatrix} \cdot \begin{pmatrix} 1 & Z \\ 0 & 1 \end{pmatrix} \cdot \begin{pmatrix} 0 & -j\omega m_2 \\ \frac{1}{j\omega m_2} & 0 \end{pmatrix} = \pm \begin{pmatrix} m_1/m_2 & 0 \\ \frac{Z}{\omega^2 m_1 m_2} & m_2/m_1 \end{pmatrix}$$

where the positive sign is used for coupling loops wound in the same sense, the negative sign is used for coupling loops wound in the opposite sense. The resonator is modelled as a series LRC circuit, so its series impedance Z is

$$Z = R + j\omega L + \frac{1}{j\omega C} = R + j\omega_0 L\left(\frac{\omega}{\omega_0} - \frac{\omega_0}{\omega}\right), \quad \text{with resonant frequency} \quad \omega_0 = \frac{1}{\sqrt{LC}}$$

Writing $\Delta\omega = \omega - \omega_0$, for frequencies close to resonance (i.e. $\Delta\omega << \omega - \omega_0$, an almost exact approximation for a high Q resonator) then

$$Z \approx R + 2jL\Delta\omega = R\left(1 + 2j\frac{\omega_0 L}{R}\frac{\omega - \omega_0}{\omega_0}\right) = R\left(1 + 2jQ_0\frac{\omega - \omega_0}{\omega_0}\right)$$

where $Q_0 = \omega_0 L / R$ is the unloaded quality factor of the resonator. Hence, the four elements of the coupled resonator's transfer matrix are

$$a = \pm\frac{m_1}{m_2}, \quad b = 0, \quad c = \pm\frac{Z}{\omega^2 m_1 m_2} \approx \frac{R}{\omega^2 m_1 m_2}\left(1 + 2jQ_0\frac{\omega - \omega_0}{\omega}\right), \quad d = \pm\frac{m_2}{m_1}$$

In terms of these transfer matrix elements, the S parameters of the coupled resonator are

$$S_{11} = \frac{a + (b/Z_0) - cZ_0 - d}{a + (b/Z_0) + cZ_0 + d} \qquad S_{22} = \frac{-a + (b/Z_0) - cZ_0 + d}{a + (b/Z_0) + cZ_0 + d}$$

$$S_{21} = \frac{2}{a + (b/Z_0) + cZ_0 + d} \qquad S_{12} = \frac{2(ad - bc)}{a + (b/Z_0) + cZ_0 + d}$$

Hence $S_{21} = S_{12} = \pm\dfrac{2\sqrt{g_1 g_2}}{g_1 + g_2 + 1 + 2jQ_0\dfrac{\omega - \omega_0}{\omega_0}} \rightarrow |S_{21}|^2 = \dfrac{4g_1 g_2}{(g_1 + g_2 + 1)^2 + 4Q_0^2\left(\dfrac{\omega - \omega_0}{\omega_0}\right)^2}$

where coupling coefficients at ports 1 and 2 are defined by

$$g_1 = \frac{\omega_0^2 m_1^2}{Z_0 R} = \frac{\omega_0 m_1^2 Q_0}{L}, \qquad g_2 = \frac{\omega_0^2 m_2^2}{Z_0 R} = \frac{\omega_0 m_2^2 Q_0}{L}$$

Similarly, the voltage (and power) reflection coefficients at ports 1 and 2 are

$$S_{11} = \frac{g_1 - g_2 - 1 - 2jQ_0\dfrac{\omega - \omega_0}{\omega_0}}{g_1 + g_2 + 1 + 2jQ_0\dfrac{\omega - \omega_0}{\omega_0}} \rightarrow |S_{11}|^2 = \frac{(g_1 - g_2 - 1)^2 + 4Q_0^2\left(\dfrac{\omega - \omega_0}{\omega_0}\right)^2}{(g_1 + g_2 + 1)^2 + 4Q_0^2\left(\dfrac{\omega - \omega_0}{\omega_0}\right)^2}$$

$$S_{22} = \frac{g_2 - g_1 - 1 - 2jQ_0\dfrac{\omega - \omega_0}{\omega_0}}{g_1 + g_2 + 1 + 2jQ_0\dfrac{\omega - \omega_0}{\omega_0}} \rightarrow |S_{22}|^2 = \frac{(g_2 - g_1 - 1)^2 + 4Q_0^2\left(\dfrac{\omega - \omega_0}{\omega_0}\right)^2}{(g_1 + g_2 + 1)^2 + 4Q_0^2\left(\dfrac{\omega - \omega_0}{\omega_0}\right)^2}$$

Typical plots of these power transmission and reflection coefficients for a high Q resonator (with asymmetric coupling) are shown in Fig. 3.

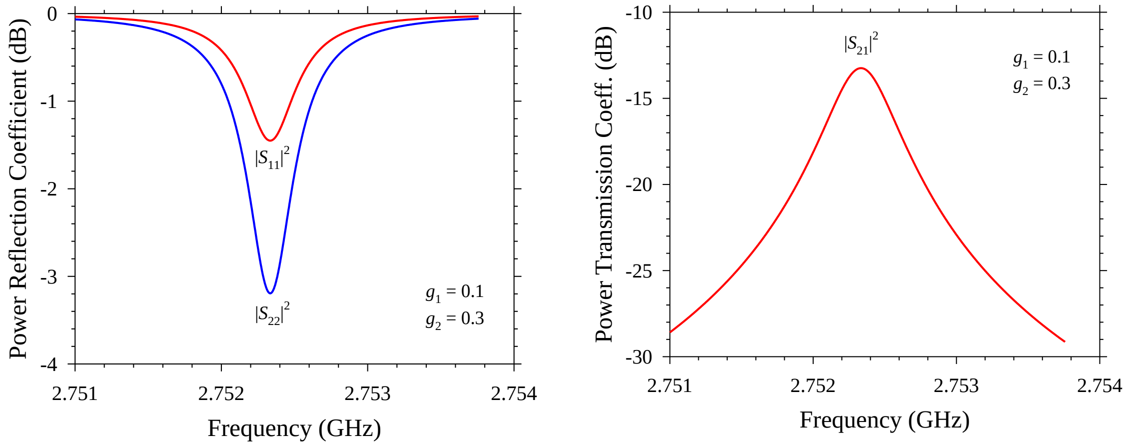

***Figure 3**: The power reflection and transmission coefficients for a high Q resonator. The coupling coefficients are 0.1 and 0.3 at ports 1 and 2, respectively (i.e. asymmetric coupling, strongest at port 2, hence the greater reflection dip at resonance).*

If the coupling coefficients at ports 1 and 2 need to be measured separately (e.g. if the coupling is asymmetric), then at resonance

$$\left|S_{11}\right|_0^2 = \left(\frac{g_1 - g_2 - 1}{g_1 + g_2 + 1}\right)^2, \quad \left|S_{22}\right|_0^2 = \left(\frac{g_2 - g_1 - 1}{g_1 + g_2 + 1}\right)^2$$

from which g_1 and g_2 can be found. Clearly, if $\left|S_{11}\right|_0^2$ and $\left|S_{22}\right|_0^2$ are measured and found to be equal (to within experimental error) then the coupling may be assumed to be symmetric.

APPENDIX B

OPTICAL MICROSCOPE IMAGES OF PBF SAMPLES

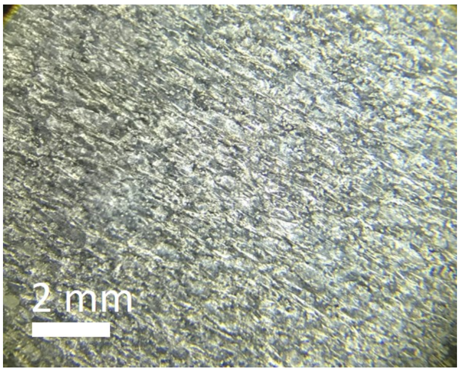

a)

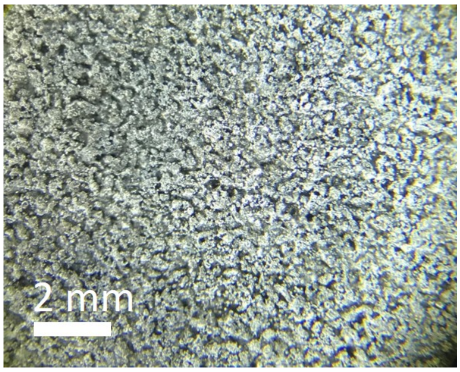

b)

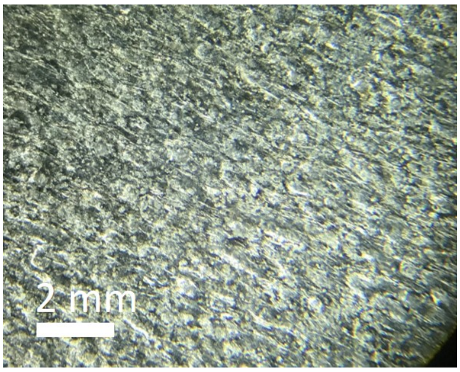

c)

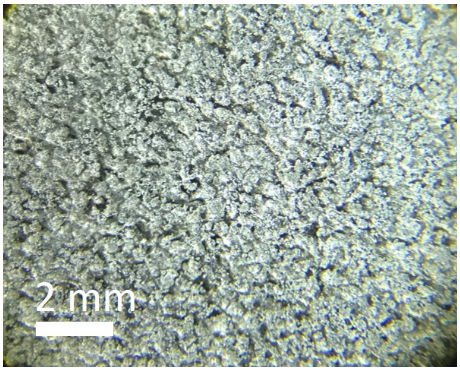

d)

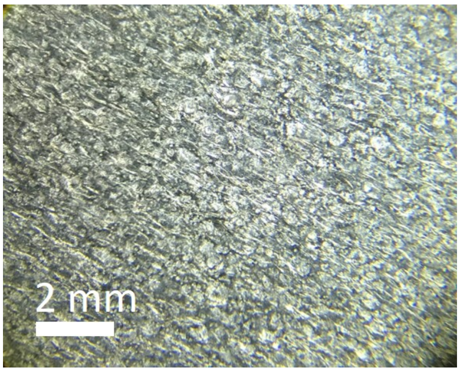

e)

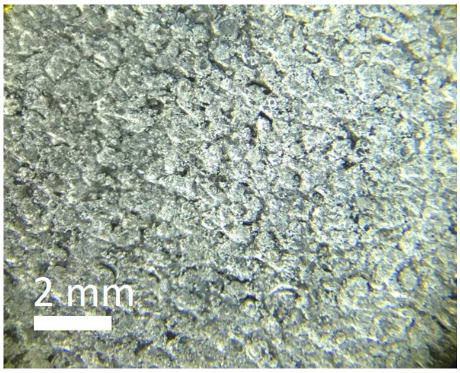

f)

Figure B.1: Optical microscope image of 45° upskin (left) and downskin (right) for laser powers, a) and b) = 80 W; c) and d) = 120 W; e) and f) = 180 W.

APPENDIX C

RMS SURFCACE ROUGHNESS MEASUREMENT

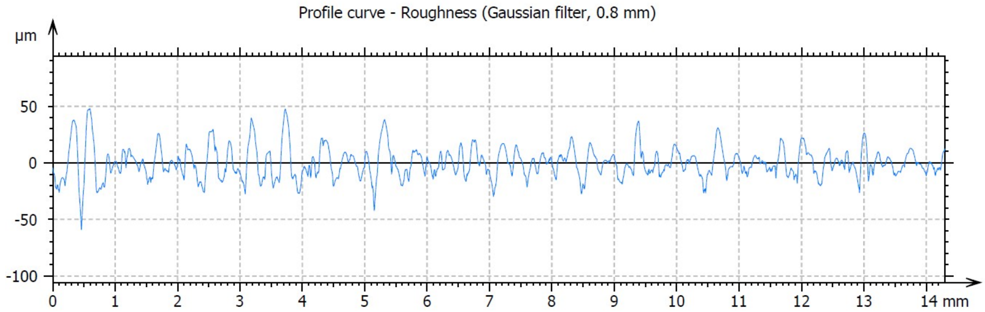

Figure C.1: Surface roughness of AlSi10Mg 'As built' vertical sample. $R_\mathrm{q} = 12.1$ μm.

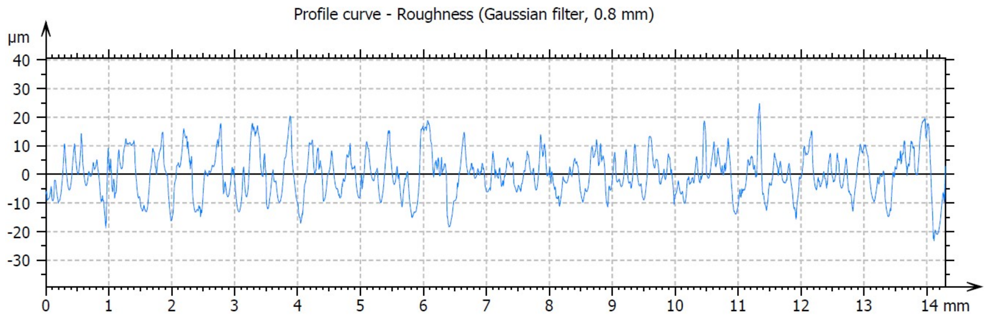

Figure C.2: Surface roughness of AlSi10Mg 'Bead blast' vertical sample. $R_\mathrm{q} = 6.26$ μm.

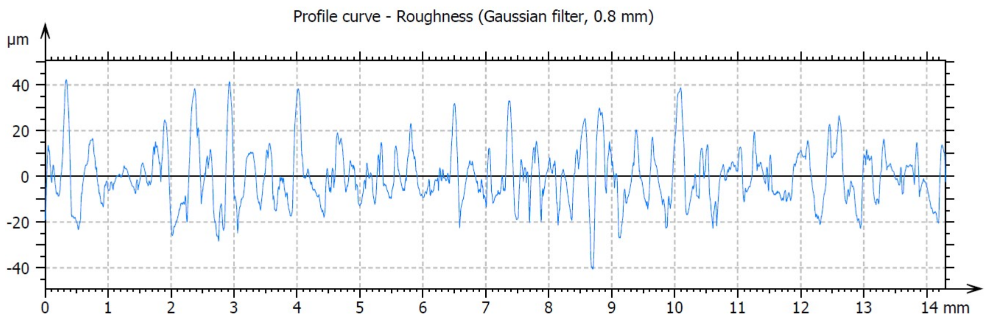

Figure C.3: Surface roughness of Silver plated AlSi10Mg 'As built' vertical sample. $R_\mathrm{q} = 10.9$ μm.

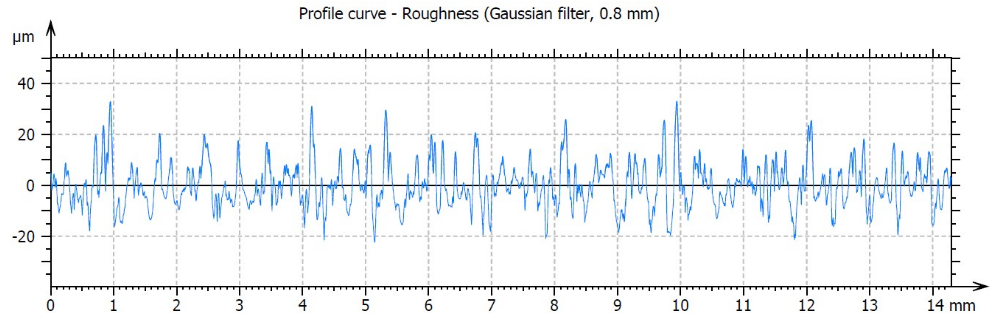

Figure C.4: Surface roughness of AlSi10Mg ‘Bead blast’ vertical sample. R_{q} = 8.13 μm.

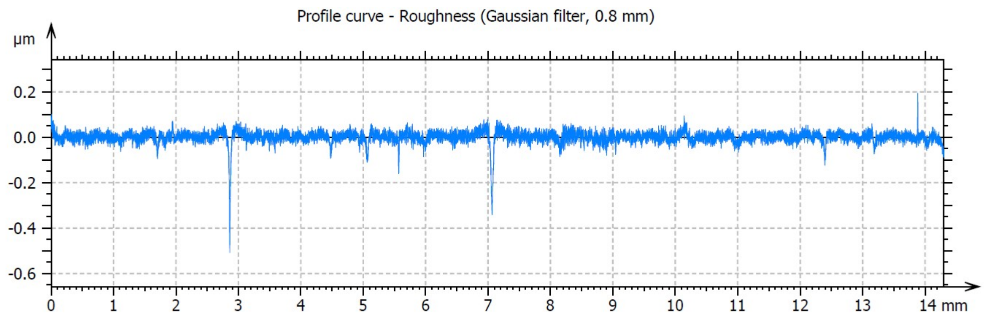

Figure C.5: Surface roughness of ‘Mirror polished’ AlSi10Mg vertical sample. R_{q} = 0.024 μm.

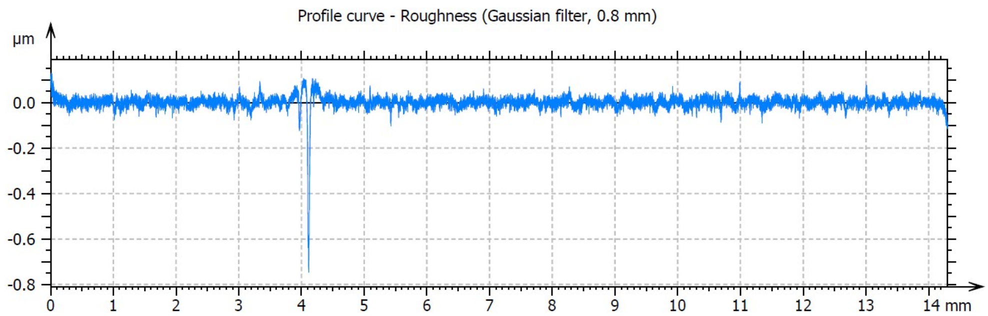

Figure C.6: Surface roughness of ‘Mirror polished’ AlSi10Mg horizontal sample. R_{q} = 0.024 μm.

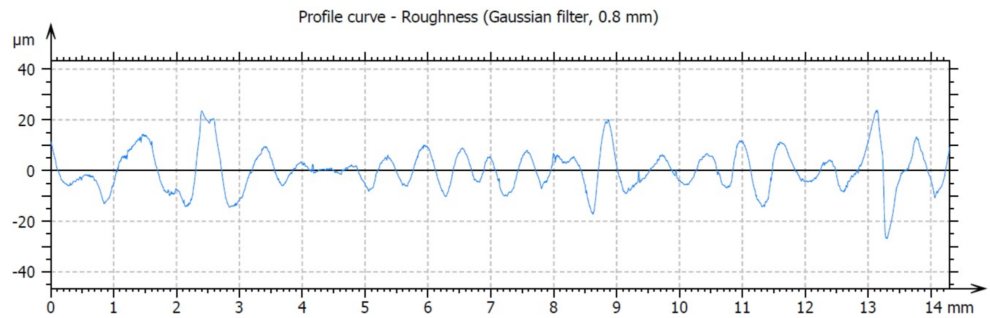

Figure C.7: Surface roughness of ‘As Built’ AlSi10Mg horizontal sample. R_{q} = 4.04 μm.

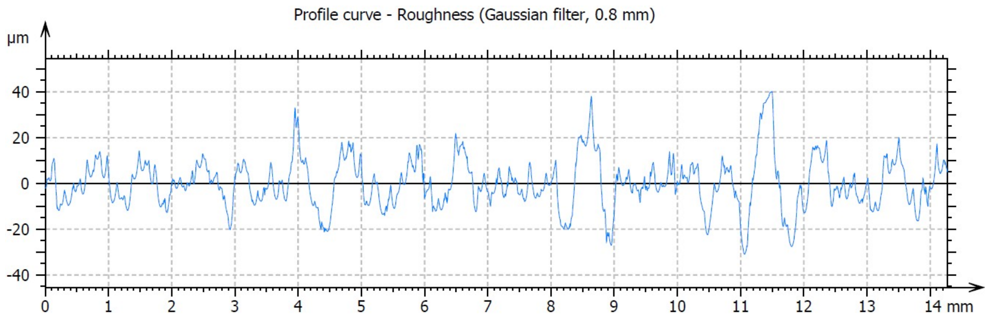

Figure C.8: Surface roughness of 'Bead blast' AlSi10Mg horizontal sample. $R_{\mathrm{q}} = 6.71\ \mu$m.

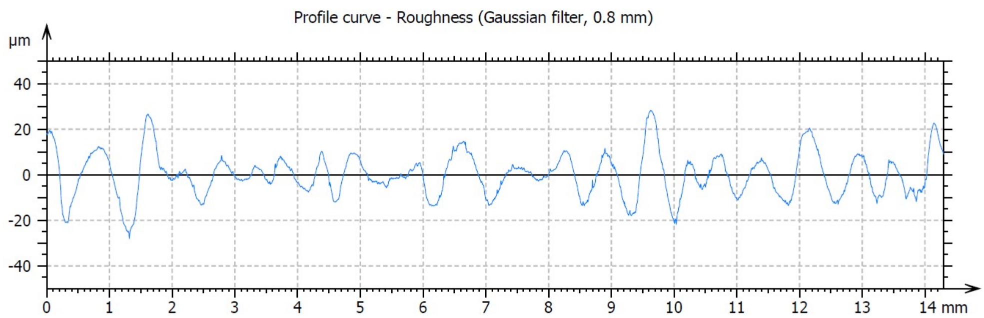

Figure C.9: Surface roughness of silver plated 'As Built' AlSi10Mg horizontal sample. $R_{\mathrm{q}} = 4.64\ \mu$m.

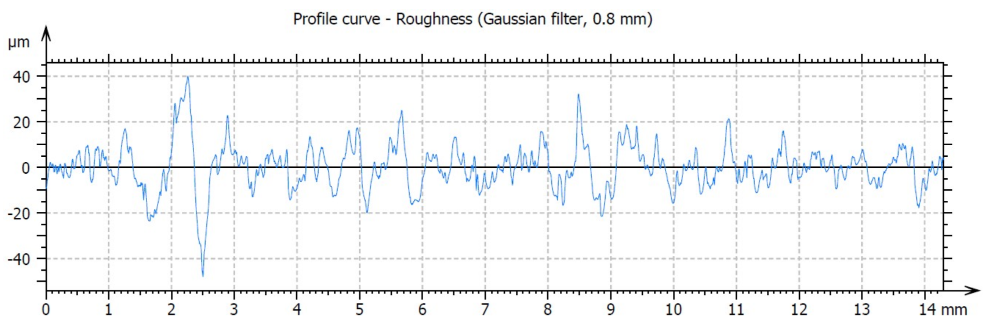

Figure C.10: Surface roughness of silver plated 'Bead blast' AlSi10Mg horizontal sample. $R_{\mathrm{q}} = 6.45\ \mu$m.

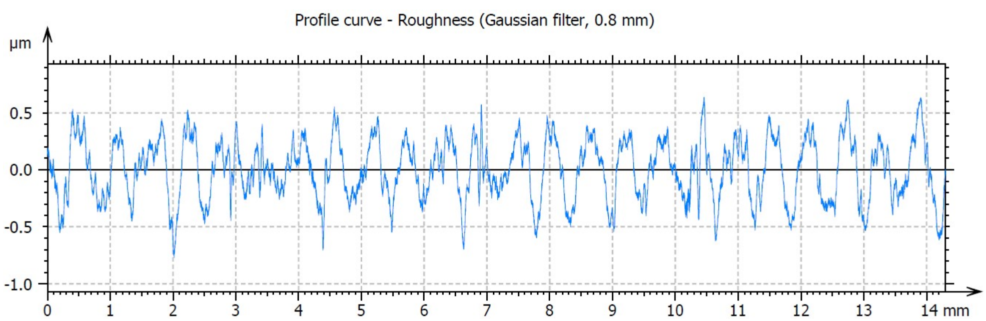

Figure C.11: Surface roughness of copper PCB sample. $R_{\mathrm{q}} = 0.24\ \mu$m.